Combining Zinc Oxide and Silver for Potential Optoelectronic Applications

Jessica H.J. Chai

A thesis submitted in partial fulfilment

of the requirements for the degree of

Doctor of Philosophy

in

Electrical and Computer Engineering

at the

University of Canterbury,

Christchurch, New Zealand.

February 2010

Abstract

Semiconductors represent the enabling technology that underpins the many advances that define modern society. One semiconductor that shows considerable promise in the fabrication of new devices is zinc oxide (ZnO). A fundamental understanding of the properties of a material is required in order to exploit its properties. The behaviour of dopants and defects relevant to optoelectronic device fabrication is of particular interest. However, acceptor doping of ZnO is currently controversial, as successful and reproducible acceptor doping has not yet been achieved. Acceptor doping of ZnO using silver (Ag) is explored in this thesis to contribute towards the understanding of defect introduction in ZnO. In addition, there is also increasing interest in exploring materials with unconventional properties, commonly referred to as metamaterials, particularly for optical applications. The previously unexplored unique combination of Ag and ZnO may enable the fabrication of those devices.

Several key factors that affect heteroepitaxy film quality, and ultimately its properties, are buffer layers and substrate temperature. A lattice match between sapphire and ZnO was provided by using buffer layers of 1 nm magnesium oxide (MgO) and 7.9 nm low temperature ZnO. The highest quality film was grown at the highest temperature (800°C), with rms roughness of 2.9 nm, carrier concentration of 3.6×10^{16} cm^{-3}, and mobility of 105 cm^2/Vs. In contrast, dopant (Ag) incorporation occurs more readily below 600°C, with dopant incorporation of up to 10^{20} cm^{-3} measured. Ag manifests as a deep acceptor (up to 94% substitutionally on Zn lattice sites), as evident from decreasing carrier concentration with increasing Ag flux, and DLTS measurements indicating an acceptor trap at 319 meV. This suggests that Ag is suitable for introducing compensation in ZnO, but Ag acceptors are not sufficiently shallow to result in p-type material. However, the unique combination of ZnO and Ag also enables the fabrication of a novel device, namely a superlens. Initial experimental results show the possibility of imaging a 100 nm line as 132 nm, compared with the diffraction-limited resolution of 332 nm for the same line feature.

Acknowledgement

No body of work can be achieved alone, and this thesis is no exception. I would like to thank my supervisor Assoc. Prof. Steve Durbin for providing endless guidance in planning experiments and then interpreting subsequent results. I would also like to thank my associate supervisor Prof. Richard Blaikie for useful discussions regarding issues during the process development of EBL. Throughout this thesis work, I have learnt many experimental skills. I would especially like to thank Dr. William Lee and Dr. Chito Kendrick for training me in the operation of the MBE system, as well as providing a close-knit feel from working together on many long growth runs. I also had the pleasure of working with Dr. Martin Allen in the fabrication of ZnO devices. Towards the later part of this thesis work, I also had the pleasure of working with Dr. Robert Burke on the superlens project. I also would like to thank Ms. Helen Devereux and Mr. Gary Turner for keeping the laboratory running.

To further understand the ZnO and ZnO:Ag growths, it was necessary to perform measurements using equipment unavailable in the nanofabrication laboratory. I had the opportunity to work with Dr. Paul Miller, Dr. Rueben Mendelsberg, and Prof. Roger Reeves from the Department of Physics and Astronomy here at the University of Canterbury, on PL of ZnO and ZnO:Ag films. I have also had the opportunity to visit Leipzig University to work with Dr. Holger von Wenckstern, Mr. Matthias Schmidt and Mr. Alexander Lajn on DLTS and TAS of ZnO devices. I was also able to visit La Trobe University and University of Auckland to work on SIMS measurements with Prof. Jim Metson. Dr. John Kennedy at GNS Science also provided many valuable measurements using RBS. Mr. Kevin Doyle and Prof. Thomas Myers also provided interesting results from variable field Hall effect measurements on several ZnO samples.

Finally, I would like to thank the Tertiary Education Commission, the Marsden Fund, and the MacDiarmid Institute for Advanced Materials and Nanotechnology for the financial support to enable me to undertake this research, as well as attending several national and international conferences over the years.

Table of Contents

Abstract i
Acknowledgement ii
Table of Contents iii
List of Figures vi
List of Tables xiv
List of Abbreviations xvi
Chapter 1 Introduction 1
1.1 Motivation 1
1.2 Properties of ZnO 3
1.3 Common ZnO growth techniques 4
1.3.1 Bulk ZnO Growth 4
1.3.2 Pulsed Laser Deposition (PLD) 6
1.3.3 Chemical Vapour Deposition (CVD) 6
1.3.4 Sputtering 6
1.3.5 Plasma-Assisted Molecular Beam Epitaxy (PA-MBE) 8
1.4 ZnO Doping Issues 13
1.5 Basics of a Superlens 17
1.6 Thesis Overview 24
Chapter 2 Growth and Characterisation Techniques 25
2.1 Reflection High Energy Electron Diffraction (RHEED) 25
2.2 Laser Reflection Interferometry (LRI) 26
2.3 Band-edge Thermometry (BandiT) 27
2.4 Evaporation 28
2.5 Electron Beam Lithography (EBL) 29
2.6 Reactive Ion Etching (RIE) 31
2.7 Electrical Characterisation Techniques 32
2.7.1 Current-Voltage (I-V) and Capacitance-Voltage (C-V) 32
2.7.2 Hall Effect 35
2.7.3 Thermal Admittance Spectroscopy (TAS) 40
2.7.4 Deep Level Transient Spectroscopy (DLTS) 42
2.8 Rutherford Backscattering Spectrometry (RBS) 45

2.9 Secondary Ion Mass Spectrometry (SIMS) 46
2.10 Photoluminescence (PL) 47
Chapter 3 Growth of Zinc Oxide Epilayers 50
3.1 Determining the Growth Environment 50
3.2 Substrate Temperature Measurement 57
3.3 Mitigating Lattice Mismatch Using MgO 63
3.4 Mitigating Lattice Mismatch Using LT-ZnO 71
3.4.1 Determining the LT-ZnO Thickness 71
3.4.2 Structural Effects of LT-ZnO Annealing 75
3.4.3 Effect of LT-ZnO Annealing on Electrical Properties 81
3.4.4 Effect of LT-ZnO Annealing on Optical Properties 83
3.5 Effect of Growth Temperature on Properties of HT-ZnO 84
Chapter 4 Silver Doping of ZnO 92
4.1 Background 92
4.2 Sources Contributing to Incorrect p-type ZnO Reports 93
4.3 Structural Effects of Ag Doping on ZnO 96
4.4 Effect of Ag Doping on Electrical Properties 101
4.5 Effect of Ag Doping on Optical Properties 105
4.6 Effect of Growth Conditions on Ag Doping of ZnO 109
4.7 Defect Levels Introduced by Ag Doping 112
4.8 Distribution of Impurities 117
Chapter 5 Use of Ag and ZnO as a Superlens Structure 121
5.1 Background 121
5.2 Fabrication of Test Patterns 122
5.3 Minimising the Sidewall Deposit 134
5.4 Planarisation of Mask Patterns 139
5.5 Ag/ZnO Stack Fabrication 142
5.5.1 DC Sputtering of Ag 143
5.5.2 RF Sputtering of ZnO 146
5.6 Initial Multilayer Ag/ZnO Stack Results 147
5.6.1 Imaging Substrate Preparation 148
5.6.2 Initial Experimental Results 150
5.7 Modified Mask Pattern 154
Chapter 6 Conclusions and Future Work 159

6.1 Undoped ZnO Growth 159
6.2 Silver Doped ZnO 161
6.3 Use of Ag and ZnO as a Superlens Structure 165
References 168
Appendix A : Film Identification 182
Appendix B : Example Growth Procedure 184
Appendix C : Multipeak Fitting Results for LT PL 187
Appendix D: Lithography Sample Identification 190
Appendix E: Superlens Fabrication Procedure 191
Appendix F: Vapour Pressure Data 192
Appendix G: Negative Refractive Index 193

List of Figures

Fig. 1.1. Ball and stick representation of ZnO crystal structures: (a) cubic rocksalt (B1), (b) cubic zinc blende (B3), and (c) hexagonal wurtzite (B4).. 4
Fig. 1.2. Schematic illustration of processes that occur during sputtering. 7
Fig. 1.3. Schematic of an MBE growth chamber [21]. 8
Fig. 1.4. Theoretical flux curves calculated using equation (1.2) for Ag, Mg and Zn. 10
Fig. 1.5. Illustration of the surface processes occurring during film growth by MBE [30]. 12
Fig. 1.6. (a) Layer by layer or Frank-van der Merwe, (b) layer plus island or Stranski-Krastanov, (c) island or Volmer-Weber mode. Θ represents the coverage in monolayers [35]. 13
Fig. 1.7. The relationship between E_{FS} and CBM/VBM of several semiconductors, as taken from ref. [54]. 15
Fig. 1.8. The location of the Fermi level stabilization energy (E_{FS}) in several II–VI compounds, as taken from ref. [52]. 16
Fig. 1.9. Image transfer from an aperture of width x that is (a) non diffraction limited when $x \geq \lambda_{DL}$, and (b) that is diffraction limited $x < \lambda_{DL}$.. 19
Fig. 1.10. Ray diagrams showing the differences in the effects on propagating (blue lines) and evanescent (red lines) waves travelling through a lens of either negative or positive refractive indices. 21
Fig. 1.11. Schematic diagram showing the experimental arrangement for planar lens lithography using a single silver imaging layer [88]. 22
Fig. 1.12. Sample configuration for superlensing experiment by Fang et al. [87]. 23
Fig. 1.13. Superlens structure containing a slab of alternating Ag and ZnO layers, on top of a PMMA-planarised Cr mask pattern. 24
Fig. 2.1. Examples of typical RHEED patterns. 25
Fig. 2.2. Schematic of an LRI setup 26
Fig. 2.3. Illustration of fit to the absorption edge of a bandedge spectrum [92] ... 27
Fig. 2.4. ZnO calibration data from kSA. 28

Fig. 2.5. Example of an e-beam evaporator setup. 29
Fig. 2.6. Comparison between positive and negative resist. 29
Fig. 2.7. Superlens test pattern. (not to scale) 31
Fig. 2.8. Schematic of processes that typically occur during anisotropic etching of a film/substrate with the structure defined by a RIE resistant mask layer. ... 32
Fig. 2.9. An example of a semi logarithmic I-V plot illustrating how I_S can be obtained. 33
Fig. 2.10. An example of a $1/C_j^2$ versus V plot illustrating how V_{bi} can be obtained. 34
Fig. 2.11. Van der Pauw contact layout for Hall effect measurements. 36
Fig. 2.12. Schematic illustrating the Hall effect. 36
Fig. 2.13. Example of parallel conduction paths in a heteroepitaxially grown film. 38
Fig. 2.14. Band diagram demonstrating charging and discharging of trap states under TAS, where E_T is the trap level. 41
Fig. 2.15. Example of a typical TAS measurement, where $C(\omega)$ is the measured capacitance and $G(\omega)$ is the measured admittance. 41
Fig. 2.16. Extraction of activation energy of trap level E_a from an Arrhenius plot. 42
Fig. 2.17. Capacitance transient at various temperature [112]. 43
Fig. 2.18. Example of a DLTS spectrum with two hole traps (HT_1 and HT_2) and two electron traps (ET_1 and ET_2). 44
Fig. 2.19. Key processes in an RBS measurement. 45
Fig. 2.20. Example of a sample sputtered using Cs^+ ions to obtain a positive mass spectrum. 46
Fig. 2.21. Typical experimental setup for PL measurements [116]. 47
Fig. 2.22. Radiative transitions observed with photoluminescence [95]. 48
Fig. 3.1. Comparison of Zn flux measured with the Zn shutter either left open or left closed for a period of time. 52
Fig. 3.2. Zn flux QCM readings with the Zn cell varied between 428°C and 500°C. 53
Fig. 3.3. Zn Δf readings (a) of all datapoints, (b) after ignoring first 4 datapoints. 53

Fig. 3.4. Growth rate plots for substrate temperature of 700°C, RF power of 400 W and oxygen flow rate of 0.5 sccm. 54
Fig. 3.5. Selected reported growth rate of films as a function of (a) Zn beam equivalent pressure (BEP) [120], (b) Zn flux [121]..... 55
Fig. 3.6. Growth rates of a ZnO film at oxygen flow rate of 0.5 sccm, RF power of 400 W, Zn flux fixed at 4.0 x 10^{14} atoms/cm^2s and the substrate temperature varied from 400°C to 700°C. 56
Fig. 3.7. Growth rate data reported by Ko et al. [122] (a) ZnO growth rates vs Zn beam flux obtained by RHEED intensity oscillations at various substrate temperatures. 56
Fig. 3.8. Micristar and BandiT outputs for a desired thermocouple temperature of 450°C. 58
Fig. 3.9. Thermal coupling route from heater to epitaxial layer. 59
Fig. 3.10. Micristar and BandiT outputs for a desired thermocouple temperature of 650°C. 60
Fig. 3.11. Plot of thermocouple temperature when the power to the heater was fixed at 29.1%. 61
Fig. 3.12. Measured average BandiT temperature (i.e. substrate surface temperature) at various heater output. 62
Fig. 3.13. Schematic illustration of (a) lattice-matched (homoepitaxy), (b) strained, and (c) relaxed heteroepitaxial structures [2]. 64
Fig. 3.14. Evolution of RHEED pattern as observed over a 10s MgO growth period. 66
Fig. 3.15. Change in rod spacing as observed in real-time RHEED. 67
Fig. 3.16. RHEED image of (a) initial Al_2O_3 substrate, and (b) after 10 s MgO growth. 68
Fig. 3.17. RHEED image of (a) initial Al_2O_3 substrate, (b) 10 s MgO growth, (c) 30 s MgO growth, and (d) 60 s MgO growth.. 69
Fig. 3.18. Change in normalised rod spacing as observed in real-time RHEED.. 69
Fig. 3.19. Top view SEM images of surface of a film grown with the MgO parameters listed in Table 3.7 (a) before etching, and (b) after etching. 70
Fig. 3.20. RHEED image of (a) MgO buffer layer just before LT-ZnO growth, (b) after 15 s LT-ZnO growth, (c) after 30 s LT-ZnO growth, (d) after 1 min LT-

ZnO growth, and (e) after 1 min 30 s LT-ZnO growth, (f) end of 2 min LT-ZnO growth. 74
Fig. 3.21. Normalised lattice spacing over the LT-ZnO growth period, for the RHEED images shown in Fig. 3.20. 75
Fig. 3.22. RHEED images showing the surface morphology of various layers.....77
Fig. 3.23. RHEED images showing the surface morphology of various layers.....78
Fig. 3.24. RHEED images of LT-ZnO annealed under O_2 plasma at (a) before annealing, (b) 1 min, (c) 1 min 30 s, (d) 2 min, (e) 2 min 30 s. 79
Fig. 3.25.Top view SEM images of HT-ZnO layers with the LT-ZnO annealed under different conditions listed in Table 3.10 and Table 3.12.....80
Fig. 3.26. AFM images of HT-ZnO layers with the LT-ZnO annealed under different conditions listed in Table 3.10 and Table 3.12.....81
Fig. 3.27. 4 K PL of various samples grown on annealed LT-ZnO.. 83
Fig. 3.28. Fitted Gaussian peaks (crosses) for various LT-ZnO annealed samples, compared with peaks reported by Meyer et al. (dashed lines) [118] 84
Fig. 3.29. Top view SEM images of ZnO films grown at (a) 400°C, (b) 600°C, (c) 700°C, and (d) 800°C. 85
Fig. 3.30. AFM images of ZnO films grown at (a) 400°C, (b) 600°C, (c) 700°C, and (d) 800°C. 86
Fig. 3.31. 5 μm by 5 μm rms roughness for films grown at different substrate temperatures. 87
Fig. 3.32. 4K PL of near stoichiometric and nominally undoped ZnO films grown between 400°C to 800°C. 88
Fig. 3.33. Room temperature Hall effect measurements of undoped ZnO films grown at several temperatures. 90
Fig. 4.1. Schematic of the structure used in ZnO:Ag doping experiments. 96
Fig. 4.2. Top view SEM of ZnO films grown at (a) undoped, (b) undoped, (c) undoped, (d) 4×10^9 Ag flux atoms/cm^{2}s, (e) 4×10^9 Ag flux atoms/cm^{2}s, (f) 4×10^9 Ag flux atoms/cm^{2}s, (g) 4×10^{10} Ag flux atoms/cm^{2}s, (h) 4×10^{10} Ag flux atoms/cm^{2}s, (i) 4×10^{10} Ag flux atoms/cm^{2}s, (j) 4×10^{11} Ag flux atoms/cm^{2}s, (k) 4×10^{11} Ag flux atoms/cm^{2}s, and (l) 4×10^{11} Ag flux atoms/cm^{2}s.....98

Fig. 4.3. RHEED images showing the evolution of surface morphology for a film doped with a Ag flux of 4×10^{20} atoms/cm^{2}s and grown at 400°C. 99
Fig. 4.4. RBS channelling results of Ag doped ZnO films about the [0001] direction. 100
Fig. 4.5. Lattice spacing calculated from RHEED of Ag doped films grown at 600°C under stoichiometric growth conditions. 101
Fig. 4.6. Electron concentration of undoped and ZnO:Ag films determined by single magnetic field Hall effect. 102
Fig. 4.7. Mobility of undoped and ZnO:Ag films determined by single magnetic field Hall effect. 104
Fig. 4.8. Resistivity of undoped and ZnO:Ag films determined by single magnetic field Hall effect. 105
Fig. 4.9. 4 K PL for various ZnO:Ag films grown at 800°C. 106
Fig. 4.10. 4 K PL for various ZnO:Ag films grown at 600°C. 107
Fig. 4.11. 4 K PL for various ZnO:Ag films grown at 400°C. 108
Fig. 4.12. Dominant peak position energy shifts with Ag doping for growth at 600°C. 109
Fig. 4.13. RHEED images of O-rich films grown (a) undoped, (b) with Ag flux of 4×10^9 atoms/cm^{2}s, and (c) with Ag flux of 2×10^{11} atoms/cm^{2}s. All films were grown at 600°C. 110
Fig. 4.14. 4 K PL of Ag doped films grown at 600°C under O-rich conditions. 111
Fig. 4.15. Broad spectrum 4 K PL of Ag doped films grown at 600°C under O-rich conditions. 112
Fig. 4.16. Frequency response of an AgO_x diode fabricated on a sample doped with a Ag flux of 4×10^{10} atoms/cm^{2}s and grown at 600°C. 113
Fig. 4.17. Frequency response of a AgO_x diode fabricated on an undoped sample grown at 800°C. 114
Fig. 4.18. DLTS spectrum of an undoped ZnO film, grown at 800°C, with an AgO_x contact, using various rate windows. 114
Fig. 4.19. DLTS spectrum of an undoped ZnO film, grown at 800°C, with an AgO_x contact, using lower rate windows to clarify the ET2 spectrum. 115
Fig. 4.20. Arrhenius fits to the HT1, ET1 and ET2 trap levels observed in the DLTS spectrum for the AgO_x contact on an undoped ZnO film. 116

Fig. 4.21. Effect of 1-1.5 hour oxygen annealing on a film grown with a Ag flux of 4×10^{10} atoms/cm^{2}s, grown at 600°C under stoichiometric conditions. 116
Fig. 4.22. (a) Positive ion (Cs^+), and (b) negative ion (O) mass spectrum for a 1.5×10^{19} Ag atoms/cm^3 doped film grown at 600°C under stoichiometric conditions. 118
Fig. 4.23. Depth profiling for a 1.5×10^{19} Ag atoms/cm^3 doped film grown at 600°C under stoichiometric conditions, using a positive ion mass spectrum. 119
Fig. 5.1. Schematic of the structure for EBL of test patterns. 123
Fig. 5.2. Effects of underdeveloping and overdeveloping on a negative tone resist, as seen in a cross section. 124
Fig. 5.3. SEM images of a 100 nm line feature exposed at 100 μAs/cm^2 and developed for (a) 40 s, (b) 80 s, (c) 100 s. 124
Fig. 5.4. Total width of features measured using SEM for 100 nm, 300 nm and 500 nm line features exposed at 100 μAs/cm^2 and developed using ma-D 532 for various developing times. 125
Fig. 5.5. SEM images of a 100 nm line feature exposed at (a) 70, (b) 100, (c) 200 μAs/cm^2. 126
Fig. 5.6. Total width of features measured using SEM for 50 nm to 500 line features exposed at various doses and developed using ma-D 532 for 80s. 126
Fig. 5.7. SEM image of a mask pattern after Cr lift-off, using an exposure dose of 100 μAs/cm^2 and a developing time of 80 s. 127
Fig. 5.8. Total width of 100 nm line features exposed at different doses and developed using ma-D 525 for various developing times 128
Fig. 5.9. Total width of 100 nm line features exposed at various doses and developed using ma-D 525 for 30s. 129
Fig. 5.10. Lithography process using bilayer resist structure. 130
Fig. 5.11. SEM image of bilayer resist stack with the PMGI layer baked at 150°C and subsequent exposure and development at 20 μAs/cm^2 and 40 s, respectively. 131
Fig. 5.12. Total width of 100 nm line features exposed at 20 μAs/cm^2 and developed using ma-D 525 for various times. 132

Fig. 5.13. Total width of 300 nm line features exposed at 20 μAs/cm^2 and developed using ma-D 525 for various times. 132
Fig. 5.14. Mechanisms of area and line exposures. 133
Fig. 5.15. Width of line exposures at various doses and developing times. 133
Fig. 5.16. SEM image of a line created by a line exposure dose of 240 pAs/cm^2 and developed for 35s. 134
Fig. 5.17. Differences in AFM scans using (a) a conventional tip, and (b) a hi-res tip, on the same features..... 135
Fig. 5.18. SEM images of mask pattern fabricated using optimum parameters. 136
Fig. 5.19. AFM cross section of the structure in Fig. 5.18(a). 136
Fig. 5.20. SEM images of mask pattern fabricated using optimum parameters, but with no sidewall deposits.. 137
Fig. 5.21. AFM cross section of the structure in Fig. 5.20(a). 137
Fig. 5.22. Sample positions on substrate holder for e-beam evaporation. 138
Fig. 5.23. SEM images of samples at position (a) A, (b), B, (c) C, and (d) D.... 139
Fig. 5.24. AFM images of the sample after (a) RIE etching, (b) baking overnight. 141
Fig. 5.25. AFM images of the sample after (a) Cr deposition, (b) after planarization. 142
Fig. 5.26. SEM images of 10 nm Ag films grown at (a) 25 W, (b) 100 W, (c) 125 W, (d) 150W. 143
Fig. 5.27. Growth times to deposit 10 nm of Ag at various DC power. 144
Fig. 5.28. AFM images of 10 nm Ag films grown at a DC power of (a) 25 W, (b) 100 W, (c) 125 W, (d) 150 W. 145
Fig. 5.29. Rms roughness of Ag films at various DC power. 145
Fig. 5.30. RF power ramp for ZnO target. 146
Fig. 5.31. (a) SEM, and (b) AFM image of a 10 nm ZnO film on quartz. 146
Fig. 5.32. Configuration used for imaging experiments using the superlens. 147
Fig. 5.33. Thicknesses of AZ MiR 701 photoresist after diluting with different ratios. 149
Fig. 5.34. AFM image of AZ MiR 701 (diluted to 1:4 ratio with EBR solvent) on top of a BARC layer. 150

Fig. 5.35. AFM image and line profile for sample 59A-1 (60 s exposure and 60 s developing time). 151
Fig. 5.36. AFM image and line profile for sample 59A-2 (80 s exposure and 60 s developing time). 152
Fig. 5.37. AFM images and line profiles for (a) PMMA only (180s exposure time), (b) two layer stack (360s exposure time), and (c) ten layer stack (999.9s exposure time). 153
Fig. 5.38. AFM images of (a) Cr apertures 100 nm wide and 1 μm apart, (b) after planarization with the plasma asher, (c) after growth of ten layer Ag/ZnO stack. 155
Fig. 5.39. AFM image and line profile of 100 nm lines from a 10 layer Ag/ZnO stack exposed at 405 nm for 1 hour and developed for 2 s. 156
Fig. 5.40. AFM image and line profile of 100 nm lines from a 140 nm PMMA stack exposed at 405 nm for 1 hour and 20 minutes, and developed for 2 s. 156
Fig. 5.41. AFM image and line profile of 100 nm lines from a 10 layer Ag/ZnO stack exposed at 405 nm for 1 hour and 20 minutes, and developed for 2 s. 157
Fig. G.1. Reflection and refraction at the interface between materials with opposite handedness. 193

List of Tables

Table 1.1. Summary of selected reported electrical characteristics for Ag doped ZnO. 17
Table 2.1. Explanation of parameters for Eqs. (2.5) to (2.9). 35
Table 3.1. Summary of growth parameters used in growth rate study. 51
Table 3.2. Summary of parameters for growth rate studies shown in Fig. 3.4 and 3.5..... 55
Table 3.3. Summary of thermocouple and surface temperature differences for thermocouple temperatures between 450°C and 650°C. 60
Table 3.4. Time taken to reach the vicinity of the saturation temperature for the exponential fit in Fig. 3.11. 61
Table 3.5. Properties of several potential ZnO growth substrates [9]. 63
Table 3.6. Summary of reported ZnO growths using MgO/LT-ZnO buffer layers via PAMBE. 65
Table 3.7. Conditions for optimised MgO buffer layer growth. 67
Table 3.8. Selected results of reported LT-ZnO growth on c-plane sapphire using PA-MBE. 72
Table 3.9. Conditions for LT-ZnO buffer layer growth..... 73
Table 3.10. Annealing parameters for various LT-ZnO buffer layers. 75
Table 3.11. Growth parameters for HT-ZnO layers for samples A1 to A4. 76
Table 3.12. Summary of conditions for vacuum annealed LT-ZnO. 77
Table 3.13. Electrical characterisation of films with different LT-ZnO annealing conditions. 82
Table 3.14. Growth parameters used in HT-ZnO substrate temperature study. ... 85
Table 3.15. FWHM of the dominant 4 K PL peaks for near stoichiometric and nominally undoped ZnO films grown at various substrate temperatures. 89
Table 3.16. Hall effect results on a sample grown at 800°C, using both conventional and variable magnetic field Hall effect measurements. 91
Table 4.1. Summary of parameters from selected p-type ZnO reports. 94
Table 4.2. Electrical properties of Ag doped ZnO as reported in ref. [66]. Mobility data was not provided in ref. [66]. 95

Table 4.3. RBS channeling results of two Ag doped ZnO films along the [0001] direction, showing the majority of Ag is incorporated on Zn sub-lattice sites. 100
Table 4.4. Hall effect measurements of a 1.5 × 10^{19} Ag/cm^3 doped ZnO film grown at 600°C.....102
Table 4.5. Summary of growth rates for different growths under O-rich conditions. 109
Table 4.6. Summary of Hall effect measurements for films grown under O-rich conditions at a growth temperature of 600°C.....110
Table 5.1. RIE etching parameters. 140
Table 5.2. Plasma asher parameters for creating a planarised PMMA layer. 142
Table 5.3. Summary of exposure and developing time experiments with sample Cr-59A.....151
Table 5.4. Summary of correct exposure and developing times for various structures and exposure wavelengths. 154

List of Abbreviations

Abbreviation	Description
1LO	First longitudinal
2LO	Second longitudinal
AFM	Atomic force microscopy
Ag	Silver
Ag_i	Silver interstitial
AgO_x	Silver oxide
Ag_{Zn}	Substitutional silver on zinc site
Al_2O_3	Alumina or sapphire
ARC	Anti-reflective coating
A_T	Transverse free A-exciton
AX	Acceptor bound exciton
BARC	Bottom anti-reflective coating
BEP	Beam equivalent pressure
BET	Bandedge thermometry
BPE	Branch-point energy
CB	Conduction band
CBED	Convergent beam electron diffraction
CBM	Conduction band minimum
CMP	Chemomechanical polishing
CNL	Charge neutrality level
Cr	Chrome
Cs^+	Positively charge caesium ions
C-V	Capacitance-voltage
CVD	Chemical vapour deposition
DAP	Donor-acceptor-pair
DIW	De-ionised water
DL	Diffraction limited
DLTS	Deep level transient spectroscopy
DMZn	Dimethyl zinc
DOF	Depth-of-focus
DX	Donor bound exciton
EB evap.	Electron beam evaporation
EBL	Electron beam lithography
ECP	Emissivity-corrected pyrometry
E_F	Fermi level
E_{FS}	Fermi level stabilisation energy
ehp	Electron-hole-pair
EPL	Electron-projection lithography
EUSP	Electrostatic-enhanced ultrasonic spray pyrolysis
EUV	Extreme ultraviolet lithography
FE	Free exciton
FFT	Fast fourier transform
FWHM	Full width half maximum
Ga	Gallium

Abbreviation	Description
GaN	Gallium nitride
GR	Growth rate
HCl	Hydrochloric acid
He	Hellium
He-Cd	Hellium-cadmium
Hg	Mercury
HMDS	Hexamethyldisilazane
HMW	High molecular weight
HT	High temperature
HV	High vacuum
InN	Indium nitride
In-Sn	Indium-Tin
IPL	Ion-projection lithography
IR	Infra-red
I-V	Current-voltage
kSA	k-Space associates
LED	Light emitting diode
Li	Lithium
Li_i	Lithium interstitial
Li_{Zn}	Substitutional lithium on zinc site
LMW	Low molecular weight
LO	Longitudinal
LRI	Laser reflection interferometry
LT	Low temperature
LT-ZnO	Low temperature zinc oxide
MCF	Multiple-carrier fit
MFC	Mass flow controller
Mg	Magnesium
MgO	Magnesium oxide
NA	Numerical aperture
NBE	Near bandedge
NIM	Negative index material
N_O	Substitutional nitrogen on oxygen site
O^+	Atomic oxygen species
O-rich	Oxygen-rich
PA-MBE	Plasma-assisted molecular beam epitaxy
PEB	Post exposure bake
PEDOT/PSS	Poly(3,4-ethylenedioxythiophene)poly(styrenesulfonate)
PIXE	Particle-induced x-ray emission
PL	Photoluminescence
PLD	Pulsed laser deposition
PMMA	Poly(methyl metacrylate)
PR	Photoresist
QCM	Quartz crystal microbalance
QMSA	Quantitative mobility spectrum analysis
RBS	Rutherford backscattering spectrometry
RBS-C	Rutherford backscattering spectrometry channelling
RHEED	Reflection high-energy electron diffraction
RIE	Reactive ion etching
SEM	Scanning electron microscopy

Abbreviation	Description
SIMS	Secondary ion mass spectrometry
SSP	Single sided polished
TAS	Thermal admittance spectroscopy
TCE	Trichloroethane
TES	Two-electron-satellite
UHV	Ultra-high vacuum
UVA	Ultraviolet light, type A
VB	Valence band
VBM	Valence band maximum
VFH	Variable field Hall effect
V_O	Oxygen vacancies
V_{Zn}	Zinc vacancies
$ZnCl_2$	Zinc chloride
Zn_i	Zinc interstitials
ZnO	Zinc oxide
ZnO:Ag	Silver doped zinc oxide
Zn-rich	Zinc-rich
ZnSe	Zinc selenide
ZnTe	Zinc telluride

Chapter 1

Introduction

1.1 Motivation

Throughout history, there are certain technological advances which characterise specific eras. For example, we have the agriculture age where humans changed from being hunter-gatherers to farmers [1]. We have the 19th century industrial age where manual labour-based manufacturing transitioned to machine-based manufacturing. Similarly, modern times can be described as the semiconductor age. The invention of the bipolar transistor in 1947 [2] transformed how we now work and play. The transistor enables the operation of modern devices such as computers and cellphones, which many use for both work and leisure activities.

The most commonly used semiconductor is silicon, due to its abundance in nature as silica, and well developed bulk single crystal growth and device fabrication techniques. Also important are the availability of high quality Si substrates and its ability to form a high quality, chemically resistant native oxide [2]. The foundation of many of today's semiconductor devices are based on fundamental building blocks such as diodes and transistors made from Si. There are many devices that are currently ubiquitous, such as ipods, DVD players, TVs, microwaves, cellphones and computers, which would not exist without this humble semiconductor. However, the fact that it is an indirect narrow bandgap semiconductor limits its usefulness for optical applications. Thus, different material systems are required: for example, LEDs made from combinations of InGaAsP, or AlGaAs, cover wavelengths between 780 to 1550 nm. These near infrared LEDs are typically used in optical fiber communications systems and

indicator display applications [3]. However, for applications such as blue laser diodes (for DVDs), and solid-state lighting, a wide bandgap material is required. Initially, such devices were made from ZnSe as it has a bandgap of 2.7 eV [4]. However, as a result of work by Shuji Nakamura and others, this was superseded by GaN (which has a bandgap of 3.4 eV [5]) as ZnSe devices are limited to low drive currents [6]. One of the key factors that determine the efficiency of an LED is the exciton binding energy of the semiconductor. Excitons have a higher density at temperatures where the exciton binding energy is higher than the thermal energy [7]. Therefore, GaN is more efficient at room temperature due to its higher exciton binding energy of 26 meV, compared to 20 meV for ZnSe, since the thermal energy at room temperature is 25.9 meV [8].

Even as work continues on refining GaN and its alloys to meet an ever-increasing range of applications, another similar semiconductor, ZnO, is starting to emerge as a possible replacement. While ZnO has a similar wide bandgap (3.37 eV), it also has a significantly larger exciton binding energy of 60 meV compared to 26 meV for GaN. This therefore allows for more efficient room temperature emission since the exciton binding energy is much higher than the thermal energy. Furthermore, the availability of high quality single crystal substrates, higher radiation hardness for space applications and compatibility with biological materials, makes ZnO an exciting material for many semiconductor applications [9, 10].

While this may give the impression that ZnO is a new and exotic semiconductor, ZnO has in fact been in use for thousands of years. One of the earliest uses of ZnO was as a component in white paint [11]. Currently, ZnO is used as an important ingredient in sunscreens as it strongly absorbs radiation in the ultraviolet, type A (UVA) spectrum [12]. In addition, ZnO is used in rubber manufacture to activate vulcanisation [13], in dental fillings through mixing with eugenol [14] and even as part of corrosion prevention in cements [15] and nuclear reactors [16]. In electronics, polycrystalline ZnO is already used to make varistors [17, 18]. However, recent progress in understanding the electronic properties of ZnO and improved material growth techniques may finally enable the use of ZnO in an optoelectronic device.

A common problem with the deposition of ZnO epitaxial films is the use of sapphire as a substrate. Lattice mismatch between the substrate and the ZnO epitaxial layer results in a high degree of defect formation. In addition, substrate out-diffusion can result in Al donor incorporation. The inclusion of both of these types of defects typically results in a high background electron concentration, which degrades the electrical properties, and consequently result in an inferior device. Therefore, a multi-layer buffer layer structure is investigated to reduce these effects, as discussed in Chapter 3.

The use of ZnO in high efficiency optoelectronic devices will likely require the fabrication of a pn junction, which therefore requires both n-type, and p-type material. The nature of the difficulty in achieving p-type ZnO is still controversial, with the best acceptor dopant currently under debate. Most p-type doping efforts have focused on the group I or V dopants. However, material with both high hole concentration and high hole mobility has yet to be reproducibly achieved, possibly due to compensating hole-killer defect formation. A less well-studied group of dopants are the group IB dopants. In particular, in Chapter 4, Ag is examined as a candidate acceptor through in-situ doping during PAMBE since the acceptor defects form more favourably under conditions that minimise native hole-killer defect formation, namely oxygen-rich conditions.

Another application employing both Ag and ZnO is in a metamaterial known as a superlens. Superlenses are of interest due to the diffraction limit hampering further progress in photolithography. Currently reported superlens structures use single layers of Ag and PMMA as the metal and dielectric layers, respectively. Studies by collaborators at Purdue University found that improved resolution can be achieved using multiple thin layers of alternating Ag and ZnO layers, if the structure approaches the homogenised limit. The fabrication and assessment of prototype structures are described in Chapter 5.

1.2 Properties of ZnO

The three known crystal structures of ZnO are rocksalt (B1), zinc blende (B3) and wurtzite (B4), as shown in Fig. 1.1. The most common form is the wurtzite structure as this is the form crystallised under equilibrium conditions. Zinc blende

ZnO may be grown on cubic substrates [9], while its rocksalt structure is only stable under high pressures [9]. The lattice parameters of the wurtzite unit cell are a = 3.2495 Å and c = 5.2069 Å. This hexagonal lattice consists of two interconnecting sublattices of Zn and O atoms. Each sublattice consists of an atom of one kind surrounded by four atoms of the other kind. This configuration results in polar asymmetry along the hexagonal axis, which gives rise to its piezoelectricity and spontaneous polarisation [9, 17, 19].

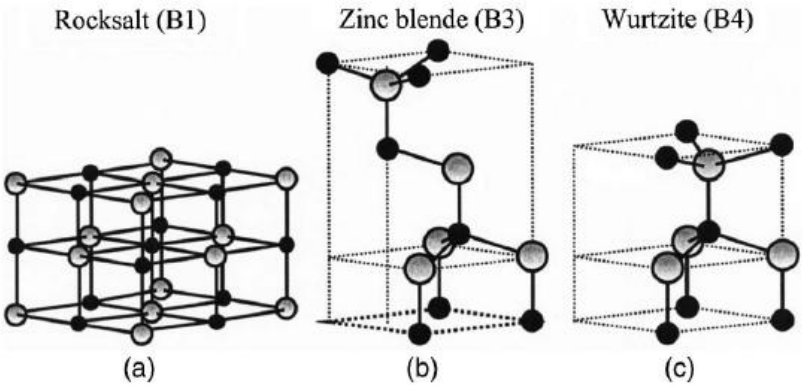

Fig. 1.1. Ball and stick representation of ZnO crystal structures: (a) cubic rocksalt (B1), (b) cubic zinc blende (B3), and (c) hexagonal wurtzite (B4). The shaded gray and black spheres denote Zn and O atoms, respectively [9].

The usefulness of a semiconductor is primarily determined by its electronic structure [20]. As ZnO is a direct bandgap semiconductor with a bandgap of 3.4 eV at 300 K and an exciton binding energy of 60 meV for the A exciton [9, 17, 21], UV excitonic emission can be sustained at room temperature and above. ZnO is currently utilised in the fabrication of transparent thin film transistors and as a visible light transparent coating for optical devices. Furthermore, these properties have stimulated research regarding using ZnO for short wavelength devices, such as blue LEDs in solid state lighting or laser diodes for DVDs [9, 21].

1.3 Common ZnO growth techniques

ZnO is prepared by a wide range of techniques, some of which are reviewed here.

1.3.1 Bulk ZnO Growth

Bulk growth of ZnO is achieved mainly by hydrothermal, vapour phase or melt growth [9]. In a hydrothermal growth system, ZnO single crystal seeds and KOH/LiOH solutions are placed in an autoclave under high temperature and

pressure [9]. ZnO then precipitates at regions of lower temperature. Some of the lowest electron concentration materials, 2.5×10^{14} cm^{-3} [22], have been achieved via the hydrothermal growth method. In vapour phase growth, ZnO source powder is placed at the hot end of a horizontal tube, where a carrier gas is then used to transport the material to precipitate at the cooler end of the tube [9]. Eagle Picher has achieved an electron concentration of 9×10^{16} cm^{-3} using vapour phase growth [22]. Another mature bulk growth technique is melt growth. This has been used successfully with silicon but is more difficult with ZnO due to its high melting point (1975°C) [21]. In melt growth, RF energy is used as a source of induction heating to create molten ZnO. A crucible is then slowly moved from the heated zone to re-crystallise the melt [9]. Cermet Inc. has achieved ZnO substrates with an electron concentration of 6.9×10^{16} cm^{-3} using melt growth [22]. The availability of high quality bulk ZnO therefore enables the use of these substrates for deposition of either ZnO or GaN epitaxial layers with low lattice mismatch.

Bulk ZnO substrates allow for the possibility of homoepitaxy growth, but homoepitaxy studies are still at their infancy, compared to heteroepitaxy. The growth rates of bulk crystals are very slow, and currently available bulk substrates are very expensive (US$ 350 for 10 mm by 10 mm bulk ZnO, compared to US$ 50 for 50 mm diameter (0001) Al_2O_3 substrates). Further, the surface defects of untreated bulk substrates are unsuitable for growth of high structural quality homoepitaxial films. The two main techniques used for removing the surface damage are chemomechanical polishing (CMP) [23, 24] and thermal annealing [23]. After CMP, the surface is no longer completely transparent as CMP can introduce additional surface defects while removing the as-grown surface defects [23, 24]. The decrease in transparency may be an issue for optoelectronic applications. Furthermore, etching results in a rougher surface, complicating subsequent epitaxy growth. Annealing can improve the step morphology of the surface but may also result in desorption and subsequent degradation of the surface morphology [23]. The optimum surface treatment is currently under debate and results are not very reproducible, likely due to variation in the surface of the as-grown bulk substrate.

Consequently, it is more typical for devices to be fabricated from thin films grown heteroepitaxially on sapphire substrates. Sapphire substrates are far cheaper than bulk substrates, as well as being completely transparent in the UV range, and hence are well suited for optoelectronic applications. Sapphire substrates represent a mature surface preparation technology, which enables the manufacture of material with reproducible properties. As a result, sapphire is currently used commercially to grow epitaxial GaN. In addition, using bulk ZnO substrate for device fabrication is unnecessary as only a thin film is required as the active area. Hence, thin films are more typically used for device fabrication.

1.3.2 Pulsed Laser Deposition (PLD)

A popular ZnO thin film growth technique is pulsed laser deposition (PLD). In PLD, high power laser pulses are used to ablate a target of the desired material, which produces a plume of the target material that interacts with the background ambient before condensing on a substrate. Some key advantages of PLD are the ability to deposit multi-component materials and compatibility with reactive gas ambient over large pressure ranges [9, 17, 25]. However, PLD has a major drawback, namely the tendency to deposit particulates on the film, thereby reducing its quality and uniformity [21, 26]. It is also difficult to scale to large wafer areas in a production setting.

1.3.3 Chemical Vapour Deposition (CVD)

Another growth technique that has been widely studied is chemical vapour deposition (CVD), as it has the ability to allow for large scale production [9]. In CVD, a carrier gas delivers the chemical reactions of vapour phase precursors to the growth zone. In the case of ZnO, the precursors used are typically $ZnCl_2$ or dimethyl zinc (DMZn). However, CVD suffers from several disadvantages due to the precursor used. Specifically, precursors are typically toxic, explosive and/or corrosive, and have hazardous byproducts [27].

1.3.4 Sputtering

A relatively simple thin film growth technique is sputtering. The key processes that occur during sputter deposition of thin films are shown in Fig. 1.2. In sputtering, ions (Ar^+) in a plasma (glow discharge) are accelerated towards the

target using either a negative bias on the target (DC magnetron sputtering) or RF power bias (RF magnetron sputtering). The accelerated ions hit the target and eject material from the target (via a transfer of momentum), which then deposits onto a substrate to form a thin film [28].

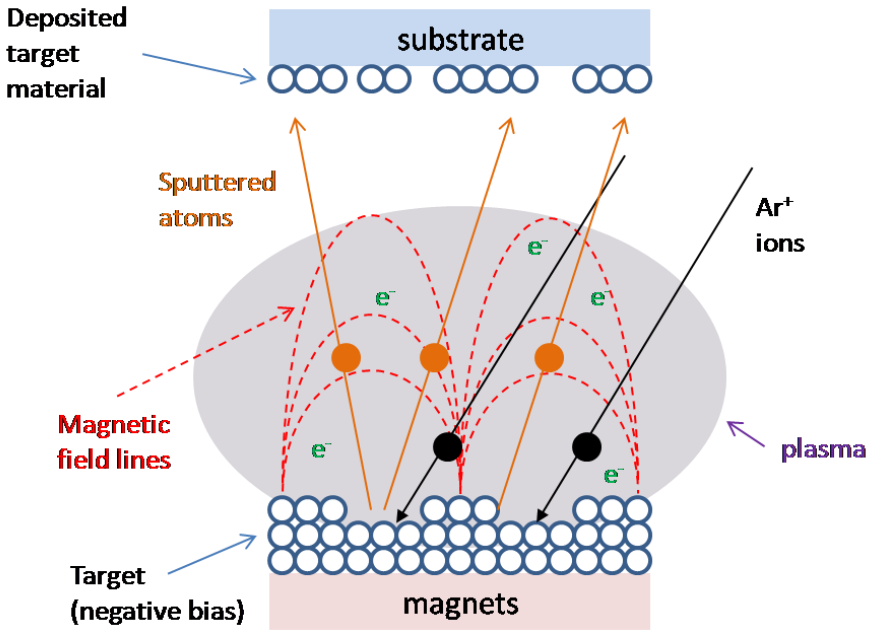

Fig. 1.2. Schematic illustration of processes that occur during sputtering.

RF sputtering is typically used when the target is insulating. With an insulating target such as ZnO, a charge will build up on the target surface if a DC bias is applied to an insulating target. The charge build-up cannot be dissipated due to the non-conducting nature of the target. This results in repulsion of further ion bombardment and consequently stopping the sputtering process. Hence, DC sputtering is only suitable for conducting targets. Confinement of the plasma near the target is also improved via the use of a magnetic field, and hence the term, magnetron sputtering [29]. This confinement is desired to trap the electrons in the plasma for longer and consequently increase the chance of ionising collisions, thereby creating a denser plasma at lower voltages [28].

Sputtering is widely used due to its ability to deposit just about any material as the film composition can mirror that of the target material. This allows for stoichiometric transfer of material from metals, insulators and alloys [29]. Reactive gases such as O_2 can also be introduced concurrently to change the composition of the desired thin film. In this thesis, a BOC Edwards Auto 500 thin

film deposition system was used to perform DC sputtering for Ag deposition and RF sputtering for both ZnO and AgO_x deposition.

1.3.5 Plasma-Assisted Molecular Beam Epitaxy (PA-MBE)

In addition to PLD, CVD, and sputtering, molecular beam epitaxy (MBE) is also commonly used in the deposition of compound semiconductors. MBE is used commercially to fabricate semiconductors such as GaAs and InP. In MBE, Knudsen cells or gas sources produce molecular or atomic beams of particular source materials. These beams are directed towards a substrate that is typically held at elevated temperatures, resulting in thin film deposition [30]. A schematic representation of the MBE chamber used at the University of Canterbury is shown in Fig. 1.3. The key parts are the ion pump (which maintains ultra-high vacuum (UHV) under idle times), a turbomolecular pump (for maintaining high vacuum (HV) during growth), a substrate heater, effusion cell sources (for the Zn, Mg and Ag sources), and a RF plasma source (for reactive oxygen species).

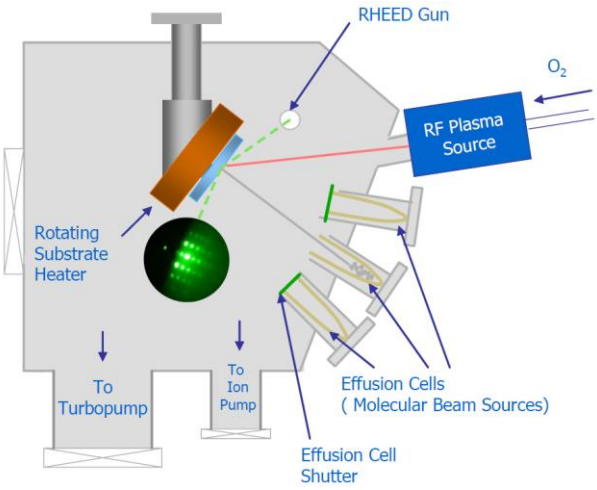

Fig. 1.3. Schematic of an MBE growth chamber [21].

The mean free path of gas molecules [30] is given by

$$L = 3.11 \times 10^{-24} \frac{T}{pd^2} \qquad (m) \tag{1.1}$$

where L is the mean free path (m), T is the temperature (K), p is the pressure (Pa), and d is the diameter of the gas molecules (m). In this thesis, film deposition occurs at 2.4×10^{-6} Torr (0.000312 Pa) and 1×10^{-5} Torr (0.0013 Pa) for ZnO and MgO film depositions, respectively. Therefore, with reactants typically having

diameters around 200 pm [31], the mean free path of the reactants are on the order of metres [28]. In contrast, the distance between the source and the substrate is typically around 20 cm. This allows for the preservation of the beam nature of mass transport [30]. Additionally, as substrates are degassed outside the growth chamber before entering it, the ultra clean nature of the growth chamber is maintained, allowing for growth of materials in a low impurity background. Another advantage of an ultrahigh vacuum (UHV) environment is that it allows for the use of a powerful in-situ characterisation tool, namely reflection high-energy electron diffraction (RHEED).

Before each growth, a substrate is first degreased using trichloroethane (TCE), acetone, and methanol. The substrate is then dried using N_2 gas. This substrate is then mounted on a 76 mm diameter molybdenum block using In or $In_{0.52}Sn_{0.48}$ solder (for growth above 650°C) before being introduced to the UHV system via a load-lock. Prior to introducing the substrate into the growth chamber, each substrate is outgassed at 650°C for an hour in the transfer tube. When a growth is to be performed, the outgassed substrate is transferred onto the substrate heater of the growth chamber. In placing the growth block on the substrate heater, a thermocouple is pressed to its backside. As there will be a gradient in temperature between the thermocouple location and the substrate surface from radiative and conductive heat losses, the substrate tends to be at a lower temperature than what is measured by the thermocouple. Implications of this effect are discussed in Section 3.2. All temperature measurements in this thesis are the thermocouple readings.

The Zn, Mg and Ag sources are provided via Knudsen effusion cells. Zn (6N) is provided via an 80 cc dual zone effusion cell with a 1 mm aperture. The 1 mm aperture restricts the beam flow and allows for a beam flow approaching the ideal Knudsen cell, but is primarily intended to reduce oxidation of the Zn source material. The 1 mm aperture sits approximately one-third from the top of the crucible for the Zn cell. The Ag (5N) and Mg (4N) sources are provided from 60 cc conical effusion cells. The flux from the effusion cell can be estimated using the Knudsen effusion equation [30],

$$I_A = 1.118 \times 10^{22} \frac{pA_e}{r_A^2 \sqrt{MT}} \tag{1.2}$$

where I_A is the impinging rate per unit of substrate area (atoms·cm^{-2}s^{-1}), p is the pressure in the effusion cell (Torr), A_e is the orifice area (cm^2), r_A is the distance from the effusion cell orifice to the substrate surface (cm), M is the molecular weight of the evaporating species (g·mol^{-1}), and T is the temperature (K). Vapour pressure curves for Ag, Mg and Zn are taken from ref. [32] and reproduced in Appendix F. A_e is 13.20 cm^2 for both the Ag and Mg effusion cells, whereas A_e is 0.01 cm^2 for the Zn effusion cell. r_A is 20 cm for all effusion cells. The theoretical flux curves for Ag, Mg, and Zn are shown in Fig. 1.4. As the flux used in MBE growth is typically around 10^{14} atoms/cm^{2}s, the Mg and Zn cells are usually operated between 350 – 400°C. Ag is used as a dopant and hence has a much larger cell temperature range, namely between 620 – 760ºC.

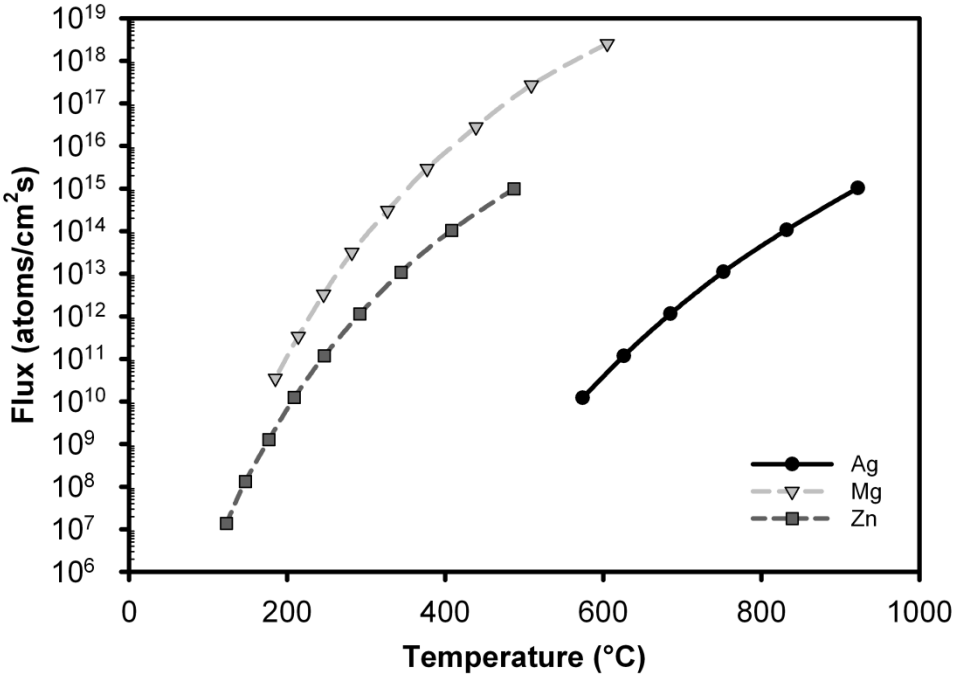

Fig. 1.4. Theoretical flux curves calculated using equation (1.2) for Ag, Mg and Zn.

While Fig. 1.4 can be used to estimate initial temperatures needed to achieve the desired flux, in-situ flux determination is achieved through a quartz crystal microbalance (QCM). In-situ flux measurements are taken using a water-cooled QCM, which is lowered close to where the substrate would sit during growth. Unloaded, the QCM operates at approximately 6 MHz. The measured frequency

then starts to decrease as material is deposited on it. The frequency difference (Δf) is sampled every 5 seconds and corresponds to a particular flux value (Γ). The flux value can be solved using the Sauerbrey equations [5, 33],

$$\Delta M = \frac{\Delta f \times \sqrt{\phi_q \times D_q} \times \pi \times d}{2 \times {F_0}^2 \times t} \tag{1.3}$$

and

$$\Gamma = \frac{\Delta M \times N_A}{M} \tag{1.4}$$

where ΔM is the change in mass (g), Δf is the crystal frequency change (Hz), ϕ_q is the shear modulus of quartz (2.95×10^{11} g·cm^{-1}·s^{-2}), D_q is the density of the quartz (2.648 g·cm^{-3}), d is the diameter of the quartz (0.5 cm), F_0 is the frequency of the clean crystal (6 MHz), t is the sample time (5 s), N_A is Avogadro's number (6.02×10^{23} molecules·mol^{-1}), and M is the molecular weight of the measured deposited material (g·mol^{-1}). Chapter 3 discusses stability issues studies using such a measurement method.

While solid sources are turned into molecular beams using effusion cells, the reactive oxygen species are provided from an Oxford Applied Research HDP21 inductively coupled RF plasma source. In such a plasma source, RF power is used to excite pure O_2 gas into active oxygen species, which may consist of neutral molecular oxygen O_2, molecular oxygen ions O_2^+, neutral atomic oxygen O, and atomic oxygen ions O^+ [21, 34]. The flow rate of the O_2 gas is controlled by a mass flow controller (MFC) and is set at 0.5 and 2 sccm for ZnO and MgO depositions, respectively. A previous study using the MBE system at the University of Canterbury [21] found that excessive RF powers may lead to increased dislocation density through increased pit formation. Nevertheless, it was also found that higher RF powers resulted in greater cracking efficiency and the smoothest films. Hence, the compromise was found to occur at 400 W, which is the RF power used throughout this thesis.

The main processes during MBE are governed by surface kinetics, as illustrated schematically in Fig. 1.5. The impinging adatoms arrive on the surface of a substrate and may react with the crystal lattice in several ways [29, 30]. The

arriving atom may re-evaporate immediately upon contact with the growing surface (desorption). If the impinging atoms do not re-evaporate, they are then adsorbed onto the surface via physisorption, where the atom is attracted to the surface through van der Waals forces, or via chemisorption, where there is an electron transfer/chemical reaction between the impinging atoms and the surface. These absorbed atoms then diffuse some distance across the surface before finally incorporating into the crystal lattice of the substrate (nucleation) or growing film (epitaxial growth).

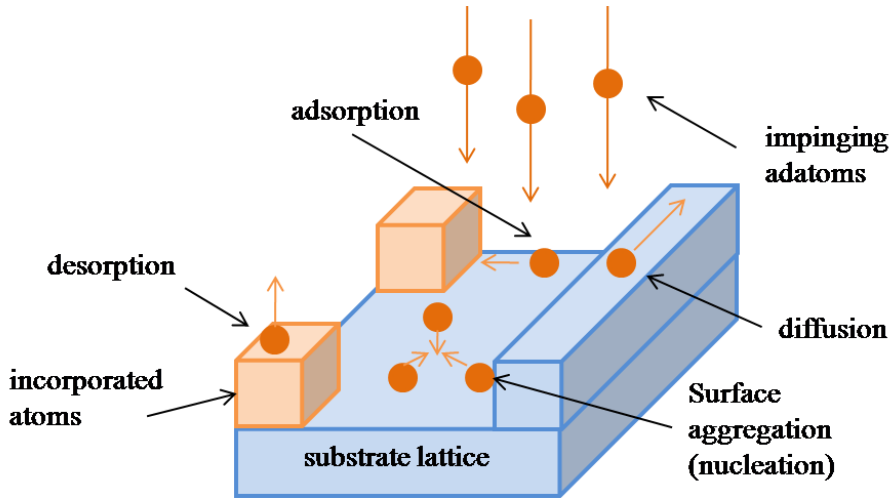

Fig. 1.5. Illustration of the surface processes occurring during film growth by MBE [30].

There are several possible growth modes, as illustrated schematically in Fig. 1.6. In layer-by-layer or Frank-van der Merwe growth, the strong bonding between the film and the substrate results in successful wetting, as the surface energy is minimised. This is the growth mode most desired when growing epitaxial semiconductor films as surface roughness and dislocation densities are minimised. If the adatoms are more strongly bonded to each other than to the surface, then they unsuccessfully wet the surface, resulting in small clusters aggregating into islands. Such a growth mode is known as island or Volmer-Weber growth. This growth mode is usually undesirable, as the resultant film tend to be rough and inhomogeneous. It is also possible to have a combination of island and layer-by-layer growth (Stranski-Krastanov), which may occur when the surface energy changes from monolayer to monolayer. This growth mode is most typical of epitaxial growth [29, 30].

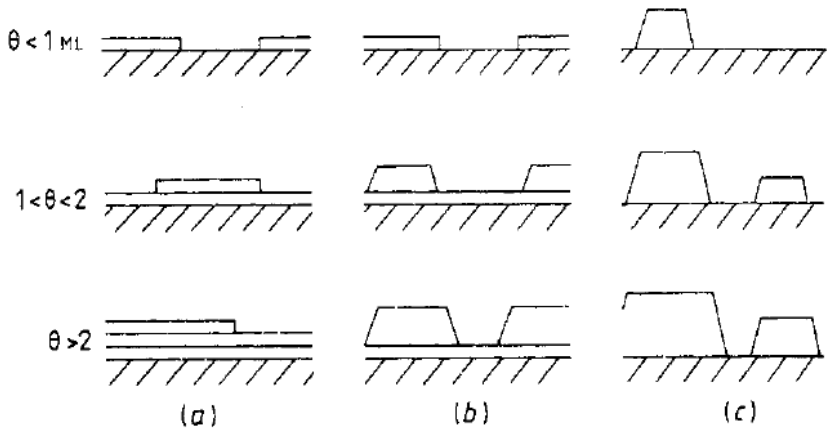

Fig. 1.6. (a) Layer by layer or Frank-van der Merwe, (b) layer plus island or Stranski-Krastanov, (c) island or Volmer-Weber mode. Θ represents the coverage in monolayers [35].

1.4 ZnO Doping Issues

In order for a semiconductor to be useful in making optoelectronic devices, it must be able to be doped n-type and p-type, as device applications require control over electrical properties. As grown, ZnO is normally n-type due to the presence of intrinsic defects (for example, O vacancies (V_O) and Zn interstitials (Zn_i) [36]) or unintentional H incorporation during film deposition [37]. However, the exact dominant n-type defect is presently a matter of debate [17, 37, 38]. There are numerous successful reports regarding highly conductive n-type ZnO films, with typical n-type dopants being Al, Ga or In substituting for Zn sites [9, 39-41]. ZnO:Ga films with resistivity as low as 1.2×10^{-4} Ω cm [41] and electron concentration in the 10^{20} cm^{-3} range [40] have been reported.

P-type ZnO, in contrast, remains a highly controversial subject due to stability and reproducibility issues. One of the most widely studied acceptors is lithium (Li). Theoretically, Li should form a shallow acceptor, with the (-1/0) transition level lying at 40 meV [42]. However, Li is more likely to occupy interstitial sites and form shallow donors due to its small atomic radius [9]. Therefore, even though Li may be suitable for creating semi-insulating ZnO, it appears unsuitable as a dopant to turn ZnO p-type due to competing formation of Li_{Zn} and Li_i [43].

Group V dopants such as nitrogen have also been widely studied as a result of successful p-type doping of another II-VI semiconductor via PA-MBE, namely ZnSe [44, 45]. As nitrogen has a similar electronic core structure and ionic radius to O, N_O should form readily and strain effects due to N_O incorporation can be

minimised [17]. However, the true picture is more complicated as nitrogen doping requires a Zn-rich growth condition for high nitrogen incorporation [46, 47]. This leads to increased formation of self-compensating defects such as V_O and Zn_i, which compensates for N_O [48-50]. Hence, nitrogen doping has not succeeded in reproducibly high hole concentration, high mobility and/or low resistivity p-type ZnO.

Such asymmetry in doping properties is typical of some semiconductors such as GaN, ZnSe, and ZnTe. The doping asymmetry may be caused by limited solubility of desired dopants, desired dopants producing deep defect levels or spontaneous formation of compensating defects [51]. Spontaneous formation of compensating defects has been explained in terms of the Fermi level stabilisation energy (E_{FS}) [52]. E_{FS} is the Fermi energy determined solely by native defects. Experimentally, E_{FS} is determined by inducing a sufficiently high damage density such that the Fermi energy stabilises at a certain energy and is unchanged with further damage [52]. Therefore, E_{FS} is an intrinsic property of a material. The term (but not the definition) of E_{FS} has changed over time and is therefore also known in recent literature as the charge neutrality level (CNL) [53] or branch-point energy (BPE) [54].

The implication of the existence of an E_{FS} level for every semiconductor means that the act of doping to change the Fermi level (E_F) induces increased formation of compensating native defects via lowering of their corresponding formation energy to return E_F back to E_{FS}. For example, InN is a semiconductor in which it is notoriously difficult to detect p-type conduction due to the existence of a surface accumulation layer [55]. Figure 1.7 shows that E_{FS} for InN lies inside the conduction band minimum (CBM), resulting in charge accumulation due the bulk band structure. Therefore, InN is naturally n-type [55].

A similar effect exists when one analyses the E_{FS} for GaN. With an E_{FS} close to the CBM (Fig. 1.7), few compensating acceptor native defects will be formed when n-type doping, resulting in high electron concentration n-type films. However, should there be a desire to dope GaN p-type, there is a large energy difference needed to shift E_F closer to the VBM. The further away E_F needs to be from E_{FS}, the lower the formation energy of donor native defects and hence the

larger the concentration of self-compensating hole-killer defects to compensate for the introduced acceptors [38].

There have been only a few published studies regarding determining the E_{FS} level for ZnO [52, 54, 56, 57]. As shown in Figs. 1.7 and 1.8, the reported E_{FS} level for ZnO is either within the CBM or close to the CBM. This implies doping asymmetry issues, similar to those that occur with other semiconductors, such as GaN and InN, with a similar relative E_{FS} level. The ease of n-type, but the difficulty in p-type doping of ZnO appears to support this explanation. Therefore, unconventional dopant techniques or dopant types have been proposed in order to overcome these self-compensating problems when attempting to dope ZnO p-type.

As well as p-type doping asymmetry, n-type doping asymmetry exists, as reported by studies with ZnTe. It is easy to dope ZnTe p-type but very difficult to dope n-type [58]. E_{FS} for ZnTe is closer to the valence band maximum (VBM) than the CBM (Fig. 1.8). This means that E_F needs to be moved less to be closer to the VBM for shallow p-type doping, compared with the much larger energy difference needed to achieve n-type doping. In contrast to InN, GaN and ZnO, attempts at n-type doping of ZnTe results in spontaneous formation of compensating acceptor defects, which neutralise some of the extrinsic donors introduced.

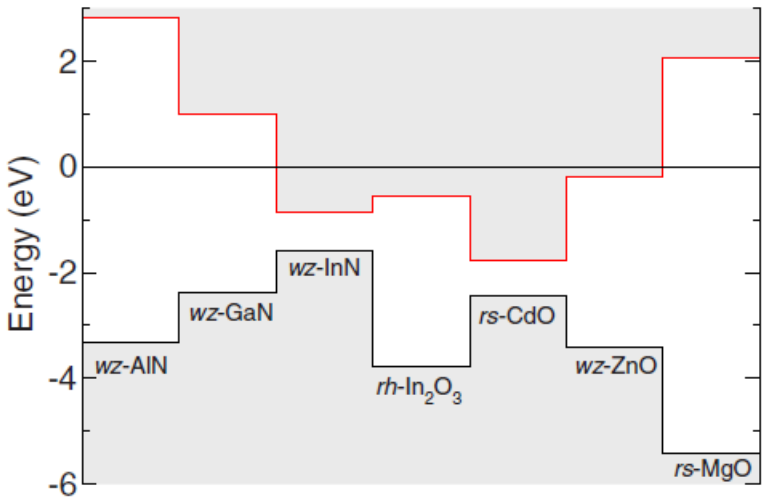

Fig. 1.7. The relationship between E_{FS} and CBM/VBM of several semiconductors, as taken from ref. [54]. The CBM and VBM have been drawn with those levels adjusted so that E_{FS} lies at 0 eV.

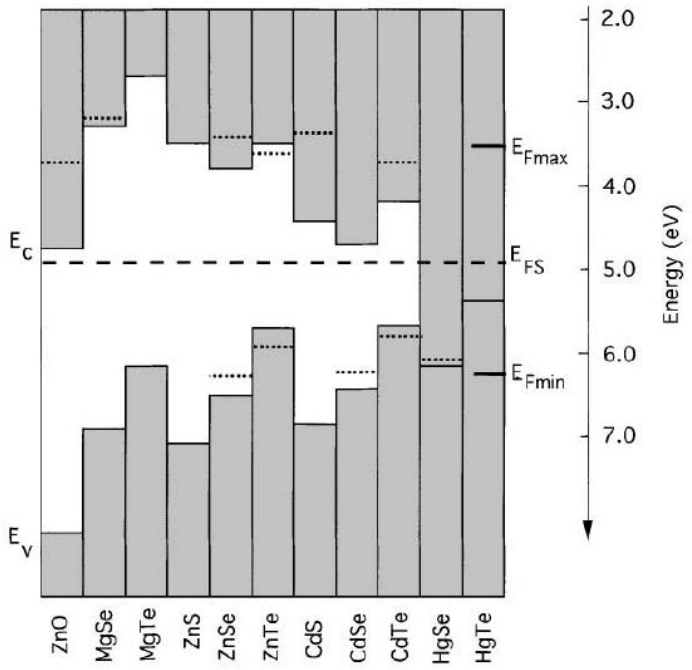

Fig. 1.8. The location of the Fermi level stabilization energy (E_{FS}) in several II–VI compounds. From ref. [52].

A potential method to overcome this self-compensation problem is by reducing the likelihood of defect formation. Yan et al. [50] recently published first principles calculations advocating group IB dopants as potential acceptors for ZnO, particularly Ag. Ag was found to have the lowest ionisation energy (0.4 eV above VBM) among the group IB dopants investigated. Ag_{Zn} forms more readily under O-rich growth conditions, which may also alleviate the self-compensation issue. Further, Ag is highly soluble in ZnO, which therefore allows for a high dopant concentration. A study by Wan et al. [59], which located the Ag_{Zn} level at 0.444 eV above VBM, appears to confirm the findings of Yan et al. Recently, Hu et al. [60] used hybrid density functional approximations to calculate transition levels at 0.18 and 0.38 eV above the VBM for Ag_{Zn}^{0} and Ag_{Zn}^{1-}, respectively. In addition, $Ag_{i,O}^{1+}$ was found to lie at 0.24 eV below the CBM. Hu et al. postulated that the PL emission at 3.17 eV reported for ZnO:Ag films is possibly due to one of the aforementioned defect levels.

Currently, there are few experimental reports of Ag doping [61-73]. Table 1.1 shows that reported electrical measurements for Ag doped ZnO varies widely between different growth techniques and also annealing is sometimes, but not always, necessary. While some groups may report p-type ZnO:Ag, when one

looks at their complete series of measurements, care is needed to interpret the results as a sudden switch of carrier type is suspicious. Furthermore, Hall voltages are very sensitive to fluctuations when measurements are performed on either highly conductive or highly resistive samples. Therefore, there are still many unresolved issues and hence Chapter 4 presents an extensive Ag doping study with both analysis of the obtained experimental results [62] and scrutiny of the surrounding literature.

Table 1.1. Summary of selected reported electrical characteristics for Ag doped ZnO.

Growth technique	Carrier concentration (cm^{-3})	Mobility (cm^2/Vs)	Resistivity (Ω cm)	Carrier type	Other effects	Ref.
EUSP[+]	1.61×10^{14}	7.86	4.92×10^{3}	p	-	[74]
EB evap.*	5.01×10^{21}	-	7.35×10^{-3}	p	-	[66]
EB evap.*	5.09×10^{19}	1.69	7.35×10^{-2}	p	-	[75]
RF sputter*	2.24×10^{16}	1.83	152	p	Semi-insulating as grown	[68]
PLD	6.0×10^{17}	2.32	54	p	-	[73]
PLD	5.9×10^{19}	2.87	0.00198	p		[76]
RF sputter	-	-	-	-	ρ decreased due to Ag aggregation	[77]
EB evap.	-	-	1.2×10^{5}	-	Enhanced UV emission	[78]
DC sputter*	Rectifying I-V of "p-n" junction claimed				Enhanced UV emission	[61]

[+] Electrostatic-enhanced ultrasonic spray pyrolysis
*denotes electrical properties measured after annealing
Evap. denotes evaporation

1.5 Basics of a Superlens

Beyond application in optoelectronic devices, ZnO has potential to form a novel device as a component in a metamaterial. A metamaterial is a material that gains its properties not from its constituent atoms, but from its structure. A metamaterial is therefore essentially a structure that has been engineered to have properties that do not occur naturally. In recent years, metamaterials have gained increasing interest due to their applications in "invisibility" [79], or as a "perfect lens" that can image below the diffraction limit [80]. Imaging beyond the diffraction limit is of particular interest in photolithography.

Due to the dominance of electronics in daily life, innovators continually push the limits as to what is possible with the current state-of-the-art. One factor that enables the fabrication of electronic devices is lithography. Hence, there is currently a great deal of interest in continually pushing the boundaries of lithography capabilities to make next generation devices. Traditionally, several aspects of photolithography were incrementally improved to further extend the use of photolithography. However, reduction to nanometre scale resolution requires increased complexity, and viable alternatives are being actively sought.

Two key figures of merit in a lithography process are resolution (R) and depth-of-focus (D_F) [81], given by

$$R = k_1 \frac{\lambda}{NA} \tag{1.5}$$

and

$$D_F = \pm k_2 \frac{\lambda}{NA^2} \tag{1.6}$$

The resist process parameters are represented by k_1 and k_2, λ is the wavelength of the light, and NA is the numerical aperture. Improvements in lenses have greatly reduced lens aberrations and NA, with the highest NA currently being 0.92 [81]. By introducing a high index of refraction between the lens and the wafer (immersion lithography), it is possible to increase NA beyond 1.0 [81]. However, additional process steps naturally incur further costs.

A key metric in photolithography is the diffraction limit, where features smaller than the wavelength of light cannot be adequately resolved. Figure 1.9 illustrates why such a diffraction limit exists. Essentially, an image transfer via an aperture will ideally be a perfect replica of the aperture. The light intensity on the imaging surface (i.e. resist) is ideally a square wave (Fig. 1.9(a)). However, such a "square wave" has many frequency components. If the aperture width is less than the wavelength, then some of the high frequency components (i.e. evanescent waves) of the "square wave" are lost as they exponentially decay. This results in a waveform that has lost some of its high frequency components since the transfer function representing the imaging medium has a cut-off at λ_{DL}, as shown in Fig.

1.9(b). This leads to only the lower frequency components (i.e. propagating waves) being transferred. Effectively, a medium with a positive refractive index acts as a low pass filter with exponential decay of the intensity above the frequency cut-off represented by the frequency of the imaging light source.

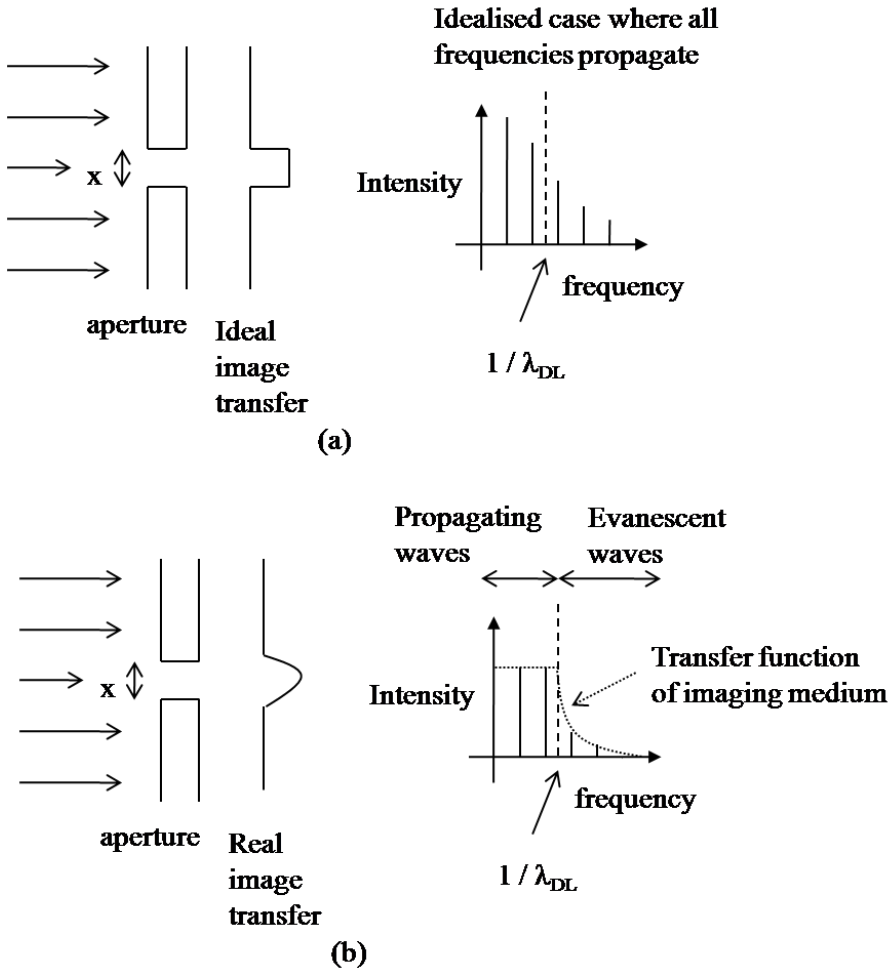

Fig. 1.9. Image transfer from an aperture of width x that is (a) non diffraction limited when $x \geq \lambda_{DL}$, and (b) that is diffraction limited $x < \lambda_{DL}$. DL represents diffraction limited.

To further delay diffraction limits from having an impact, the wavelength used for photolithography has been continually reduced. Currently, excimer lasers such as KrF (248 nm), ArF (193 nm), and F_2 (157 nm), are available in production use [81]. Several options for producing wavelengths below 157 nm do exist [81], namely Ar_2^* (126 nm), and hydrogen Lyman-α line (121.5 nm). However, these light sources are far from commercialisation. Furthermore, as the wavelength is reduced, the number of transparent materials available for making resists or lenses is reduced as well.

As optical lithography is ultimately limited by diffraction, there is increased interest to develop alternative lithography techniques. Examples include x-ray lithography, extreme ultraviolet lithography (EUV), electron beam lithography (EBL), electron-projection lithography (EPL), ion-projection lithography (IPL), and imprint lithography [81]. None of these techniques is ready/suitable for mass production yet. Furthermore, even if the problems inherent with each technique are solved, there are still significant costs associated with replacing existing lithography setups.

One possibility for bypassing all the issues associated with developing completely new lithography processes is by using a lens that will enable subwavelength resolution using the Hg lamp source. In 1968, Veselago theorised that metamaterials can be fabricated to have properties such as a negative index of refraction [82]. Metamaterials do not violate any laws of physics, but still have reverse Snell's law, Doppler shift, and Cerenkov radiation. The refractive index n is given by

$$n = \pm\sqrt{\varepsilon\mu} \tag{1.7}$$

If either ε or μ is negative, this leads to n being imaginary, where the complex component of n will absorb/reflect the incoming waveform. Negative permittivity requires electric resonance, whereas negative permeability requires strong magnetic resonance. Therefore when both ε and μ are negative, n is negative [82-84], and the material supports propagating waves (i.e. the material appears transparent to both electric and magnetic fields). However, while metals typically exhibit negative ε in frequencies below the characteristic plasma frequencies, μ is always positive [85].

In 2000, Pendry [86] proposed that a slab of negative index media (NIM) could be a 'perfect lens', where the evanescent waves are enhanced instead of decaying, as demonstrated in Fig. 1.10 [79, 85, 87]. Evanescent waves are enhanced by coupling to resonant surface waves such as surface plasmon polaritons. While perfect lensing has been demonstrated using photonic crystals at microwave frequencies [83], achieving such beam bending and refocusing at optical

wavelengths is more difficult due to the diminishing magnetic susceptibility of suitable natural materials [88]. However, the electric and magnetic responses are decoupled in the near field [86], allowing for enhanced resolution to be achieved using materials with a negative permittivity only. This approximation to a "perfect lens" is known as a superlens. The superlens has lower resolution than a perfect lens as the evanescent waves are not enhanced to the same degree as with a perfect lens. However, subwavelength imaging can still be achieved with a superlens. The near field is defined as the quasistatic limit, where the dimensions of the imaging material are significantly smaller than the wavelength used for imaging [85]. Pendry proposed Ag as a superlens material due to it having a negative ε at optical frequencies and hence having potential to achieve a superlens effect for transverse magnetic (TM) polarised light; this has been demonstrated experimentally recently [89].

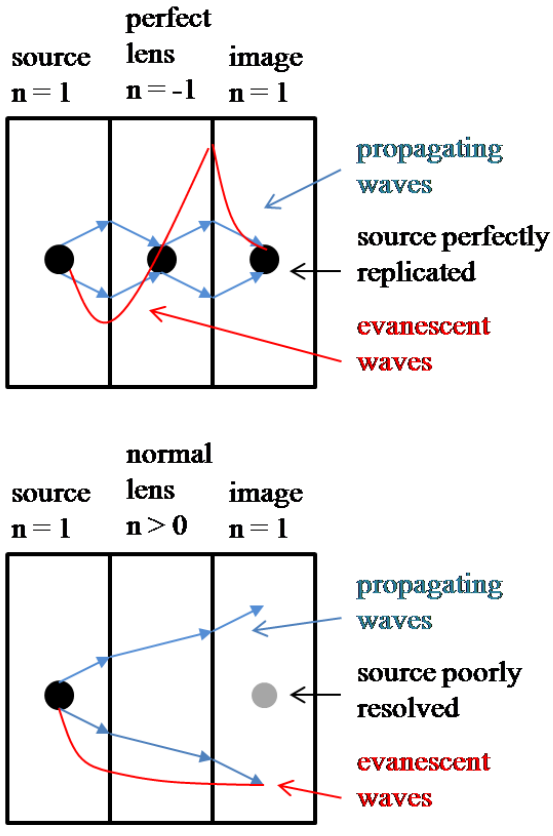

Fig. 1.10. Ray diagrams showing the differences in the effects on propagating (blue lines) and evanescent (red lines) waves travelling through a lens of either negative or positive refractive indices.

A material with optical anisotropy where all plane-wave components from the image propagate can achieve improved subwavelength resolution [90]. This anisotropy at IR and optical frequencies can be achieved using a metal-insulator structure. There are several reports [80, 87-89, 91] on the successful fabrication and testing of such a superlens structure. All experimental reports employed the i-line of the Hg lamp (365 nm). Melville et al. [89, 92] employed a 25/50/10-PMMA/Ag/SiO_2 structure (Fig. 1.11). In this structure, the mask patterns were created using EBL on a tungsten coated coverslip with 120 nm PMMA. The PMMA pattern was transferred onto the tungsten film via RIE with SF_6 plasma. After removing the PMMA layer, another PMMA layer was spin coated and then etched down to 25 nm for planarisation. Ag and SiO_2 were then sputtered onto the PMMA to complete the structure. Using the mercury i-line (365 nm), Melville et al. [89, 92] achieved a maximum resolution of 145 nm, well below the resolution limit of 243 nm. The image depth achieved was ~ 5 nm and line-edge roughness comparable to the half-pitch of the resolved gratings. Broadband and filtered i-line exposures showed similar results, most likely due to the self-filtering nature of such a lens. That is, the lens will appear opaque for wavelengths outside the resonance condition [89].

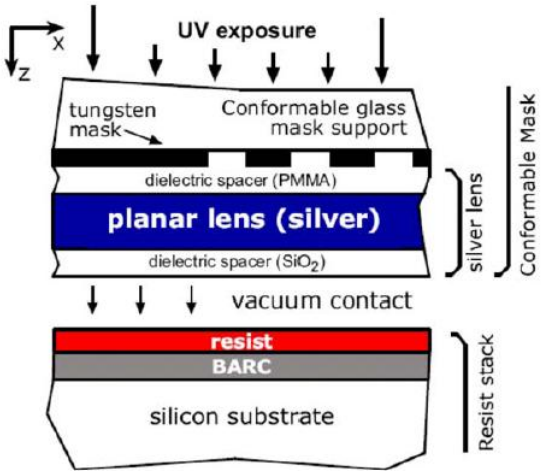

Fig. 1.11. Schematic diagram showing the experimental arrangement for planar lens lithography using a single silver imaging layer [89].

Fang et al. [88] have also successfully fabricated a Ag based superlens structure (Fig. 1.12). A mask pattern was created using focused ion beam (FIB) milling on the 50 nm Cr that was e-beam evaporated onto a quartz substrate. They spin coated 1 μm of PMMA (495 kg/mol), which was then O_2 plasma etched down to

40 nm to planarise the patterned Cr layer. About 35 nm of Ag was then e-beam evaporated onto the PMMA layer. Using fast Fourier transform (FFT) or full-width half-maximum (FWHM) measurements, they found that the maximum resolution possible with their test structure was an 82 nm average line-width. Their evidence for beyond subwavelength-diffraction limited imaging stems from their 40 nm test line width transferred as an average width of 89 nm with their superlens. Their control experiment with an equivalent 75 nm thick PMMA layer in place of the superlens resulted in an image with an average width of 321 nm instead.

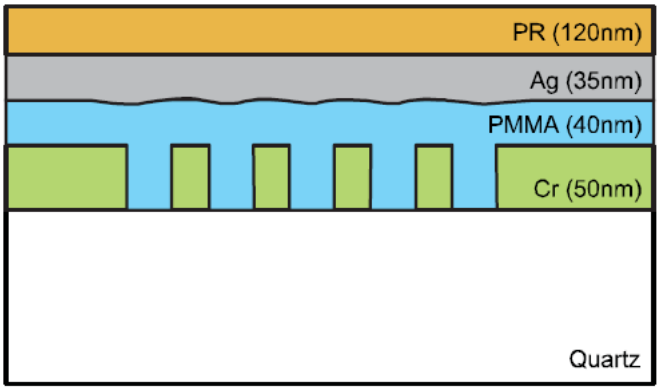

Fig. 1.12. Sample configuration for superlensing experiment by Fang et al. [88].

Thus far, experimental reports have primarily concentrated on a single Ag layer as the superlens structure. Melville et al. [89, 92] have explored a double layer silver lens stack, PMMA/Ag/SiO_2/Ag/SiO_2, to further improve the resolution. It was found that the transmission was greater, as manifested in an exposure time decrease from 720 s to 420 s. However, no clear resolution improvement was found, and was possibly due to the detrimental effects from compounding roughnesses with multiple silver-dielectric surfaces.

Theoretically, it is possible to increase the resolution of the superlens through homogenisation. To create a homogenised structure, several periods of alternating Ag and dielectric layers are required. Recall that the evanescent wave enhancement occurs within the Ag layer. By having many thin metal and dielectric layers with the permittivity matching and with opposite signs, the evanescent waves can be enhanced multiple times, resulting in improved resolution. Hence, such a periodic stack structure is explored experimentally in

Chapter 5. From simulations performed by collaborators at Purdue University, the stack structure to test is shown in Fig. 1.13.

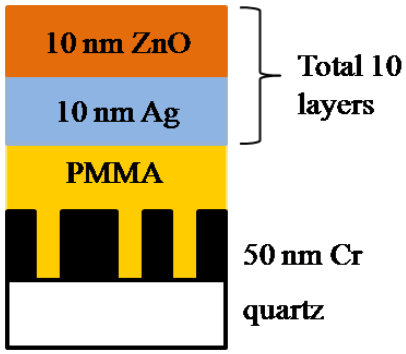

Fig. 1.13. Superlens structure containing a slab of alternating Ag and ZnO layers, on top of a PMMA-planarised Cr mask pattern.

1.6 Thesis Overview

This thesis provides an insight into the growth and properties of ZnO thin films, specifically in their nominally undoped and Ag doped forms. After a basic introduction to the properties and deposition of ZnO and Ag thin films in Chapter 1, the various growth and characterisation techniques used throughout this work is described in Chapter 2. Chapter 3 presents undoped ZnO deposition using plasma-assisted molecular beam epitaxy. Results regarding challenges in heteroepitaxy and growth parameters reproducibility are discussed. Following on from optimised parameters obtained from undoped ZnO growth, Chapter 4 will discuss why p-type material reproducibility may be difficult to obtain, as well as potential for measurements to give the wrong carrier type. A comprehensive in-situ Ag doping study is also presented. Chapter 5 describes the implementation of a novel Ag-ZnO stack-based metamaterial as a superlens structure. Detailed fabrication challenges and their solutions are presented. Chapter 6 will give a brief conclusion and outline some possible future work based on the findings of this thesis.

Chapter 2

Growth and Characterisation Techniques

2.1 Reflection High Energy Electron Diffraction (RHEED)

RHEED is a very powerful tool, commonly employed during MBE growth. In this thesis, a Staib RH20s 20 kV RHEED system was used in conjunction with a k-Space Associates kSA 400 CCD capture and analysis system. In RHEED, a high energy beam (20 keV) is directed at a low glancing angle (1°-3°) to the surface [29, 30]. The shallow penetration depth of the beam means that the near surface region of the substrate, and then the film, is probed, allowing for real-time monitoring of the surface morphology and film growth rate.

A RHEED pattern of a crystalline surface consists of a direct beam spot, specular reflection spot, shadow-edge and reciprocal lattice pattern. For smooth surfaces, there is true electron reflection diffraction, resulting in streaky patterns (Fig. 2.1(a)). For a rougher surface, there exists transmission-reflection diffraction, resulting in spotty patterns (Fig. 2.1(b)). When a surface is highly textured but polycrystalline, the electron diffraction is represented by concentric arcs (Fig. 2.1(c)) [30].

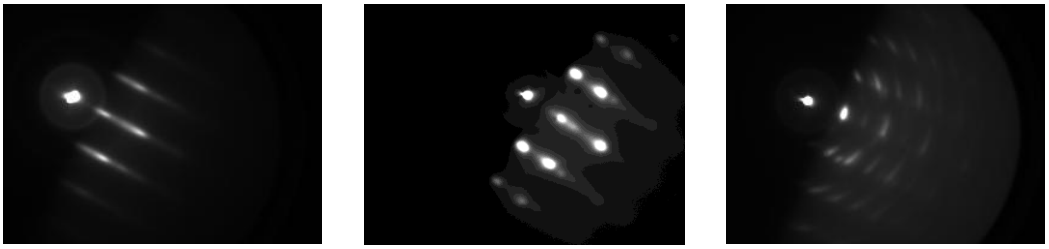

Fig. 2.1. Examples of typical RHEED patterns. (a) Smooth, single crystalline film; (b) rough, single crystalline film; (c) polycrystalline film.

As well as real-time monitoring of surface morphology, specular spot intensity oscillations can be used to measure the growth rate. The oscillatory behaviour arises from non-diffracted electrons scattered as a surface grows layer-by-layer. This oscillation occurs with a period equal to the growth time of each monolayer. As such, these oscillations only occur if layer-by-layer growth occurs preceding 2D nucleation on atomic terraces [29]. RHEED oscillations may also be absent if growth occurs via additions of adatoms to step edges, as opposed to random nucleation on terraces, or if three-dimensional growth occurs [30].

2.2 Laser Reflection Interferometry (LRI)

As the film growth performed in this thesis did not comply with the conditions for RHEED oscillations, laser reflection interferometry (LRI) was used to measure the growth rate. In LRI, a laser diode with a wavelength λ is used to illuminate the growing film. A photodiode then collects the resulting reflection from the film and film-substrate interface, as shown in Fig. 2.2. Due to interferences between the reflections, the resultant signal is periodic with each period corresponding to the optical pathlength of λ/2n [30].

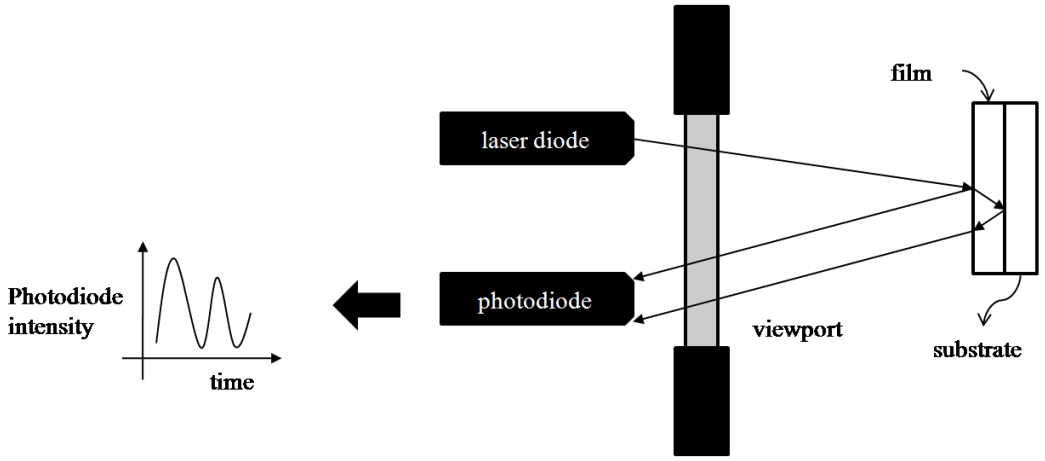

Fig. 2.2. Schematic of an LRI setup.

The growth rate R_t (nm/hr) is given by

$$R_t = \frac{\lambda/4n}{\Delta t} \times 3600 \tag{2.1}$$

where λ is the laser diode wavelength (625 nm), n is the film refractive index at λ, and Δt is the time taken (in seconds) for half an oscillation to occur.

2.3 Band-edge Thermometry (BandiT)

Another useful in-situ characterisation tool is band-edge thermometry (BET); in this work, a system from kSA named BandiT was used. As with LRI, BandiT illuminates the film with a light source and measures the resulting reflection. However, unlike LRI, the light source is not a laser diode, but a broadband lamp. In BET, a surface is illuminated with a broadband light source, and then the absorption edge of the resultant reflection is calculated. The absorption edge is dependent on the bandgap of the material, which has a known dependence on the temperature of the material. Hence, the surface temperature can be inferred by measuring the absorption edge. This is important as substrate temperature during growth often has a major effect on the resultant film quality. Figure 2.3 shows an example of a band-edge reflection characteristic and illustrates how the bandedge and hence the substrate temperature can be extracted. An advantage of using BET over more typical intensity dependent, emissivity-corrected pyrometers (ECP) is that BET directly measures the absorption edge. Therefore, such measurements are not as severely affected by a change in viewport transmission (i.e. film coating on the viewport) or stray IR sources (such as heater and source materials).

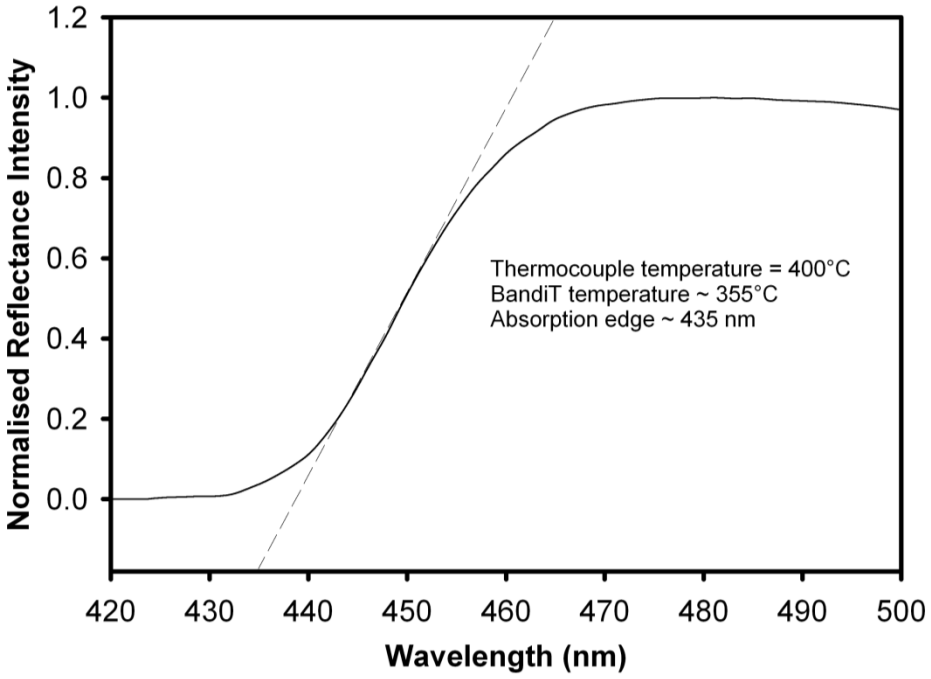

Fig. 2.3. Illustration of fit to the absorption edge of a bandedge spectrum [93]. The material is a m-plane hydrothermally grown ZnO substrate held at a temperature of 400°C. A measured absorption edge of 435 nm corresponds to a substrate temperature of 355°C.

As ZnO has not yet been previously investigated with such a system, kSA was provided with a bulk ZnO substrate in order to create a calibration file, shown in Fig. 2.4. Section 3.2 describes temperature measurements using BandiT and the modifications made to the growth process as a result of this study.

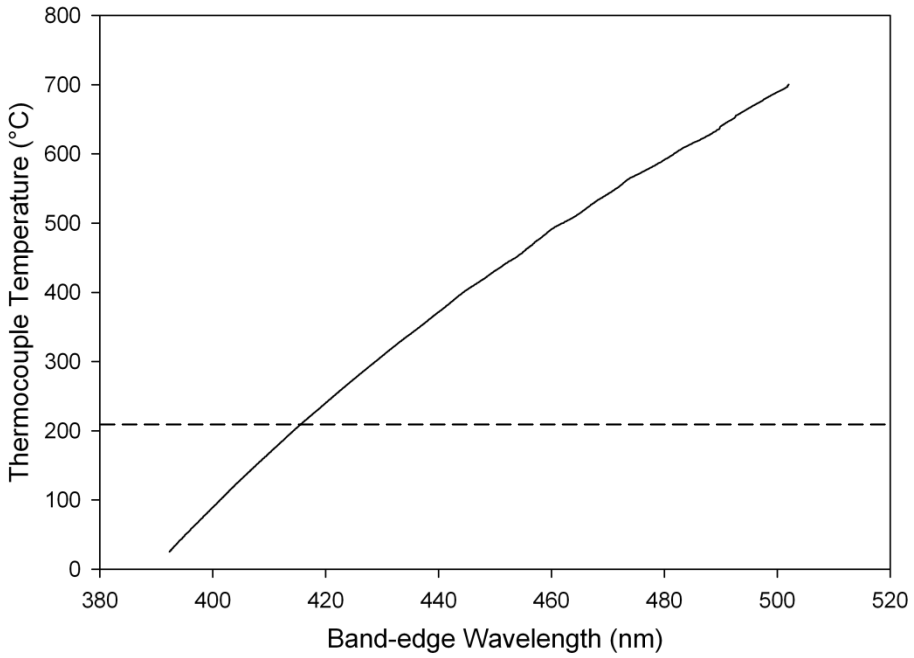

Fig. 2.4. ZnO calibration data from kSA. The dashed line indicates the minimum substrate temperature for reliable BandiT measurements using the current lamp setup. By switching to a Xenon lamp, it is possible to measure from room temperature onwards.

2.4 Evaporation

Evaporation is a widely used thin film deposition technique, in which a target material is heated to create a vapour, which then condenses onto a substrate. The target material may consist of either granules or thin wires. The heating may result from passing a current through an intermetallic material, and subsequently sublimating the source material (thermal evaporation), or by using a beam of electrons to heat up a crucible containing the evaporant (electron-beam evaporation). In this thesis, only electron-beam (e-beam) evaporation was employed and hence only this method will be described in this section.

In e-beam evaporation, a filament is heated to provide a source of electrons, which are then accelerated towards the source material. This high energy bombardment vapourises the source material for subsequent deposition onto a substrate (see Fig. 2.5) [28]. E-beam evaporation was conducted in the same

apparatus as sputtering, namely the BOC Edwards Auto 500 system. For evaporating Cr granules in a graphite crucible, the e-beam source was usually set at 5 kV and 24 mA, with the rastering turned on, at typical process pressures of around 10^{-5} mbar. Ohmic contacts on ZnO for electrical characterisations were also formed by e-beam evaporating Ti and Pt (or Au).

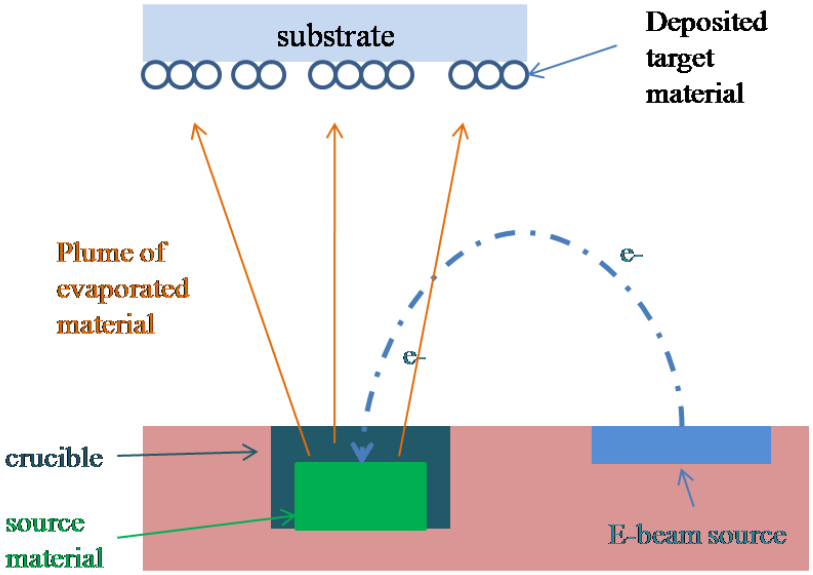

Fig. 2.5. Example of an e-beam evaporator setup.

2.5 Electron Beam Lithography (EBL)

Lithography is the process by which a pattern defined on a mask is transferred into a radiation-sensitive material (resist) that covers a semiconductor surface [2]. Exposed parts of the resist either dissolve (positive resist) or remain (negative resist) after developing in a suitable solution, as illustrated in Fig. 2.6.

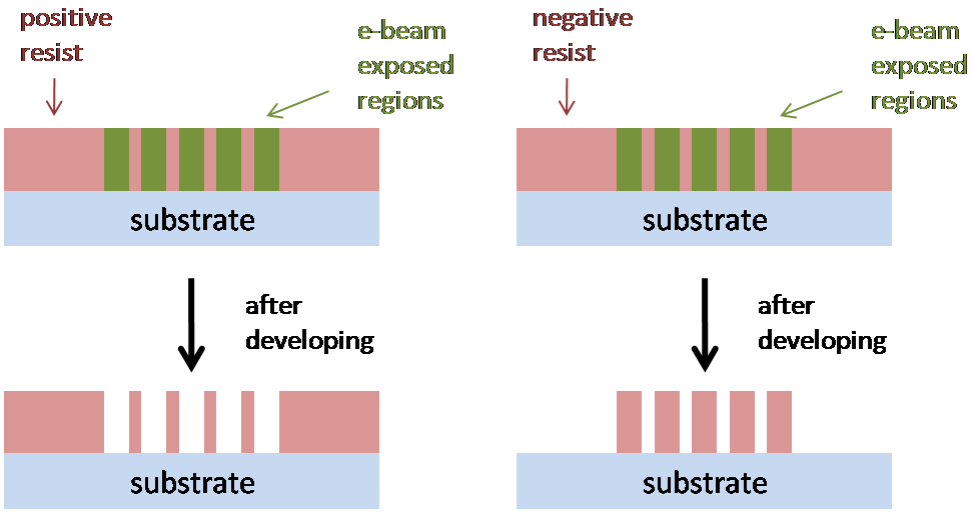

Fig. 2.6. Comparison between positive and negative resist.

Optical lithography is commonly used to make electronic devices and employs a UV source ($\lambda \approx 0.2\text{-}0.4$ μm) as an exposure medium. At the University of Canterbury, the limits of optical lithography are in the micrometer length scales. For the desired feature sizes of hundreds of nanometres, it is necessary to turn to electron beam lithography (EBL) using a Raith 150 EBL tool. A tungsten thermionic-emission cathode or single-crystal lanthanum hexa-boride is used to generate a beam of electrons. Condenser lenses are used to focus the e-beam to a spot size of approximately 20 to 30 nm. Beam-blanking plates are used to turn the electron beam on and off for exposing specific areas on a resist-coated substrate on a precision mechanical stage.

The advantage of using EBL is that complex and submicron patterns can be easily generated without the use of a mask. However, as a pattern is generated in beam size increments, EBL is significantly slower than the large-scale exposure that optical lithography possesses. Hence, EBL is typically used to create photomasks for photolithography or for research scale patterning [2]. In this work, EBL was used to produce the sub-micron slits for creating the Cr test pattern on a quartz substrate. Chapter 5 contains details of the challenges and results of that work.

Depending on the pattern to be created, a positive or negative e-beam resist may be employed. Figure 2.7 shows a typical test pattern for the superlens structure described in Chapter 5. As the pattern to be created has a much smaller total area than the rest of the 10 mm by 10 mm quartz substrate, the fastest and most sensible way to create this pattern is by using a negative resist, when going through a lift-off process route. Micro Resist Technology ma-N 2403 negative tone e-beam/deep UV resist was used as it was the only negative e-beam resist available in-house. Approximately 50 nm of Cr is then deposited on the resist-coated substrate and upon lift-off in Remover PG from Micro Resist Technology, the resultant substrate is mainly covered with Cr except for areas where the e-beam has defined the pattern shown in Fig. 2.7.

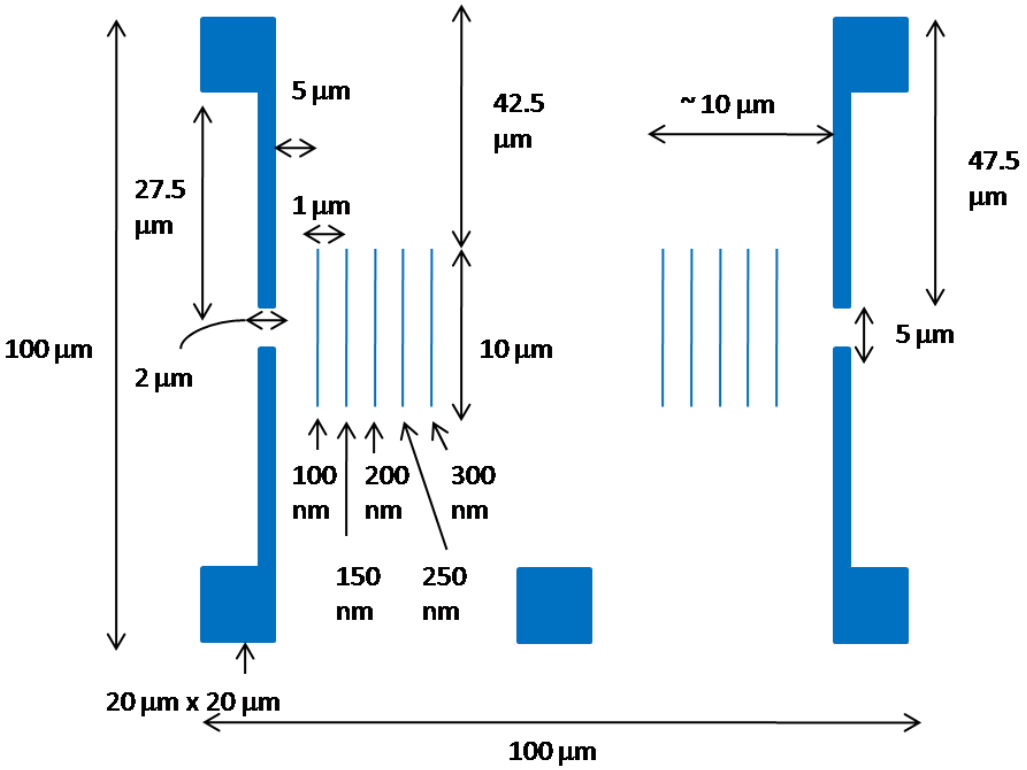

Fig. 2.7. Superlens test pattern. (not to scale)

There is another issue to consider when using EBL on an insulating substrate such as quartz. In particular, there is charging on the resist from the e-beam due to the lack of a conducting path to ground. These trapped surface charges result in deflection of incoming electrons and hence a distorted pattern, which defeats the purpose of performing high precision lithography using EBL. To mitigate this and to provide a conducting path for the e-beam, a thin layer of the conducting polymer PEDOT/PSS was spin-coated on the resist [94]. Section 5.2 contains detailed discussion on further challenges of creating such a test structure.

2.6 Reactive Ion Etching (RIE)

Generally, at some stage, lithography will employ one or more steps. Wet etching involves dissolving a material by immersing in a chemical solution. For example, for thickness measurements of MBE grown ZnO, part of the sample is masked by applying a photoresist drop, with the uncovered areas then etched away using dilute hydrochloric acid (HCl). As well as chemical etching, dry etching can also be used. Dry etching involves dissolving material using reactive ions or some sort of vapour phase etchant. Dry etching is usually slower than wet etching but it offers more dimensional and shape control [95].

In reactive ion etching (RIE), RF plasma (usually oxygen or SF_6) is used to create reactive gas species. Since the substrate or sample is biased compared to another electrode, electrons in the plasma are attracted to the surface. Depending on the composition of the gas, the selected material is then dissolved, as shown in Fig. 2.8. The degree of anisotropy as well as etch rate depend on the process pressure, gas flow and the RF power. The application of RIE in the superlens structure is explained in Chapter 5.

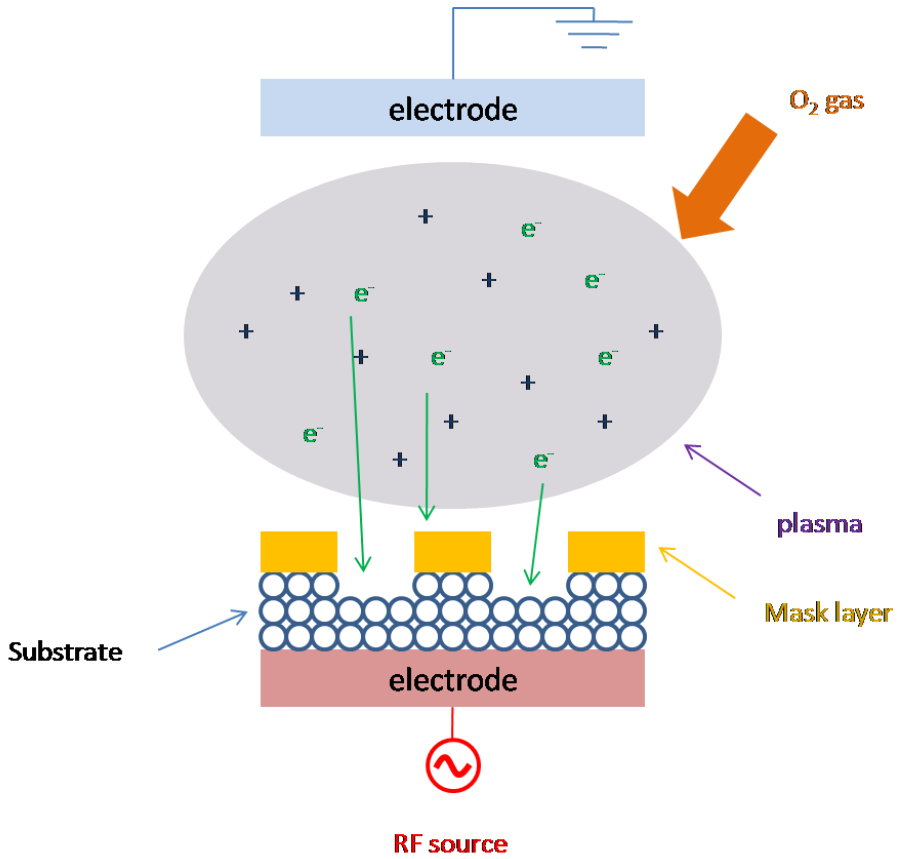

Fig. 2.8. Schematic of an anisotropic etching of a film/substrate with the structure defined by a RIE resistant mask layer.

2.7 Electrical Characterisation Techniques

2.7.1 Current-Voltage (I-V) and Capacitance-Voltage (C-V)

In this thesis, current-voltage (I-V), capacitance-voltage (C-V), Hall effect, thermal admittance spectroscopy (TAS) and deep level transient spectroscopy (DLTS) measurements, were performed using Ti/Pt for Ohmic contacts and AgO_x for Schottky contacts. I-V measurements were performed using a Hewlett Packard 4155A Semiconductor Parameter Analyser, C-V measurements using a Philips

PM6304 RCL meter, and Hall effect measurements using an HEM-2000 Hall effect measurement system. Both TAS and DLTS measurements were performed using home-built systems at Leipzig University.

The thermionic current-voltage relationship of a Schottky barrier diode is given by [96]

$$I = I_S \left[exp\left(\frac{qV}{\eta kT}\right) - 1 \right] \tag{2.2}$$

where I is the measured current (A) at the input voltage (V), I_S is the saturation current (A), q is the elementary charge (1.6×10^{-19} C), η is the ideality factor, k is the Boltzmann constant (1.38×10^{-23} J/K), and T is the temperature (K). Since T is usually 300 K and V >> kT/q (25.9 meV), Eq. (2.2) can be simplified and rearranged to yield an expression for the diode ideality factor

$$\eta = \frac{q}{kT} \frac{1}{(d(\ln I)/dV)} \tag{2.3}$$

which, for a laterally homogeneous diode dominated by thermionic emission and neglecting image force lowering effects, should be unity. Another figure of merit for a Schottky diode is the barrier height ϕ_B [96], given by

$$\phi_B = \frac{kT}{q} \ln\left(\frac{AA^*T^2}{I_S}\right) \tag{2.4}$$

where A is the Schottky contact area in (m^2), A^* is the Richardson constant (32 $AK^{-2}cm^{-2}$ for ZnO [97]), and I_S is the saturation current calculated by extrapolating the semi-logarithmic current versus voltage plot to V = 0, as demonstrated in Fig. 2.9.

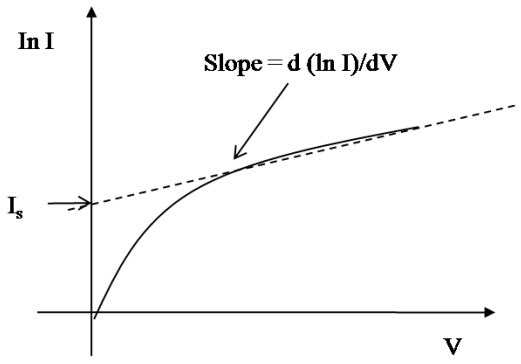

Fig. 2.9. An example of a semi-logarithmic I-V plot illustrating how I_S can be obtained.

Another commonly employed electrical measurement is capacitance-voltage (C-V) measurement using a Schottky diode. C-V measurements are useful to show if there is a change in conduction throughout the material or even just to measure the net donor concentration N_D (if n-type), to supplement Hall effect results. Most C-V analysis assumes a one-sided abrupt junction such that the depletion region is mainly in one side of the junction, which is valid for a Schottky diode since the depletion region will be formed on the semiconductor side, rather than the Schottky contact side. The capacitance per unit area C_j of a Schottky diode having built-in voltage V_{bi} is given by

$$C_j = \frac{C}{A} = \sqrt{\frac{q\varepsilon_S N_B}{2(V_{bi} - V)}} \tag{2.5}$$

where the doping concentration N_B is given by [2]

$$N_B = \frac{-2}{q\varepsilon_S} \frac{1}{\left(d\left(1/C_j^2\right)/dV\right)} \tag{2.6}$$

The built-in potential V_{bi} can be determined by extrapolating the inverse C_j^2 versus voltage plot to $1/C_j^2 = 0$, as demonstrated in Fig. 2.10.

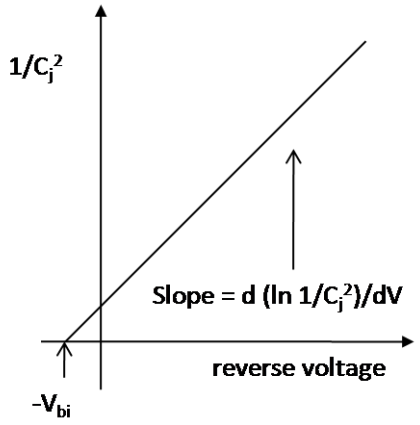

Fig. 2.10. An example of a $1/C_j^2$ versus V plot illustrating how V_{bi} can be obtained.

The effective barrier height ϕ_B [96] is given by

$$\phi_B = -V_{bi} + \frac{2kT}{q} + V_O \tag{2.7}$$

where the Fermi level with respect to the conduction band V_O [96] is given by

$$V_O = \frac{kT}{q} \ln \frac{N_C}{N_D} \tag{2.8}$$

and the effective density of states in the conduction band N_C [98] is given by

$$N_C = 2\left(\frac{2\pi m_n kT}{h^2}\right)^{\frac{3}{2}} \tag{2.9}$$

Table 2.1 provides an explanation for all the parameters listed in Eqs. (2.5) to (2.9).

Table 2.1. Explanation of parameters for Eqs. (2.5) to (2.9).

Description	Symbol	Units
Depletion layer capacitance per unit area	C_j	F/cm^2
Depletion layer capacitance	C	F
Schottky diode / junction area	A	cm^2
Elementary charge	q	1.6×10^{-19} C
Semiconductor permittivity	$\varepsilon_S = \varepsilon_{ZnO}\varepsilon_0$	F/cm
Dielectric constant	ε_{ZnO}	8.66 [25]
Permittivity in vaccum	ε_0	8.854×10^{-14} F/cm
Built-in potential	V_{bi}	V
Applied potential	V	V
Carrier concentration	N_B	cm^{-3}
Effective barrier height	ϕ_B	V
Fermi level with respect to the conduction band	V_O	V
Boltzmann constant	k	1.38×10^{-23} J/K
Temperature	T	K
Effective density of states in the conduction band	N_C	cm^{-3}
Net donor concentration	N_D	cm^{-3}
Electron mass	$m_n = m_e\, m_O$	kg
Electron effective mass	m_e	0.24 [25]
Electron rest mass	m_O	9.11×10^{-31} kg
Planck constant	h	6.63×10^{-34} J·s

2.7.2 Hall Effect

A simple yet powerful technique to evaluate the electrical properties of a material is the Hall effect measurement. This technique is typically used to measure the carrier concentration, carrier-type and mobility of a material, in conjunction with resistivity measurements [96]. The most commonly used geometry is the van der Pauw geometry [99], as shown in Fig. 2.11.

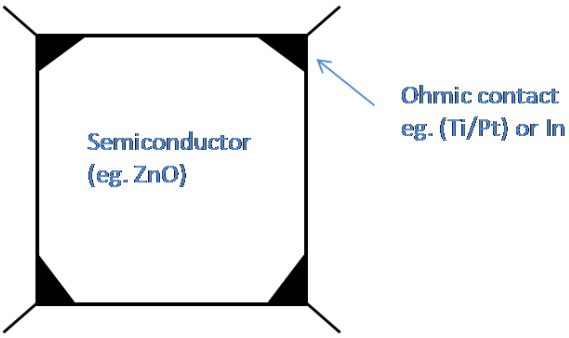

Fig. 2.11. Van der Pauw contact layout for Hall effect measurements.

The basic principles in a Hall effect measurement are illustrated in Fig. 2.12. For example, assume a p-type semiconductor. Firstly, a suitable constant current is applied in the x direction. Then a magnetic field is applied in the z direction, resulting in the Lorentz force exerting an upwards force on the holes. This results in an electric field forming due to the separation of carriers in the y direction, as shown in

$$E_y = R_H J_p B_z \tag{2.10}$$

where E_z is the electric field, R_H is the Hall coefficient, J_p is the hole current density, and B_z is the applied magnetic field. R_H (negative for electrons and positive for holes) is given by

$$R_H = \frac{d}{q n_s} \tag{2.11}$$

where d is the film thickness and n_s is the sheet concentration.

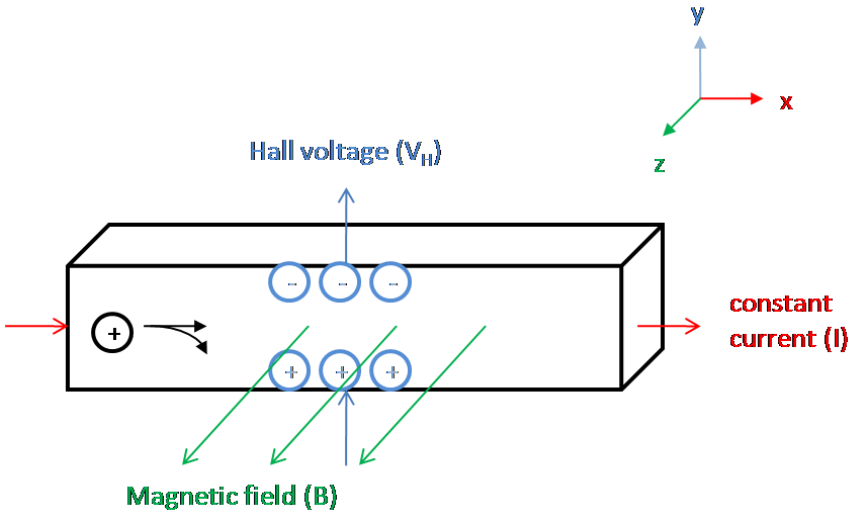

Fig. 2.12. Schematic illustrating the Hall effect.

The van der Pauw equation can be used to calculate sheet resistance (Ω):

$$exp\left(\frac{-\pi R_{horiz}}{R_S}\right) + exp\left(\frac{-\pi R_{vert}}{R_S}\right) = 1 \tag{2.12}$$

where R_S is the sheet resistance (Ω), and R_{horiz} and R_{vert} are the resistances measured between different edge points on the sample. The bulk resistivity ρ (Ω cm) can then be calculated by considering the thickness of the sample d (cm).

$$\rho = R_S d \tag{2.13}$$

The Hall voltage V_H is experimentally determined by measuring the induced electric field from the application of a magnetic field. As the electric field and hence V_H has a sign dependence, the majority carrier type can be deduced from its sign. A positive V_H indicates a p-type sample, and negative V_H indicates n-type material. The sheet concentration n_S (cm^{-2}) is then given by

$$n_S = \frac{IB}{qV_H} \times 10^{-4} \tag{2.14}$$

where I is the current (A), B is the magnetic field strength (0.51 T), and V_H is the Hall voltage (V). The bulk concentration n_b (cm^{-3}) is easily calculated by employing

$$n_b = \frac{n_S}{d} \tag{2.15}$$

The Hall mobility μ_H ($cm^2V^{-1}s^{-1}$) is then given by

$$\mu_H = \frac{1}{qn_S R_S} \tag{2.16}$$

While these simplified calculations are suitable for homogeneous and single carrier samples, in reality many materials, especially heteroepitaxial grown ZnO, are inhomogeneous. Inhomogeneity can result in distinct parallel conduction paths, which can include surface defect generated carriers, bulk carriers, and interface / buffer layer carriers (Fig. 2.13).

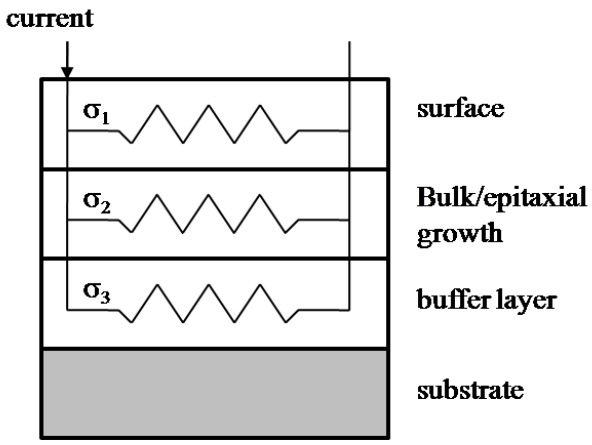

Fig. 2.13. Example of parallel conduction paths in a heteroepitaxially grown film.

A measurement of the conductivity of a sample contains contributions from each individual conducting path, as represented by

$$\sigma_{TOTAL} = \sum \sigma_i \tag{2.17}$$

where the sheet resistance r_i of each layer is given by

$$r_i = q\mu_i n_i \tag{2.18}$$

Thus, a degenerate layer for either σ_1 or σ_3 will have a high conductivity, and can result in that layer dominating the conductivity value, instead of solely measuring σ_2.

A variable magnetic field Hall effect (VFH) measurement can be used to separate the different carriers and therefore extract the relevant bulk mobility and carrier concentration. VFH has previously been extensively used in HgCdTe studies [100-102] due to the existence of multiple distinct carrier populations and inhomogeneities characteristic of that material. To put it simply, VFH uses different magnetic field strengths to affect carriers of different mobilities, allowing for separation of groups of carriers.

The effect of carriers in an electric field [5] can be described by

$$J = \sigma E \tag{2.19}$$

where J is the current density, σ is the conductivity, and E is the electric field from the applied J. Referring back to Fig. 2.12, the holes will predominantly move in the x-direction due to the applied electric field E_x, with some deflection in the y-direction due to the applied magnetic field B_z. Similarly, holes under the induced electric field E_y will predominantly move in the y-direction, with some deflection in the x-direction due to B_z. Therefore, in order to take into account inhomogeneities, the conductivity is actually a tensor, and hence Eq. (2.19) is more accurately represented by

$$\begin{bmatrix} J_x \\ J_y \end{bmatrix} = \begin{bmatrix} \sigma_{xx} & \sigma_{xy} \\ \sigma_{yx} & \sigma_{yy} \end{bmatrix} \begin{bmatrix} E_x \\ E_y \end{bmatrix} \tag{2.20}$$

where σ_{xx}, σ_{yy}, σ_{xy} and σ_{yx} are the conductivities along the xy-plane. If the semiconductor is assumed to be isotropic in-plane, this gives rise to $\sigma_{xx} = \sigma_{yy}$ and $\sigma_{yx} = -\sigma_{xy}$ from symmetry [103]. Thus, Eq. (2.20) can be rewritten as

$$J_x = \frac{\sigma_{xx}^2 + \sigma_{xy}^2}{\sigma_{xx}} E_x \tag{2.21}$$

This then allows one to solve for the Hall coefficient and resistivity using the following equations:

$$R_H = \frac{\sigma_{xx}/B}{\sigma_{xx}^2 + \sigma_{xy}^2} \tag{2.22}$$

and

$$\rho = \frac{\sigma_{xx}}{\sigma_{xx}^2 + \sigma_{xy}^2} \tag{2.23}$$

By assuming the same relaxation time, velocity and effective mass of each carrier in each layer, the conductivities σ_{xx} and σ_{xy} are given by

$$\sigma_{xx} = \sum_j \frac{n_j e \mu_j}{1 + \mu_j^2 B^2} \tag{2.24}$$

and

$$\sigma_{xy} = \sum_j S_j \frac{n_j e \mu_j^2 B}{1 + \mu_j^2 B^2} \tag{2.25}$$

where n_j and μ_j are the carrier density and mobility, respectively, of layer j, and S_j is +1 for holes and -1 for electrons [99]. Both Eqs. (2.24) and (2.25) also show a dependence on the magnetic field B. Thus, by observing the change in the conductivity of each layer from applying varying magnetic fields, one can model and extract the carrier concentration and mobility of each carrier. The experimentally obtained conductivities and Hall voltages are typically solved using quantitative mobility spectrum analysis (QMSA) or multiple-carrier fitting (MCF) to calculate the conductivity tensors [5, 21]. Chapters 3 and 4 describe the application of VFH to analyse electrical properties of undoped and Ag doped ZnO samples, respectively.

2.7.3 Thermal Admittance Spectroscopy (TAS)

To understand the carrier concentration calculated from Hall effect measurements, it is necessary to understand the defect levels contributed by various introduced impurities or native defects. One technique to investigate defect levels is called thermal admittance spectroscopy (TAS). TAS relies on the frequency and temperature dependence of depletion layer capacitance. The alternating voltage of frequency $\omega = 2\pi f$ modulates the Fermi level to cause periodic charging and discharging of the traps [104, 105], as illustrated in Fig. 2.14, where W is the depletion layer width, E_T is the trap level, and ΔW is the additional depletion layer induced under a reverse bias V_R.

In TAS, a zero bias is applied at 300 K and then the sample is cooled to fill the trap(s) with carriers. The capacitance is then measured at several frequencies while the sample is slowly heated up to room temperature. Once the trapped carriers receive sufficient thermal energy, they will be released into the valence or conduction band, depending on whether holes or electrons were trapped. This manifests as a step change in the capacitance (C) or a peak in the admittance (G) (see Fig. 2.15), at $\omega = 2e_n$ [106], where e_n is the trap emission rate.

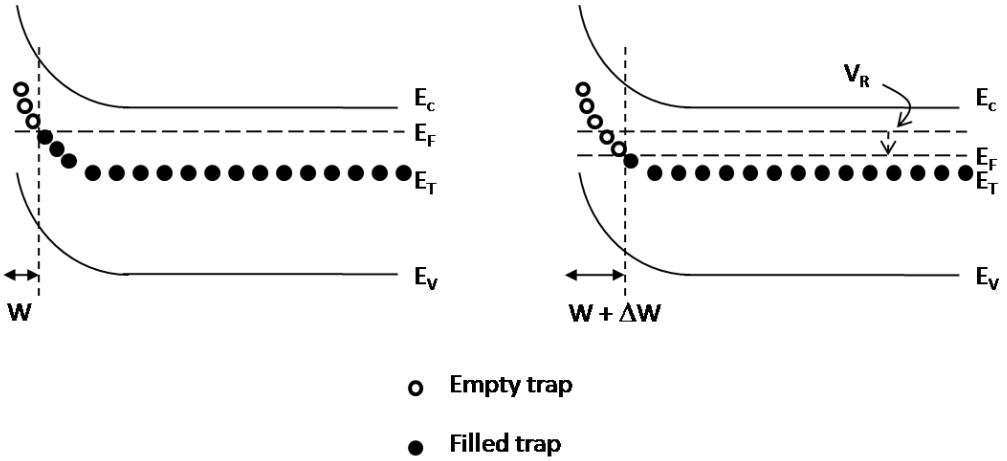

Fig. 2.14. Band diagram demonstrating charging and discharging of trap states under TAS, where E_T is the trap level.

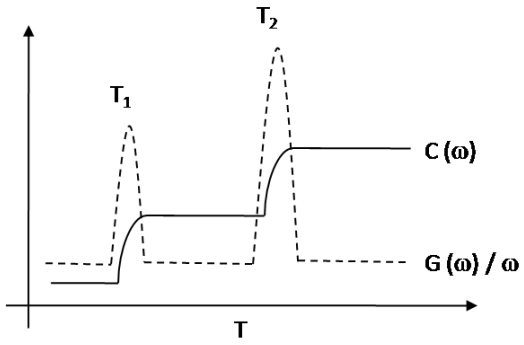

Fig. 2.15. Example of a typical TAS measurement, where C(ω) is the measured capacitance and G(ω) is the measured admittance. T_1 and T_2 are the two different trap states measured.

Each trap level has a thermal emission rate e_n (s^{-1}), given by [107]

$$e_n = \sigma_n \nu_n N_C exp\left(\frac{-E_T}{kT}\right) \tag{2.26}$$

where σ_n is the thermal cross-section capture cross section (cm^2), and ν_n is the thermal velocity given by

$$\nu_n = \sqrt{\frac{3kT}{m^*}} \tag{2.27}$$

In addition, N_c is the effective density of states in the conduction band given by Eq. (2.9), E_T is the trap energy level (eV), T is the temperature (K), and k is the Boltzmann constant (1.38×10^{-23} J/K).

By assuming a temperature independent capture cross-section [107, 108], Eq. (2.26) can be represented by

$$e_n = B_n T^2 exp\left(\frac{-E_T}{kT}\right) \tag{2.28}$$

where B_n is the emission coefficient ($s^{-1}K^{-2}$), given by

$$B_n = 16\pi\sigma_n m_n k^2/h^3 \tag{2.29}$$

Thus, one can experimentally determine the trap level E_a (eV) by creating an Arrhenius plot, as shown in Fig. 2.16.

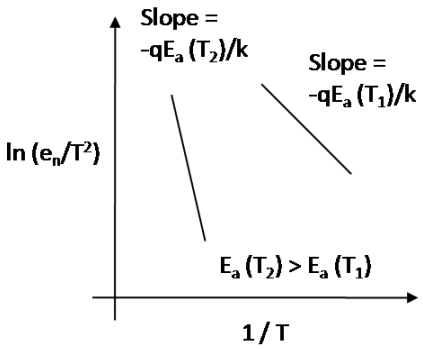

Fig. 2.16. Extraction of activation energy of trap level E_a from an Arrhenius plot.

The trap concentration N_T (cm^{-3}) is then given by [109]

$$N_T = 2N_B \frac{\Delta C}{C_S} \tag{2.30}$$

where N_B is the doping density (cm^{-3}), ΔC is change in capacitance due to "freeze-out" of the defect [105, 109] and C_S is the steady-state, high frequency limit capacitance [110].

2.7.4 Deep Level Transient Spectroscopy (DLTS)

A complementary and newer technique to TAS is deep level transient spectroscopy (DLTS). TAS is advantageous when the material is highly resistive [96] or the diode has low rectification, preventing the use of DLTS. However, DLTS is superior to TAS when there is a high concentration of a dominant defect such that E_F is pinned, preventing the detection of other traps with TAS [111]. In addition, DLTS has greater sensitivity, larger range of observable traps, and ability to distinguish between minority and majority carrier traps [112]. The difference between TAS and DLTS measurements lies in that TAS is a steady-state measurement, whereas non-equilibrium measurements are made in DLTS.

Therefore, while TAS and DLTS should yield the same number of trap states most of the time, DLTS may detect more traps than TAS. Therefore, DLTS is more widely used due to its advantages over TAS.

As with TAS, the Fermi level is modulated according to Fig. 2.14. The difference between TAS and DLTS is that a pulse is created such that the capacitance value extracted is the capacitance transient associated with a change in the depletion region width as the diode returns from an initial non-equilibrium state to equilibrium [96, 112] (Fig. 2.17). The measured capacitance is the capacitance difference between t_1 and t_2 as measured by a selected rate window. The peak that appears in the collection of capacitance differences corresponds to a particular trap level.

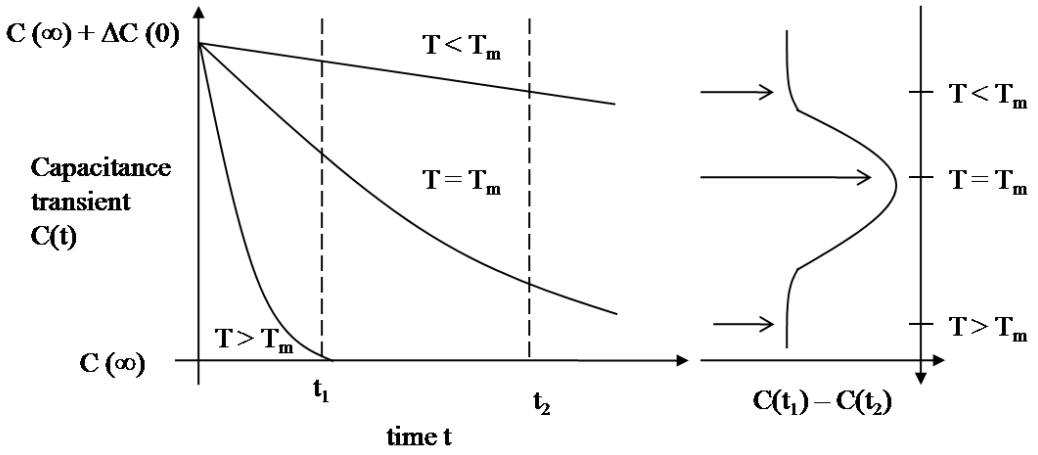

Fig. 2.17. Example capacitance transient at various temperatures [113].

The change in capacitance $\Delta C(T) = C(t_1) - C(t_2)$ has a maximum at $T = T_m$, as $\Delta C(T)$ is close to zero outside T_m. Therefore, assuming an exponential decay in the capacitance transient [113], one can derive

$$\frac{d(\Delta C)}{dT} = 0 = \frac{d(\Delta C)}{de_n}\frac{de_n}{dT} = \frac{de_n}{dT}\left[-t_1 e^{-e_n t_1} + t_2 e^{-e_n t_2}\right] \tag{2.31}$$

which gives a maximum signal at $e_n(T_m)$, as given by

$$e_n(T_m) = \frac{\ln(t_2/t_1)}{(t_1 - t_2)} \tag{2.32}$$

Hence, the dependence of e_n on T can be found by varying T_m, which depends on t_2 and t_1. It is common to vary t_1 and t_2 (i.e. change the rate window), while

keeping the ratio t_2/t_1 constant [113]. In this thesis, the emission rate e_n is such that $e_n = r_w \times 1.13$, where r_w is the rate window used (Hz or s^{-1}), which depends on the expected ranges of trap levels to be detected since particular rate windows are optimised for detecting particular capacitance transients. The factor of 1.13 arises from the weighting function used to measure the capacitance transients during measurements [114, 115]. While a slower rate window can be used to detect slow responding traps, noise becomes more prevalent. Therefore, it is useful to employ several rate windows to rule out artefacts due to noise.

Majority carrier traps can be detected by applying a reverse bias pulse, whereas minority carrier traps can be observed by using a forward bias pulse. As with TAS, the activation energy of a trap is obtained through an Arrhenius plot, with e_n given by Eq. (2.32) [112]. An example of a DLTS spectrum showing four different trap levels is shown in Fig. 2.18. Hence, DLTS is a very powerful tool for identifying the various deep level traps in a material. In this thesis, DLTS measurements were performed by Holger von Wenckstern from Leipzig University in Germany, using a home-built DLTS setup.

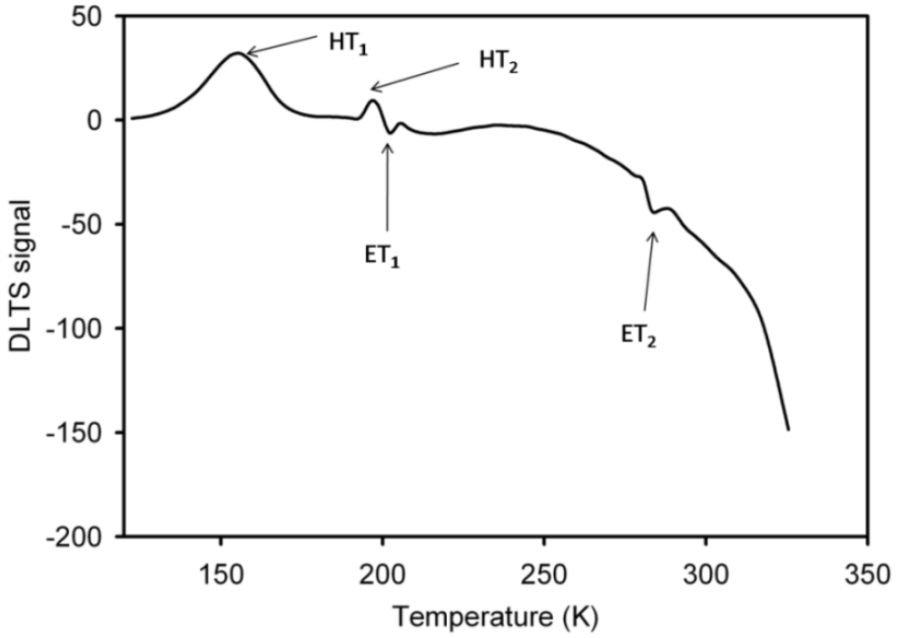

Fig. 2.18. Example of a DLTS spectrum with two hole traps (HT_1 and HT_2) and two electron traps (ET_1 and ET_2). The illustration is that of a generic material with multiple trap levels.

2.8 Rutherford Backscattering Spectrometry (RBS)

Ion beam techniques are invaluable in investigating the composition of a material. One such technique is Rutherford backscattering spectrometry (RBS), which is based on bombarding a sample with He^+ ions (alpha particles) and then measuring the energy of the backscattered He^+ ions, as shown schematically in Fig. 2.19 [96]. A small proportion of He^+ ions is elastically scattered when they "collide" with nuclei in the sample. The repulsion force depends on the mass of the atom. Hence, one can determine the element type by measuring how much the He^+ ions were backscattered. By having a calibrated yield for the expected elements to detect, the concentration of those elements can be measured. In addition, the energy and number of backscattered ions allows for the determination of the elemental distribution and thickness of the sample [116, 117].

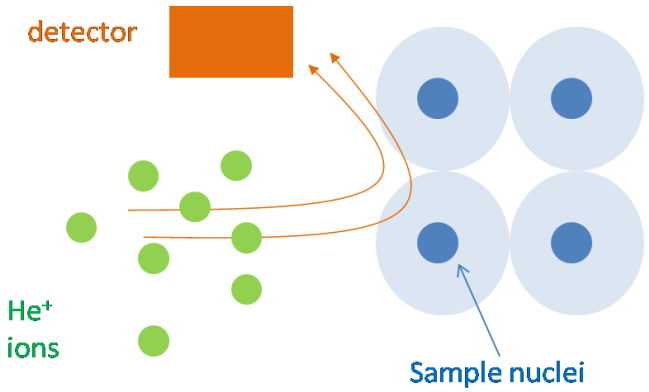

Fig. 2.19. Key processes in an RBS measurement.

Particle induced x-ray emission (PIXE) is also performed simultaneously with RBS. In addition to backscattered He^+ ions measured during RBS, characteristic x-rays are also emitted from the sample [118]. As each element has unique x-ray emissions consisting of K, L and M lines, elemental identification is possible [118]. An advantage of PIXE is that elements that are close in mass, identified as a single RBS signal, can be distinguished by their x-ray emissions.

As the backscattering yield is highly dependent on the alignment of the ion beams with the arrangement of the atoms in the sample, RBS channelling (RBS-C) experiments can be used to assess implantation damage or arrangement of dopants in a semiconductor. For example, if the backscattering yield of a host atom and a dopant atom are similar along a particular crystallographic direction, then the host

and dopant atoms occupy the same sub-lattice. In this thesis, RBS, PIXE and RBS-C have been used to investigate the composition of Ag doped ZnO epilayers. All ion beam measurements were performed by Dr. John Kennedy at GNS Science using a 0.5 mm collimated 2 MeV $^4He^+$ beam with samples mounted in a two-axis target manipulator. The backscattered particles were detected by a surface barrier detector placed at 165° with an energy resolution of 15 keV. The detector limit is around 10^{19} cm^{-3}, with experimental errors typically up to 10%.

2.9 Secondary Ion Mass Spectrometry (SIMS)

Another very powerful beam technique is secondary ion mass spectrometry (SIMS). Key SIMS processes are schematically illustrated in Fig. 2.20. In SIMS, the sample is sputtered using ions such as Cs^+, O_2^+, O^- or Ar^+ (primary ions). The resultant ejected materials are mostly neutral but some may be either positively or negatively charged (secondary ions). The mass/charge ratios of these ions are then detected by a mass spectrometer [96]. Since only the mass/charge ratio is measured, it is up to the operator to make an intelligent estimate as to the possible ions that have been detected based on some previous knowledge as to the possible composition of the material.

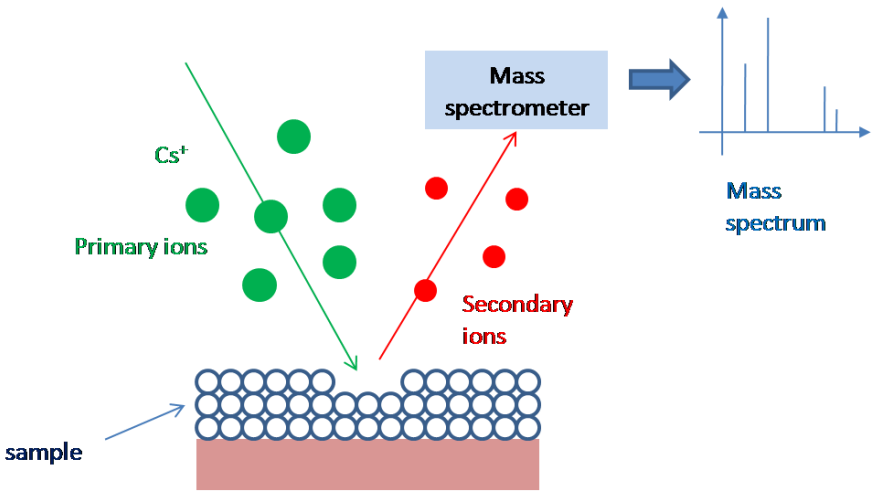

Fig. 2.20. Example of a sample sputtered using Cs^+ ions to obtain a positive mass spectrum.

An important factor is that the yield of ejected atoms (or secondary ion yield) depends on the primary ion used. Higher secondary ion yields are obtained for electropositive elements when using electronegative ions and vice versa. Hence the selection of the primary ions will affect the subsequent results as well [96].

Therefore, by recording the mass spectrum and sputtering time (dynamic SIMS), it is possible to generate a depth profile of the elemental composition of material. Such a composition distribution is useful in the study of heterostructures or semiconductor doping. In this thesis, SIMS was performed at La Trobe University, Australia using an ION-TOF GmbH ToF-SIMS IV instrument. The sputtered area was typically 500 μm × 500 μm and the beam energy varied between 500 eV and 2 keV.

2.10 Photoluminescence (PL)

A non-destructive characterisation technique for investigating the electronic structure of a material is photoluminescence (PL). An example of a typical PL setup is shown in Fig. 2.21. For ZnO samples investigated in this thesis, the 325 nm line of a He-Cd laser was used for excitation. The PL emission of the resultant photons emitted were then collimated and focused into a SpeX1700 spectrometer, which was calibrated using known transitions of a low-pressure Hg lamp. These measurements have been taken by Paul Miller and Rueben Mendelsberg from the Physics and Astronomy department at the University of Canterbury.

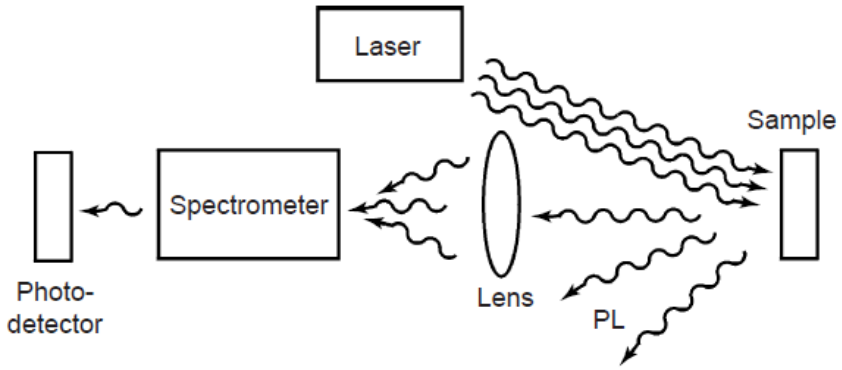

Fig. 2.21. Typical experimental setup for PL measurements [119].

PL allows for the identification of impurities that produce radiative recombinations [96] and therefore can be used to interpret Hall effect, SIMS and TAS/DLTS data. PL emissions can involve several different kinds of recombination processes, as shown in Fig. 2.22. Band-to-band transitions occur when a hole in the valence band (VB) recombines with an electron in the conduction band (CB), which yields an emission at approximately the bandgap of the material. Band-to-band emissions dominate room temperature emissions but

are rarely observed at low temperatures [96]. However, it is more common to observe excitonic emissions at low temperatures. There is a Coulombic attraction between a free electron and hole pair (ehp) due to their opposite charges. The electron can then orbit around the hole in a hydrogen-like manner, creating an excited state commonly referred to as a free exciton (FE) [96, 120]. Since an exciton is electrically neutral, while it can move through a crystal, neither photoconductivity nor current occurs as a result. The energy level is also smaller than the band-to-band emission as it is reduced by the excitonic binding energy (approximately 60 meV in ZnO). A free hole (or electron) can also combine with a neutral donor (or acceptor) to form a positively (or negatively) charged excitonic ion called a bound exciton (BE). Such a BE is commonly referred to as a donor bound exciton (DX) or an acceptor bound exciton (AX). The hole (or electron) moves in an orbit around the donor (or acceptor) [96]. Another common recombination is a donor-acceptor pair recombination (DAP), where an electron on a neutral donor recombines with a hole on the neutral acceptor.

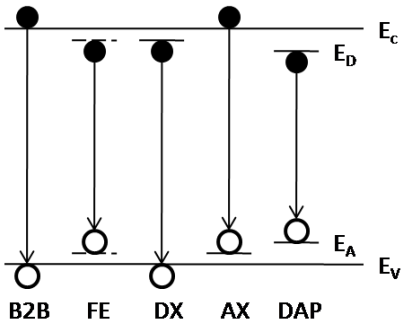

Fig. 2.22. Radiative transitions observed with photoluminescence [96].

Low temperature (4 K) PL normally yields closely spaced emissions at the NBE or two-electron satellite (TES) regions for the ZnO samples in this thesis [121]. TES transitions are related to DX transitions in that the donor electron associated with a DX transition is excited to a higher state using the necessary energy from exciton as it recombines, instead of remaining in the ground state. This result in a red-shifted DX emission, commonly refer to as the TES transition [122]. Either Gaussian

$$Intensity = k0 + k1 \times \exp\left[-\left(\frac{(energy - k2)}{k3}\right)^2\right] \tag{2.33}$$

or Lorentzian

$$Intensity = k0 + \frac{k1}{(energy - k2)^2 + k3} \tag{2.34}$$

fitting is typically used to deconvolute those closely spaced emissions. The energy location of each emission is related to the type of impurity incorporation, or structural defect in a sample [9, 121, 123]. For example, emissions at 3.3628 eV (I_4) and 3.3608 eV (I_6) correspond to H and Al incorporation, respectively, in an unstrained ZnO bulk sample [121]. Therefore, PL, especially low temperature PL (LT PL), is a very powerful tool in investigating the optical properties of a material.

Chapter 3

Growth of Zinc Oxide Epilayers

3.1 Determining the Growth Environment

An important factor in determining properties of a thin film is the growth environment. For nominally undoped ZnO films, a stoichiometric growth environment is generally desired as deviation from stoichiometry represents increased formation of native defects. For doping, either O-rich or Zn-rich growth environments are preferred, depending on the dopants used. Therefore, it is necessary to be able to determine the type of growth environment desired for the particular growth experiment.

Zn and O adatoms diffuse up to a certain length before being chemisorbed and incorporated into the lattice. Non-incorporated species tend to re-evaporate as Zn has a high vapour pressure, and growth typically occurs at an elevated temperature (>500°C). Therefore, if the substrate temperature and oxygen flux are held constant, the growth rate will depend on the Zn flux only. Initially, the growth rate will increase linearly with increasing Zn flux since Zn adatoms are the limiting factor. In this case, such a growth regime is known as O-rich conditions. The point at which the Zn and O flux are equal is called the stoichiometric region. When the Zn flux exceeds the O flux, the growth rate will saturate, as there is a limit to the number of available O adatoms. Such a region is known as the Zn-rich growth regime.

In the set of experiments described here, the oxygen flow rate was fixed at 0.5 sccm for ZnO growth, the RF plasma power at 400 W, and the substrate

temperature at 700°C. The growth rates were then measured as the Zn flux was varied between 1.6×10^{14} and 9.8×10^{14} atoms/cm^{2}s. As growth was performed on sapphire, a combination of MgO and low temperature ZnO (LT-ZnO) buffer layers were used to accommodate for the lattice mismatch, using parameters developed as part of a previous study [21], summarised in Table 3.1.

Table 3.1. Summary of growth parameters used in growth rate study.

	O_2 flow rate (sccm)	RF power (W)	Substrate temperature (°C)	Growth time (min:sec)	Mg or Zn flux (atoms/cm^{2}s)
MgO	2	400	750	0:8	2.75×10^{14}
LT-ZnO	0.5	400	450	1:10	6.39×10^{14}
HT-ZnO	0.5	400	700	varies	varies

Since this type of growth rate experiment requires accurate knowledge of the Zn flux, it is necessary to have confidence in the Zn flux measured from the QCM. It should be noted that such flux measurements do not measure the exact flux that arrives on a substrate. Flux arriving on a water-cooled QCM has a higher sticking coefficient than flux arriving on a substrate at elevated temperature. Furthermore, there can be slight differences between the substrate position and the location of the QCM. Nevertheless, flux measurements using a QCM do give a good indication as to the amount of flux that is directed at a substrate.

From earlier growth experiments by a previous study [21], it was determined that the measured flux takes a finite amount of time before giving a consistent reading. Furthermore, if too many measurements are taken, the QCM may exhibit heating effects and give erroneous results. It is also desirable to take the least amount of flux measurements as possible as it is necessary to vent the growth chamber, and subsequently spend several days baking and outgassing the system, should there be a need to change the crystal for the QCM.

To resolve this issue, the Zn flux, via the frequency difference (Δf) on the QCM, was measured for different Zn cell temperatures. The Zn flux was then calculated using Eqs. (1.3) and (1.4), with the molecular weight M being 65.409 g/mol. It takes some time for the flux to stabilise if the effusion cell shutter has been closed just prior to measurements, as shown in Fig. 3.1. If the shutter covering the

effusion cell was previously closed, then it takes at least 180 seconds before the flux stabilises at the steady-state (growth) flux value, as shown through an exponential fit. Such situations occur regularly, as it is common to need multiple effusion cells for a growth. Hence, it is necessary to leave the shutter of the effusion cell to be measured open for at least three minutes before lowering the QCM into the growth path to measure the flux.

It should be noted that one set of flux measurements (red triangle) had a higher steady-state value than the other set of flux measurements (black circle) because the Mg effusion cell was in use for one (red triangle), but not the other (black circle). It has been observed that the Mg effusion cell shutter is inadequate in properly shuttering off the Mg flux, typically resulting in a "blowby" Mg flux that manifests as an additional frequency difference of 3 Hz.

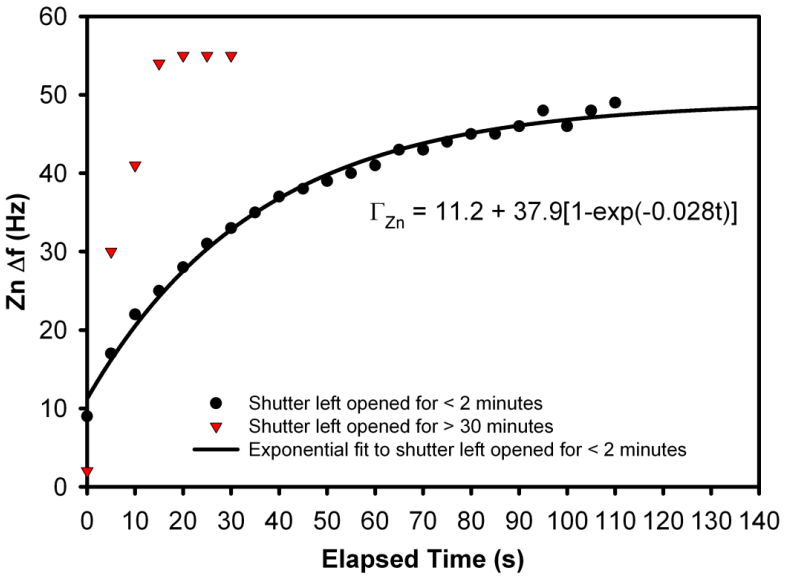

Fig. 3.1. Comparison of Zn flux measured with the Zn shutter either left open or left closed for a period of time. At both times, the Zn cell was operated at 500°C.

It is also necessary to establish the minimum number of readings necessary to have confidence in the flux measured, and also the readings where QCM heating effects start dominating and skewing the flux measurements. There is a clear transient before the flux reaches a steady state value, as shown in Fig. 3.2. After opening the shutter, it is possible that there exist some shutter vibrations, which can disturb the flux. Another possible source of the observed transient may be due to crystal transient effects. With readings taken at five second intervals, up to the first four readings (20 s) are not representative of the true flux value. This is

confirmed by observing that the spread in Δf is significantly reduced by discarding the first four readings, as shown from the comparison between Fig. 3.3(a) and (b). There does not appear to be any significant benefit in taking an excessive number of readings, as shown by the rather consistent behaviour shown in Fig. 3.2. Therefore, once a few readings agree or after 10 readings (50 s), the true flux has been measured. It is also interesting to note that the measured flux for temperatures below 440°C is similar to the theoretical flux as calculated from Eq. (1.2).

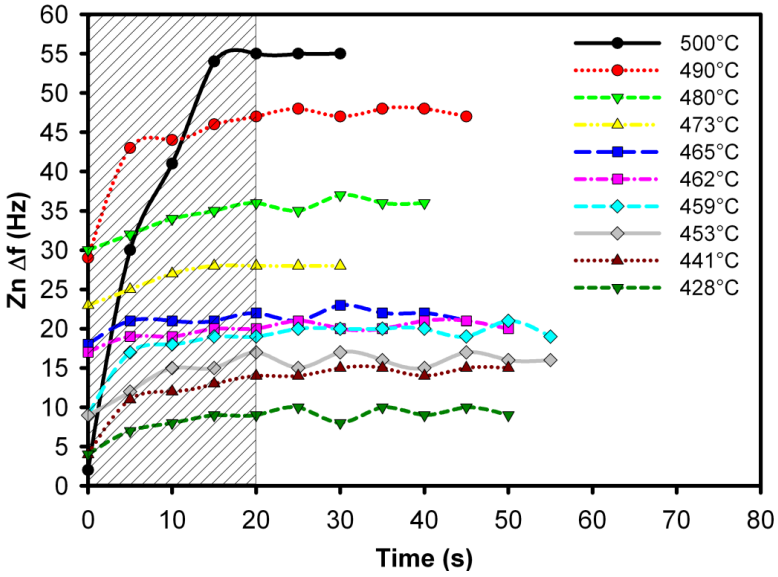

Fig. 3.2. Zn flux QCM readings with the Zn cell varied between 428°C and 500°C. The shaded and unshaded regions represent the unstable and steady-state flux regions, respectively.

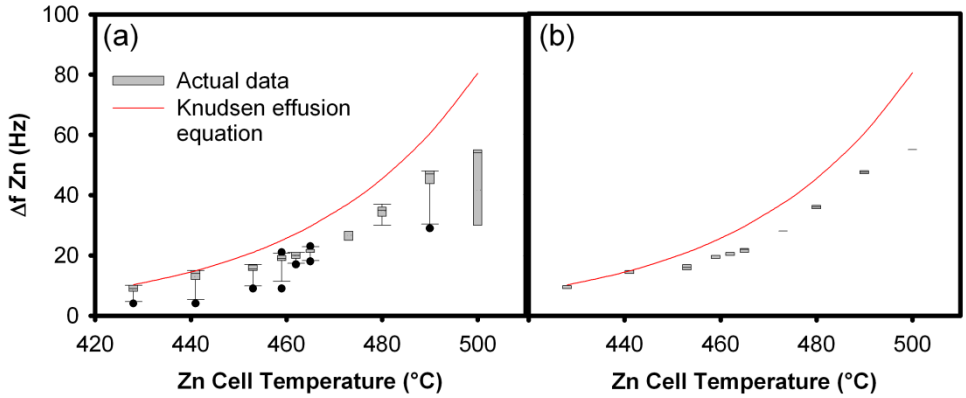

Fig. 3.3. Zn Δf readings (a) of all datapoints, (b) after ignoring first 4 datapoints. The boundary of the box closest to zero indicates the 25th percentile, a line within the box marks the median, and the boundary of the box farthest from zero indicates the 75th percentile. Whiskers (error bars) above and below the box indicate the 90th and 10th percentiles. The filled circles indicate outlying points and the dotted line indicate the mean. The red line represents the expected Zn Δf as calculated from the Knudsen effusion equation.

After establishing the limitations inherent to the QCM, the next step was to perform growth rate experiments to map the growth regions. The growth rate as a function of Zn flux at a fixed substrate temperature (700°C), RF power (400 W), and oxygen flow rate (0.5 sccm) is shown in Fig. 3.4. Assuming that the stoichiometric region is the knee-point between the "linear" portion and the saturation portions of the plot, the stoichiometric point is where the Zn flux is approximately 4.0×10^{14} atoms/cm^{2}s, with a growth rate of approximately 210 nm/hr. Below and above 4.0×10^{14} atoms/cm^{2}s are the O-rich and Zn-rich regions, respectively.

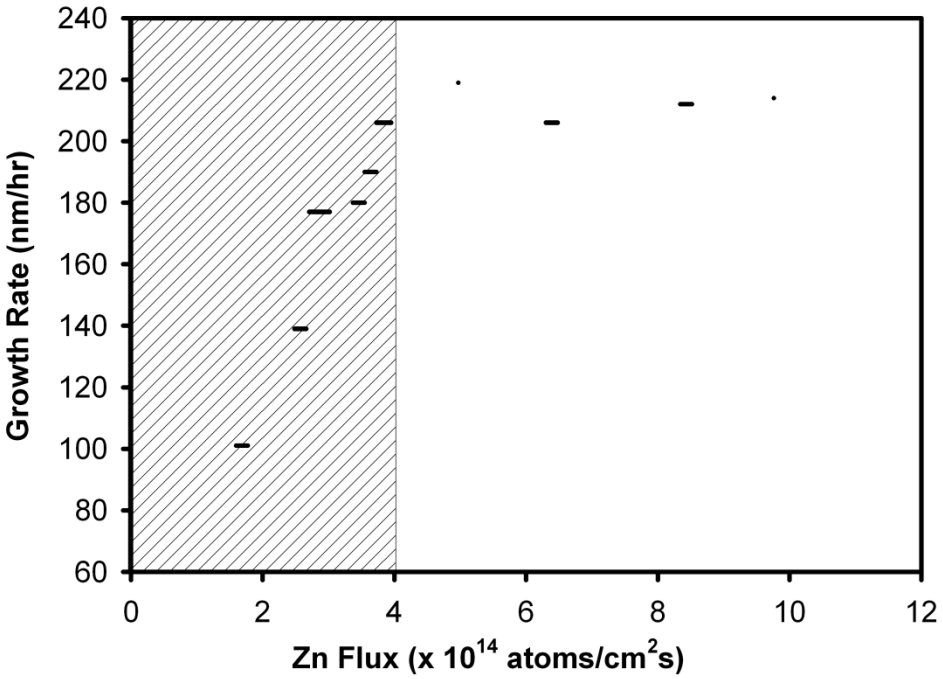

Fig. 3.4. Growth rate plots for substrate temperature of 700°C, RF power of 400 W and oxygen flow rate of 0.5 sccm. The line at each growth rate represents the range of Zn flux measured after each growth. Shaded area represents O-rich region. Boundary between shaded and unshaded areas is the stoichiometric region.

However, the exact position of the knee-point can be open to interpretation as experimental variations mean that the transition between the O-rich and Zn-rich region is rarely a sharp, unambiguous point. This is demonstrated in other reported studies [124, 125] shown in Fig. 3.5. Note that the data points in Fig. 3.5 actually fluctuate slightly, in contrast to the straight lines drawn by those authors. Interestingly, Hirano et al. [124] also found that the stoichiometric point occurs when the growth rate starts saturating at 200 nm/hr, quite similar to Fig. 3.4, even

though the growth parameters were slightly different to those used in this thesis (see Table 3.2).

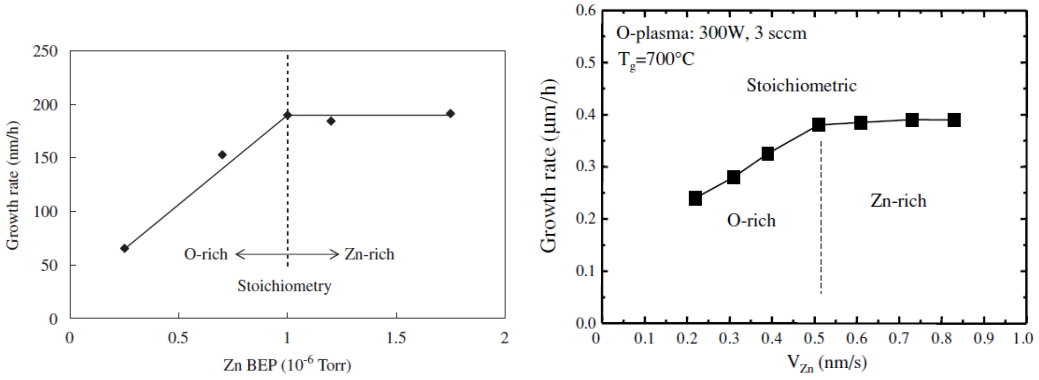

Fig. 3.5. Selected reported growth rate of films as a function of (a) Zn beam equivalent pressure (BEP) [124], (b) Zn flux [125].

Table 3.2. Summary of parameters for growth rate studies shown in Fig. 3.4 and 3.5.

	Sapphire orientation	Substrate Temperature (°C)	Oxygen flow rate (sccm)	RF power
This thesis	c-plane	700	0.5	400
Hirano [124]	a-plane	600	1	350
Cho [125]	c-plane	700	3	300

The growth regions identified through Fig. 3.4 are only valid for the selected parameters used. The growth rates are also different for different growth temperatures as adatoms are less likely to re-evaporate at lower growth temperatures, thereby increasing the growth rate. It is also possible for temperature to shift the stoichiometric points compared to growth at 700°C. There is an approximately 17% increase in the growth rate at 400°C, compared to 700°C, as shown in Fig. 3.6. Therefore, the flux of 4.0 x 10^{14} atoms/cm^{2}s is at least past the stoichiometric point for all four temperatures measured. The higher growth rates for lower temperatures are also not unexpected as the sticking coefficient is higher at lower temperatures, therefore allowing more chemisorption between the Zn and O atoms, and hence higher growth rates of the ZnO layers.

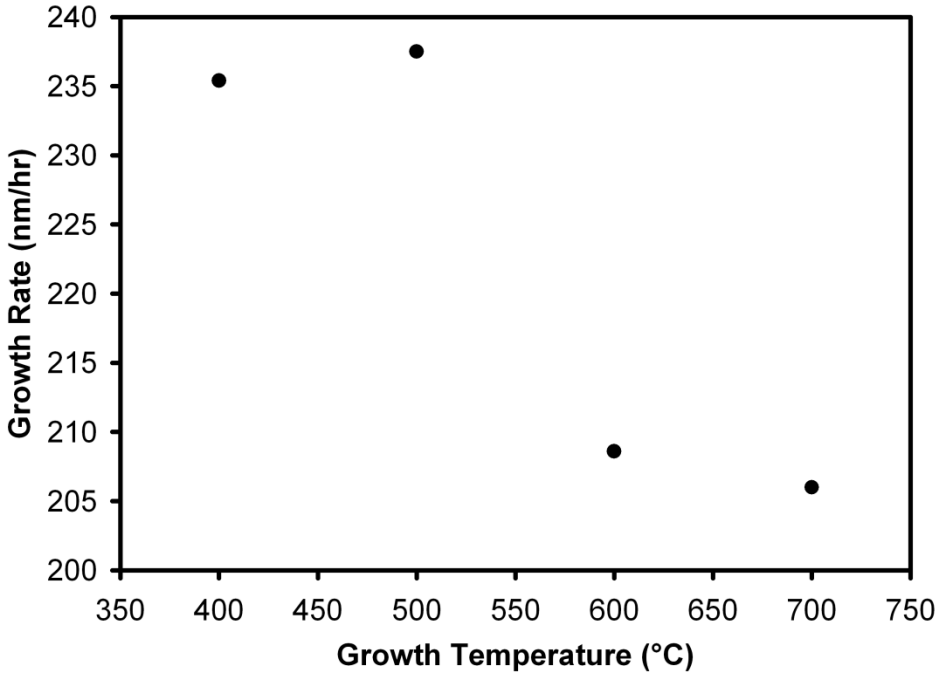

Fig. 3.6. Growth rates of a ZnO film at oxygen flow rate of 0.5 sccm, RF power of 400 W, Zn flux fixed at 4.0 x 10^{14} atoms/cm^{2}s and the substrate temperature varied from 400°C to 700°C. Note that all of these growths were done on the same film run, with a 15 minute ramp and 30 minute soak between substrate temperatures.

Ko et al. [126] reported that the stoichiometric point is very similar for higher growth temperatures of 500°C – 600°C, as shown in Fig. 3.7. However, there is a significant Zn flux change to acquire the stoichiometric point at lower temperatures. Therefore, we can infer that for higher growth temperatures (600°C – 800°C), a flux of 4.0 x 10^{14} atoms/cm^{2}s is close to the stoichiometric point but that same flux is likely to be Zn-rich for temperatures below 600°C.

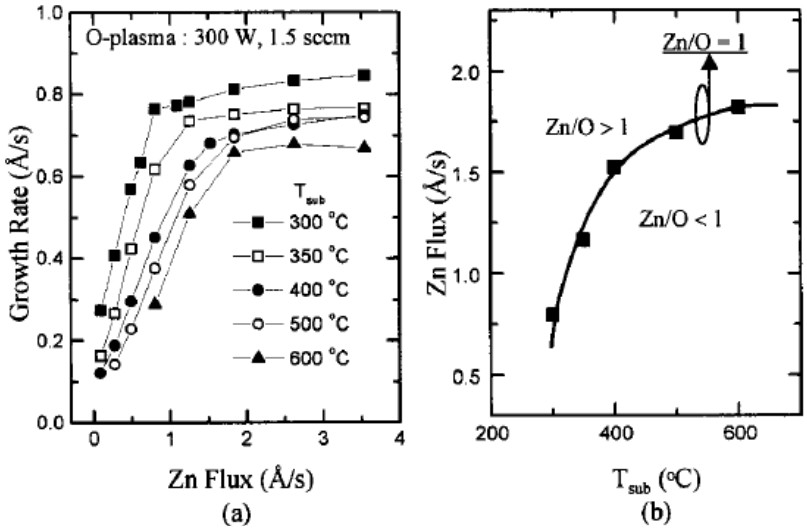

Fig. 3.7. Growth rate data reported by Ko et al. [126] (a) ZnO growth rates vs Zn beam flux obtained by RHEED intensity oscillations at various substrate temperatures. (b) Zn/O ratio diagram as a function of substrate temperature, obtained from data (a).

3.2 Substrate Temperature Measurement

High-quality epitaxial thin film growth usually requires elevated growth temperatures to ensure sufficient energy is available for adatoms to diffuse to the appropriate lattice sites. Having a stable substrate temperature is especially important during long growth runs. If the temperature varies significantly during growth, then conditions are changing during growth. Doping also requires careful control of growth temperatures due to the temperature dependent incorporation of dopants.

Several methods can be employed to determine the substrate temperature. One common technique is optical pyrometry, where the radiation intensity of the substrate is measured to ascertain the temperature of that substrate [127]. However, pyrometry is affected by coated viewports and stray light sources [128]. Another commonly employed technique is measuring the temperature using a thermocouple embedded near the substrate or heater element. In the MBE system used in this thesis, the substrate temperature is measured by a type D thermocouple in mechanical contact with a 76 mm diameter molybdenum growth block. Essentially, the substrate temperature is inferred by assuming that the temperature of the growth block is the same as the substrate temperature. In practice, there will be temperature differences between the growth block and the substrate non-ideal thermal coupling. Even though indium-tin bonding is used to bond the substrate to the growth block, sapphire is a poor thermal conductor. Furthermore, coating the substrate eventually affects its emissivity.

To investigate the temperature difference between the thermocouple and the substrate, a non-contact temperature measurement technique called BandiT (k-Space Associates Inc., USA) was used to measure the actual surface temperature of the substrate. To put it simply, BandiT utilises the fact that the absorption bandedge of a semiconductor substrate has a temperature dependence that can be calibrated. Hence, by measuring the bandedge through a reflectivity measurement, the temperature of the semiconductor substrate can be determined.

The test substrate used was a 10 mm by 10 mm m-plane hydrothermally grown ZnO substrate indium-tin bonded to a 76 mm diameter molybdenum block. The

temperature was increased linearly from room temperature to 450, 550 and 650°C, respectively, over a period of 30 minutes, for each of the three terminal temperatures. Three key features can be observed in Fig. 3.8. Firstly, the surface temperature appears to follow the power supplied to the heater. The decreasing surface temperature at constant thermocouple temperature is due to the entire heater setup being a large thermal mass. Therefore, it is necessary to apply a significant amount of power to the heater to ensure that the thermocouple initially reaches the desired temperature quickly. However, once at the desired temperature, this large thermal mass begins to equilibrate, and consequently requires less power to the heater to maintain the thermocouple temperature. This results in decreasing power being applied to the heater. However, the thermal coupling between the substrate and the heater is much weaker. Hence, there is a decrease in the substrate temperature over time due to the reduction in the radiative power provided by the heater.

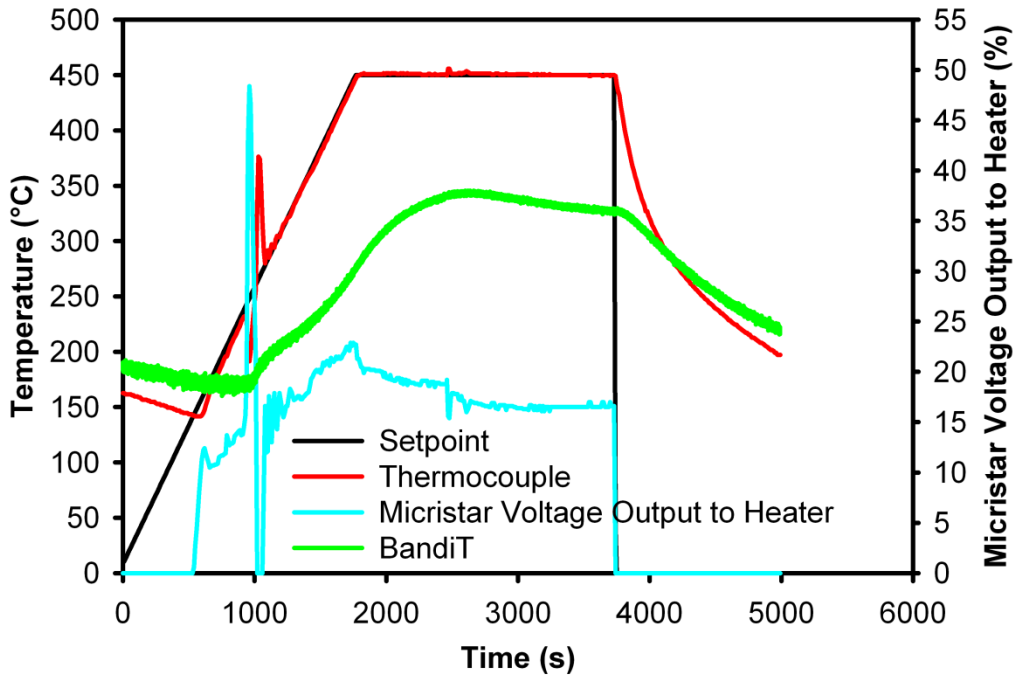

Fig. 3.8. Micristar and BandiT outputs for a desired thermocouple temperature of 450°C. The substrate was heated to 450°C over 30 minutes and left to soak at 450°C for 30 minutes. Finally, the heater was turned off to the substrate to let the substrate cool down to room temperature.

Secondly, there is a delay between the thermocouple showing that it has reached the desired setpoint temperature and the substrate surface actually reaching its maximum temperature. The existence of a delay further confirms the poor thermal conductivity of the substrate. This delay is up to 15 minutes and therefore means that growth should not start until at least 15 minutes after the setpoint is reached, as time needs to be allocated for the surface temperature to stabilise.

Thirdly, the maximum surface temperature (346°C) is approximately 100°C lower than the desired setpoint temperature (450°C). Such an offset is not unexpected as there is a non-ideal thermal coupling between the thermocouple, molybdenum block, bonding solder, and sapphire substrate, as illustrated in Fig. 3.9.

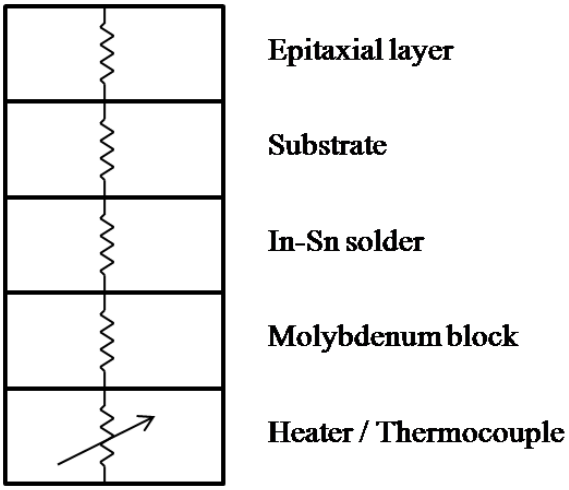

Fig. 3.9. Thermal coupling route from heater to epitaxial layer. Variable clamping of the sample block is represented by the variable resistor symbol.

Similar effects were observed for other thermocouple temperatures, as summarised in Table 3.3. An offset of approximately 100°C exists for both the desired thermocouple temperatures of 450°C and 650°C. Therefore, any growth within this temperature range may actually be 100°C lower than expected. The agreement between the thermocouple and surface temperature for 550°C is the exception rather than the norm, and cannot yet be explained. In addition, the surface temperature decays over time in the same trend as that observed in Fig. 3.8. Furthermore, the time delays between reaching the desired thermocouple temperature and the maximum surface temperature range between 10 to 15 minutes.

Table 3.3. Summary of thermocouple and surface temperature differences for thermocouple temperatures between 450°C and 650°C.

Desired thermocouple temperature (°C)	Maximum surface temperature (°C)	Surface temperature drop (°C/30min)	Time Delay between reaching desired thermocouple temperature and a surface temperature peak (s)
450	346	20	864 (14.4 mins)
550	554	49	350 (5.8 mins)
650	556	27	577 (9.6 mins)

One possibility to counteract the decreasing surface temperature is by keeping the power applied to the heater constant once both are reasonably stable. The effect of keeping the heater output constant after the thermocouple has reached a steady state value of 650°C is shown in Fig. 3.10. As expected, the surface temperature could be maintained at 520°C to 530°C.

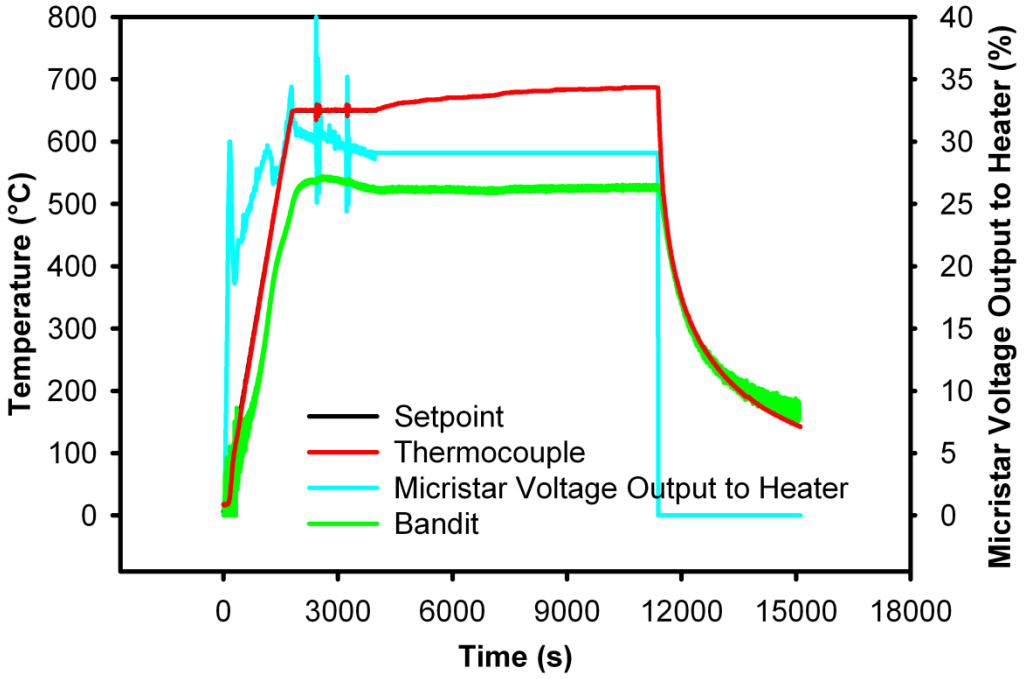

Fig. 3.10. Micristar and BandiT outputs for a desired thermocouple temperature of 650°C. The substrate was heated to 650°C over 30 minute. Then the Micristar voltage output to the heater was fixed at 29.1% for 2 hours. Finally, the heater was turned off to the substrate to let the substrate cool down to room temperature.

However, as heat was constantly being applied even when the thermocouple has reached equilibrium, an exponential rise in the thermocouple temperature was detected, as shown in Fig. 3.11. Using an exponential fit, one can calculate that it

takes up to 2.8 hours to reach 686°C, which is 99% of the saturation temperature of 693°C, as summarised in Table 3.4.

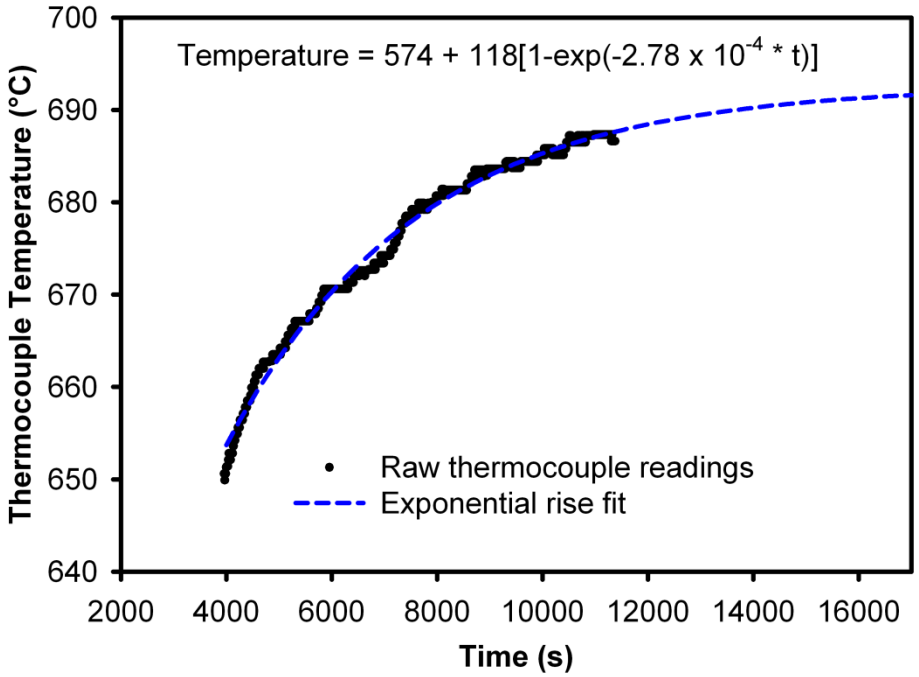

Fig. 3.11. Plot of thermocouple temperature when the power to the heater was fixed at 29.1%. Original data taken from Fig. 3.10.

Table 3.4. Time taken to reach the vicinity of the saturation temperature for the exponential fit in Fig. 3.11.

Temperature (°C)	% of saturation temperature	Time taken to reach temperature (hours)
693	100	> 6
686	99	2.8
658	95	1.2
624	90	0.5

A series of experiments was also conducted to find the relationship between the power supplied to the heater and the surface temperature. Figure 3.12 shows that there is a quadratic relationship in the form of

$$BandiT = -346.4 + 52.3 \times P_{Output} - 0.8 \times P_{Output}^2 \tag{3.1}$$

Hence, an alternative method to deduce the surface temperature is by using the heater output value to infer the surface temperature, after giving sufficient time for the surface temperature to stabilise.

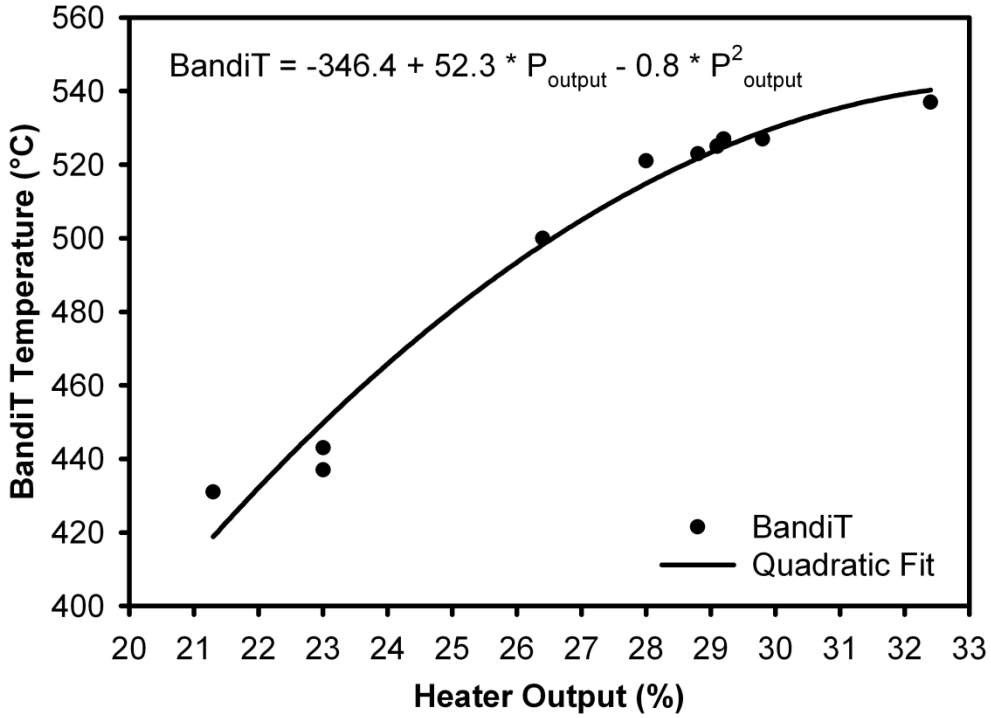

Fig. 3.12. Measured average BandiT temperature (i.e. substrate surface temperature) as a function of heater output. Both values are in their steady state.

These series of experiments have shown that interpretation of the actual surface temperature can be tricky, due to the limitation of all measurement techniques. Hence, it is necessary to choose one to rely on predominantly and design a control system to use that as a feedback. Currently, we are still using the Micristar-controlled heater with the thermocouple reading as the temperature quoted throughout this thesis. However, it may be necessary in the future to link the BandiT temperature feedback to the Micristar in order to control the heater by actually monitoring the surface temperature, thereby giving a better measure of the actual growth temperature. However, it should be kept in mind it is not possible to directly measure the substrate temperature of UV transparent substrates such as sapphire, as it requires a minimum thickness (~ 400 nm) of ZnO for adequate absorption to occur. Therefore, a possible compromise may be to rely on the thermocouple temperatures initially, and then use BandiT to maintain the growth temperature once a thick enough layer has been grown. Alternatively, the use of a non UV transparent substrate will enable accurate surface temperature measurements from the start of growth.

3.3 Mitigating Lattice Mismatch Using MgO

Another factor that influences the quality of an epitaxial film is the substrate. Many different substrates can be used to grow epitaxial ZnO. Each substrate has different crystal structures, lattice parameters and thermal expansion coefficients; common ones employed for ZnO are summarised in Table 3.5. Ideally, ZnO should be grown homoepitaxially on a ZnO substrate. However, issues with surface damage due to polishing [23, 24], diffusion of impurities from the ZnO substrate to the epitaxial ZnO layer [129], limited availability of epitaxy ready substrates for growth, and high cost of ZnO substrates have thus far limited the use of ZnO substrate as a substrate material. Nevertheless, some recent successes [130, 131] with homoepitaxial ZnO growth are very encouraging.

Table 3.5. Properties of several potential ZnO growth substrates [9].

Material	Crystal Structure	Lattice Parameters a (Å) c (Å)	Lattice Mis-match to ZnO (%)	Thermal Expansion Coefficient α_a (10^{-6} K^{-1}) α_c (10^{-6} K^{-1})
ZnO	Hexagonal	3.252 5.213	0	2.9 4.75
GaN	Hexagonal	3.189 5.185	1.8	5.17 4.55
Al_2O_3	Hexagonal	4.757 12.983	18.4% after 30° in-plane rotation	7.3 8.1
Si	Cubic	5.430	40.1	3.59
$ScAlMgO_4$	Hexagonal	3.246 25.195	0.09	

There are three main types of epitaxial growth; lattice-matched (homoepitaxy), strained heteroepitaxy, and relaxed heteroepitaxy, as illustrated in Fig. 3.13. If the substrate has a larger (or smaller) lattice than the epilayer, the epilayer will have tensile (or compressive) strain in the growth direction, and be under compressive (or tensile) strain perpendicular to the interface, as shown in Fig. 3.13(b). Such growth is also known as pseudomorphic growth [29], in that the epilayer attempts to "fit" onto the substrate. However, above a critical thickness, eventually misfit dislocations will form to relieve the accumulated strain, resulting in subsequent layers being relaxed into the epilayer's preferred lattice spacings [2].

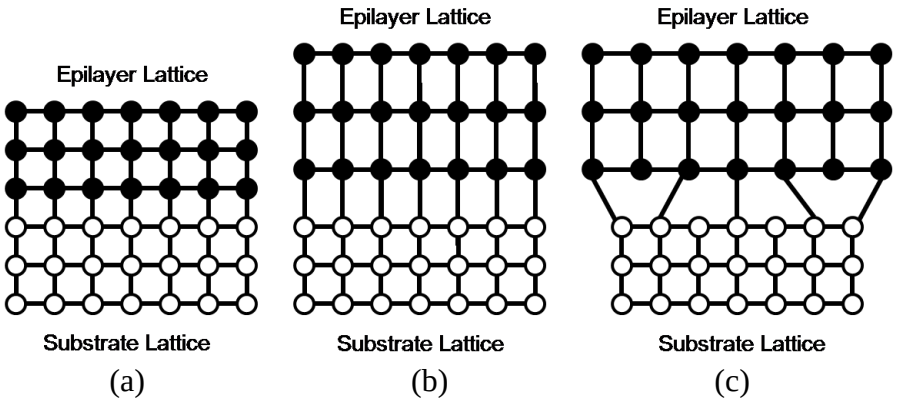

Fig. 3.13. Schematic illustration of (a) lattice-matched (homoepitaxy), (b) strained, and (c) relaxed heteroepitaxial structures [2].

A popular substrate for ZnO growth is c-plane sapphire, as it is inexpensive, transparent to visible wavelengths, and available as a large area wafer. However, as Table 3.5 shows, there are large differences in the lattice parameters between ZnO (a = 3.252 Å, c = 5.213 Å) and Al_2O_3 (a = 4.757 Å, c = 12.983 Å), resulting in a 18.4% lattice mismatch even after a 30° in-plane rotation to align with the oxygen sub-lattice of Al_2O_3 [132]. As such, ZnO films grown directly on sapphire tend to form in the Stranski-Krastanov mode, resulting in many grain boundaries and hence a poor structural quality film [133]. Nevertheless, it is still possible to exploit the advantages of growing on sapphire by employing suitable buffer layers to mitigate the lattice mismatch between ZnO and sapphire.

One type of buffer layer between ZnO and sapphire is a thin magnesium oxide (MgO(111)) buffer layer. MgO is pseudomorphic below its critical thickness (0.3 nm) [134], with a (111) cubic bulk structure above its critical thickness. Several groups [125, 134-141] have reported reduced dislocations and/or improved epilayer quality via the use of a MgO buffer layer. MgO(111) grows on $Al_2O_3(0001)$ with the epitaxial relationship $MgO[\overline{1}\overline{1}0]//Al_2O_3[2\overline{1}\overline{1}0]$ and $MgO[\overline{1}\overline{1}2]//Al_2O_3[01\overline{1}\overline{0}]$ [140]. Table 3.6 summarises reported MgO/LT-ZnO buffer layer structures. Several groups [136, 138] have reported that the rms roughness and XRD FWHM of the resultant ZnO epilayers are reduced with the introduction of a MgO buffer layer, compared with growth directly on sapphire. Furthermore, the optimum strain relaxation and hence reduction in dislocation density is achieved at the start of the three-dimensional growth of MgO. Therefore, the optimum MgO growth time was decided by monitoring the

RHEED pattern during growth and terminating growth at the point when the RHEED pattern starts to turn spotty.

Table 3.6. Summary of reported ZnO growths using MgO/LT-ZnO buffer layers via PAMBE. RMS roughness, ω-RC (rocking curve) and D^0X FWHM values are for the resultant ZnO epilayers employing the MgO/LT-ZnO buffer layers.

MgO growth parameters	RHEED images	RMS roughness (nm)	(0002) ω-RC FWHM (arcsec)	D^0X FWHM (meV)	Ref.
1.5 to 2 nm thick, RF at 300W, O_2 at 1.5 sccm, T_{growth} of 500°C, 0.01Å/s growth rate, O-rich	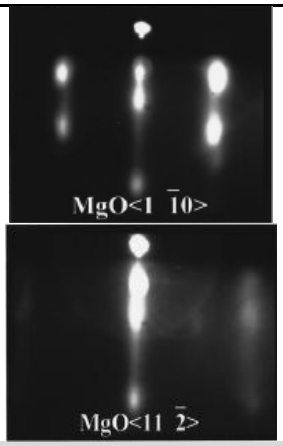	0.8 nm for 10 μm × 10 μm scan	13	3.2	[135, 138, 140]
T_{growth} of 700°C and then 490°C, anneal at 800°C for 25 min, 0.01Å/s growth rate	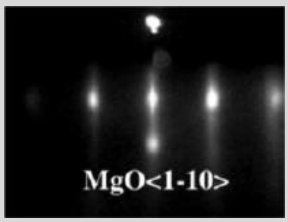	0.3 nm for 2.5 μm × 2.5 μm scan	15		[125, 136, 137]
2 to 4 nm thick, RF at 400W, T_{growth} of 700°C, 0.05Å/s growth rate, O-rich	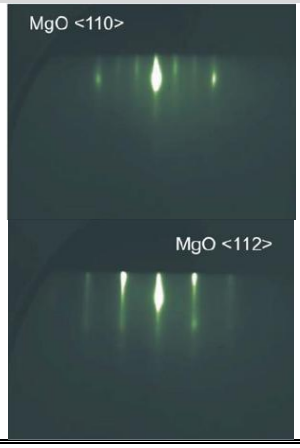	0.26 nm for 2 μm × 2 μm scan	25		[134, 142]

Figures 3.14 and 3.15 show the evolution in the RHEED pattern and lattice spacing, respectively, over a typical 10 s MgO growth period. Initially, the RHEED image and lattice spacing of the nucleating MgO layer is very similar to the underlying sapphire substrate, indicating 2D pseudomorphic growth [136].

Pecz et al. [134] estimated that pseudomorphic MgO growth can occur for MgO thicknesses less than 0.3 nm. After approximately four seconds of growth, the MgO layer enters the 2D-3D transition mode, as indicated by appearance of weak spots on the rods of the RHEED images. The lattice spacing has also reduced significantly by approximately 4%. At the conclusion of growth at 10 s, the growth is entering the 3D growth mode, with the lattice spacing reduced by approximately 8-9% compared to the sapphire substrate, consistent with previously reported values [125, 140], and with bulk parameters as the expected in-plane lattice mismatch between rock-salt MgO(111) and sapphire (0001) is 8.4% [143].

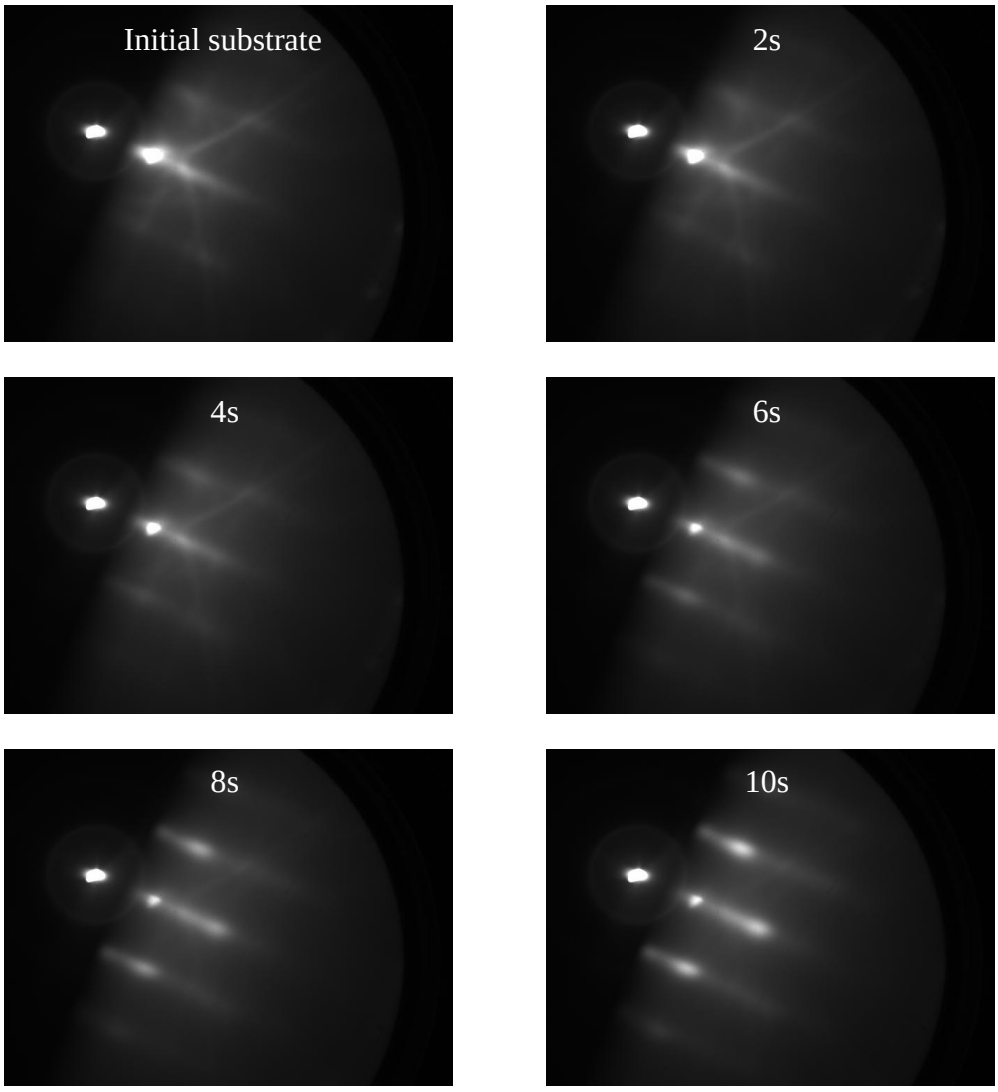

Fig. 3.14. Evolution of RHEED pattern as observed over a 10 s MgO growth period.

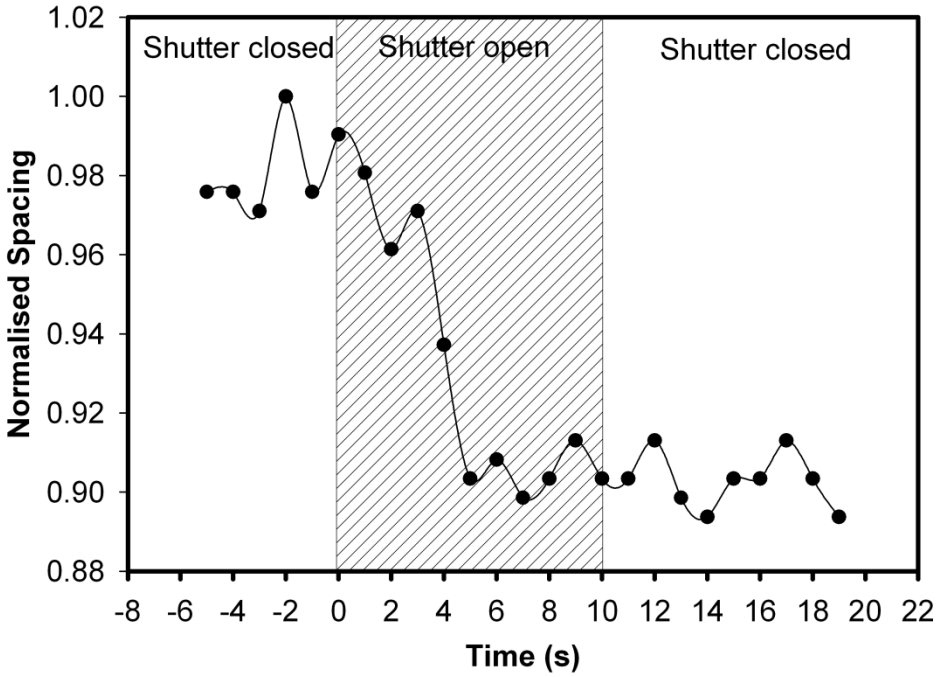

Fig. 3.15. Change in rod spacing as observed in real-time RHEED. The spacing is the average spacing between the middle rod (the same rod where the specular spot lies) and a rod on either side of that middle rod. The spacing is then normalised to the spacing of the sapphire substrate.

Table 3.7 shows the conditions used for the optimised MgO buffer layer growth. The RHEED images in Fig. 3.16 shows a change from streaky and narrow rod spacing (Fig. 3.16(a)) to a spottier and wider rod spacing (Fig. 3.16(b)), indicating a change from a smooth, Al_2O_3 surface with hexagonal symmetry to a rougher and cubic MgO structure. The cross pattern (green overlay) evident in Fig. 3.16(b) is a typical diffraction pattern for a (111) cubic structure [144], which is the equilibrium crystal structure of bulk MgO [145]. This indicates that the MgO is likely relaxed after 10 s of growth under the conditions listed in Table 3.7.

Table 3.7. Conditions for optimised MgO buffer layer growth.

O_2 flow rate (sccm)	RF power (W)	Substrate temperature (°C)	Growth time (sec)	Mg flux (atoms/cm^{2}s)
2	400	750	10	2.96×10^{14}

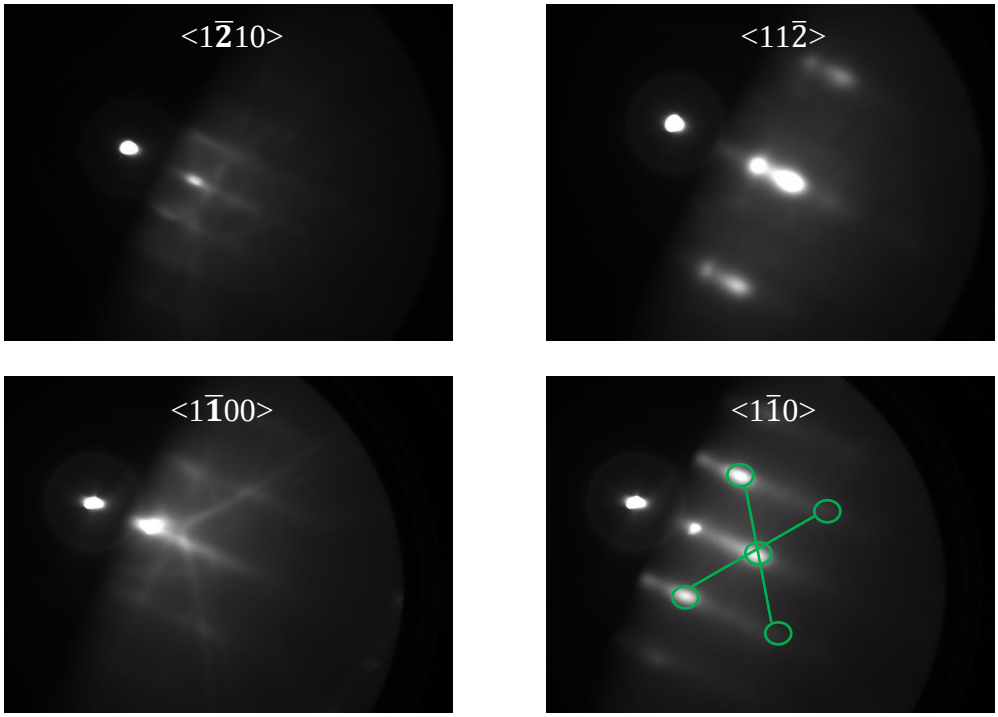

Fig. 3.16. RHEED image of (a) initial Al_2O_3 substrate, and (b) after 10 s MgO growth. The green overlay of circles and lines indicates a typical cross pattern for a (111) cubic structure.

A longer MgO experiment was undertaken to confirm what occurs during this heteroepitaxial growth. The RHEED images in Fig. 3.17 shows a clear trend from a smooth hexagonal sapphire surface, with streaks and Kikuchi lines, to a rough cubic surface, consisting of spots and a cross pattern. It should be noted that the streaks (Fig. 3.17(b)) to spots (Fig. 3.17(c)) transition on the rods in the RHEED patterns were not solely due to surface roughening. The spot appearance was due to the presence of 3D MgO islands with mixed 60° in-plane rotation [146]. The intensity of the spots became more pronounced with increasing MgO thickness (Fig. 3.17(c) to (d)) due to an increase in those 3D features. Such in-plane rotation effects have been previously observed with deposition of (111) MgO on (0001) 6H-SiC [146] and (0001) GaN [147].

The change in the lattice spacing is evident from Fig. 3.18. The 60 s MgO growth has a lattice spacing reduction of approximately 9% compared to sapphire, consistent with the 8.5% lattice mismatch between (0001) Al_2O_3 and (111) MgO [134]. The 10 s growth for this particular experiment is slightly thinner than for the films mentioned earlier as the Mg flux is lower, which might explain the differences between this lattice spacing change compared to others discussed

earlier. Nevertheless, it can be concluded that since one observed both a cross pattern and a lattice spacing change of 9%, the optimum MgO growth conditions is sufficient to obtained the desired (111) MgO thin buffer layer. The MgO buffer layer thickness has been reported to be optimal when both of those conditions are satisfied.

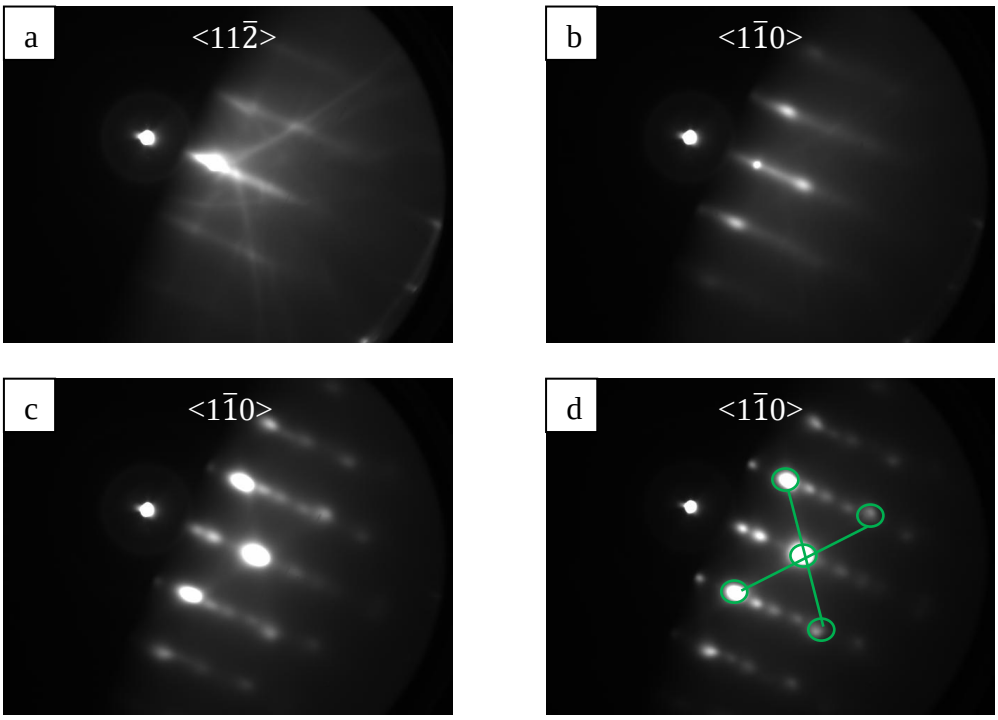

Fig. 3.17. RHEED image of (a) initial Al_2O_3 substrate, (b) 10 s MgO growth, (c) 30 s MgO growth, and (d) 60 s MgO growth. The green overlay of circles and lines indicates a typical cross pattern for a (111) cubic structure.

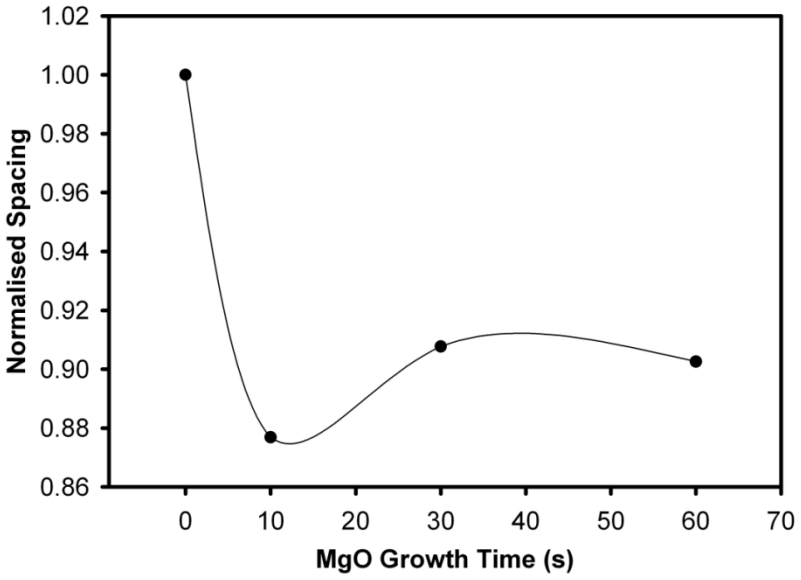

Fig. 3.18. Change in normalised rod spacing as observed in real-time RHEED. The line is intended as a guide to the eye.

As well as acting as a buffer layer, MgO can also determine the polarity of subsequent ZnO growth, via controlling the thickness of the MgO layer [148, 149]. Since ZnO has a wurtzite structure, the lack of inversion symmetry leads to the possibility of Zn- or O-polar growth forms. The polarity determines the growth mode, impurity incorporation, piezoelectricity, spontaneous polarization, and surface stability [150]. It has been reported that O-polar ZnO typically has smaller FWHM of (002) and (105) ω-scans [151], slower growth rate [148, 149, 151], and lower rms roughness [143]. Control of polarity during growth is therefore an important issue.

One technique to determine the polarity of a film is by using wet etching, as different polarities etch at different rates [152]. A small piece of each of several films was patterned with a step using photolithography. A solution containing 1:1000 HCl:de-ionised water (DIW) was then used to etch each sample for 10 seconds. The resultant surface, as observed using SEM, is shown in Fig. 3.19. As Fig. 3.19(b) shows rough hillocks instead of hexagonal pits [152, 153], it can be concluded that the MgO conditions listed in Table 3.7 result in an O-polar film.

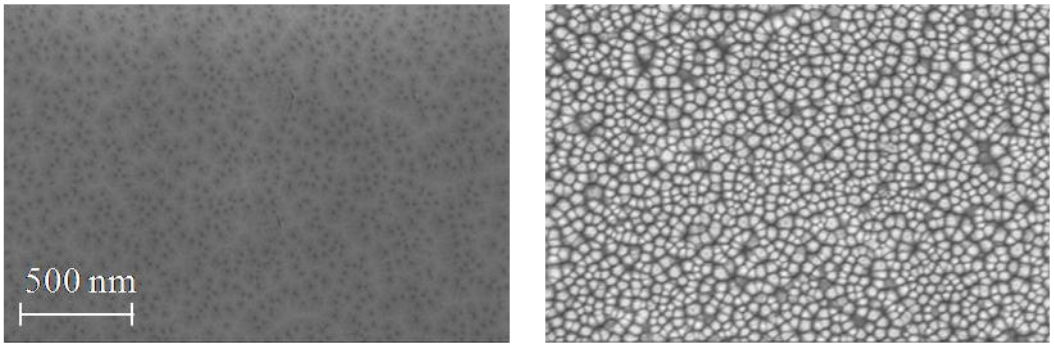

Fig. 3.19. Top view SEM images of surface of a film grown with the MgO parameters listed in Table 3.7 (a) before etching, and (b) after etching.

To further confirm that the MgO growth conditions used in Table 3.7 do not result in a Zn-polar film, one can analyse the thickness of MgO. The polarity of the overlaying ZnO epilayers can be determined by the thickness of the underlying MgO buffer layer [143]. According to Kato et al. [148], the ZnO polarity changed from O-polar to Zn-polar for a MgO thickness greater than 2 nm, as confirmed by convergent beam electron diffraction (CBED). Minegishi et al. [149] reported that MgO has a pseudomorphic structure when less than 0.8 nm, and a rock-salt

structure above 1.3 nm, with the in-plane lattice constant saturating after 1.3 nm thickness. They also found that for a MgO layer less than 2.7 nm, the subsequent ZnO film were O-polar; above 3 nm, films will be Zn-polar.

A previous study using the MBE system at the University of Canterbury [21] determined that the MgO grown using a Mg flux of 2.96×10^{14} cm^{-3}, oxygen flow rate of 2 sccm and RF power of 400 W, is approximately 1 nm. As this was grown over 10 s, the growth rate is 0.1 nm/s. Since the Mg flux used for all MgO growth in this thesis is approximately half the Mg flux, but with the same oxygen flow rate and RF power, the MgO growth rate will be approximately 0.05 nm/s, if one assumes an O-rich condition. Using a 10 s growth time, this gives a MgO thickness of 0.5 nm. If the MgO was grown under Mg-rich conditions instead, then the MgO thickness is 1 nm. Nevertheless, a MgO thickness of 0.5 to 1 nm is well within the requirement for O-polar growth, and is far from the 2 nm to 3 nm thickness which would switch the polarity from O-polar to Zn-polar. Hence both the wet etching and MgO thickness analysis support the assertion that all films grown using the MgO buffer layer parameters in Table 3.7 will produce an O-polar ZnO thin film.

3.4 Mitigating Lattice Mismatch Using LT-ZnO

3.4.1 Determining the LT-ZnO Thickness

Although the MgO buffer layer reduced the lattice mismatch between sapphire and ZnO by half (18.4% to ~9%), immediately depositing ZnO at high (> 500°C) temperatures on the MgO buffer layer will result in a poor structural quality film due to the lattice mismatch. A thin low temperature ZnO (LT-ZnO) layer can be used to accommodate for the strain in the lattice mismatch between MgO and ZnO [140]. Table 3.8 shows that in general, reported LT-ZnO layers are 3 nm to 15 nm thick and grown between 300°C and 500°C. Annealing of the LT-ZnO layer is also frequently employed, with the annealing temperatures of between 700°C to 800°C for 5 minutes, and sometimes under O_2 plasma as well.

As the consensus from the literature (see Table 3.8) is that a low growth rate (~ 0.002 nm/s) is desirable in growing LT-ZnO, the O_2 flow rate was lowered to 0.5 sccm, the lowest possible flow rate while still maintaining a stable O_2 plasma.

Low to moderate growth temperatures (350°C to 600°C) are also recommended by the literature. If too high a substrate temperature is chosen, then the adatoms have enough energy to settle on the desired ZnO lattice sites, which when grown on a cubic surface, will result in island growth. If too low a substrate temperature is chosen, the buffer layer may contain too many dislocations. Hence, a moderately low growth temperature of 450°C was chosen. The remaining growth parameters are listed in Table 3.9.

Table 3.8. Selected results of reported LT-ZnO growth on c-plane sapphire using PA-MBE.

LT-ZnO growth parameters	**Carrier concentration (cm^{-3})**	**Mobility ($cm^2/V{\cdot}s$)**	**RMS roughness (nm)**	**(0002) ω -RC FWHM (arcsec)**	**Ref.**
20-40 nm thick, RF at 350W, T_{growth} of 350°C, anneal at 650°C	$1\text{-}5 \times 10^{18}$	40 - 60	6	30	[154]
6 nm thick, T_{growth} of 350°C, anneal at 750°C for 5 min	4×10^{17}	92		27	[134, 155]
35 min growth, T_{growth} of 500°C, O-rich	1.6×10^{17}	145			[141]
3 nm thick, RF at 400W, T_{growth} of 300°C, anneal at 700°C for 5 min			0.26	25	[142]
15 nm thick, T_{growth} of 480°C, anneal at 750°C under O_2 plasma for 5 min	2.1×10^{16}	98	< 0.8 nm for 10 μm by 10 μm scan	13	[135, 138, 140]
T_{growth} of 490°C, anneal at 800°C for 25 min			0.3 nm for 2.5 μm by 2.5 μm scan	22	[136]
15 nm thick, T_{growth} of 500-600°C, anneal at 800°C for 5 min	6×10^{18}	~ 35			[156]
3 nm thick, T_{growth} of 490°C, anneal at 750°C under O_2 plasma for 5 min, 0.002 nm/s growth rate			< 1 nm for 2.5 μm by 2.5 μm scan	18	[125]

Table 3.9. Conditions for LT-ZnO buffer layer growth.

O_2 flow rate (sccm)	RF power (W)	Substrate temperature (°C)	Growth time (min)	Zn flux (atoms/cm^{2}s)
0.5	400	450	2	4.3×10^{14}

It is desirable to have a thick enough buffer layer such that all of the strain from the MgO to ZnO lattice mismatch is accommodated. However, it is undesirable to have too thick a buffer layer as this can result in 3D growth of the subsequent ZnO epilayer [156]. Therefore, the LT-ZnO growth time was decided by observing the RHEED pattern during growth and stopping the growth when the RHEED pattern degraded. The surface morphology evolution of the LT-ZnO buffer layer is shown in Fig. 3.20. Initially, ZnO nucleates under island growth, as evident from the spotty RHEED pattern (Fig. 3.20(b)). After 30 s of LT-ZnO growth, the dominant growth mode is still island formation, as the ZnO has not adequately covered the MgO surface (Fig. 3.20(c)). However, after 1 minute of LT-ZnO growth, the RHEED pattern becomes streaky (Fig. 3.20(d)), indicating 2D growth. At this stage, the thin ZnO layer has completely covered the MgO surface. After 1 minute and 30 seconds of LT-ZnO growth, the RHEED pattern starts to become spotty again (Fig. 3.20(e)). Such surface roughening occurs due to inadequate energy for the adatoms to rearrange themselves at desirable lattice sites at low growth temperatures. The LT-ZnO growth is then terminated after 2 minutes due to a clear roughening of the surface (Fig. 3.20(e)). If growth was continued, the surface may become too rough for further annealing to recover the smooth surface, resulting in a poor structural quality epitaxial layer.

As the total LT-ZnO growth time is too short for using LRI to measure the growth rate, it is inferred from a previous thicker growth. Figure 3.6 shows that the growth rate at 400°C and at 500°C are 235 nm/hr and 238 nm/hr, respectively. If one assumes that any growth at 450°C proceeds at around 237 nm/hr, since identical O_2 flow rate and Zn flux are used, a growth time of 2 minutes gives an estimated LT-ZnO thickness of 7.9 nm. This is within the range of LT-ZnO thickness values reported in literature (see Table 3.8).

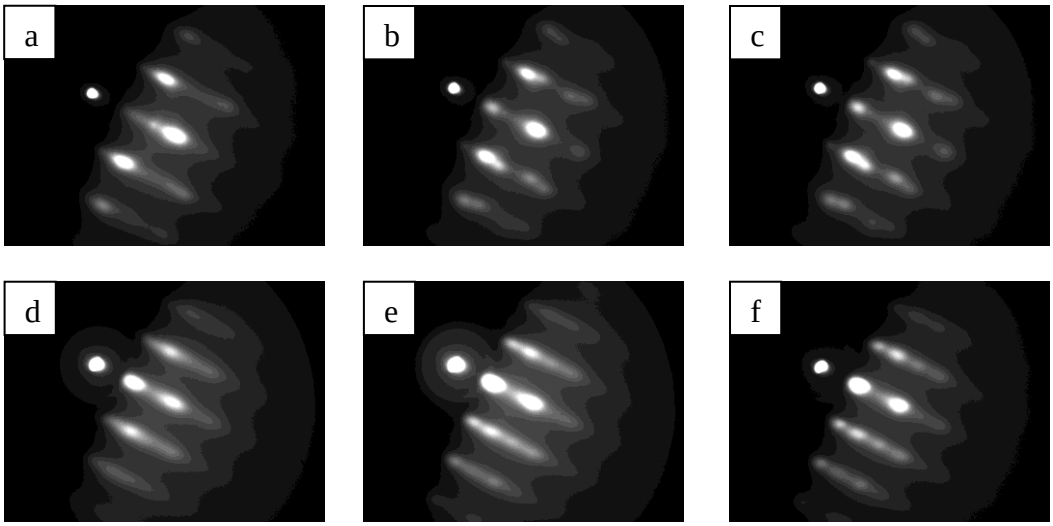

Fig. 3.20. RHEED image of (a) MgO buffer layer just before LT-ZnO growth, (b) after 15 s LT-ZnO growth, (c) after 30 s LT-ZnO growth, (d) after 1 min LT-ZnO growth, and (e) after 1 min 30 s LT-ZnO growth, (f) end of 2 min LT-ZnO growth.

To further confirm that 7.9 nm of LT-ZnO is sufficient for mitigating the lattice mismatch between MgO and ZnO, the lattice spacing from RHEED patterns are analysed. The lattice spacing is still changing up to 60 s of LT-ZnO growth (Fig. 3.21), indicating that strain has not been completely relieved, consistent with spotty RHEED patterns in Fig. 3.20(b) and (c). From 60 s LT-ZnO growth onwards, there is no further change in the lattice spacing. This indicates that the strain due to lattice mismatch between MgO and ZnO has now been relieved. Close to that point, the RHEED pattern is streaky, as shown in Fig. 3.20(d). By the end of growth, the RHEED pattern is spotty, as Fig. 3.20(f), due to the effects of transitioning from 2D to 3D growth. This is due to adatoms having shorter diffusion lengths at low temperature growth, thereby promoting island growth mode [132].

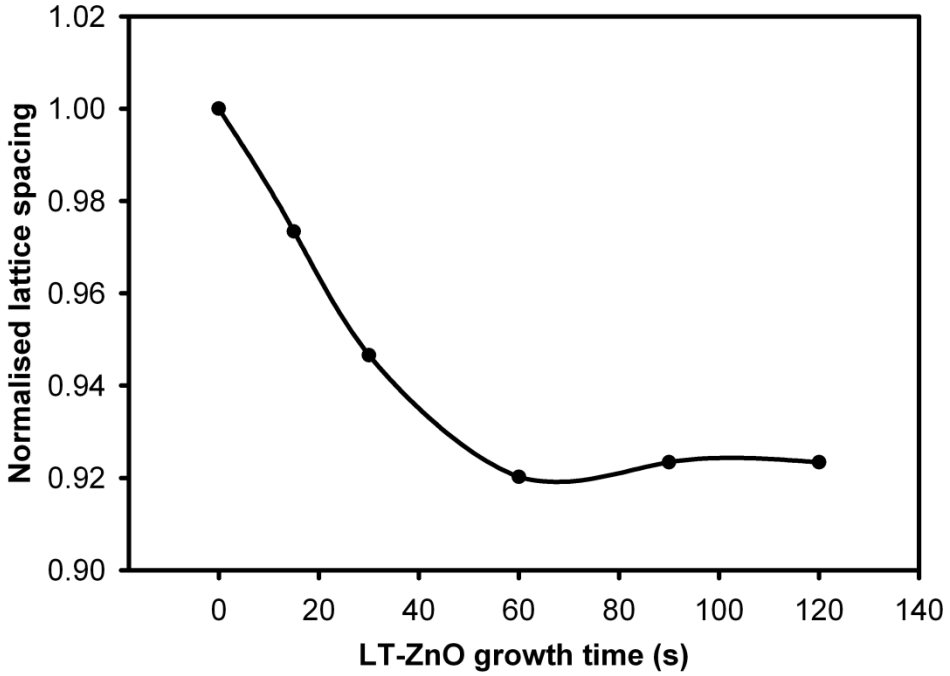

Fig. 3.21. Normalised lattice spacing over the LT-ZnO growth period, for the RHEED images shown in Fig. 3.20.

3.4.2 Structural Effects of LT-ZnO Annealing

Now that suitable growth conditions for LT-ZnO growth have been established, the next step is to investigate the effect of LT-ZnO annealing on HT-ZnO growth. It has been reported that annealing the LT-ZnO at 750°C for 5 minutes [134], 800°C for 30 minutes under O_2 plasma [156], 850°C for 10 minutes [141], or 750°C for a few minutes under O_2 plasma [135], is required to recover streaky RHEED patterns. Due to the variety of reported annealing conditions, several LT-ZnO films were annealed under O_2 plasma or in vacuum, over a range of durations, to investigate the best annealing technique, as listed in Table 3.10. The growth parameters for subsequent HT-ZnO layers are listed in Table 3.11.

Table 3.10. Annealing parameters for various LT-ZnO buffer layers.

Sample	Annealing Temperature (°C)	Annealing Time (min)	Annealing Ambient	Time Until HT-ZnO Growth (min)[+]	HT-ZnO Growth Temperature (°C)
A1	800	3.5	O_2 plasma*	45	700
A2	800	3.5	O_2 plasma*	5	700
A3	800	30	Vacuum	45	700
A4	Unannealed	-	-	45	700

* O_2 plasma set at 0.5 sccm and 400 W.

[+] Time between the end of the LT-ZnO annealing and the start of the HT-ZnO growth.

Table 3.11. Growth parameters for HT-ZnO layers for samples A1 to A4.

O_2 flow rate (sccm)	RF power (W)	Substrate temperature (°C)	Growth time (hours)	Zn flux (atoms/cm^{2}s)
0.5	400	700	3	4.0×10^{14}

Figure 3.22 shows that LT-ZnO annealing conditions can have a significant effect on the surface morphology of the LT-ZnO buffer layer before HT-ZnO growth, consistent with literature reports (see Table 3.8). Each sample has a similar surface morphology after a two minute LT-ZnO growth at 450°C, as shown in Fig. 3.22(a). Therefore, one can conclude that each of the four samples A1 to A4 start with a similar unannealed LT-ZnO buffer layer, and that subsequent changes in the surface morphology are due to the buffer layer treatments. There is significant improvement in the LT-ZnO surface morphology with a short O_2 plasma treatment, as evident from the change from a spotty-streaky surface of Fig. 3.22(a) to the streaky RHEED patterns of samples A1 and A2, shown in Fig. 3.22(b). Annealing in vacuum does not appear to improve the surface morphology at all, as observed by the similar RHEED patterns for sample A3, shown in Fig. 3.22(a) and (b).

However, it should be noted that due to the time lag between the end of the LT-ZnO buffer layer annealing and the start of subsequent HT-ZnO growth at a lower temperature of 700°C, the streaky RHEED pattern (Fig. 3.22(b)) has been replaced by a spotty RHEED pattern (Fig. 3.22(c)) for sample A1. The degradation due to the time lag can be mitigated by having a shorter ramp down time to the growth temperature of 5 minutes, instead of the usual 45 minutes (15 minutes ramp plus 30 minute stabilisation time), as shown by the streaky RHEED patterns maintained for sample A2. As the time for the change in temperature is significant (45 minutes), the buffer layer is essentially unintentionally vacuum annealed throughout that time. The poorer quality LT-ZnO buffer layer after vacuum annealing is confirmed by the spottier RHEED patterns of the intentionally vacuum annealed film A3. Interestingly, subsequent HT-ZnO growth at 700°C consistently have very similar RHEED patterns, implying similar surface morphology regardless of annealing conditions.

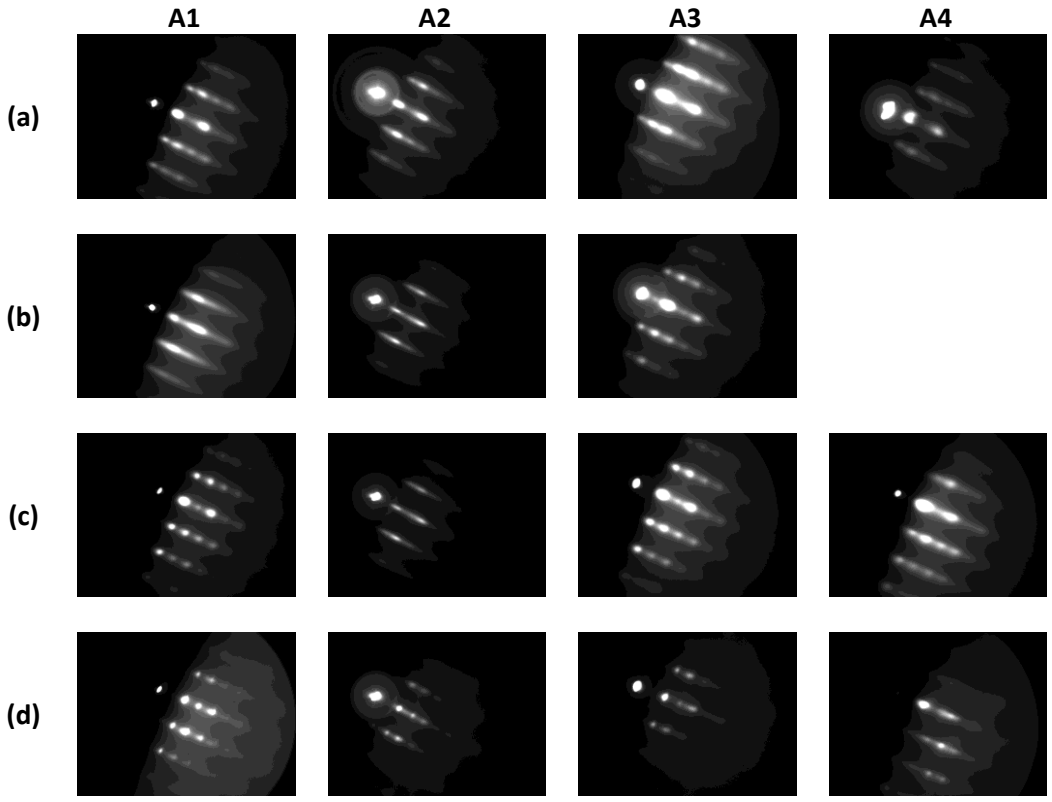

Fig. 3.22. RHEED images showing the surface morphology of various layers. (a) After 2 min LT-ZnO growth at 450°C. (b) After LT-ZnO annealing according to the conditions in Table 3.10. RHEED pattern for A1 is actually taken at 2.5 minutes into the annealing. However, no significant difference was noticed between 2.5 minutes and 3.5 minutes of O_2 plasma annealing. (c) Just before HT-ZnO growth. (d) After 3 hour HT-ZnO growth.

To clarify the effect of the annealing occurring during ramp up/down to the growth temperature, samples with varying ramp up/down conditions were analysed. Table 3.12 gives a summary of the various conditions for both intentional and unintentional vacuum annealed LT-ZnO samples.

Table 3.12. Summary of conditions for vacuum annealed LT-ZnO.

Sample	Position of substrate	Time between end of LT-ZnO growth and growth of HT-ZnO layer	HT-ZnO growth temperature (°C)
A3	growth position during first annealing; facing away for second annealing	15 min ramp from 450°C to 800°C, then leave at 800°C for 30 min. 10 min ramp from 800°C to 700°C, then leave at 700°C for 30 min.	700
A4	Facing away	15 min ramp from 450°C to 700°C, then leave at 700°C for 30 min	700
A5	Facing away	15 min ramp from 450°C to 800°C, then leave at 800°C for 30 min	800

A determinant of the surface morphology just before the HT-ZnO growth is the ramping up/down time from the LT-ZnO growth/treatment temperature to the HT-ZnO growth temperature, as shown in Fig. 3.23. The RHEED patterns just before HT-ZnO growth at 700°C appear similar to their corresponding RHEED patterns after LT-ZnO growth/treatment. However, the RHEED pattern of the LT-ZnO just before HT-ZnO growth at 800°C appears much streakier than just after LT-ZnO growth, indicating surface morphology improvement. The lack of such an improvement for the 800°C intentionally annealed sample A3 may be because such annealing occurs at the growth position. The shutter in front of the O_2 plasma is likely insufficient at keeping the plasma from reaching the growth position, and hence there could be some degradation during annealing for a fairly long annealing time of 30 minutes. It is also possible for degradation to occur during the ramp down from 800°C annealing temperature to the 700°C growth temperature. Nevertheless, either annealing for 3.5 min under O_2 plasma and shortly thereafter starting the growth of the HT-ZnO layer (sample A2), or unintentionally annealing the LT-ZnO layer during the ramp up to the growth temperature of 800°C (sample A5), give the best morphology.

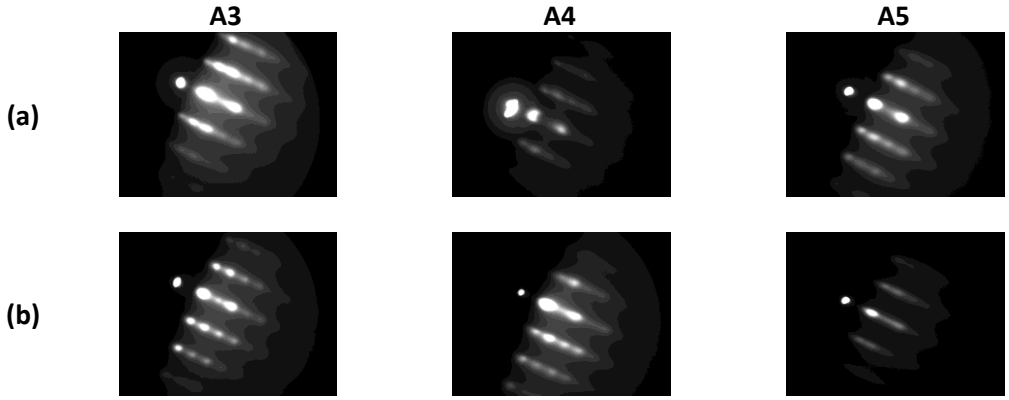

Fig. 3.23. RHEED images showing the surface morphology of various layers. (a) After 2 min LT-ZnO growth at 450°C. (b) Just before HT-ZnO growth.

It should be noted that the O_2 plasma annealing time was decided by monitoring the RHEED and terminating the annealing when no further improvement is observed. This was found to occur at 2 minutes annealing time (Fig. 3.24(d)). Therefore, it is possible that the 3.5 minutes annealing time employed was more than necessary for recovery of a smooth buffer layer surface.

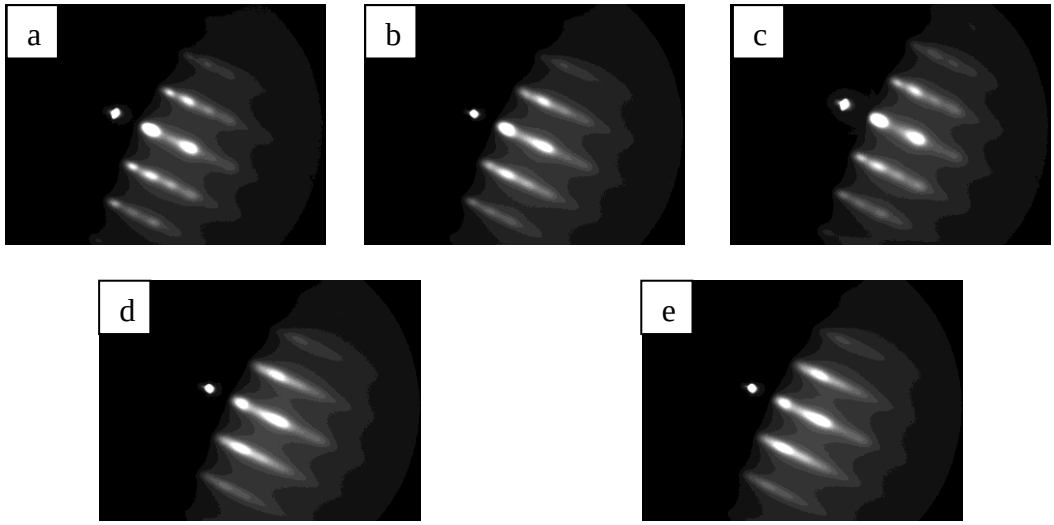

Fig. 3.24. RHEED images of LT-ZnO annealed under O_2 plasma at (a) before annealing, (b) 1 min, (c) 1 min 30 s, (d) 2 min, (e) 2 min 30 s.

Another way to clarify the surface morphology improvement on the subsequent HT-ZnO layers is via scanning electron microscopy (SEM), shown in Fig. 3.25. Interestingly, both samples A1 and A3 have very rough morphology, with multiple inversion domains, consistent with spotty RHEED patterns. As samples A1 and A3 are O_2 plasma and vacuum annealed samples, the annealing ambient is not likely the cause of the inversion domains. The plasma power of 400 W may be too damaging to the LT-ZnO surface, resulting in a poor quality surface for subsequent HT-ZnO growth.

While both samples A1 and A3 have different annealing ambients, since sample A3 was held at the growth position for the entire annealing time, inadequate shuttering of O_2 plasma source may mean that there is a small amount of O_2 plasma annealing happening throughout the entire 30 minute of (supposedly) vacuum annealing. Furthermore, the similarity between samples A1 and A3 at different annealing ambients can be explained by the same 45 minutes ramp down time to get from the 800°C annealing temperature to the 700°C growth temperature. This is supported by the far smoother and inversion domain free HT-ZnO layer of sample A2, since the only difference between samples A1 and A2 is the ramp down time to the growth temperatures: 45 minutes for sample A1, and 5 minutes for sample A2.

However, sample A4, which was grown at 700°C and has no LT-ZnO annealing treatment, has no inversion domains as well. This proves that the growth

temperature of 700°C was not the reason for the inversion domains. Additionally, the smooth surface and inversion domain free surface for growth at 800°C (sample A5) prove that the high annealing temperature of 800°C is not detrimental to surface morphology either. Rather, the cause of inversion domain formation appears to be the long ramp down time after annealing, regardless of annealing conditions. It is worth noting that the surface morphology of samples A2 and A5 are very similar to that published by Jung et al. [156] for their optimised LT-ZnO growth.

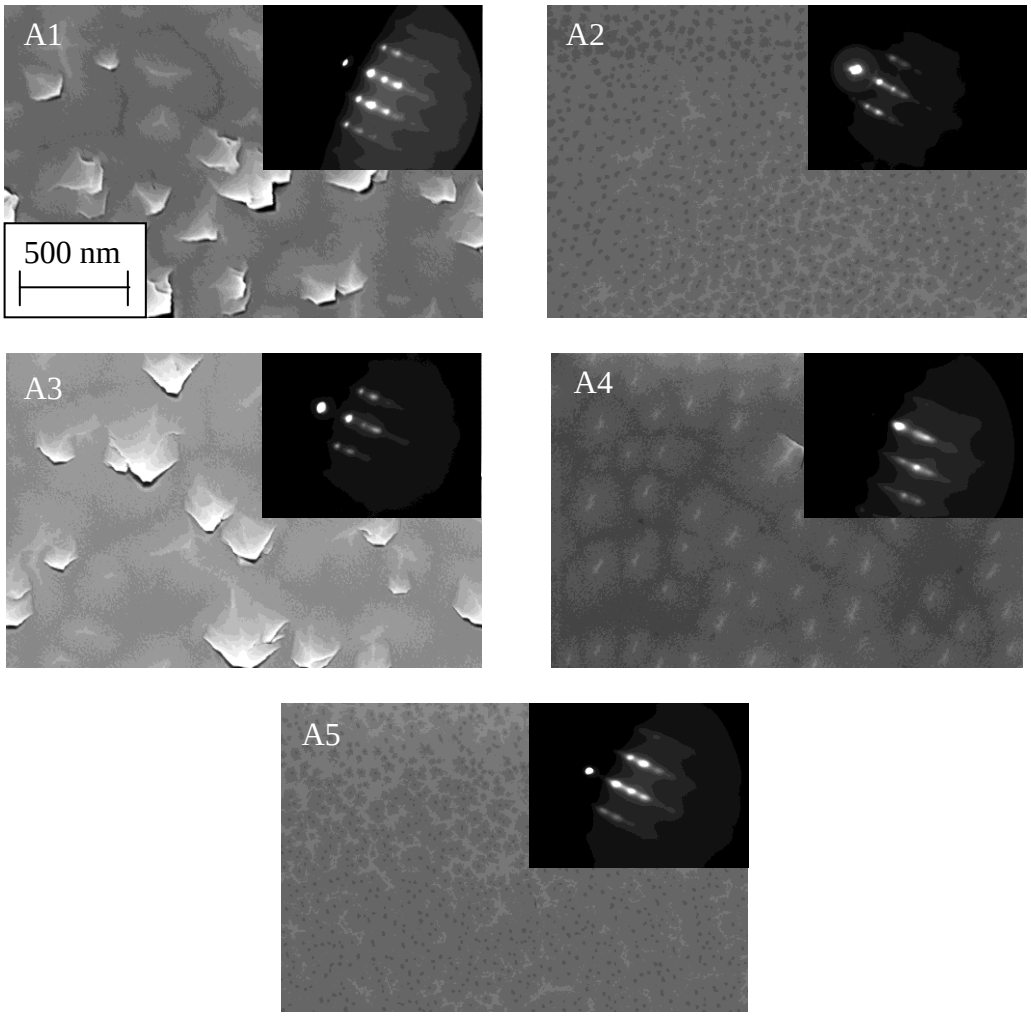

Fig. 3.25.Top view SEM images of HT-ZnO layers with the LT-ZnO annealed under different conditions listed in Table 3.10 and Table 3.12. Insets are corresponding RHEED images.

Another technique commonly used to quantify the structural quality of films is atomic force microscopy (AFM). Figure 3.26 shows that samples A1 and A3 have the worst rms roughness (21.9 nm and 18.3 nm, respectively), consistent with RHEED and SEM images shown in Fig. 3.25. However, if the time between the

end of LT-ZnO annealing and growth of HT-ZnO layer is significantly reduced, then the roughness of the resultant film is 6.3 nm. Interestingly, the unannealed sample A4 has even lower rms roughness (4.7 nm) than any of the annealed samples. The degradation of the rms roughness with LT-ZnO annealing implies that LT-ZnO annealing introduces additional dislocations and may not be as advantageous as reported by others.

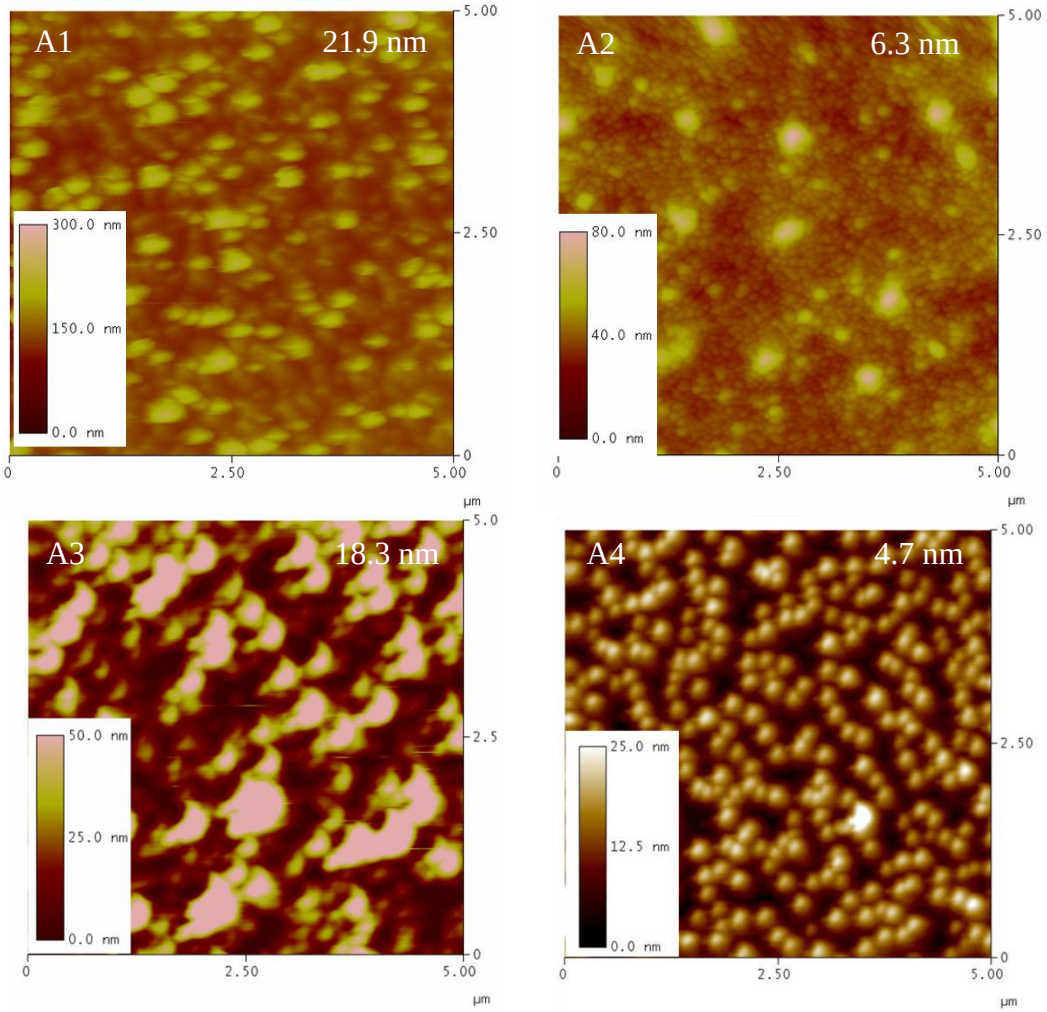

Fig. 3.26. AFM images of HT-ZnO layers with the LT-ZnO annealed under different conditions listed in Table 3.10 and Table 3.12. Rms roughness of a 5 µm by 5 µm scan size is listed within each figure.

3.4.3 Effect of LT-ZnO Annealing on Electrical Properties

Ultimately, the goal is to fabricate devices out of ZnO, and so its electrical properties are of interest. Tampo et al. [157] reported that employing LT-ZnO buffer layer annealing confers improvement in both mobility and carrier concentration, with vacuum annealing found to be superior to O_2 or O^+ annealing. Table 3.13 shows that annealing did indeed increase the mobility, but with

detrimental effect on the carrier concentration. In fact, the carrier concentration increased and the mobility decreased for samples A1 and A3. This is not unexpected as structural analysis revealed poorer morphology for those samples, likely due to the long time lag between the end of the LT-ZnO annealing and the start of the HT-ZnO growth. This is confirmed by the improvement in the mobility for sample A2, where the LT-ZnO layer was annealed for 3.5 minutes under O_2 plasma and the HT-ZnO layer grown 5 minutes after the end of the annealing. However, it is interesting to note that the two samples that were O_2 plasma annealed (A1 and A2) had consistently higher carrier concentrations. This suggests that O_2 plasma annealing somehow introduced additional donor-like defects into the LT-ZnO layer, consistent with earlier findings where the rms roughness for an unannealed LT-ZnO sample had lower roughness than all LT-ZnO annealed samples.

In contrast to the effects of LT-ZnO annealing on carrier concentration and mobility, annealing did not appear to affect the resistivity of the films. Nevertheless, the overall best annealing condition was with sample A2, which involved 3.5 minute annealing under O_2 plasma, contrary to the findings of Tampo et al., but consistent with the superior structural properties measured. Even though an increase in the carrier concentration was observed, the carrier concentration is still within the same order of magnitude, whereas the mobility has increased substantially from 13 to 50 cm^2/Vs. Therefore, to improve the overall electrical properties of films, the LT-ZnO buffer layer should be O_2 plasma annealing for no more 3.5 minutes, and the HT-ZnO growth should be started within 5 minutes of the end of the LT-ZnO annealing.

Table 3.13. Electrical characterisation of films with different LT-ZnO annealing conditions. Sample A1 and A2 both have a LT-ZnO layer annealed at 3.5 min under O_2 plasma. The HT-ZnO layer for samples A1 and A2 are grown 45 minutes and 5 minutes, respectively, after annealing the LT-ZnO layer. Sample A3 has a vacuum annealed LT-ZnO layer with the HT-ZnO layer started 45 minutes after annealing the LT-ZnO layer. Sample A4 is a sample with an unannealed LT-ZnO layer. The HT-ZnO layer for all films A1 to A4 were grown at 700°C.

Sample	Carrier concentration (cm^{-3})	Mobility (cm^2/Vs)	Resistivity (Ω cm)
A1	5.7×10^{17}	8	1.3
A2	8.9×10^{17}	50	1.4
A3	3.8×10^{17}	12	1.4
A4 (unannealed)	3.5×10^{17}	13	1.4

3.4.4 Effect of LT-ZnO Annealing on Optical Properties

The effect of LT-ZnO annealing conditions can also be clearly observed in the 4 K PL of the as-grown films, as shown in Fig. 3.27. Emissions related to H (I_4) and Al (I_6) appear to dominate for samples A1 and A3, which are overall poorer quality films as found earlier. The I_4 line for samples A1 and A3 indicates significant H contamination, most likely from growth chamber parts outgassing during growth. In contrast, for the best LT-ZnO annealed material (A2), more primary or NBE features were observed, in addition to multiple LO phonon replicas. However, there appears to be significant strain effects in sample A2, the origin of which is currently unknown.

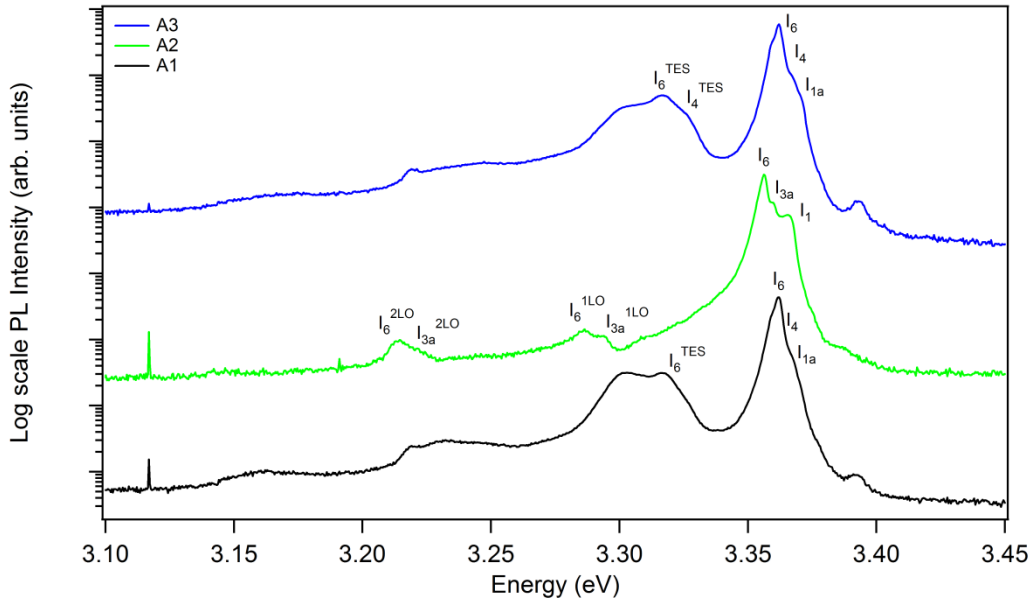

Fig. 3.27. 4 K PL of various samples grown on annealed LT-ZnO. Sample A1 and A2 both have a LT-ZnO layer annealed at 3.5 min under O_2 plasma. The HT-ZnO layer for samples A1 and A2 are grown 45 minutes and 5 minutes, respectively, after annealing the LT-ZnO layer. Sample A3 has a vacuum annealed LT-ZnO layer. The HT-ZnO layer for sample A3 was started 45 minutes after annealing the LT-ZnO layer.

To check for any strain related shifts, one can compare the fitted peaks with values reported in literature. As shown in Fig. 3.28, the peaks assigned for samples A3 and A1 are all within 1 meV compared to emissions from a bulk material. Therefore, one can have confidence that the peak assignments are correct, and that those material are only slightly strained.

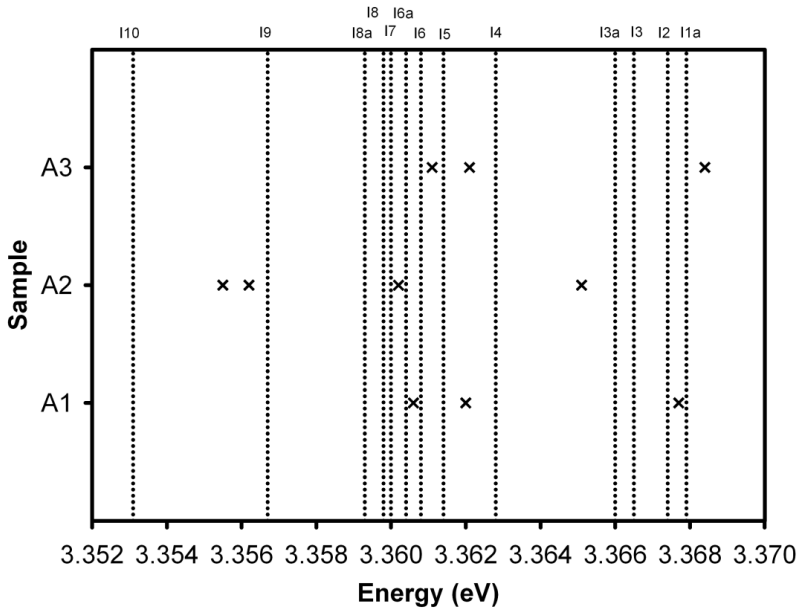

Fig. 3.28. Fitted Gaussian peaks (crosses) for various LT-ZnO annealed samples (refer to Table 3.10), compared with peaks reported by Meyer et al. (dashed lines) [121]

3.5 Effect of Growth Temperature on Properties of HT-ZnO

In earlier sections, optimum conditions for buffer layer growth were established. As well as flux ratio and buffer layer conditions, a major determinant of high temperature (HT) ZnO quality is the substrate temperature. In this case, HT-ZnO refers to the ZnO epitaxial layer. Therefore a series of experiments were performed, where the growth temperature was varied from 400°C to 800°C. All growth was performed under similar conditions to that listed in Table 3.14, except for the growth at 700°C, where the MgO growth time was only 8 s. The total HT-ZnO growth time was three hours.

The surface morphology is greatly affected by the substrate temperature for the growth of the HT-ZnO layer, as shown in Fig. 3.29. At 400°C, the surface has many large and irregular features (Fig. 3.29(a)). This is most likely due to insufficient energy for the adatoms to diffuse along the lattice, resulting in a predominantly island growth mode. For temperatures between 600°C to 700°C, the surface is covered with many small pits and several hillocks (Fig. 3.29(b) and (c)). For the highest growth temperature of 800°C, the surface is essentially featureless and is populated by many small pits (Fig. 3.29(d)), similar to the growth at 600°C, but without the hillocks formation.

Table 3.14. Growth parameters used in HT-ZnO substrate temperature study. Growth at 700°C had a thinner MgO buffer layer that was grown for only 8 s.

O_2 flow rate for MgO (sccm)	MgO growth time (s)	O_2 flow rate for ZnO (sccm)	RF power (W)	LT-ZnO growth time (min)	HT-ZnO substrate temperature (°C)	Zn flux (atoms/cm^{2}s)
2	10	0.5	400	2	400 - 800	4.0×10^{14}

Jung et al. [158] reported that the RHEED pattern is spotty for growths at 680°C and 800°C, but streaky RHEED patterns for growth between 720°C and 760°C. In contrast, the RHEED patterns in Fig. 3.29 are consistently streaky-spotty for the entire growth temperature series. It appears that the growth at 800°C is the best structurally, which is only slightly higher than that reported by Jung et al. (720-760°C) [156, 158], but with very similar morphology to that of Jung et al. However, Chen et al. [132] reported that growth between 600°C and 650°C resulted in fairly featureless films, while growth outside that range resulted in significant crystallite formation. The discrepancy between reported optimum growth temperatures and those found in this thesis can be easily explained by the different heater setup in each growth system. As discussed in Section 3.2, measuring the substrate temperature is very challenging, and is highly dependent on the growth chamber setup. Buffer layer variation also complicates direct comparisons.

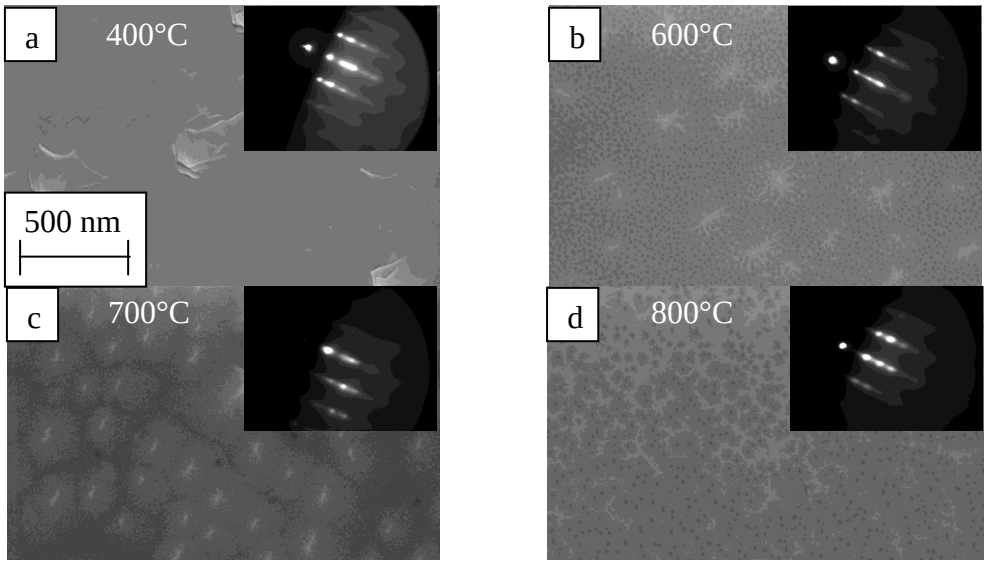

Fig. 3.29. Top view SEM images of ZnO films grown at (a) 400°C, (b) 600°C, (c) 700°C, and (d) 800°C. Insets are the corresponding RHEED images.

Figures 3.30 and 3.31 show that there is a clear trend in decreasing rms roughness with increasing substrate temperature, with the minimum rms roughness of 2.9 nm achieved for the HT-ZnO grown at 800°C. Growth at 600°C and at 800°C leads to very similar morphology to those reported by other groups, with rms roughness ranging from 0.8 to 4 nm [125, 135, 138, 158, 159]. It is also interesting to note that there appears to be a negative exponential relationship between roughness and substrate temperature, implying that temperatures above 800°C may result in films with even lower roughness.

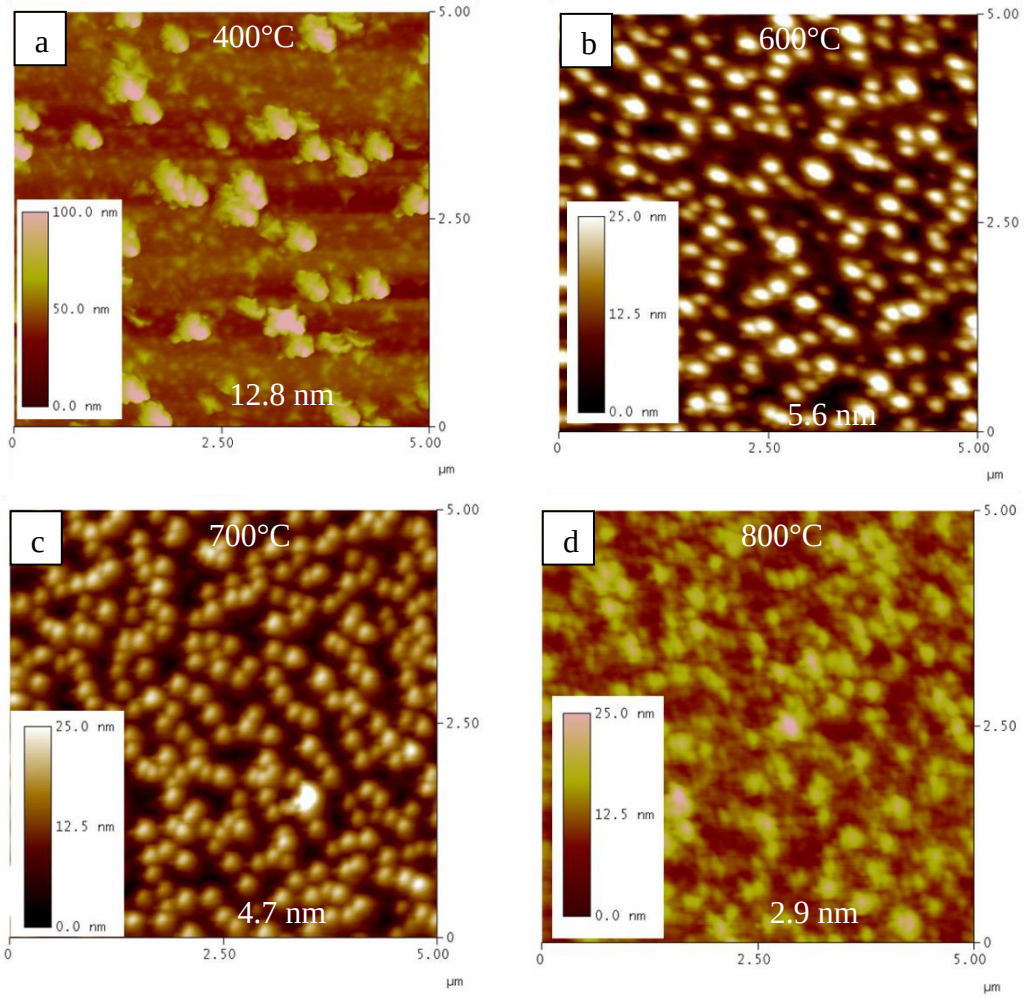

Fig. 3.30. AFM images of ZnO films grown at (a) 400°C, (b) 600°C, (c) 700°C, and (d) 800°C.

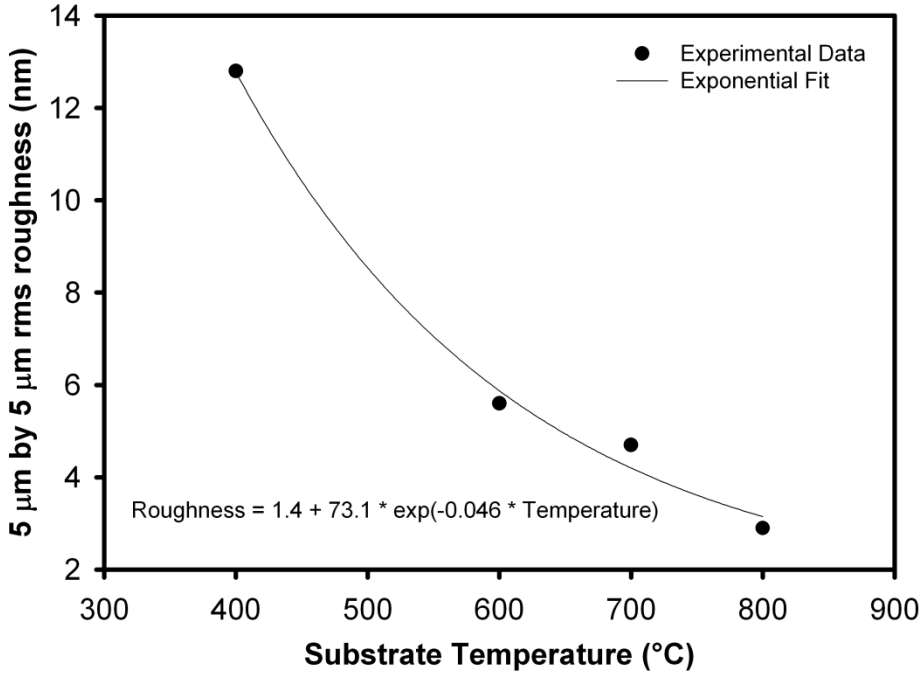

Fig. 3.31. 5 μm by 5 μm rms roughness for films grown at different substrate temperatures.

As expected all LT PL spectra for this series of films are dominated by neutral donor bound excitons. The films grown at 600°C and 800°C have two main emissions related to In (I_9) and Al (I_6), as shown in Fig. 3.32. The main impurity for the film grown at 800°C appears to be due to In, as indicated by the dominance of the I_9 line. This indicates that there is major In contamination from the In-Sn solder. Furthermore, there is Al contamination as well, as indicated by a strong I_6 peak. The source of the Al is most likely due to Al diffusion from the sapphire substrate. There also appears to be some H incorporation during growth at 800°C, as indicated by an I_4 shoulder. Interestingly, I_4 was absent in the film grown at 600°C. This therefore supports the contention I_4 is due to H outgassing from growth chamber parts (specifically, the pyrolytic boron nitride spacer in the substrate heater as determined by separate residual gas analyser experiment), the effect of which is less severe at lower substrate temperatures. Interestingly, there is also an I_{3a} peak in the 600°C grown film, which is absent in the 800°C grown film. A few groups [160, 161] have assigned I_{3a} to Zn_i, which therefore means that the growth conditions could be Zn-rich, instead of the desired stoichiometric region. As I_{3a} is a weak shoulder at the NBE, this implies that the growth at 600°C is only slightly Zn-rich, instead of highly Zn-rich, which would manifest as a stronger I_{3a} peak.

There is also a dip in the spectra near 3.30 eV due to quantum-mechanical Fano resonance [162], as seen in Fig. 3.32. This phenomenon has been previously observed in ZnO [163], and is due to resonant coupling of the I_6 exciton with the LO phonons since the total binding energy of the I_6-complex (60 meV exciton binding energy plus 16 meV exciton localization energy) is comparable to the LO-phonon energy (72 meV). Presence of a Fano resonance dip is an indication of high structural quality. Furthermore, there is additional evidence that growth at 600°C and 800°C result in high optical quality material, as indicated by two LO phonon replicas related to I_6, multiple NBE emissions resolved, and a shoulder related to the transverse free A-exciton A_T.

Unlike the multiple fine features for films grown above 600°C, the film grown at 400°C are dominated by broad peaks at 3.3567 eV (I_9) and 3.3611 eV (I_6). The presence of I_9 lines in the large range of growth temperatures investigated point to a recurring common contaminant, which implies contributions from the substrate mounting procedure. It might be advantageous to investigate an alternate mounting method to eliminate that source of contamination, as it is still present even at the low growth temperature of 400°C. As I_6 is present for both high and low temperature growths, this seems to point towards an additional source of Al contamination that is temperature independent. One possible source is the alumina discharge tube for the plasma source.

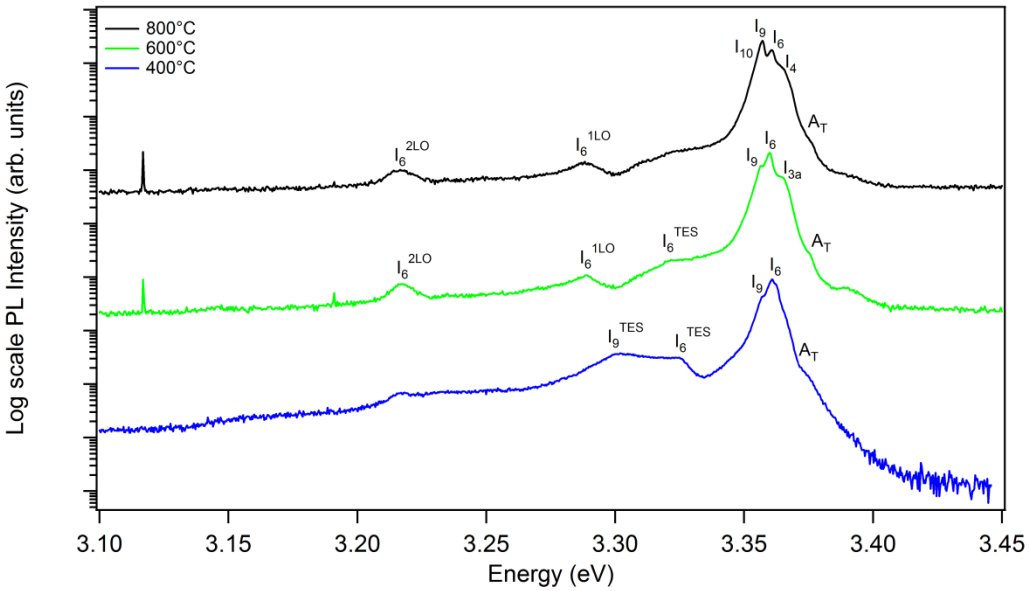

Fig. 3.32. 4K PL of near stoichiometric and nominally undoped ZnO films grown between 400°C to 800°C.

Table 3.15 shows that the full-width half maximum (FWHM) of the dominant peak decreases with temperature. This confirms that the highest growth temperature of 800°C produces the highest optical and structural quality film. Jung et al. [158] observed a minimum FWHM for growth at 720°C, with increases in the FWHM outside growth at 720°C. In contrast, a consistently decreasing FWHM with increasing growth temperature was observed for the films grown in this thesis. Nevertheless, the obtained FWHM values in Table 3.15 are close to typical FWHM values reported in literature for growth on c-plane sapphire such as 8.4 meV [158], and 3.2 meV [132, 140].

Table 3.15. FWHM of the dominant 4 K PL peak for near stoichiometric and nominally undoped ZnO films grown at various substrate temperatures.

HT-ZnO growth Temperature (°C)	FWHM of dominant 4 K PL peak (meV)
400	4.8
600	2.8
800	2.2

There is also a general trend of decreasing carrier concentration and increasing mobility as the growth temperature is increased, as shown in Fig. 3.33. This trend is not unexpected as RHEED, SEM and AFM characterisation have found that the lower the growth temperature, the greater the formation of an uneven surface filled with hillocks. This indicates that films at lower growth temperatures suffer from higher dislocation densities, which can contribute towards the electron concentration. The film with the best overall electrical properties is the film grown at 800°C, which has a carrier concentration of 1.3×10^{17} cm^{-3} and a mobility of 90.6 $cm^2/V\cdot s$.

It is known that one of the disadvantages of using buffer layers is that the buffer layer may be degenerate and characterised by a high density of dislocations. Conventional Hall effect measurements on films fabricated on such buffer layers may therefore be unable to measure the true bulk epitaxial layer, as the nature of Hall effect measurements mean that it takes an average conductivity value [164]. One way to separate multiple conduction paths in a material is using variable magnetic field Hall effect measurements. It has been reported that a ZnO thin film grown using a MgO/LT-ZnO buffer layer structure can consist of two carrier

populations; a low mobility (<100 cm^2/Vs), high concentration carrier population, and a higher mobility (130 cm^2/Vs), lower concentration carrier population [164]. Therefore, it is conceivable that the MgO/LT-ZnO buffer layer structure used in the ZnO thin film growth in this thesis can also result in multiple carrier populations.

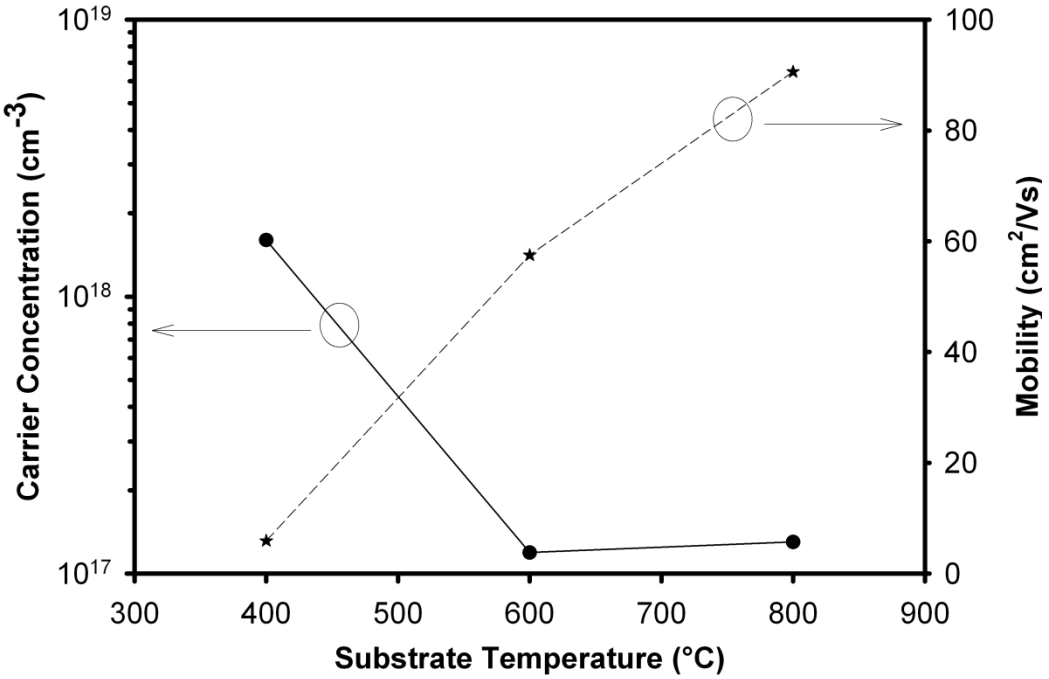

Fig. 3.33. Room temperature Hall effect measurements of undoped ZnO films grown at several temperatures.

However, Table 3.16 shows that both QMSA and MCF detected only one carrier population in the films grown in this thesis, with values close to those measured by conventional Hall effect measurements. Therefore, conventional single magnetic field Hall effect measurements are an accurate measure of the electrical properties. This also suggests that the buffer layer structure is not degenerate, even though it is most likely filled with many defects in its lattice matching and strain relieve role. Furthermore, as the electrical properties measured are similar both in normal ambient conditions and after leaving the sample for one day in the dark, there is no persistent photoconductivity in the sample grown at 800°C.

Table 3.16. Hall effect results on a sample grown at 800°C, using both conventional and variable magnetic field Hall effect measurements.

	Ambient	Conductivity (S)	Carrier Concentration (cm^{-3})	Mobility (cm^2/Vs)
Conventional 0.51T	Normal	1.90	1.3×10^{17}	91
QMSA	Normal	0.75	4.5×10^{16}	105
QMSA	1 day in dark	0.64	3.9×10^{16}	105
MCF	Normal	1.00	9.5×10^{16}	66
MCF	1 day in dark	0.84	1.0×10^{17}	51

In summary, films grown between 400°C and 800°C were characterised structurally, optically and electrically. While RHEED images did not show any significant differences between films, SEM and AFM images showed rough and hillock-filled surfaces as the growth temperature is lowered. 4 K PL measurements indicated that lower temperature growth was structurally poorer as evident from lack of LO phonon replicas and wider PL NBE emissions. Lower temperature growth also resulted in increased carrier concentrations and lower mobility. The growth at 800°C was consistently superior to all the other growth temperatures, with the lowest rms roughness of 2.9 nm, smallest FWHM of the main NBE PL peak of 2.2 meV, lowest carrier concentration of 3.6×10^{16} cm^{-3}, and highest mobility of 105 cm^2/Vs.

Chapter 4

Silver Doping of ZnO

4.1 Background

As discussed in Chapter 1, there is significant interest in ZnO as a material for short wavelength optoelectronic devices. A sizeable obstacle in the development of junction devices based on this material is the lack of stable, reproducible p-type material, thought to be attributable at least in part to a branch point energy which lies near the conduction band [54]. At present there is no consensus in the literature as to which acceptor dopant might be optimal, with the group V element N being the most extensively studied as a result of successful p-type doping of another II-VI semiconductor via plasma-assisted molecular beam epitaxy (PAMBE), namely ZnSe [44, 45]. However, N doping requires a Zn rich growth condition, which increases the formation of donor-like compensating defects such as O vacancies and Zn interstitials [48, 49]. Others [42, 48] have investigated group I elements such as Li, which are believed to have the potential to form shallow acceptors. Unfortunately, Li is more likely to incorporate interstitially due to its small atomic radius [9].

Recently, Yan et al. [50] studied the possibility of using group IB elements to overcome the problems encountered with other dopants. Among the potential dopants investigated, Ag was found to be the most favourable acceptor candidate for several reasons: It has the lowest ionisation energy; substitutional Ag forms more readily under oxygen rich conditions [50], which may alleviate the self-compensation issue; and Ag is highly soluble in ZnO [50], which allows for a high dopant concentration. Subsequent theoretical studies [59, 60] have

reaffirmed the potential of Ag as an acceptor in ZnO. Despite a considerable number of experimental reports of Ag doped ZnO [61-63, 66-70, 73, 74], no consensus have been reached regarding the effects of Ag doping in ZnO. Some groups have reported achieving p-type ZnO by Ag doping only at low substrate temperatures [73] or after post-growth annealing in O_2 [68]. Others have reported increased resistivity [78] or increased near band-edge emission [61] with Ag doping as well. However, it is possible to incorrectly identify p-type conduction if experimental data has been misinterpreted due to experimental error or limitation in the use of a technique.

4.2 Sources Contributing to Incorrect p-type ZnO Reports

One of the most common techniques for determining the carrier type is based on the Hall effect, where the carrier type is deduced from the sign of the Hall voltage. By rearranging Eqs. (2.14) to (2.16), one can obtain

$$V_H = \frac{q\mu_H \cdot d}{IB \cdot \rho} \tag{4.1}$$

where V_H is the Hall voltage (V), q is the elementary charge (1.6×10^{-19} C) , μ_H is the Hall mobility ($cm^2V^{-1}s^{-1}$), d is the sample thickness (cm), I is the current (A), B is the magnetic field strength (0.51 T), and ρ is the resistivity (Ω cm). However, a number of factors must be considered when evaluating experimental data.

One possible source of error in performing Hall effect measurements arises from contact formation. Bierwagen et al. reported that if contacts are too close to the sample interior, as opposed to contacts at the edges of the sample, measurements can indicate a low mobility p-type result on clearly n-type material [165]. Another factor to keep in mind is that V_H is calculated from the voltage difference between the perpendicular voltage with and without a magnetic field applied. Hence the resolution of the measured voltage depends on the resolution and setup of the measuring apparatus.

In many cases where authors report using Hall effect measurements to conclude that the material is p-type, the mobility is extremely low and/or the resistivity is very high, as summarised in Table 4.1. By examining Eq. (4.1), one can deduce

that the low mobility values, as shown in Table 4.1, likely result from low Hall voltages. A similar case can be made for high resistivity materials. To obtain such low Hall voltages, both the voltage with and without an applied magnetic field are either low, or have a low voltage difference. Therefore, it is possible for the voltage differences to easily switch signs (and hence the calculated carrier type), depending on the sensitivity of the measuring equipment.

Table 4.1. Summary of parameters from selected p-type ZnO reports.

Dopant	Carrier Concentration (cm^{-3})	Mobility (cm^2/Vs)	Resistivity (Ω cm)	Ref.
Ag	1.61×10^{14}	7.86	4930	[74]
Ag	2.24×10^{16}	1.83	152	[68]
Li,N	8.92×10^{18}	0.2	0.93	[166]
Li	1.01×10^{17}	3.47	17.6	[167]
Li	1.37×10^{17}	0.134	34	[168]
N	3.51×10^{17}	0.752	23.7	[169]
N	2.8×10^{18}	9	0.248*	[170]
P	6×10^{18}	1.5	0.694*	[171]
Sb	6×10^{17}	25.9	0.3	[172]

* Estimated resistivity based on given carrier concentration and mobility.

Another way to evaluate the validity of electrical measurements is by noting whether the expected trends of decreasing electron concentration with increasing resistivity, and of decreasing electron concentration with increasing hole concentration, both hold. For example, let us examine the Hall effect measurements as reported in ref. [66], reproduced in Table 4.2. Their as-grown ZnO:Ag films experience a change in carrier concentration from 2.22×10^{12} cm^{-3} (electrons) to 3.98×10^{19} cm^{-3} (holes), with the only growth condition change being an increase in deposition temperature from room temperature to 150°C. With a further 50°C increase in deposition temperature, the "hole" concentration drops by six orders of magnitude. Furthermore, the resistivity undergoes a decrease of six orders of magnitude between room temperature to 150°C, and then increases by almost five orders of magnitude at 200°C. Such extreme behaviour is strongly suggestive of noise effects in the Hall voltage, and would indicate that caution should be used in drawing conclusions from such a small sample set.

Table 4.2. Electrical properties of Ag doped ZnO as reported in ref. [66]. Mobility data was not provided in ref. [66].

Deposition Temperature (°C)	Carrier Concentration (cm^{-3})	Resistivity (Ω cm)	Carrier Type
RT	2.22×10^{12}	1.58×10^{5}	n
150	3.98×10^{19}	1.18×10^{-1}	p
200	1.86×10^{13}	7.75×10^{4}	p

When doping ZnO with Ag, it is possible for silver oxide to form, especially at high Ag concentrations. It has been reported that AgO_x has high resistivity [173-176], with Abe et al. [174] reporting AgO and Ag_2O having resistivities of 59.3 Ω cm and 7×10^8 Ω cm, respectively. Such high resistivities may explain the high resistivity of insulating highly Ag doped films [68, 78]. In addition, AgO_x can be p-type as-grown [177]. Hence, if the ZnO:Ag film contains AgO_x, then the "p-type" result obtained may be actually due to p-type AgO_x, instead of ZnO:Ag. Furthermore, AgO_x has a measured bandgap of 1.0 to 3.4 eV [173, 175, 176], with the differences due to vastly different growth conditions. Hence, the low energy low temperature PL peaks detected with Ag doping may actually be due to AgO_x, instead of an acceptor bound exciton due to Ag in ZnO.

Many of the reported Ag doped ZnO films exhibit rather poor surface morphology, and are usually characterised by strong defect band emission. Interestingly, most of the reports of acceptor bound excitons related to Ag point to a peak around 3.317 eV [68, 73, 75, 178]. It is possible that instead of a Ag related peak at 3.317 eV, what has been observed is a free electron to neutral acceptor (e, A^0) transition, reported to occur at 3.314 eV, and related to basal plane stacking faults [123]. This explanation is not too far-fetched, as many of the ZnO:Ag results reported show very rough and columnar/granular surfaces. In addition, resolution of even several meV can be difficult to achieve in typical UV PL systems.

Hence, in order to have significant confidence in the validity of results, especially to confirm p-type conduction, a variety of complementary measurements should be performed on the same sample. If Hall effect measurements, scanning

capacitance microscopy, DLTS, LT photoluminescence, SIMS, and rectifying contact formation all agree, then chances are, the material is indeed p-type.

4.3 Structural Effects of Ag Doping on ZnO

As discussed in the previous section, the role of Ag in ZnO is still uncertain. Therefore, a series of Ag doping growth experiments was performed and the films carefully characterised, bearing in mind the potential measurement artefacts. The ZnO:Ag epilayers were grown on (0001) sapphire substrates using PAMBE. A combination of thin (~1 nm) MgO and low temperature ZnO buffer layers was employed to accommodate for the large lattice mismatch between ZnO and sapphire. The conditions for the MgO and LT-ZnO growth are listed in Table 3.7 and Table 3.9, respectively. A thin (~10 nm) ZnO layer was grown at 800°C for four minutes, using the same Zn flux and plasma conditions as the LT-ZnO layer. The undoped HT-ZnO growth was performed before growth of the subsequent Ag doped epilayer to provide a smooth and lattice-matched growing surface. Stoichiometric or oxygen rich environments were provided using a Zn flux of 4×10^{14} atoms/cm^{2}s or 3×10^{14} atoms/cm^{2}s, respectively. Ag flux, supplied by solid source sublimation, was varied between 4×10^{9} atoms/cm^{2}s and 4×10^{11} atoms/cm^{2}s to provide a doping level of 10^{18} to 10^{20} Ag/cm^3 as determined by a combination of Rutherford backscattering spectrometry (RBS) and particle-induced x-ray emission (PIXE).

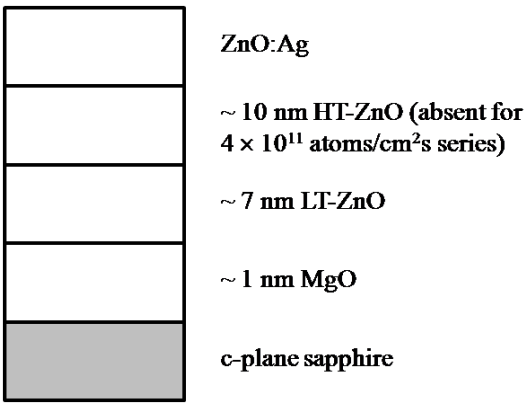

Fig. 4.1. Schematic of the structure used in ZnO:Ag doping experiments.

With Ag fluxes of 4×10^{10} to 4×10^{11} atoms/cm^{2}s and a substrate temperature of 600°C, the Ag concentration was measured to be 0.04% to 0.4%, respectively. These doping levels correspond to a Ag concentration of 1.5×10^{19} to 1.5×10^{20}

atoms/cm^3, respectively. However, with an increase in substrate temperature to 800°C, the incorporated Ag concentration remain essentially constant, even when the Ag flux was varied over two orders of magnitude. The incorporated Ag was found to range between 1.9×10^{19} to 3.8×10^{19} atoms/cm^3, with the Ag flux varied from 4×10^9 to 4×10^{11} atoms/cm^{2}s. This doping incorporation limit is not unexpected as the sticking coefficient is lower at higher temperatures and the highest Ag cell temperature (760°C) was still lower than the substrate temperature (800°C). Such doping limits with temperature have previously been observed with N doping of ZnO via PAMBE as well [179, 180].

Heavy doping can have significant effects on thin film growth, and this is evident in the SEM and RHEED images of Fig. 4.2. At Ag flux levels below 4×10^{10} atoms/cm^{2}s and a substrate temperature of 400°C (Figs. 4.2(d) and (g)), the morphology does not appear to change significantly when compared with its undoped counterpart (Fig. 4.2(a)). However, a transition in the film quality is observed for a Ag flux of 4×10^{11} atoms/cm^{2}s, as indicated by the rough surface evident in SEM and concentric arcs present in the RHEED image of Fig. 4.2(j). Similar morphology degradation is observed for growth at 600°C as well, as shown in Fig. 4.2(k). In contrast, when the substrate temperature is between 600 and 800°C, and Ag flux kept below 4×10^{10} atoms/cm^{2}s, the films all have a similar, relatively smooth morphology, as shown in Figs. 4.2(b) to (i), and (l). That is, such films are dominated by many small pits, but still have reasonably streaky RHEED patterns, which confirm the single crystal nature of such films.

Such morphology is quite different to the often granular nature of ZnO films grown by RF sputtering [68] or sol-gel [63]. However, unlike growth between 400°C and 600°C, a substrate temperature of 800°C does not result in noticeable morphology changes when the Ag flux level is varied between 4×10^9 and 4×10^{11} atoms/cm^{2}s. Both undoped and doped films grown at 800°C have essentially the same basic morphology, as shown in Figs. 4.2(c), (f), (i) and (l). The similar surface morphology is expected due to the limitation of Ag incorporation at high temperatures. These variations in morphology confirm that Ag doping can significantly deteriorate film quality, the extent of which depends strongly on growth conditions. Therefore, the polycrystalline films shown in Fig.

4.2(j) and (k) suggest an upper limit of 1.5×10^{19} Ag atoms/cm^3 in order to maintain a reasonable morphology, when the substrate temperature is below 600°C.

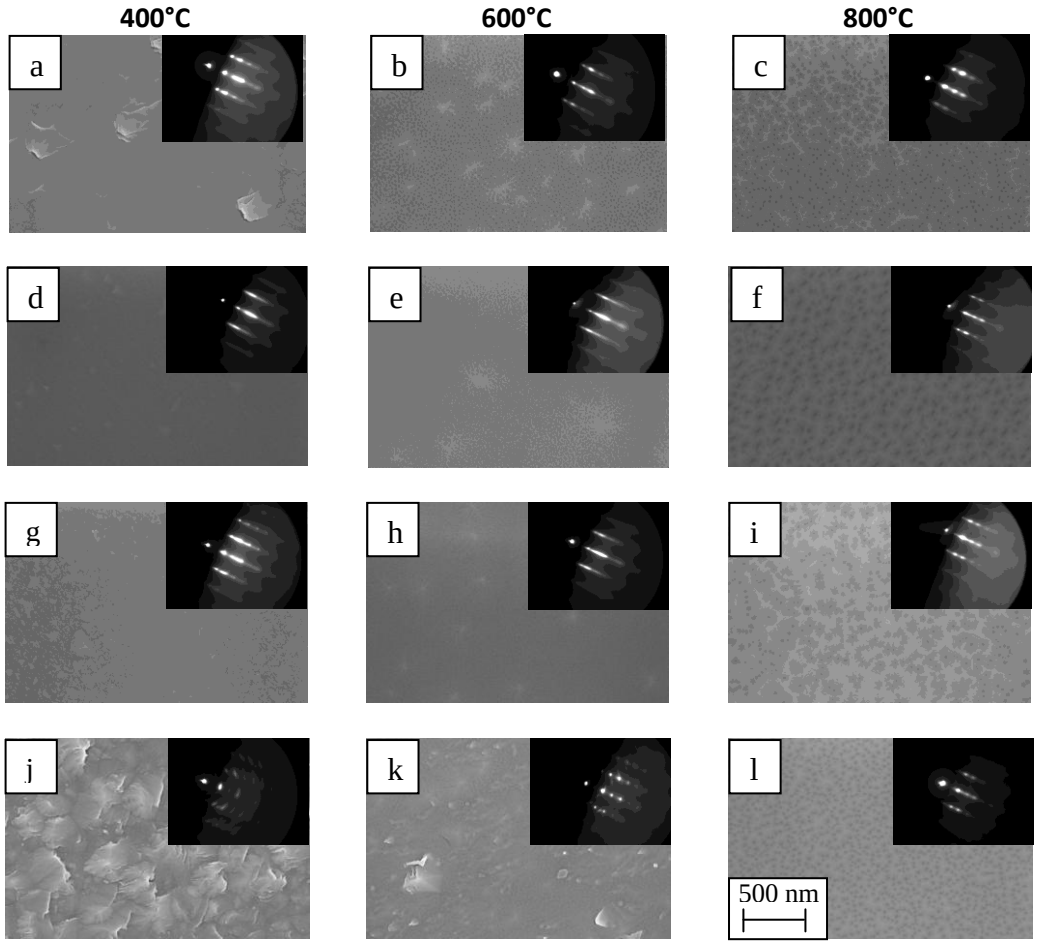

Fig. 4.2. Top view SEM of ZnO films grown at (a) undoped, (b) undoped, (c) undoped, (d) 4×10^9 Ag flux atoms/cm^{2}s, (e) 4×10^9 Ag flux atoms/cm^{2}s, (f) 4×10^9 Ag flux atoms/cm^{2}s, (g) 4×10^{10} Ag flux atoms/cm^{2}s, (h) 4×10^{10} Ag flux atoms/cm^{2}s, (i) 4×10^{10} Ag flux atoms/cm^{2}s, (j) 4×10^{11} Ag flux atoms/cm^{2}s, (k) 4×10^{11} Ag flux atoms/cm^{2}s, and (l) 4×10^{11} Ag flux atoms/cm^{2}s. Insets are the corresponding reflection high-energy electron diffraction (RHEED) images.

It should be noted that for the lowest Ag flux level of 4×10^9 atoms/cm^{2}s for growth between 400°C and 600°C, the surface appears smoother and the RHEED patterns are streakier, as shown in Figs. 4.2(d) and (e), compared to their undoped counterparts of Figs. 4.2(a) and (b), respectively. The improvement in surface morphology may be due to the extra undoped HT-ZnO grown before deposition of the ZnO:Ag layer. The additional HT-ZnO represents an enhanced buffer layer process, as it provides a smooth lattice matched surface, resulting in superior epilayer growth. A similar morphology improvement is also seen for the film grown at 600°C with a Ag flux 4×10^{10} atoms/cm^{2}s (Fig. 4.2(h)). This implies

that perhaps the buffer layer process should be modified to include this additional step.

To further understand the evolution of surface morphology with heavy Ag doping, one can evaluate the RHEED pattern changes during growth. Figure 4.3 shows that the 400°C film doped with a Ag flux of 4×10^{11} atoms/cm^{2}s starts to become highly disordered after 30 minutes of growth (Fig. 4.3(e)). This corresponds to a film thickness of 133 nm, at an LRI measured growth rate of 267 nm/hr, confirmed by both cross-sectional SEM and profilometry measurements. Therefore, it might be possible to control the degradation in crystalline quality by terminating the growth just before significant degradation occurs. Depending on the application, a 133 nm thick ZnO:Ag doped layer might be sufficient.

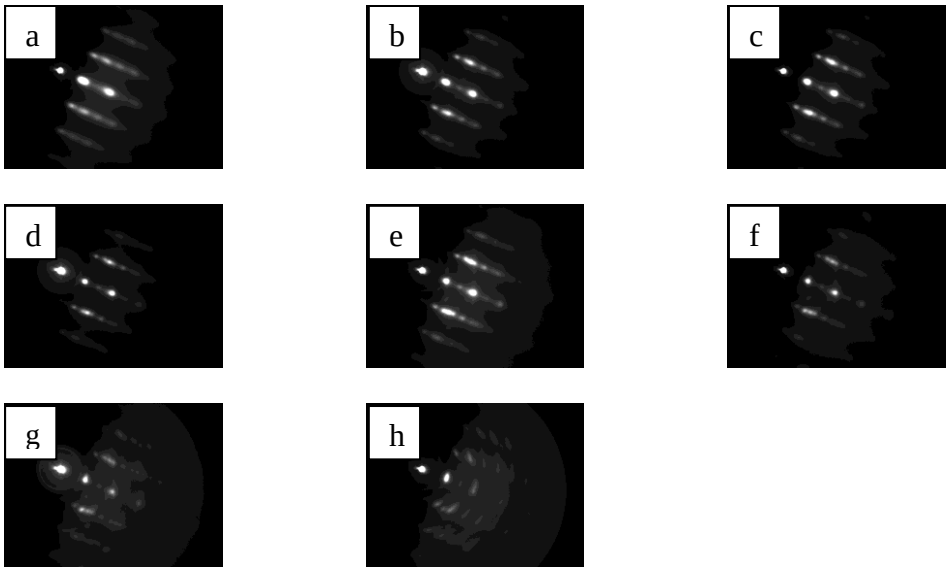

Fig. 4.3. RHEED images showing the evolution of surface morphology for a film doped with a Ag flux of 4×10^{20} atoms/cm^{2}s and grown at 400°C. RHEED image at (a) just before ZnO:Ag growth, (b) 5 minutes into ZnO:Ag growth, (c) 10 minutes into ZnO:Ag growth, (d) 20 minutes into ZnO:Ag growth, (e) 30 minutes into ZnO:Ag growth, (f) 1 hour into ZnO:Ag growth, (g) 1 hour 36 minutes into ZnO:Ag growth, and (h) end of 3 hour ZnO:Ag growth.

The incorporation of Ag on the Zn sub-lattice was quantified using RBS channeling experiments for selected films, as shown in Fig. 4.4. The significantly increased backscattered yields with films grown at a Ag flux of 4×10^{11} atoms/cm^{2}s compared with a Ag flux of 4×10^{10} atoms/cm^{2}s is due to greater disorder introduced into the film with higher doping, consistent with RHEED and SEM results in Fig. 4.2. The similarity in the backscattering yields for both Ag and Zn at each Ag flux level suggest that they occupy the same sub-lattice, as

summarised in Table 4.3. Most of the Ag (94%) incorporated substitutionally on Zn sites at a doping concentration of 1.5×10^{19} Ag atoms/cm^3, significantly higher than previously reported (30%) [71]. It is highly desirable that most of the Ag has incorporated as Ag_{Zn}, which has been theoretically predicted to be an acceptor in ZnO [50, 59]. When the doping concentration is increased by an order of magnitude, Ag_{Zn} increases proportionately, confirming the high solubility of Ag in the ZnO lattice. This means that there is potential for incorporation of a large amount of Ag acceptors into ZnO. The practical limit, then, may prove to be determined by the point at which film quality deteriorates.

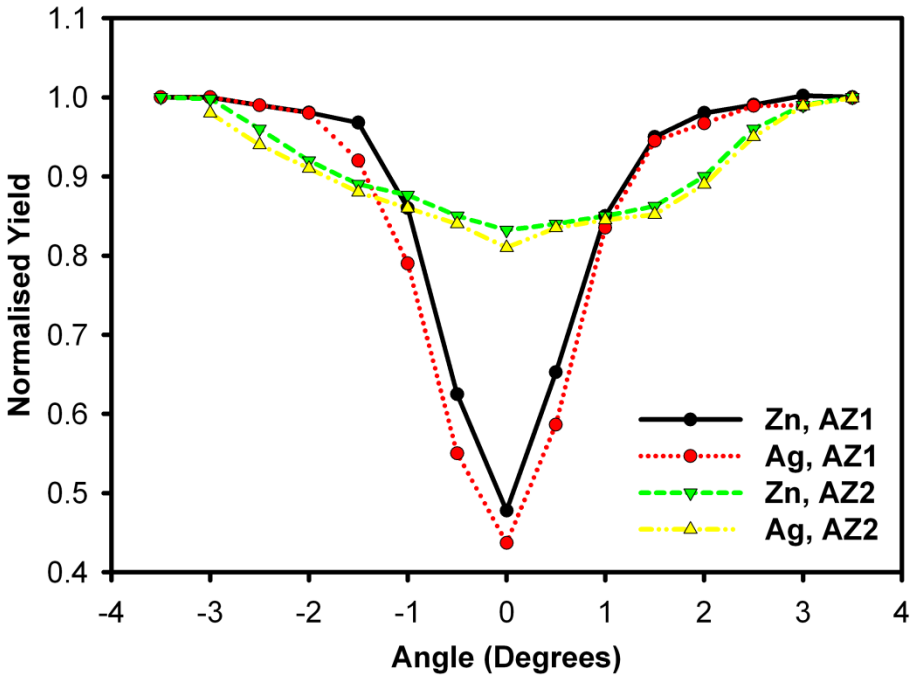

Fig. 4.4. RBS channelling results of Ag doped ZnO films about the [0001] direction. Both films are grown at 600°C. AZ1 and AZ2 are doped with 1.5×10^{19} Ag/cm^3 and 1.5×10^{20} Ag/cm^3 , respectively.

Table 4.3. RBS channeling results of two Ag doped ZnO films along the [0001] direction, showing the majority of Ag is incorporated on Zn sub-lattice sites.

Sample	Estimated Ag flux (atoms/cm^{2}s)	Substitutional Ag (atoms/cm^3)	Interstitial Ag (atoms/cm^3)
AZ1	4×10^{10}	1.4×10^{19}	8.7×10^{17}
AZ2	4×10^{11}	1.3×10^{20}	1.6×10^{19}

Another indication of the incorporation of an impurity in a material is through measuring the lattice constant, as the ionic radii of host and dopant atoms differ.

Figure 4.5 shows that there are indeed indications of lattice expansion with Ag dopant incorporation, consistent with other reports [63, 68, 69, 73, 74]. The highest Ag flux level (4×10^{11} atoms/cm^{2}s) resulted in 11.3% lattice expansion, compared to its undoped counterpart. The lattice expansion observed with Ag doping is expected as Ag^+ ions have a larger ionic radius (1.02 Å), compared to Zn^{2+} ions (0.62 Å) [61].

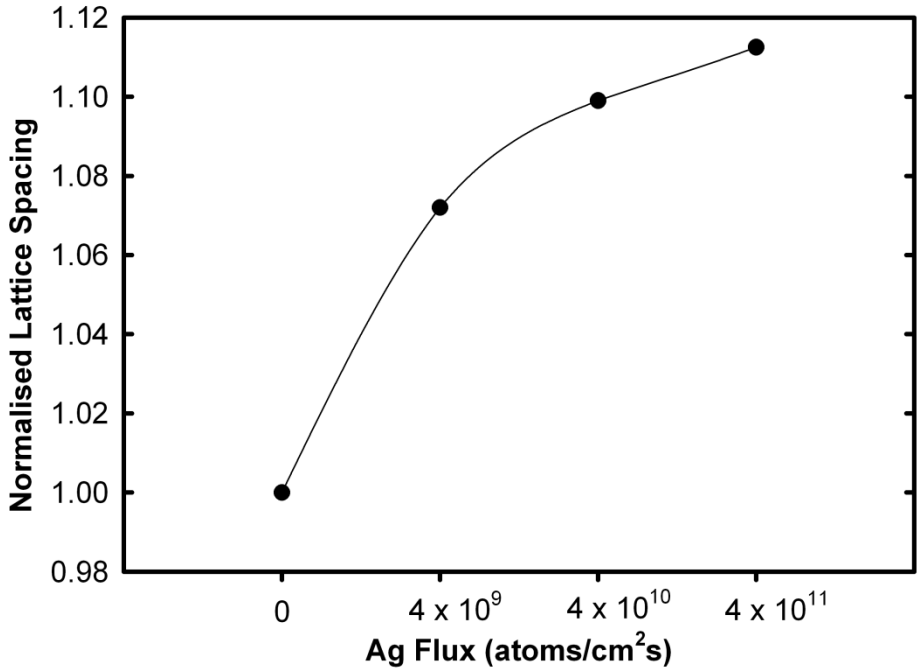

Fig. 4.5. Lattice spacing calculated from RHEED of Ag doped films grown at 600°C under stoichiometric growth conditions.

4.4 Effect of Ag Doping on Electrical Properties

Since most of the Ag was determined to have incorporated substitutionally, according to theoretical predictions [50, 59] the result should be acceptor levels introduced in the lower half of the bandgap, even if some small fraction (~6%) are compensated by interstitial complexes acting as donors. However, as can be seen in Fig. 4.6, conventional single magnetic field (0.51 T) Hall effect measurements indicate that all as-grown ZnO:Ag films are n-type (as are undoped films).

Since such measurements can be affected by contributions from the degenerate (low temperature) n-type buffer layer [164], one sample (Ag concentration of 1.5×10^{19} cm^{-3}) was evaluated using variable magnetic field Hall effect measurements. The results of multiple carrier fitting (MCF) and separate

quantitative mobility spectrum analysis (QMSA) are in good agreement with the conventional measurement result, with only one electron population at a mid 10^{16} cm^{-3} concentration required to fit the data, as summarised in Table 4.4. Therefore, conventional Hall effect measurements are suitable for electrically characterising these films.

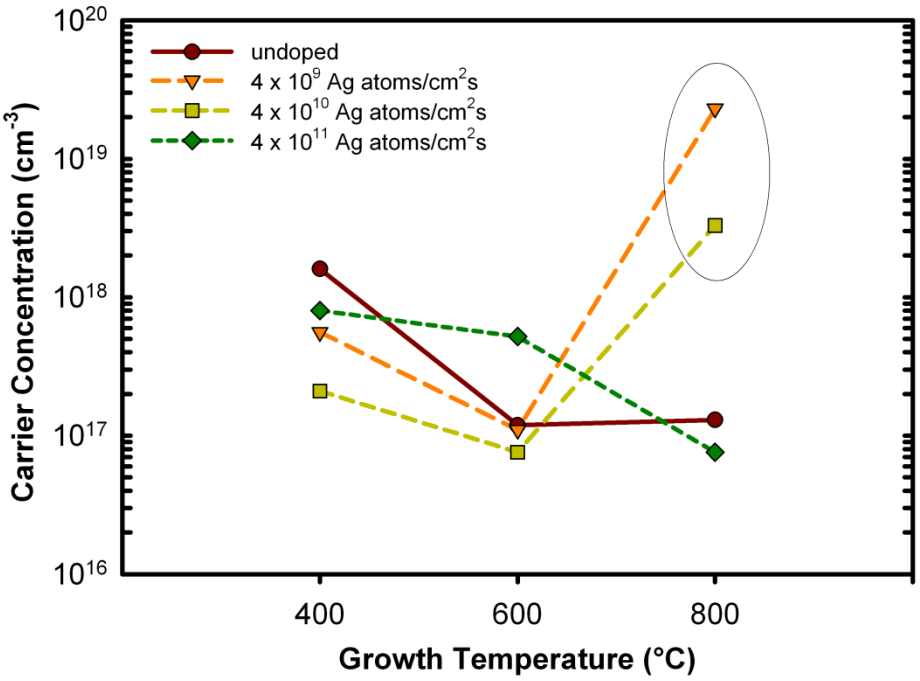

Fig. 4.6. Electron concentration of undoped and ZnO:Ag films determined by single magnetic field Hall effect. The films within the encircled area have significantly lower growth rates than the other films, possibly due to unstable Zn fluxes. Such Zn flux instability is occasionally an issue in MBE conducted under an oxygen environment.

Table 4.4. Hall effect measurements of a 1.5×10^{19} Ag/cm^3 doped ZnO film grown at 600°C. The QMSA calculated value is the peak in the fitted QMSA spectrum.

	Mobility (cm^2/Vs)	Carrier concentration (cm^{-3})	Carrier type
0.51 T Hall	71	7.6×10^{16}	n
QMSA	106	2.5×10^{16}	n
MCF	60	5.9×10^{16}	n

Nevertheless, Fig. 4.6 does show that the measured electron concentration decreases at higher Ag flux levels for growth at 400°C. This is consistent with deep acceptor behaviour where such acceptors compensate for the background electron concentration but may not be shallow enough to force the material p-type. Such deep acceptor effects have been previously observed in highly compensated bulk ZnO material [22]. While compensation levels as high as those

observed in bulk ZnO materials are not seen in these materials, the decrease in carrier concentration with increasing Ag flux for growth at 400°C does point towards some degree of compensation, providing evidence of acceptor creation. The additional decrease in carrier concentration with further increases in Ag flux supports the contention that deep acceptors have been introduced, as the only growth parameter varied for each temperature series was the Ag flux. It should be noted that the high donor concentration in the most heavily doped samples is due to the formation of donor-like structural defects during growth due to the high impurity concentration.

There is also a clear dependence of carrier concentration on substrate temperature, which is not unexpected as dopants incorporate more easily at lower growth temperatures [70]. For films grown at Ag fluxes between 4×10^9 to 4×10^{10} atoms/cm^{2}s, the electron concentration appears to reach a minimum at 600°C. Similar variation in electron concentration over the substrate temperature range has also been previously observed in nitrogen doped ZnO grown by PAMBE [179]. Therefore, in general, as long as the Ag flux is below 4×10^{10} atoms/cm^{2}s, the electron concentration is reduced, the degree of which appears to depend on the substrate temperature.

However, at the highest substrate temperature a different trend is seen which may be due, at least in part, to the temperature dependence of dopant incorporation. The different levels of doping efficiencies at different growth temperatures may also be due to the temperature dependence in the formation of particular types of defects [181]. The variety in the measured electron concentration for films grown at 800°C is possibly due to the variation in the Zn flux during growth. The growth rates for those particular films grown at Ag fluxes between 4×10^9 and 4×10^{10} atoms/cm^{2}s are approximately 30% less than other films grown at 800°C. Unstable Zn fluxes, which can arise from partial oxidation of the source material, will in turn degrade the resultant epitaxial layer quality.

When introducing impurities into a lattice, the overall structural quality tends to degrade, resulting in decreased carrier mobility. In addition, carrier mobility can be affected by ionised impurity scattering, the degree of which increases with increased dopant incorporation. Ag doping of ZnO is no exception, as shown in

Fig. 4.7. The mobility of the doped films is mostly lower than their undoped counterparts. The higher mobility for the film doped with a Ag flux of 4×10^{10} atoms/cm^{2}s and grown at 600°C is likely due to experimental variation since the carrier concentrations for films grown with Ag flux below 4×10^{10} atoms/cm^{2}s are similar. The increase in mobility for the growth at 800°C as doping level is increased is also unexpected. However, since the increase in mobility is fairly low, it is possible that those values are within experimental uncertainty. A similar argument is applicable for the trend observed for growth at 400°C.

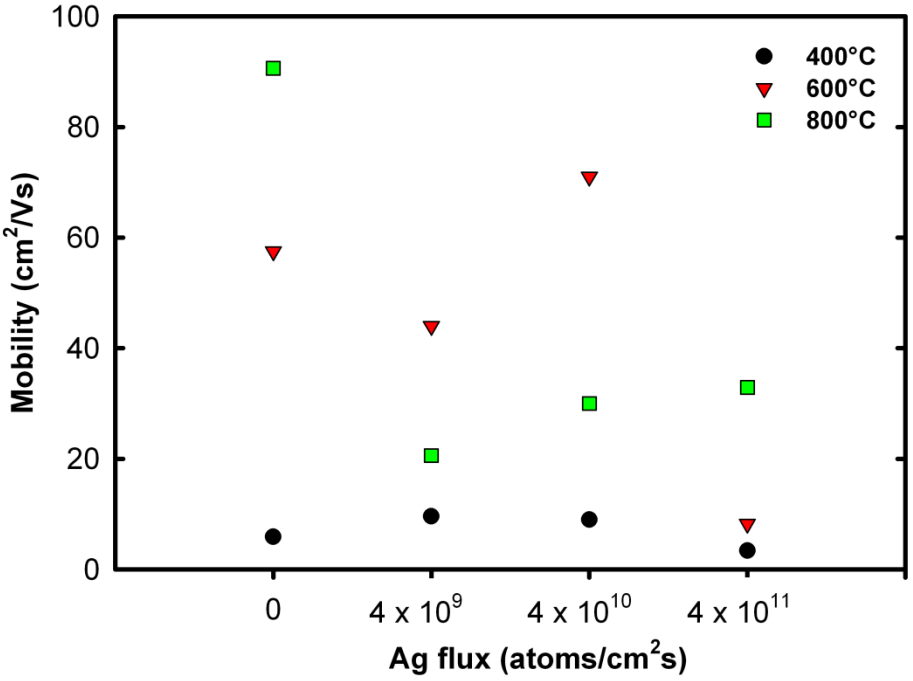

Fig. 4.7. Mobility of undoped and ZnO:Ag films determined by single magnetic field Hall effect.

With decreasing electron concentration observed in Fig. 4.6, one might expect a corresponding increase in the resistivity of such Ag doped films. However, Fig. 4.8 does not show any clear trend in the resistivity of the doped films grown at 600°C and 800°C, except for a significant increase in resistivity for the highest Ag doped film grown at 800°C. The cause of this singular resistivity increase is as yet unknown. Nevertheless, Fig. 4.8 does show that there is an increase in the resistivity with increasing doping concentration for growth at 400°C. It is possible that since the morphology is severely degraded at high doping concentration, the films become more granular and hence, are more resistive. This is possibly

evidence that increased resistivity observed by other groups [68, 73] is due to a degradation in their film quality with Ag doping.

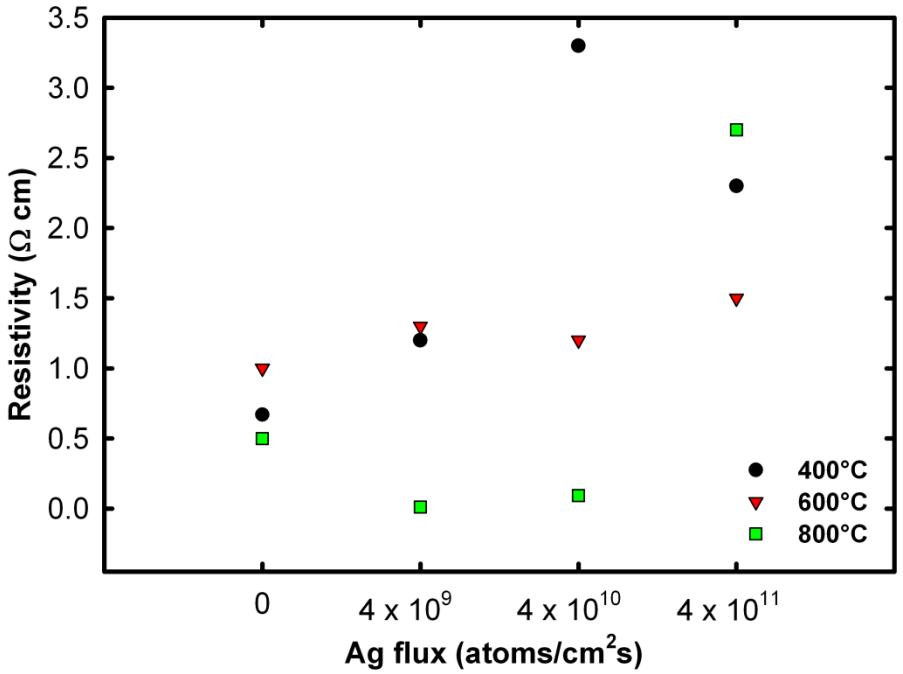

Fig. 4.8. Resistivity of undoped and ZnO:Ag films determined by single magnetic field Hall effect.

4.5 Effect of Ag Doping on Optical Properties

Outside of Hall effect measurements, one of the most common techniques employed to investigate impurities in semiconductors is photoluminescence. Neutral donor bound excitons related to In (I_9), Ga (I_{8a}), Al (I_6), and H (I_4) dominated the low temperature PL for films grown at 800°C under various Ag flux levels, as shown in Fig. 4.9. In addition, appearances of multiple LO phonon replicas and an A_T shoulder, implies films were of high structural quality. The similarity between the low temperature PL for those films was expected due to the Ag incorporation limits found from earlier RBS measurements. It should be noted that the more featureless low temperature PL related to the lowest Ag flux of 4×10^9 atoms/cm^{2}s was more likely due to its other growth factors, such as a poorer buffer layer or unstable Zn flux, rather than Ag doping.

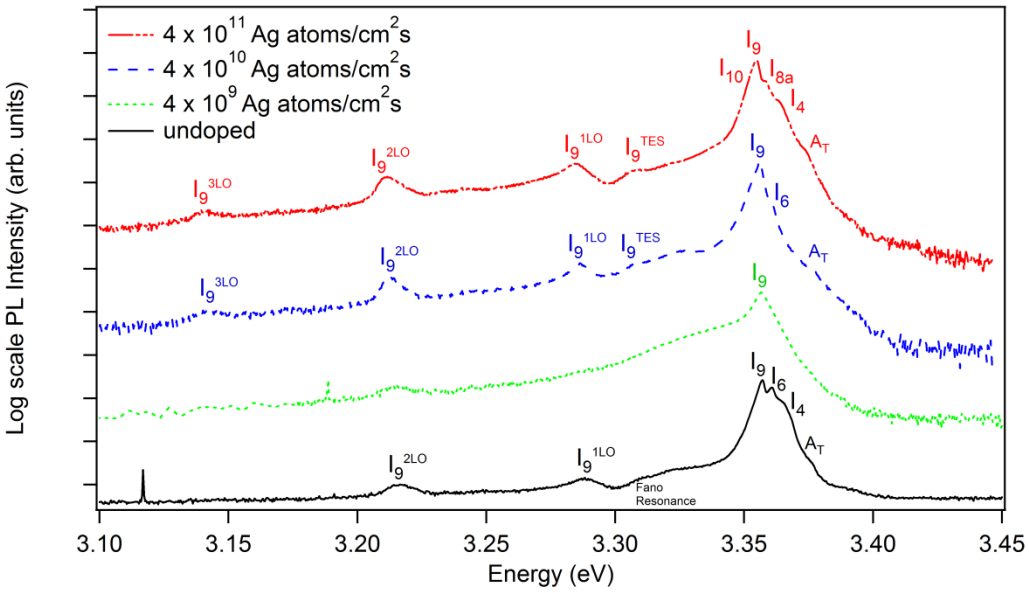

Fig. 4.9. 4 K PL for various ZnO:Ag films grown at 800°C.

Unlike the dominance of I_9 for growth at 800°C, Fig. 4.10 shows that the dominant emission for growth at 600°C is due to I_6, which is related to Al. For Ag flux levels below 4×10^{10} Ag atoms/cm^{2}s, the low temperature PL shows similar structures, which consist of LO phonon replicas, Fano resonance dip, free exciton peaks, and the same three donor bound exciton peaks. The presence of these features indicated high structural quality material, consistent with the RHEED analysis in Fig. 4.2. In contrast, the highest Ag flux level of 4×10^{11} atoms/cm^{2}s had no LO phonon replicas, indicating a poorer structural quality film. This supports the RHEED findings in Fig. 4.2, where the structural quality degraded significantly at excessive doping above 4×10^{10} Ag atoms/cm^{2}s. The appearance of an as yet unidentified peak at 3.297 eV for the highest doped film is likely due to defects as that film had a polycrystalline RHEED pattern. In addition, all doped (and undoped) films grown at 600°C had I_{3a} peaks, indicating the presence of Zn_i, implying a Zn-rich growth condition. If the growth regime was Zn-rich instead of the desired stoichiometric condition, this may be part of the reason as to why no Ag related peaks were observed, or Zn_i donors may be present in large enough concentrations to neutralise the Ag acceptors. It should also be noted that the intensity of the 1LO replica of I_6 was significantly reduced because of Fano resonance, sometimes resulting in misidentification of the 2LO peak as a donor-acceptor-pair transition due to its high relative intensity compared to the 1LO

peak. Power dependent PL did not detect any DAP transitions, confirming the assignment of the 1LO peak.

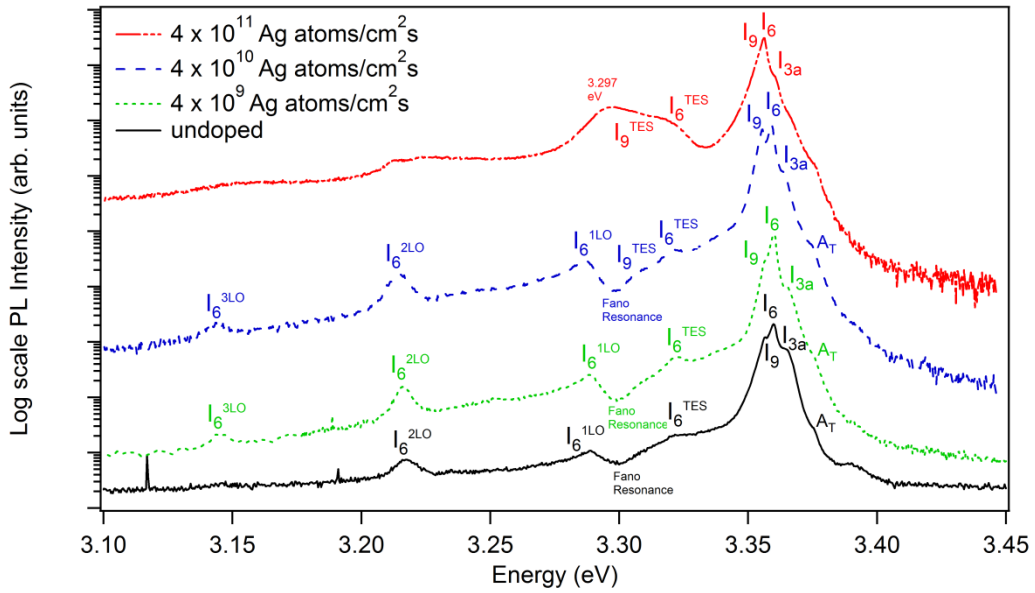

Fig. 4.10. 4 K PL for various ZnO:Ag films grown at 600°C.

As with doping experiments at 600°C and 800°C, neutral donor bound excitons related to In (I_9), Al (I_6) and H (I_4) were observed for films grown at 400°C (Fig. 4.2). Interestingly, the low temperature PL for the film grown with an Ag flux of 4×10^{10} atoms/cm^{2}s doped film had better defined features than the undoped sample grown at the same temperature. This may be due in part to the thin undoped HT-ZnO grown at 800°C, which created a smoother surface for epilayer growth, consistent with RHEED images in Fig. 4.2. In addition, the appearance of ionised donor bound excitons (I_0) related to $I_{6/6a}$ [182] suggests that there were compensating acceptors present in the film grown with a Ag flux of 4×10^{10} atoms/cm^{2}s at the low substrate temperature of 400°C. Ionised donor bound excitons only appear if compensating acceptors are present to affect the neutral donors [183]. This implies that a Ag flux level of at least 4×10^{10} atoms/cm^{2}s and growth temperatures below 400°C are necessary to significantly influence the optical properties of a sample.

As almost all the doped films have both I_9 and I_6 peaks, their presence indicates significant In and Al incorporation during growth, regardless of doping levels or growth temperatures. Possible sources of In and Al are from the In-Sn solder used

to mount the sapphire substrate to the molybdenum growth block, and the alumina discharge tube or Al impurities from the sapphire substrate [105], respectively. As both In and Al are known to be shallow donors in ZnO, eliminating or mitigating those sources are crucial for successful acceptor doping using PAMBE.

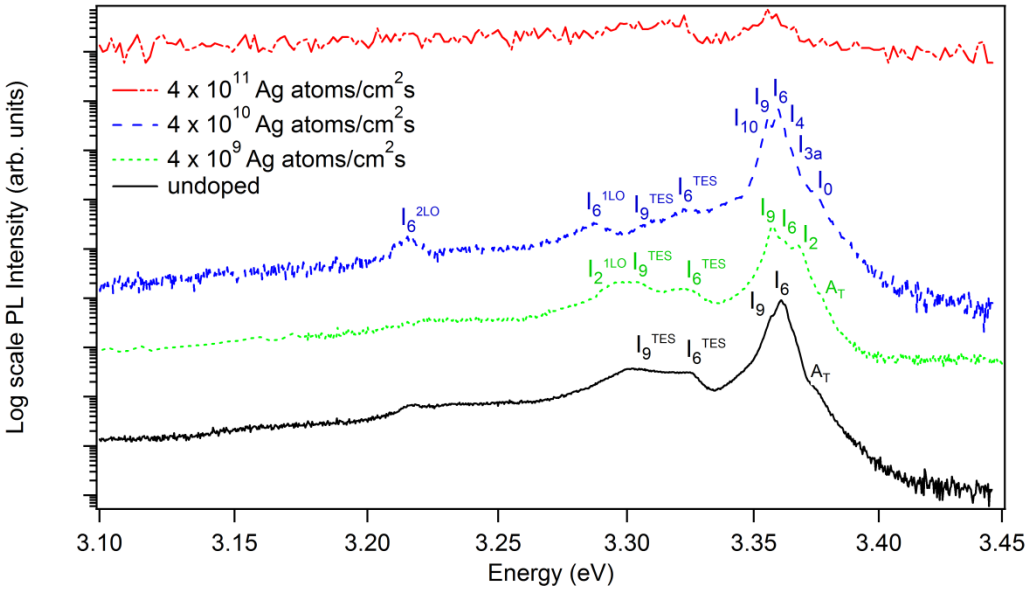

Fig. 4.11. 4 K PL for various ZnO:Ag films grown at 400°C.

A few groups have attributed Ag acceptor bound excitons to features at ~3.11 eV [72], 3.317 eV [73] or ~3 eV [50] but no evidence of these transitions, or any other attributable to Ag, was observed in the samples grown in this thesis (Figs. 4.9 to 4.11). However, a clear red-shift in the peak positions was observed with increasing Ag flux levels, as shown in Fig. 4.12. Such a red-shift with Ag doping occurs due to the larger Ag ionic radii (1.02 Å), compared to the Zn ionic radii (0.62 Å), as incorporation of Ag on Zn sites induces an increase in the lattice constant through introducing tensile stress and hence, a red-shift in the photoluminescence, consistent with the RHEED spacing analysis in Fig. 4.5. The I_6 peak red-shifted by almost 4 meV at the highest Ag flux of 4×10^{11} atoms/cm^{2}s and growth temperature of 600°C, consistent with Fig. 4.5.

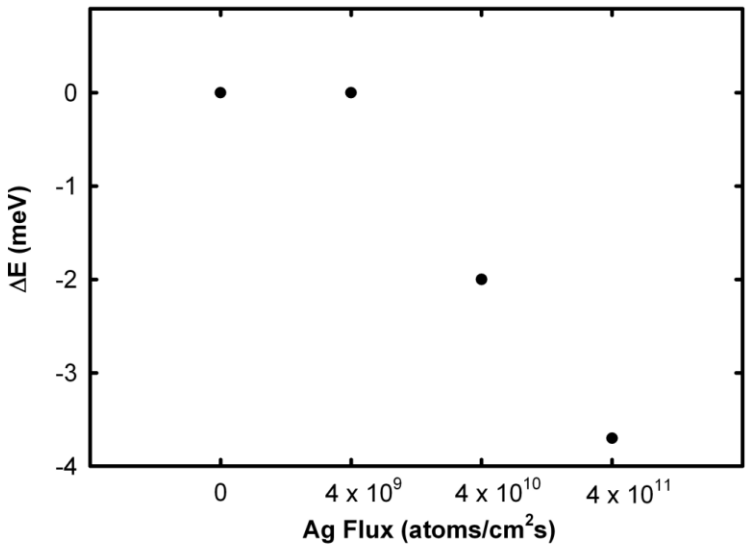

Fig. 4.12. Dominant peak position energy shifts with Ag doping for growth at 600°C.

4.6 Effect of Growth Conditions on Ag Doping of ZnO

In order to improve the incorporation of Ag in ZnO, several samples were grown under oxygen-rich (O-rich) conditions at 600°C, with all parameters being the same as for previous stoichiometric growth except for the Zn flux, which was set at 3×10^{14} atoms/cm^{2}s. Table 4.5 shows that the significantly reduced growth rate for the undoped film grown at the lower Zn flux level, compared to the previous Zn flux level, confirmed that the Zn flux should be sufficient to obtain an oxygen-rich growth environment.

Table 4.5. Summary of growth rates for different growths under O-rich conditions.

Ag flux (atoms/cm^{2}s)	Growth Rate (nm/hr)
Undoped (stoichiometric)	146
Undoped	118
4×10^9	130
2×10^{11}	145

However, there did not appear to be any significant difference in the RHEED patterns (Fig. 4.13) of the undoped and Ag doped films. While the film grown with a Ag flux of 2×10^{11} atoms/cm^{2}s did appear to be rougher, as evident from the spotty RHEED pattern (Fig. 4.13(c)), the single crystal nature was maintained. This suggests that the Ag flux level can be further increased while still maintaining the crystalline quality.

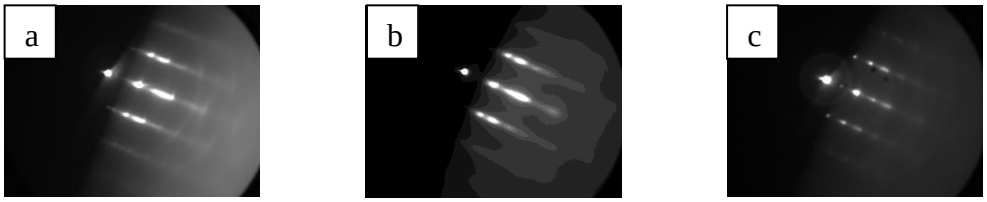

Fig. 4.13. RHEED images of O-rich films grown (a) undoped, (b) with Ag flux of 4×10^9 atoms/cm^{2}s, and (c) with Ag flux of 2×10^{11} atoms/cm^{2}s. All films were grown at 600°C.

In general, growing films outside the stoichiometric region tends to result in poorer electrical properties due to the increased formation of native defects. Table 4.6 shows that the carrier concentration and mobility did degrade when growing films under O-rich conditions, with all films measured as n-type. However, it is interesting to note that the film grown with a Ag flux of 2×10^{11} atoms/cm^{2}s appears to have a lower carrier concentration and higher mobility than the corresponding undoped, O-rich film. The improvement in electrical properties was likely due to the additional thin HT-ZnO buffer layer grown prior to Ag doped films. Therefore, the slight decrease in the electron concentration for the Ag doped films was unlikely due to Ag doping. However, the resistivity appears to increase with sufficient Ag flux. This suggests that Ag doping under O-rich conditions shows some promise. However, more Ag doping experiments under O-rich conditions should be undertaken to better understand its effects.

Table 4.6. Summary of Hall effect measurements for films grown under O-rich conditions at a growth temperature of 600°C. All Hall effect measurements were performed at room temperature using a magnetic field strength of 0.51 T.

Ag flux (atoms/cm^{2}s)	Carrier Concentration (cm^{-3})	Mobility (cm^2/Vs)	Resistivity (Ω cm)
undoped (stoichiometric)	1.2×10^{17}	58	1.0
undoped	2.9×10^{17}	39	0.6
4×10^9	1.3×10^{17}	80	0.6
2×10^{11}	1.8×10^{17}	24	1.5

Fig. 4.14 shows that as with stoichiometric samples grown at 600°C, these O-rich films were also dominated by neutral donor bound excitons related to I_9 (In), I_6 (Al), and I_{3a}. The presence of I_{3a} is perplexing, as these are O-rich films and hence Zn_i formation should be reduced. It is possible that the level of oxygen was insufficient to enter the desired O-rich region. Nevertheless, there was a decrease

in the ratio between the I_{3a} (Zn_i) and I_6 (Al) peak under O-rich conditions (0.8 to 0.6). This decrease suggests that the concentration of Zn_i was decreased in the O-rich grown film. Hence, while this provides evidence of an O-rich growth condition, a greater O/Zn ratio may be necessary to fully suppress the formation of Zn_i. An additional possibility is another peak close to the I_{3a} energy position may be red- or blue-shifted to the I_{3a} position. Since it is well known that PL peaks in ZnO are difficult to interpret, other measurements such as annealing experiments under different ambient, or magneto-photoluminesence measurements, may be necessary to clarify the origin of the "I_{3a}" peak.

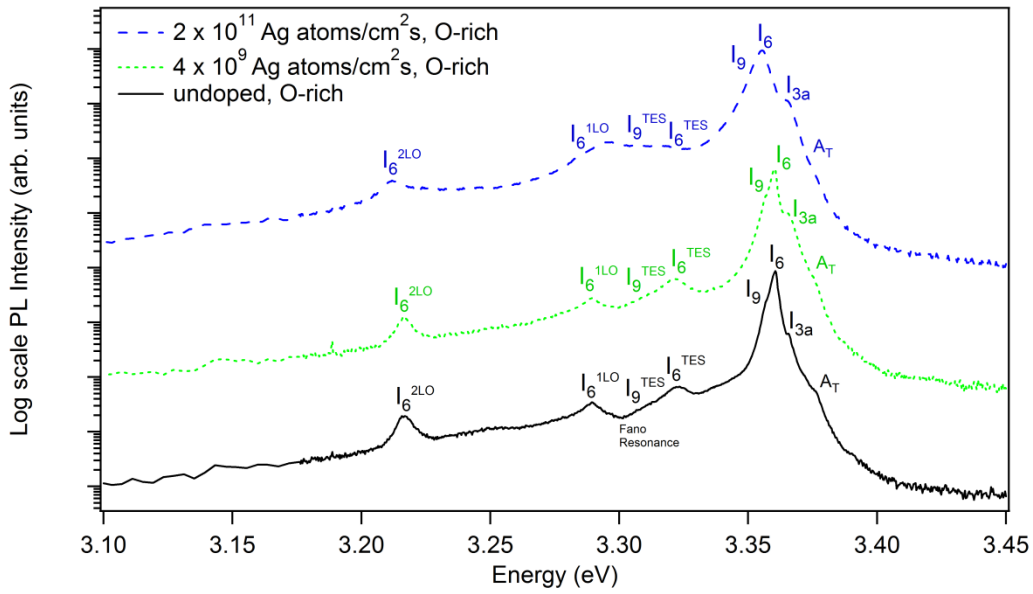

Fig. 4.14. 4 K PL of Ag doped films grown at 600°C under O-rich conditions.

It is worth noting that the frequently observed defect band centered around 2.3 eV appears to be suppressed with Ag doping (Fig. 4.15). The film grown under Ag flux of 2×10^{11} atoms/cm^{2}s was grown under O-rich conditions so it is likely that the defect band emission is mainly due to V_{Zn} [184, 185]. The incorporation of Ag could be leading to reduction of V_{Zn} through creation of Ag_{Zn} [67], thereby suppressing the defect band emission. Hence, the suppression of the defect band further supports the substitutional incorporation of Ag on Zn sites, as well as supporting the identification of the "green" defect band as being due to V_{Zn}.

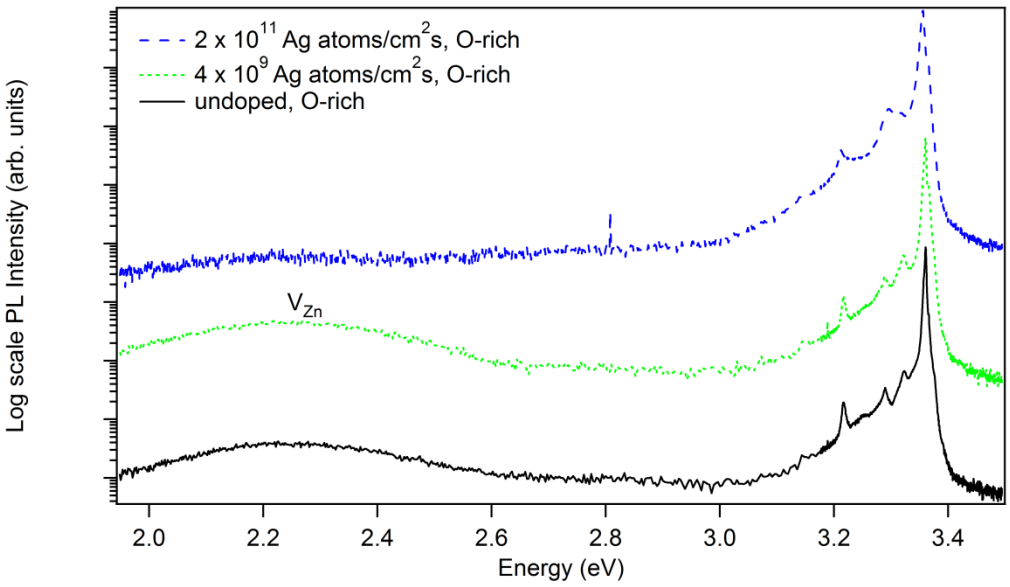

Fig. 4.15. Broad spectrum 4 K PL of Ag doped films grown at 600°C under O-rich conditions.

4.7 Defect Levels Introduced by Ag Doping

In the absence of acceptor related PL features, a better understanding of the Hall effect observations may be extracted from an experimental estimate of the proximity of Ag acceptor level(s) to the valence band maximum. These measurements are typically made by using a variable temperature technique such as deep-level transient spectroscopy (DLTS), which is limited to samples to which Schottky contacts can be made, and by the device series resistance. In the present study, extremely low capacitance response at the DLTS measurement frequency of 1 MHz was observed for diodes fabricated using ZnO:Ag samples, even using a nonstoichiometric AgO_x contact process [186], as shown in Fig. 4.16. As the DLTS setup operates at 1 MHz, the low capacitance response of the fabricated diode means that no reliable DLTS measurements can be undertaken with that particular diode.

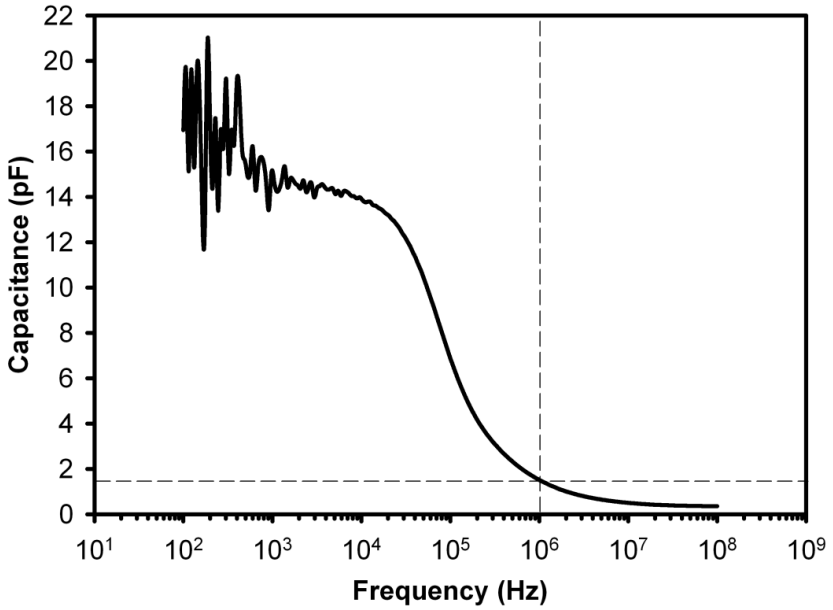

Fig. 4.16. Frequency response of an AgO_x diode fabricated on a sample doped with a Ag flux of 4 $\times$ 10^{10} atoms/cm^{2}s and grown at 600°C. The dashed lines indicate the capacitance at the DLTS measurement frequency of 1 MHz.

However, this contact process did work for undoped samples, providing an alternate pathway to investigating Ag impurities in ZnO. Kanai et al. [72] have postulated that it is possible for Ag to diffuse from an Ag contact to its underlying ZnO crystal. This was demonstrated recently for AgO_x on ZnO thin films [187]. The current-voltage measurement for such a diode fabricated on an undoped sample is shown as an inset in Fig. 4.17. Using the standard analysis detailed in Section 2.7.1, the rectification ratio, effective barrier height and ideality factor were calculated to be 20, 0.39 eV and 8.73, respectively. These figures of merit show that this diode is not of as high quality of that fabricated on bulk ZnO substrates [186]. This means that there might be limitations in using this diode in capacitance measurements. Nevertheless, Fig. 4.17 shows that this diode still have reasonable capacitance at the DLTS measuring frequency of 1 MHz, even if 1 MHz is at the start of the downward slope of the frequency response. In this case, the measured capacitance is above the detection limit of the DLTS setup, whereas the previous diode had capacitance values at the detection limit. The relatively low frequency cut-off is due to the high series resistance in this material. For better utilisation of DLTS, a lower series resistance material should be used, such as by employing a ZnO:Al Ohmic contact layer. Nevertheless, the capacitance response at 1 MHz is sufficient for DLTS measurements.

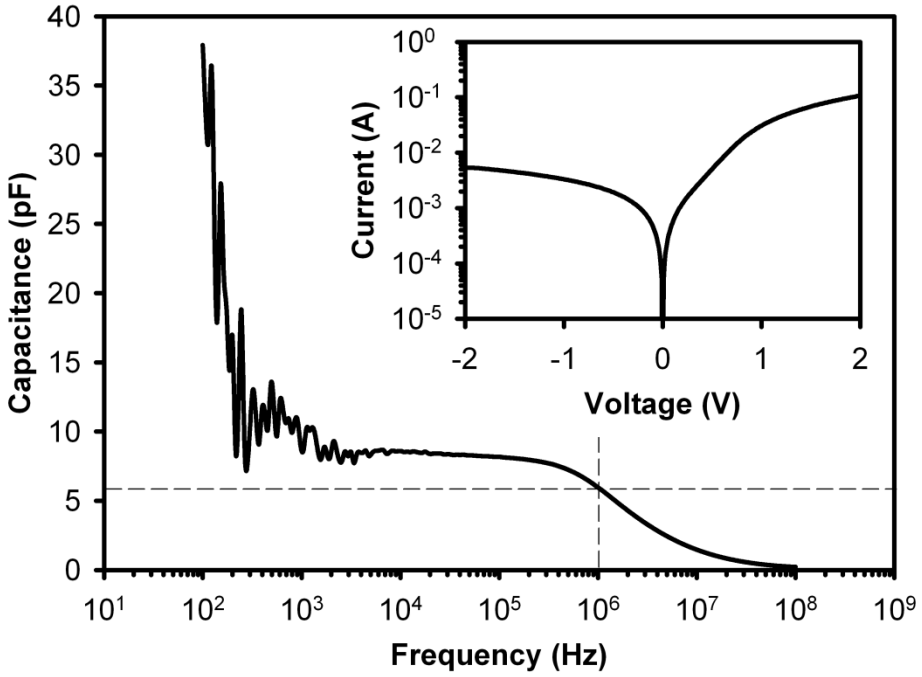

Fig. 4.17. Frequency response of a AgO_x diode fabricated on an undoped sample grown at 800°C. The dashed lines indicate the capacitance at the DLTS measurement frequency of 1 MHz. Inset is the corresponding current-voltage measurement.

The measured DLTS spectrum for such a diode is shown in Fig. 4.18, with three trap levels in evidence labelled HT1, ET1 and ET2. It should be noted that the ET2 trap level is clearer with a different set of rate windows, as shown in Fig. 4.19.

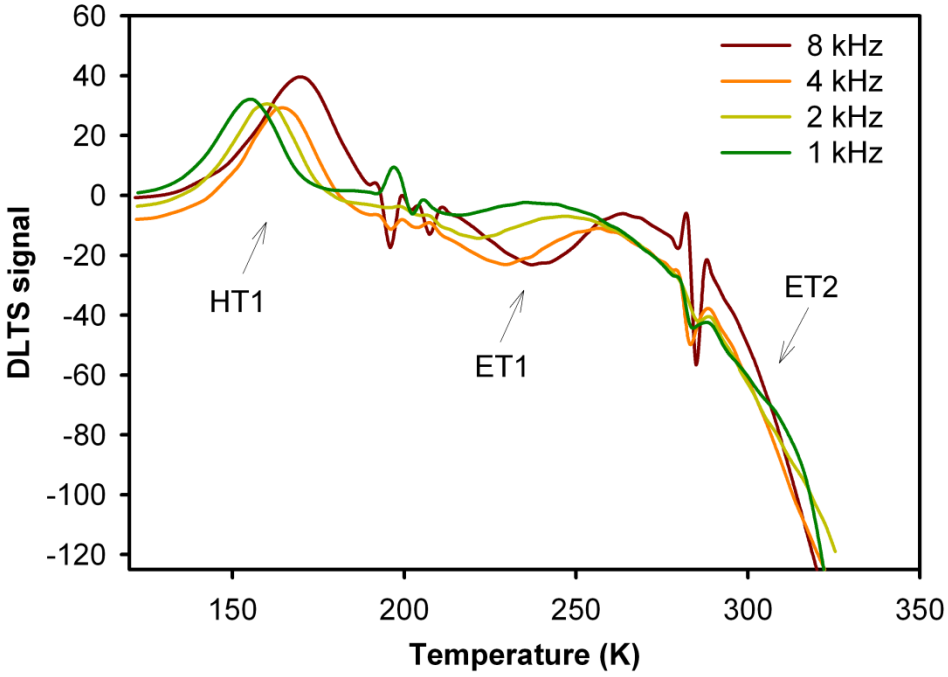

Fig. 4.18. DLTS spectrum of an undoped ZnO film, grown at 800°C, with an AgO_x contact, using various rate windows.

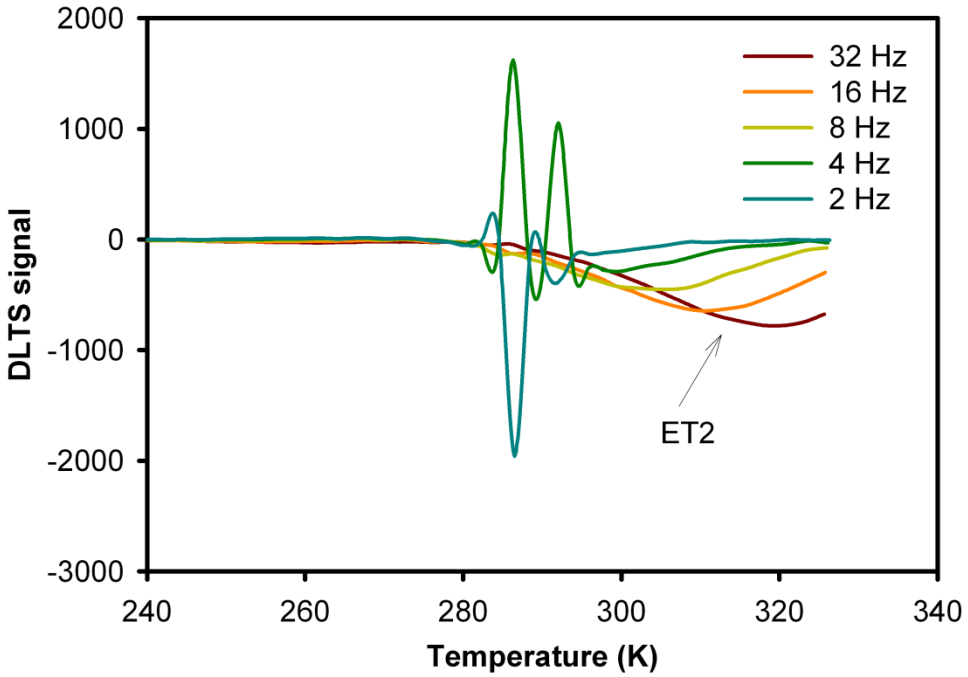

Fig. 4.19. DLTS spectrum of an undoped ZnO film, grown at 800°C, with an AgO_x contact, using lower rate windows to clarify the ET2 spectrum.

Arrhenius fits to the three trap levels are provided in Fig. 4.20, and indicate a deep hole trap at 319 meV above the VBM, close to the theoretical value of 400 meV for Ag in ZnO [50]. Hence, this deep acceptor is tentatively attributed to Ag_{Zn}, and may explain the compensating behavior observed in Hall effect measurements shown in Fig. 4.6 [62]. The 361 meV donor trap below the conduction band minimum (CBM) is attributed to E3′, which has been observed as a defect in ZnO grown by other methods [188]. It is interesting to note that the typically reported E3 defect level (~300 meV) is absent in this particular undoped sample. Due to the low impurity nature of MBE growth, it is possible that E3 is related to an extrinsic impurity that is uncommon in MBE films, but common in other growth techniques. However, more measurements are needed to clarify this hypothesis. There is also a deep donor at 834 meV, most likely due to oxygen vacancies [189]. However, as it is such a deep defect, it is unlikely to be responsible for the carrier concentration observed. As yet, the only other defect level study on MBE material reported is a Zn/O ratio study by Oh et al. [190]. Using TAS measurement, Oh et al. found shallow trap levels of between 33 meV to 46 meV are present in MBE grown material, depending on Zn/O flux ratios. However, no such defect levels were observed in TAS on the measured undoped sample, possibly due to the poor rectification of the fabricated diode.

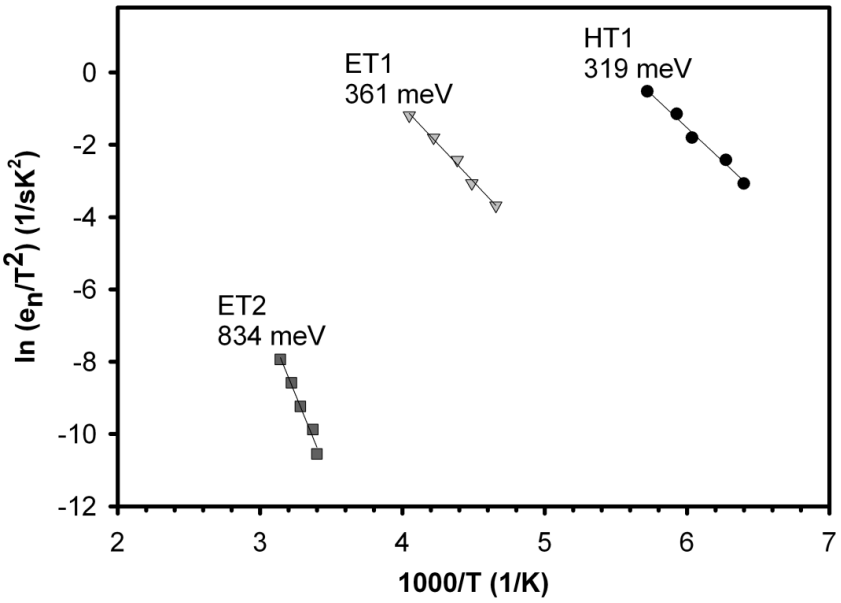

Fig. 4.20. Arrhenius fits to the HT1, ET1 and ET2 trap levels observed in the DLTS spectrum for the AgO_x contact on an undoped ZnO film.

It is worth noting that it has been reported [68] that post growth annealing may be necessary to electrically activate the dopants. However, as can be observed in Fig. 4.21, the Ag doped PAMBE-grown films only became more n-type after annealing, with an increase in electron concentration and a decrease in resistivity. The cause of this behaviour has not yet been established, but may originate from the fact that Ag can easily diffuse in ZnO, and hence the Ag may aggregate to form Ag clusters [191].

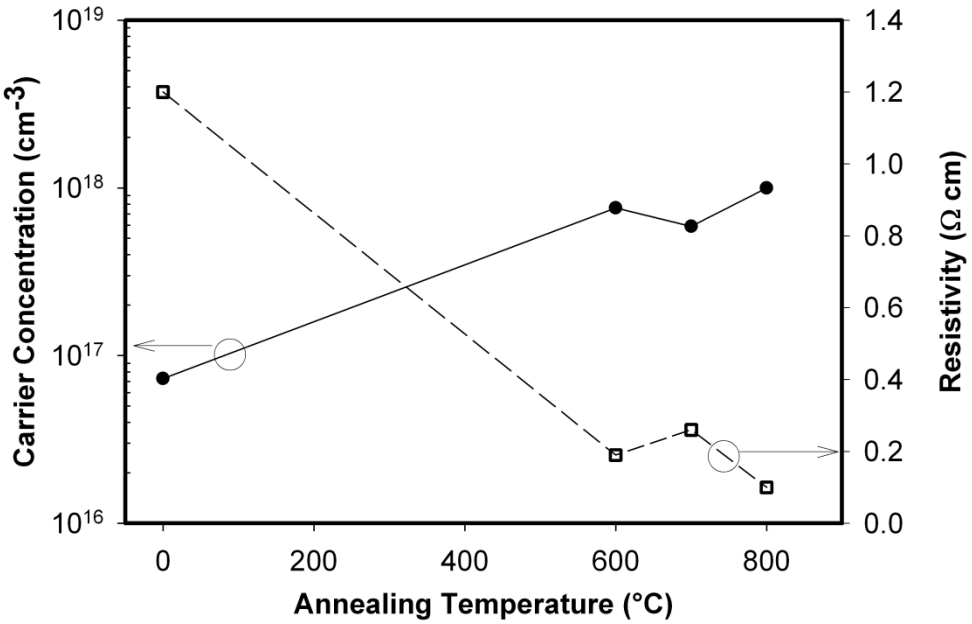

Fig. 4.21. Effect of 1-1.5 hour oxygen annealing on a film grown with a Ag flux of 4×10^{10} atoms/cm^{2}s, grown at 600°C under stoichiometric conditions.

4.8 Distribution of Impurities

While low temperature photoluminescence can provide clues as to the impurities in a material, it is only useful for optical centers near the surface (tens of nanometres) or if the surface and the rest of the bulk have similar impurity composition. A complementary and powerful technique frequently used to measure the distribution of impurities in a material is secondary ion mass spectroscopy (SIMS).

Fig. 4.22(a) and (b) show the positive (Cs^+) and negative (O) ion mass spectra for a 1.5×10^{19} Ag atoms/cm^3 doped film grown at 600°C under stoichiometric conditions, respectively. These spectra were obtained after 60 s sputtering at 500 eV to remove surface hydrocarbon contamination. Therefore, these spectra are near surface composition measurements; however, caution should be used in interpreting the relative intensities of the mass/charge signals detected due to the different ionisation efficiencies of different atoms. It might be worthwhile in the future to perform calibrations on the same SIMS equipment to enable quantitative analyses of the obtained spectra.

Nevertheless, qualitative analysis is also useful, with Fig. 4.22(a) showing that the dominant impurities were Na, Al and K. Miyamoto et al. [141] have previously reported that these impurities came from the discharge tube of their O_2 plasma source, which is the same model as that used in this thesis. Hence, it is conceivable that the Na and K detected in Fig. 4.22(a) were due to the plasma source as well. In addition, the Ag used in ZnO:Ag growth was obtained from ESPI, and contains up to 4 ppm of Na. Nevertheless, the presence of Na and K is not completely undesired, as they are also possible shallow acceptors.

However, Al incorporation is undesirable as it can form as a shallow donor [9]. The presence of Al, even at the surface, further confirms that Al incorporation was not only from Al diffusion from the sapphire substrate. As postulated earlier in Hall effect and PL analyses, it is possible that the alumina discharge tube is one of the sources of Al, consistent with SIMS results reported by Miyamoto et al. [141]. This further suggests that with this current plasma setup, p-type doping may be difficult to achieve. Furthermore, although RBS measurements suggested

substantial Ag incorporation, no Ag related peaks were detectable in the near surface spectrum. The absence of In was also unexpected, as low temperature PL suggested significant In incorporation regardless of growth conditions.

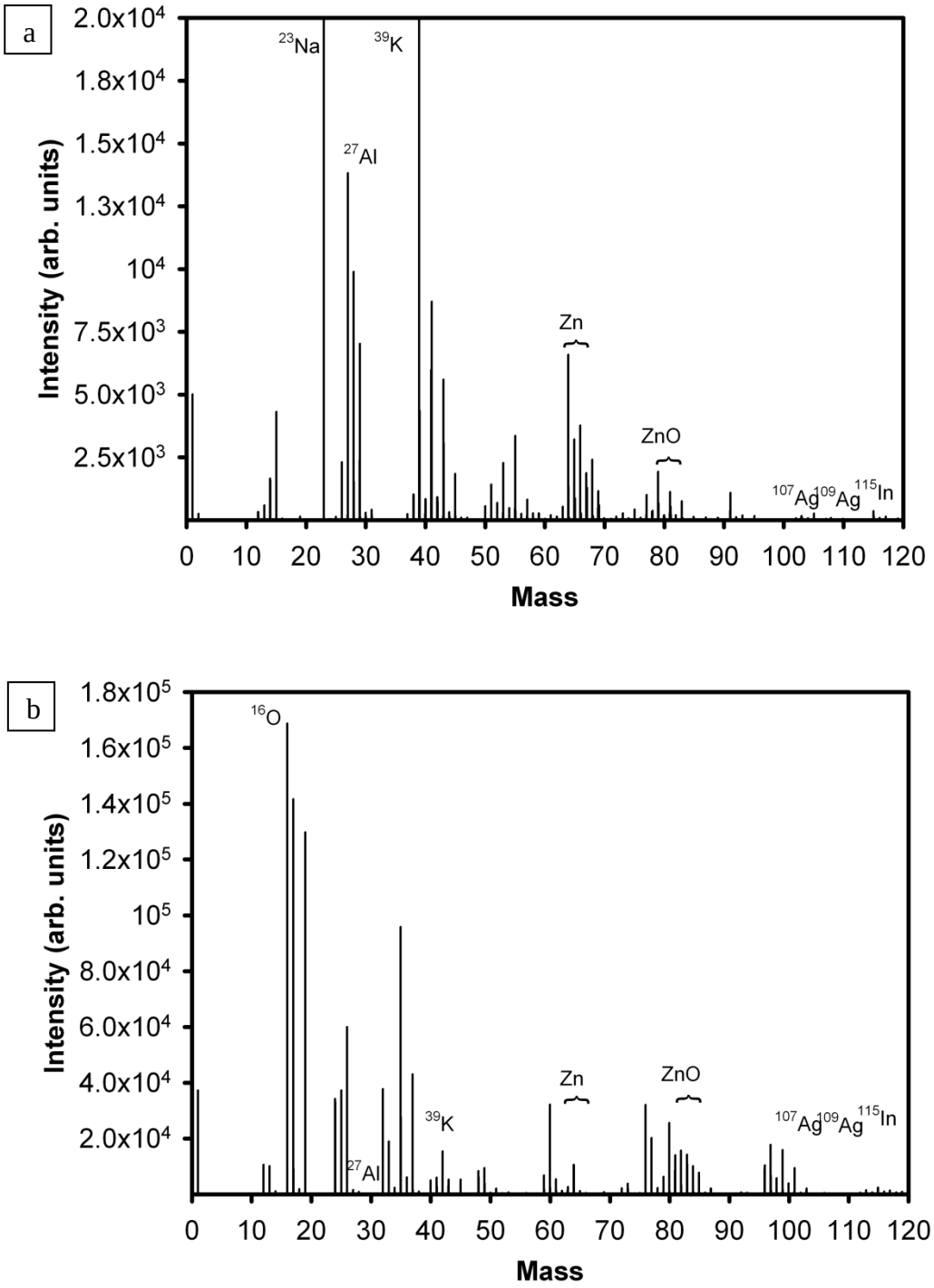

Fig. 4.22. (a) Positive ion (Cs^+), and (b) negative ion (O) mass spectrum for a 1.5×10^{19} Ag atoms/cm^3 doped film grown at 600°C under stoichiometric conditions.

As with static SIMS of the sample surface, depth profiling also did not detect any Ag in this sample, as shown Fig. 4.23. However, In was detected nearer to the interface between the (~ 500 nm) film and the sapphire substrate. The increase of In towards the surface is perplexing. One possibility is that In was incorporated during the short, undoped, HT-ZnO growth, as part of the tri-layer buffer layer process. This is supported by the low temperature PL dominance of the I_9 line for high temperature growth (800°C). Instead, the I_6 line was dominant for lower temperature growth (600°C). The presence of In at the interface suggests that while a high structural quality film can be achieved with the tri-layer buffer layer process, it may be disadvantageous in terms of increased In incorporation.

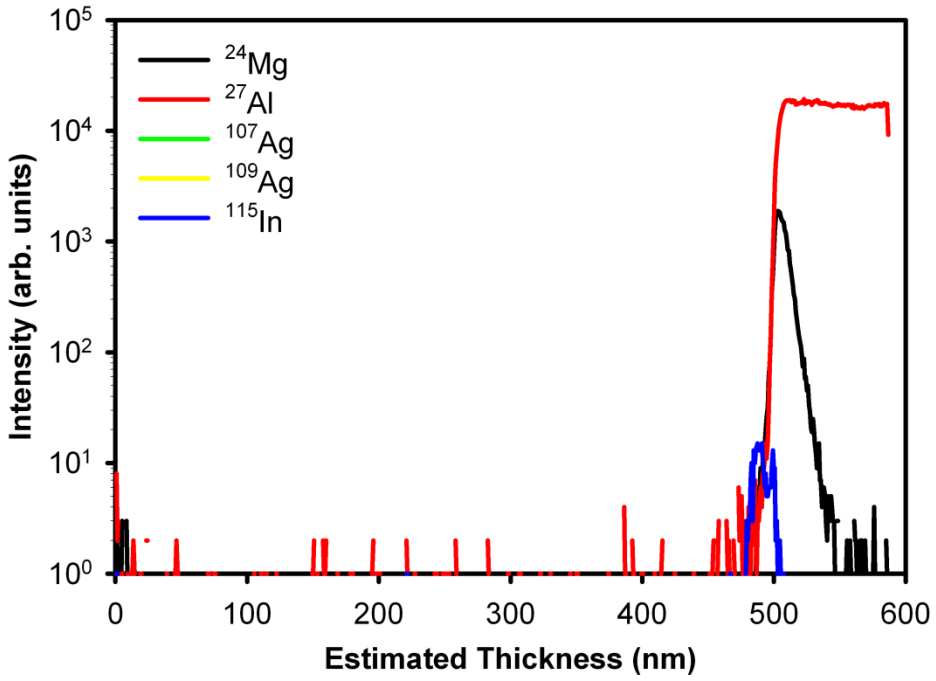

Fig. 4.23. Depth profiling for a 1.5×10^{19} Ag atoms/cm^3 doped film grown at 600°C under stoichiometric conditions, using a positive ion mass spectrum.

Another main trace element detected during the depth profiling was the Al signal. In fact, this signal was one of the dominating signals, which was consistent with low temperature PL suggesting that Al (i.e. I_6 line) was the dominant impurity in this sample. There was also a weak Al signal throughout the entire film, suggesting that there was a process related Al source, possibly from the alumina discharge tube. Furthermore, near the interface between the film and the substrate, there was an increase in the Al signal, compared to the rest of the film. Such an

increase implies diffusion from the sapphire substrate. Therefore, there were multiple sources of Al, consistent with its presence in low temperature PL.

In summary, Ag doping resulted in clear structural, electrical, and optical effects. Degradation in surface morphology were observed at Ag flux above 4×10^{11} atoms/cm^{2}s, and substrate temperatures below 600°C. RBS measurements in conjunction with PIXE found that for a film grown at 600°C, up to 94% of Ag incorporated substitutionally on Zn sites at a Ag flux of 4×10^{10} atoms/cm^{2}s. In addition, Ag incorporation resulted in increased tensile stress, with the lattice constant of ZnO:Ag increasing by 11.3% for the film grown at a Ag flux of 4×10^{11} atoms/cm^{2}s and substrate temperature of 600°C.

Despite the high level of Ag acceptors incorporated, all films were measured to be n-type, with variable magnetic field Hall effect measurements confirming the presence of only one electron population in the measured ZnO:Ag film. However, SIMS did detect significant Al incorporation throughout the film, which may account for part of the electron concentration observed. Nonetheless, films grown at 400°C did exhibit approximately an order of magnitude decrease in electron concentration at a Ag flux of 4×10^{10} atoms/cm^{2}s, compared to its undoped film. Low temperature PL for all films were found to be dominated by donor bound excitons related to In and Al. However, an ionised donor bound exciton emission was observed for the film grown at 400°C with a Ag flux of 4×10^{10} atoms/cm^{2}s, suggesting the formation of compensating acceptors, consistent with Hall effect measurements. While no Ag acceptor related peaks were observed in the low temperature PL, sufficient Ag was found to result in suppression of the defect band. Furthermore, DLTS measurements indicated that Ag acceptors lie at 319 meV above the VBM, consistent with compensating effects observed for growth at 400°C.

Chapter 5

Use of Ag and ZnO as a Superlens Structure

5.1 Background

Current photolithography uses immersion lenses to improve photolithography resolution by increasing the index of refraction of the medium. Immersion lithography essentially involves replacing the gap between the lens and the wafer surface with a higher refractive index material such as water. However, this approach is being limited by the lack of suitable high refractive index materials [88, 192]. Another way to extend the life of optical lithography is by switching to extreme ultraviolet (EUV) lithography. As the wavelengths from EUV light sources are around 13.5 nm [193], this allows for several more generations of transistor scaling following Moore's Law. Still, for this to happen, there remain a number of issues yet to be resolved, such as production line compatible light sources and suitable resists [192, 194].

Therefore, in order for most of the optical lithography setup to be reused, especially at the far lower cost Hg lamp setup, unconventional lenses can be employed. Naturally occurring materials have a positive refractive index. However, it is possible to engineer a metamaterial such that it has a negative refractive index [82, 86]. As explained in Chapter 1, a material can be synthesised such that the diffraction limit no longer exists. Thus, a unique use of ZnO is as a dielectric layer for such a material.

The resolution can be further improved by creating a homogenised stack, such that the whole superlens structure is made up of both the metal and insulator

layers. As each layer becomes thinner, the whole stack becomes more homogenised, such that the stack is characterised by a mixture of the properties of Ag and ZnO, but is neither Ag nor ZnO, creating a type of metamaterial. This chapter provides a detailed discussion of the challenges in implementation of such a structure with a Ag-ZnO stack as the metal-insulator stack, as well as experimental results obtained with these prototype structures.

5.2 Fabrication of Test Patterns

The first step in the manufacture of the superlens was the fabrication of the test pattern. A variety of linewidths was designed as the mask to be written using EBL (Fig. 2.7). Initially, each 10 mm by 10 mm quartz substrate was ultrasonically cleaned in trichloroethane (TCE), acetone and methanol, for 15 minutes each, to remove any organic contaminants. After drying off the remaining solvent with N_2 gas, a monolayer of hexamethyldisilazane (HMDS) was spin coated at 4000 rpm for 1 minute; the methyl groups of the HMDS formed a hydrophobic surface and hence improved resist wetting and adhesion [195]. A 400 nm layer of a negative tone e-beam/deep UV resist (ma-N 2403) was then spin coated onto the substrate at 4000 rpm for 1 minute, and subsequently baked in a convection oven at 95°C for 30 minutes [196].

As quartz is an insulating substrate, EBL will result in feature distortion since the surface will charge up and repel the e-beam. In order to mitigate the charging issue, a thin layer of a conducting polymer, poly(3,4-ethylenedioxythiophene) poly(styrenesulfonate), also known as PEDOT/PSS, was used [94]. The PEDOT/PSS was spin coated at 5000 rpm for 1 minute at a ramp of 2500 rpm/s. (In general, the ramp rate for the spinner should be that required to get up to the desired speed in two seconds as substrates will likely fly off if the ramp rate is too slow.) It should also be noted that the PEDOT/PSS has to be carefully applied to the underlying resist layer as the PEDOT/PSS is hydrophilic and hence does not adhere well to the resist. However, adhesion can be improved by dipping the resist-coated substrate in de-ionised water (DIW) and then drying it with N_2 gas before applying the PEDOT/PSS. The PEDOT/PSS covered substrate was then baked on a hot plate at 80°C for 2 minutes. The resist structure used for creating the test patterns is shown schematically in Fig. 5.1.

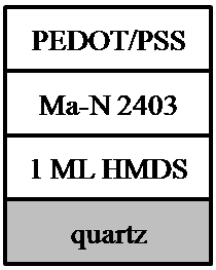

Fig. 5.1. Schematic of the structure for EBL of test patterns.

To determine the optimum dose and developing time necessary for fabrication of the test pattern shown in Fig. 2.7, a series of exposure doses and developing times were performed, and the resultant features examined using SEM. After exposure, the PEDOT/PSS was first removed by leaving the exposed substrate in de-ionised water (DIW) for a few minutes and then blown dry with N_2 gas. The developing time was varied from 40 s to 120 s, using the developer ma-D532. The exposure doses ranged from 50 to 200 $\mu As/cm^2$ using an acceleration voltage of 10 kV and an aperture size of 20 μm. To enable SEM examination of the EBL patterned features, Si substrates were initially employed instead of quartz. However, the entire resist stack was the same to ensure that there was minimal change in parameters between the two different substrates.

In a negative tone resist, the exposed areas (for both photolithography and EBL) are cross-linked to increase its molecular chain length and hence reduce its development rate. That is, the transferred pattern is what will remain after development. The effects of underdeveloping or overdeveloping on the pattern defined on a negative tone resist are shown in Fig. 5.2. Underdeveloping results in some of the resist remaining on the substrate after development, creating a “tail” at the base of the feature. This results in an overall enlarged pattern as the feature now includes this “tail”. On the other hand, overdevelopment will result in increased resist dissolution on the top of the pattern, due to the isotropic nature of developing. Hence overdeveloping will result in a triangular, instead of the desired rectangular, line feature. Furthermore, the feature size will be reduced overall as well. While overdeveloping does mean that a smaller feature can be achieved than the feature defined, it also increases the lift-off difficulty. Deposited metal will settle on the diagonal edges, preventing the lift-off solution from getting into contact with the resist and dissolving it.

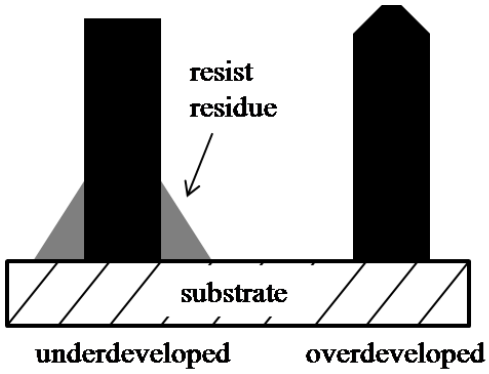

Fig. 5.2. Effects of underdeveloping and overdeveloping on a negative tone resist, as seen in a cross section.

SEM images of a 100 nm line feature exposed at 100 μAs/cm^2 and developed for various times are shown in Fig. 5.3. As expected, for short developing times (Fig. 5.3(a)), there was clearly a "tail" of resist remaining after 40 s developing. With sufficient developing (80 s) (Fig. 5.3(b)), no discernible "tail" was observed. Furthermore, with the higher developing time of 100 s, the feature had reduced in size (Fig. 5.3(c)), indicating overdevelopment. The minimum developing time was therefore 80 s, and was applicable to larger features as well, as shown in Fig. 5.4.

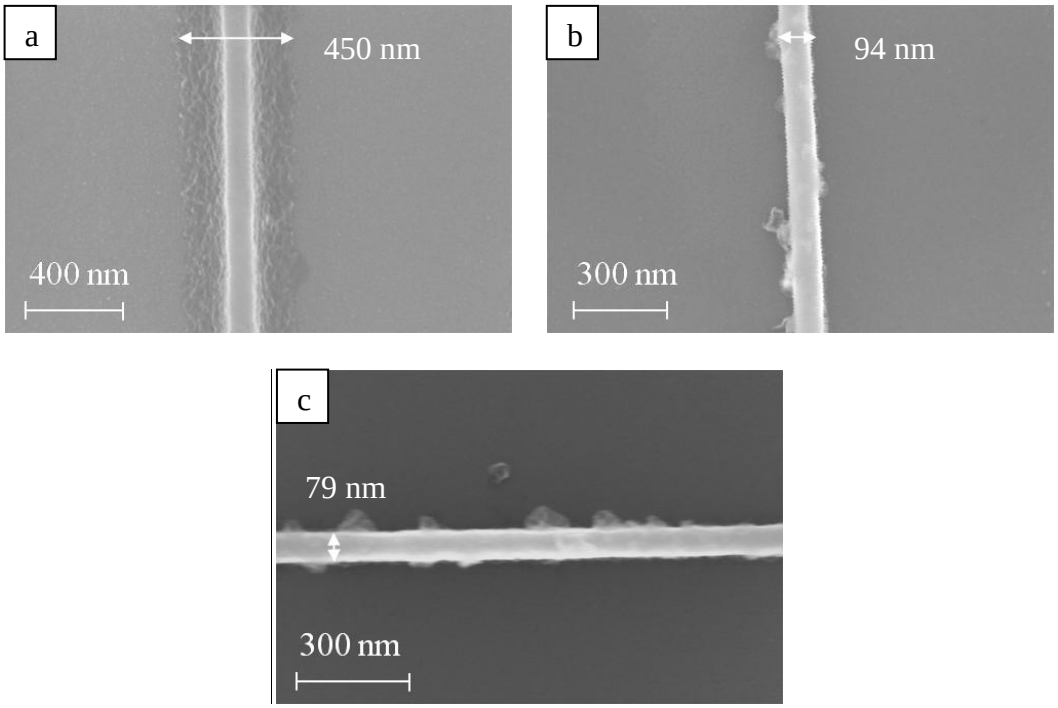

Fig. 5.3. SEM images of a 100 nm line feature exposed at 100 μAs/cm^2 and developed for (a) 40 s, (b) 80 s, (c) 100 s.

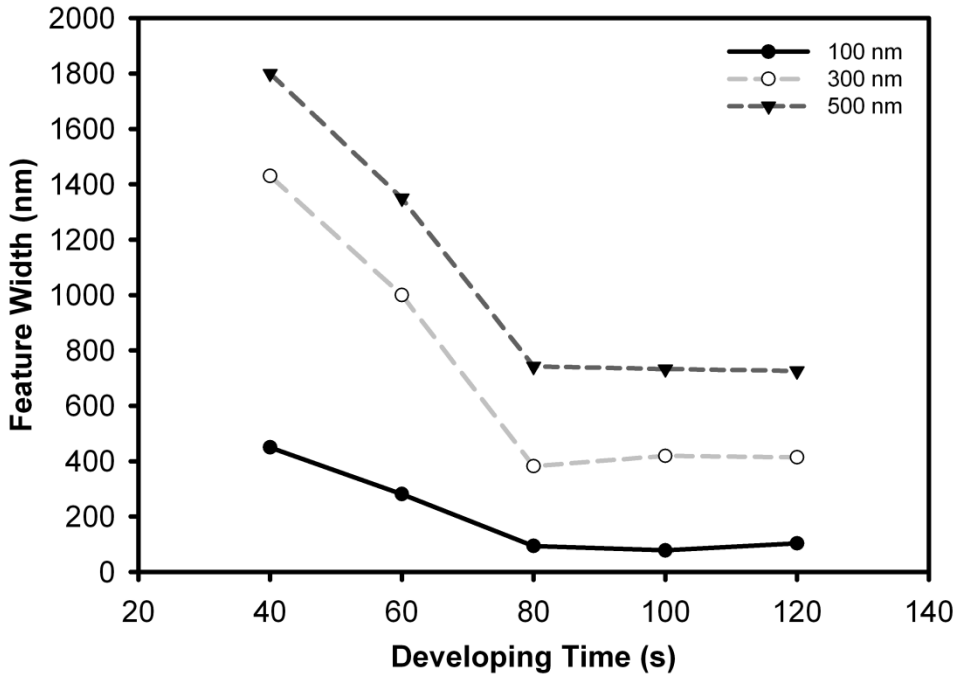

Fig. 5.4. Total width of features measured using SEM for 100 nm, 300 nm and 500 nm line features exposed at 100 μAs/cm^2 and developed using ma-D 532 for various developing times.

With a suitable developing time determined, the next step was to determine the optimum exposure dose. If a resist is underexposed, the cross-linking will not occur completely through the resist, resulting in soluble areas under the insufficiently exposed area being dissolved when developed. Such underexposure results in either no feature present or a significantly reduced feature (Fig. 5.5(a)). The absence of the 100 nm line feature for doses below 70 μAs/cm^2 (Fig. 5.6) suggests that a dose of 70 μAs/cm^2 was the minimum exposure dose required to ensure that the exposure has occurred throughout the depth of the resist.

As the exposure dose is increased, the overall feature size increases due to overexposure, as shown in Fig. 5.6. When a resist is overexposed, the feature is enlarged due to the polymer cross-linking over a larger area than that originally defined (Fig. 5.5(c)). The 100 nm line features are fairly consistent from 80 to 130 μAs/cm^2, whereas there is a steady increase in the overall width of features larger than 300 nm. It appears that different doses are required to properly expose different line widths. There is overlapping exposure on the resist for each beam size location due to overexposure and/or non-ideal focusing of the beam. This leads to a faster exposure rate for larger features. Therefore, the larger width obtained for larger target feature sizes are due to overexposure at the same

exposure dose. Hence, the optimum exposure dose for the 100 nm line feature, which is the target width for subsequent experiments, is 80-100 μAs/cm^2 ((Fig. 5.5(b)).

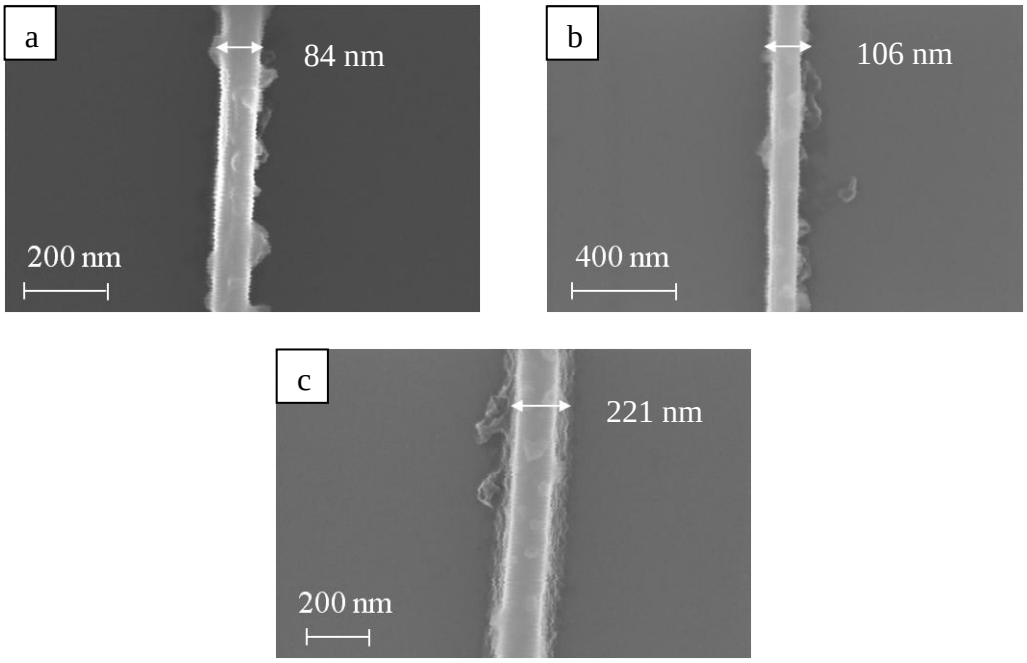

Fig. 5.5. SEM images of a 100 nm line feature exposed at (a) 70; (b) 100; and (c) 200 μAs/cm^2. Note scale change for (b).

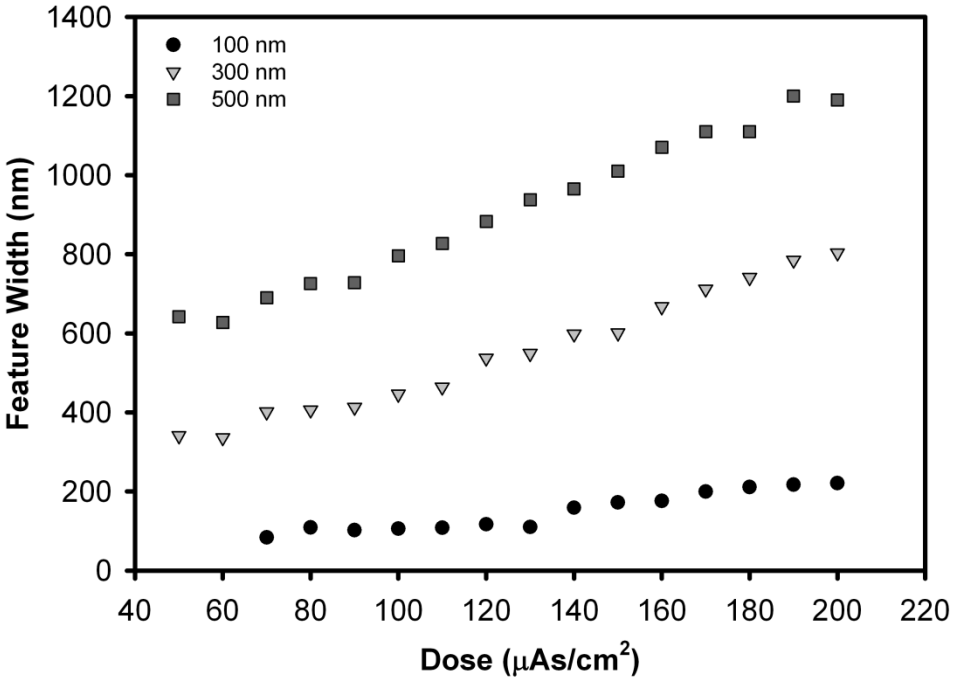

Fig. 5.6. Total width of features measured using SEM for 100 nm to 500 nm line features exposed at various doses and developed using ma-D 532 for 80 s.

Now that the optimum dose and developing time has been established, the next step is to use these parameters on a resist stack on quartz. Approximately 50 nm of Cr is evaporated onto the developed substrate, which is then soaked in acetone to lift-off/remove the Cr covered resist. This then leaves behind a mainly Cr covered substrate, with the 100 nm apertures appearing as areas that have been previously covered by the developed resist. Unfortunately, the 100 nm feature did not lift-off in a reproducible way in the first set of experiments, as shown in Fig. 5.7. Furthermore, the sidewalls of the Cr apertures are jagged and non-uniform.

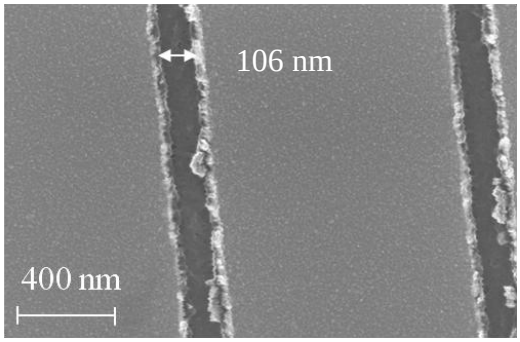

Fig. 5.7. SEM image of a mask pattern after Cr lift-off, using an exposure dose of 100 μAs/cm^2 and a developing time of 80 s.

It should be noted that the Cr is deposited via e-beam evaporation as it is more anisotropic than the isotropic nature of sputtering. Sputtering results in coated sidewalls, preventing successful lift-off. The Cr target used during e-beam evaporation was Cr granules. The Cr granules need to be ramped up carefully for a growth rate of 0.03 to 0.06 nm/s as faster growth rates result in spitting, increasing the roughness of the deposited Cr film.

It is possible that the age of resist and developer solutions could be the cause of the issues observed thus far. These particular resists and developers typically have a limited shelf life of 6 months and 12 months, respectively. The set of solutions employed to this point were in fact several years old. As a photoresist ages, the formation of particles is more likely due to the precipitation of the photo-active compound. This tends to lead to a decrease in the development rate and reduced adhesion of the resist. The degradation of the photo-active compound also results in decreased resolution [195].

Developers also degrade over time, mainly due to the absorption of CO_2 from air. This leads to decreased developer sensitivity and hence decreased development rates. A degraded developer also has reduced selectivity, resulting in dissolution of both exposed and unexposed regions [195]. Furthermore, absorption of CO_2 from air is accelerated due to the transfer of solutions to a smaller 100 mL bottle, which is opened and closed regularly. Therefore, fresh solutions were purchased to improve the fabrication of these features, assuming that the problems encountered were due to the age of the resist and developer.

Upon repeating the same procedure using these fresh solutions, it was found that the previously optimised parameters were no longer suitable. Therefore, a new set of exposure dose and developing time experiments were performed to find the optimum parameters. The substrates used were initially Si, followed by quartz once initial parameters were determined. For the patterns fabricated on quartz, a thin Au film was sputtered onto the developed surface to enable the features to be imaged using SEM. Figure 5.8 shows that the most consistent developing time to produce 100 nm line features was around 30 to 40 s for an exposure dose of 20 $\mu As/cm^2$. At a higher dose of 30 $\mu As/cm^2$, the features were overexposed and resulted in features significantly larger than the target width of 100 nm. In addition, the line widths did not follow a consistent trend with increasing developing times at the higher exposure dose.

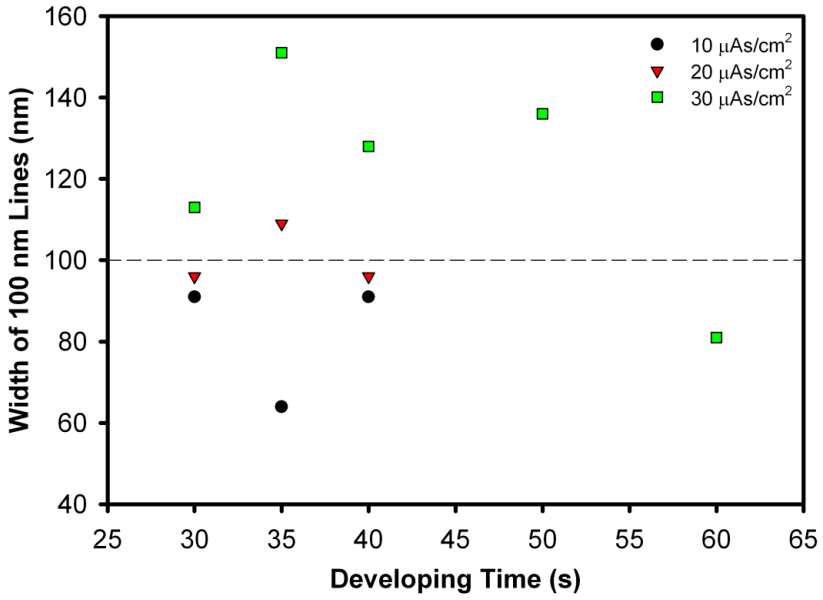

Fig. 5.8. Total width of 100 nm line features exposed at different doses and developed using ma-D 525 for various developing times. The dashed line indicates the target linewidth of 100 nm.

With the previous older resists, the optimum dose was found to be 100 μAs/cm^2. However, Fig. 5.9 shows that 100 μAs/cm^2 is now significantly overexposed, with the feature size almost doubled at that exposure dose. Applying a linear fit to Fig. 5.9 results in the linear relationship

$$\text{Width} = 74.1 + \ 1.3 \times \text{Dose} \tag{5.1}$$

where width and dose are given in nanometre and μAs/cm^2, respectively. Solving Eq. (5.1) yields an optimum dose of 20 μAs/cm^2 to obtain the desired 100 nm line feature.

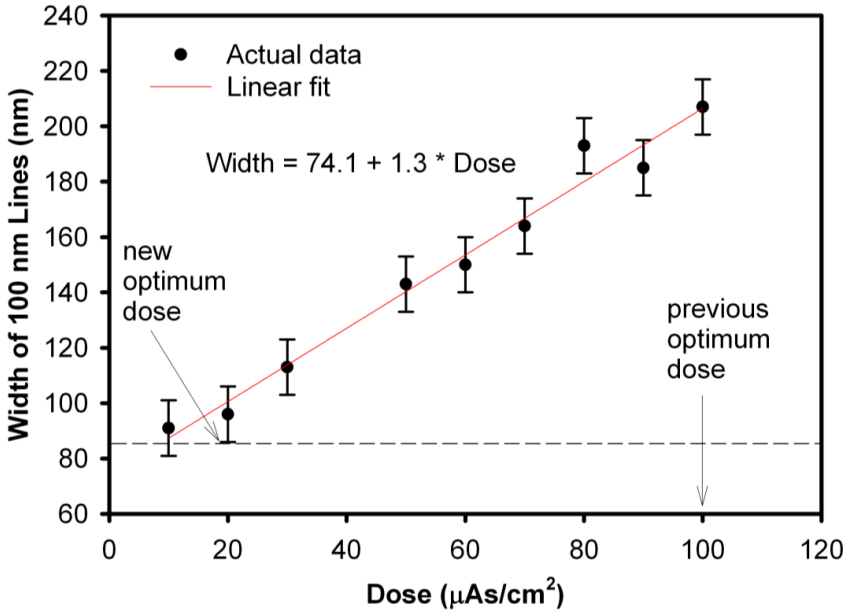

Fig. 5.9. Total width of 100 nm line features exposed at various doses and developed using ma-D 525 for 30s. The dashed line indicates the target linewidth of 100 nm.

However, even with the new set of solutions, the previously observed lift-off issues of jagged edges (similar to Fig. 5.7) and occasional failure to lift-off remains. One possible reason for the lift-off difficulty is that the ma-N 2403 is mainly used as an etching mask due to its vertical sidewalls. One possible means of overcoming this is by using a bilayer resist structure. Figure 5.10 shows the basic process for a general bilayer stack structure using MicroChem PMGI (SF5) resist. Initially, an estimated monolayer of HMDS is spin coated onto the quartz substrate at 4000 rpm for 1 minute. Then a 150 nm thick PMGI layer is spin coated at 4000 rpm for 1 minute and baked on the hot plate at 95°C to 190°C for 2

minutes. After that, the imaging resist is spin coated onto the PMGI and prebaked. After pattern formation via EBL, both the imaging resist and the PMGI are developed with the same developer. This creates a bilayer resist stack. After depositing the thin film onto the pattern, the bi-layer stack is removed using any of the typical lift-off solvents, such as acetone. The PMGI layer enables film deposits on the sidewall of the imaging resist to be removed, resulting in a cleaner lift-off.

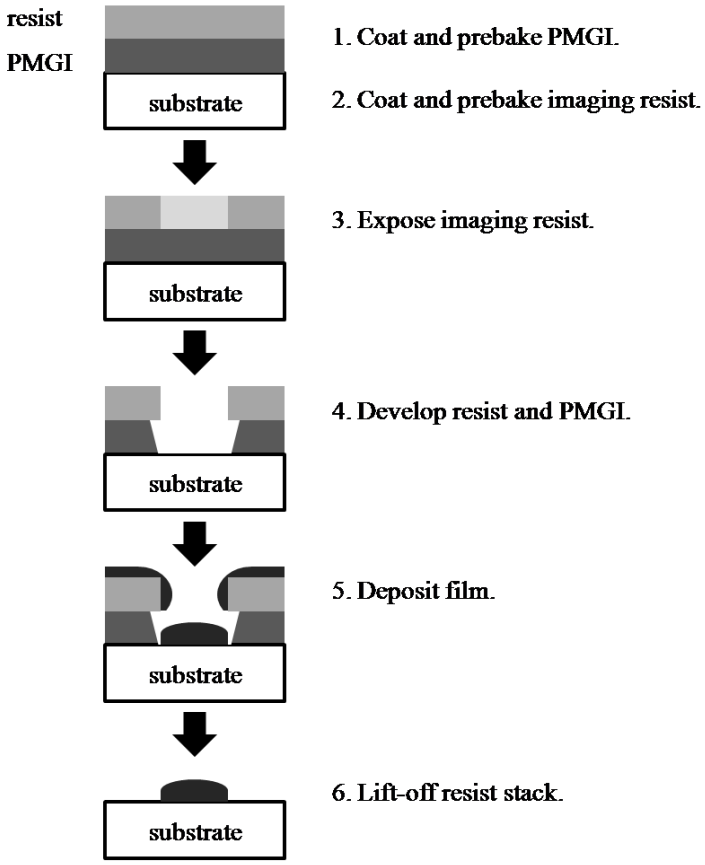

Fig. 5.10. Lithography process using bilayer resist structure.

As the isotropic dissolution and undercut of the PMGI is primarily dependent on the bake temperature, the PMGI bake temperature and developing time were varied in a series of experiments. The typical resultant feature when employing the bilayer stack structure is shown in Fig. 5.11. Note that the substrate is Si and hence what has been imaged is the actual resist stack after exposure and development. Figure 5.11 shows that while the feature has been correctly defined at 100 nm wide, there is still residual PMGI remaining after developing for 40 s. The incomplete development resulted in the actual feature being 285 nm wide, instead of 100 nm.

According to the PMGI datasheet, the recommended prebake temperature range is 150°C to 190°C. The higher the prebake temperature, the slower the dissolution of the resist, resulting in less undercut. It is not recommended to go above 190°C due to that being the glass transition temperature. It is also not recommended to go below 150°C as the resist will not be soft-baked sufficiently, resulting in high dark erosion and hence less well defined features. However, bake temperatures above 150°C were not attempted as the feature sizes achieved at 150°C were already too wide.

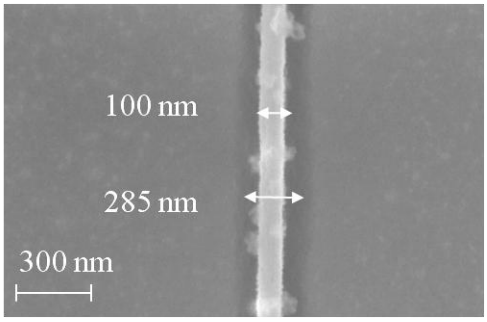

Fig. 5.11. SEM image of bilayer resist stack with the PMGI layer baked at 150°C and subsequent exposure and development at 20 μAs/cm^2 and 40 s, respectively.

At the lowest recommended PMGI bake temperature of 150°C, the overall feature size is 254 nm after 45 s developing, as shown in Fig. 5.12. However, after 50 s developing, the "100 nm" line has completely disappeared. A similar trend of decreasing width and then completely dissolved 100 nm line feature can also be seen for other bake temperatures. As the PMGI has isotropic dissolution, it is not unexpected that a 100 nm feature size was not achieved. For example, at 130°C the feature size is around 200 nm. If one assumes an isotropic dissolution, then removing the extra 100 nm resist from the outer edge will also result in removal of the resist under the feature. Hence, a 100 nm line feature will "lift-off" at the same time as the PMGI resist. Lower bake temperatures were not attempted as the ma-N 2403 resist is baked at 95°C and hence the PMGI will be indirectly baked at 95°C at the very least. The inability to control the dissolution rate of the PMGI, and the isotropic nature of dissolution, makes this bilayer structure unsuitable for this purpose. However, should there be a desire for larger features, Fig. 5.13 shows that for 300 nm linewidths, the bilayer is more forgiving in terms of its dissolution rate.

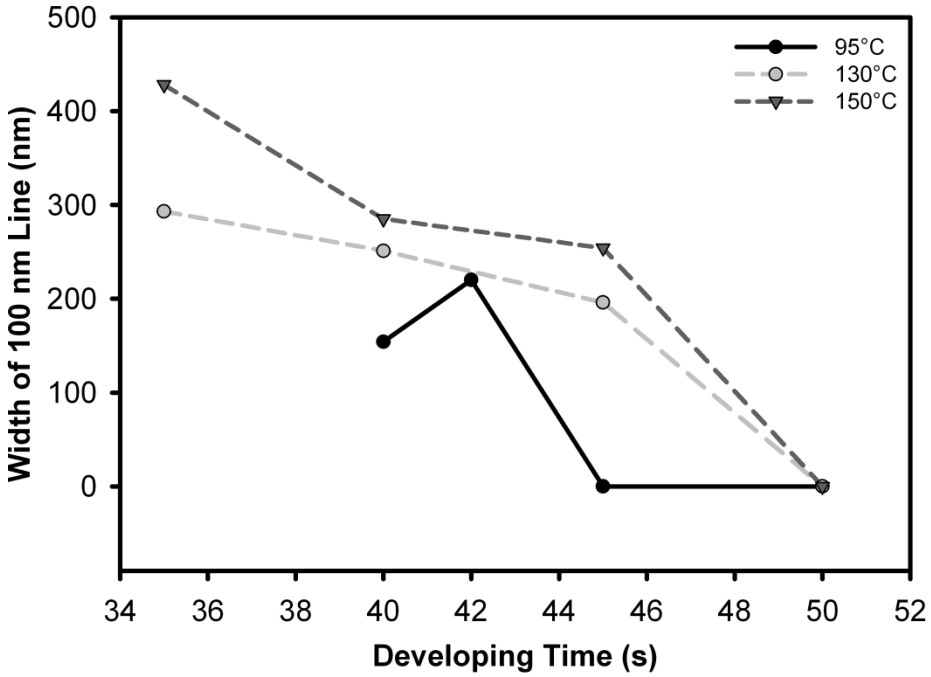

Fig. 5.12. Effective width of 100 nm line features exposed at 20 μAs/cm^2 and developed using ma-D 525 for various times.

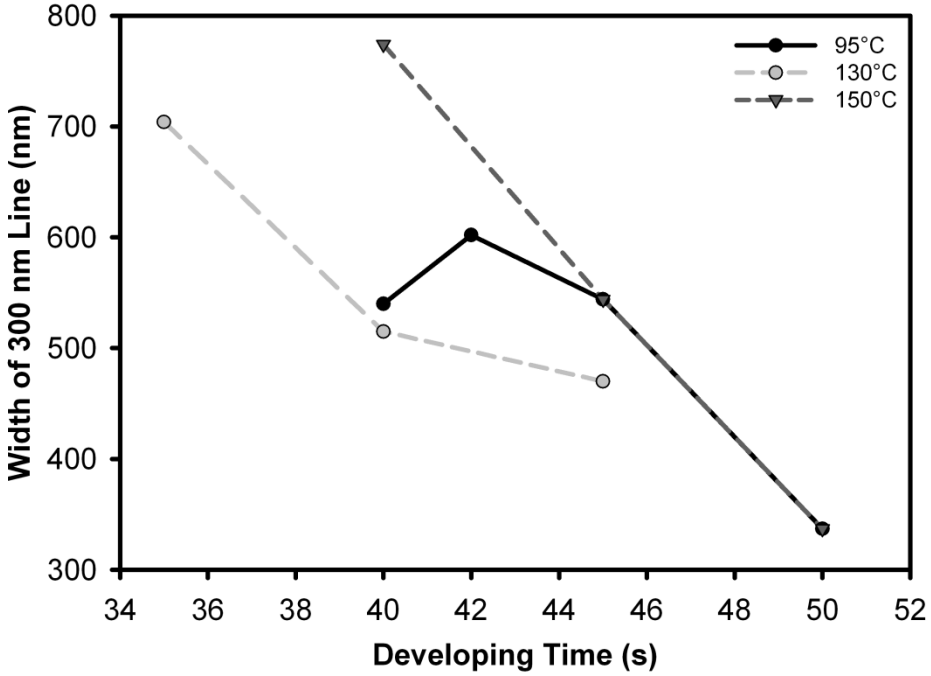

Fig. 5.13. Effective width of 300 nm line features exposed at 20 μAs/cm^2 and developed using ma-D 525 for various times.

Therefore, the originally developed single layer resist stack was used for the rest of the lithography work. To create smaller test patterns, it is necessary to move from an area exposure to a single line exposure. In an area exposure, a feature is defined by a finite area. The software then calculates the height and width of the

feature in terms of the beam size (which is approximately 20 nm to 30 nm in this thesis). The pattern is then exposed in terms of those beam features. In a line exposure, also known as a single line pass, the feature is defined as a "zero width" line. The width of the line is then solely determined by the exposure time. In theory, the absolute resolution possible is limited by the beam size.

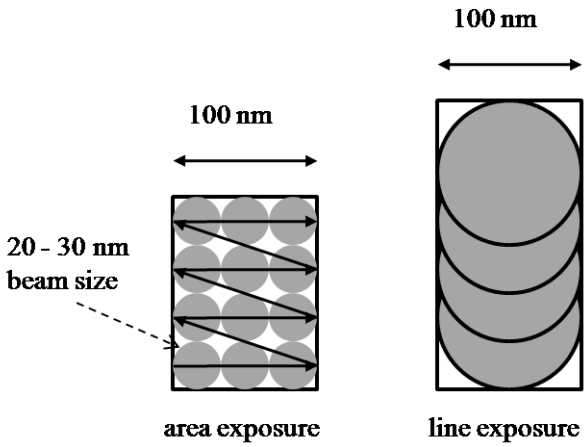

Fig. 5.14. Mechanisms of area and line exposures.

Therefore, a series of lines at different exposure doses was fabricated and examined to determine the relationship between the exposure dose and the resultant line width. At a developing time of 35 s, doses below 195 pAs/cm^2 resulted in exposure of linewidths below 100 nm, as shown in Fig. 5.15. It is possible to define even smaller linewidths by using a longer developing time of 40 s, with the smallest feature defined being 57 nm.

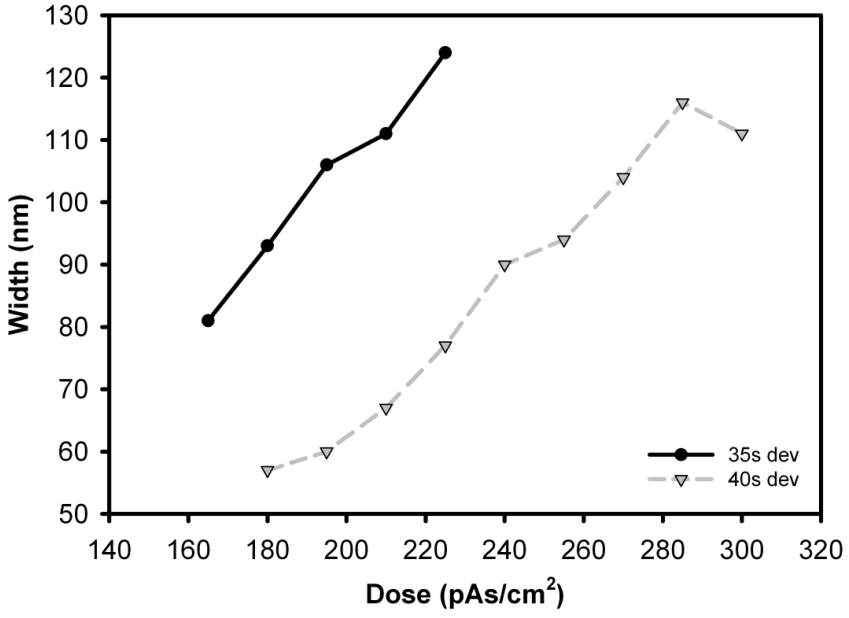

Fig. 5.15. Width of line exposures at various doses and developing times.

As it is still possible for under/overexposure and under/overdevelopment to occur, the ultimate test of the smallest feature size possible is the successful Cr lift-off. Fig. 5.16 shows that while it is possible to write smaller features, the resist stack does not lift-off cleanly due to the overexposure or overdevelopment that can occur. This is most likely due to the spreading of the beam inherent in line exposures. Such beam spreading results in a tapered line feature, which is detrimental to subsequent lift-off processes. Hence, the area exposure method is more suitable for this process. Therefore, the optimum mask pattern fabrication parameters are an area exposure dose of 20 $\mu As/cm^2$ and a developing time of 40 s.

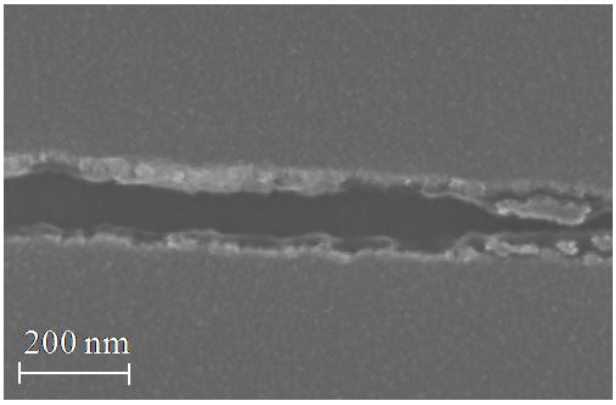

Fig. 5.16. SEM image of a line created by a line exposure dose of 240 pAs/cm^2 and developed for 35s. 50 nm of Cr has been deposited on the quartz. The aperture is the gap in the Cr as previously defined by EBL.

5.3 Minimising the Sidewall Deposit

The next step is to check the height and width of the fabricated mask patterns. Due to the sizes involved, AFM was used instead of profilometry. It should be noted that it is necessary to switch to a hi-res tip in order to adequately image the trenches, due to the existence of a sidewall angle on conventional tips. While the height information will be inaccurate with the conventional tip, it is still sufficient to detect the existence of those features, as well as to indicate the degree of sidewall deposition, as shown in Fig. 5.17.

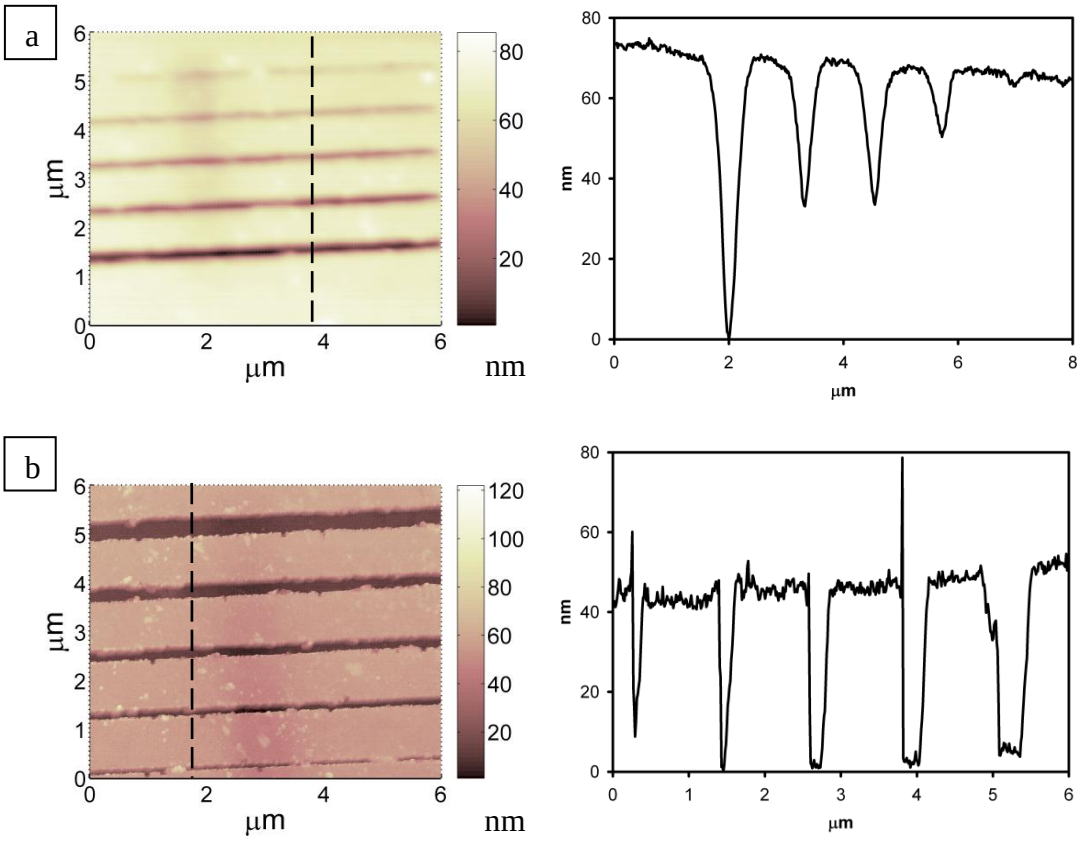

Fig. 5.17. Differences in AFM scans using (a) a conventional tip, and (b) a hi-res tip, on the same features. The dashed line indicates the location of the side view.

Typical SEM images are shown in Fig. 5.18. The 100 nm feature has successfully lifted off as a 101 nm feature (Fig. 5.18(a)). However, the other line features are typically around 50 nm larger than their intended feature size (Fig. 5.18(b) to (f)). As the goal is ultimately fabricating 100 nm line features, the deviation of larger features from their target width is not a major concern. Nevertheless, the incomplete sidewall lift-off is clearly visible even in the smallest features (Fig. 5.19.). However, the sidewall deposits do appear to decrease as feature size decreases.

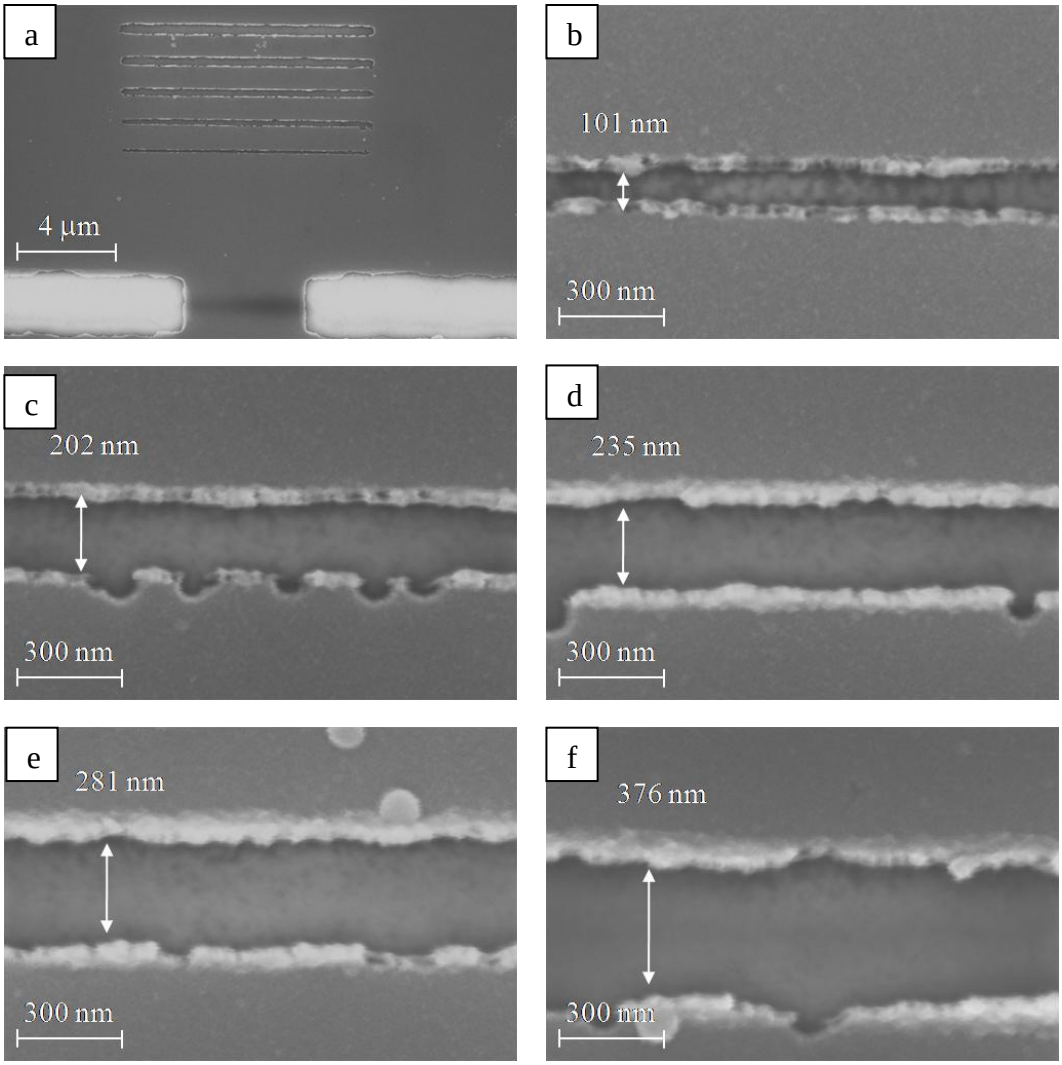

Fig. 5.18. SEM images of mask pattern fabricated using optimum parameters. (a) All 5 lines. (b) 100 nm line, (c) 150 nm line, (d) 200 nm line, (e) 250 nm line, (f) 300 nm line.

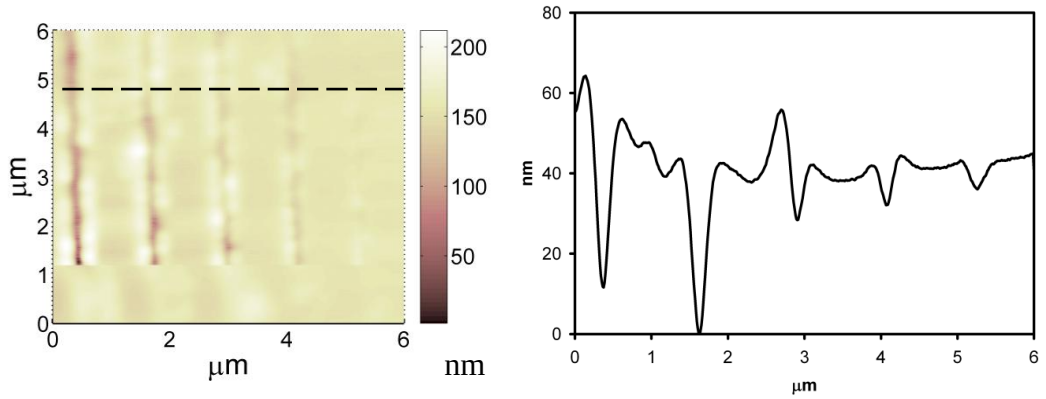

Fig. 5.19. AFM cross section of the structure in Fig. 5.18(a). The dashed line indicates the location of the side view.

It is possible to limit the sidewall deposition, as shown in Fig. 5.20. The AFM image in Fig. 5.21 confirms that there is hardly any Cr protruding out of the sides

of the apertures. However, the features are significantly larger than expected, with the exception of the 100 nm line feature in Fig. 5.20(b).

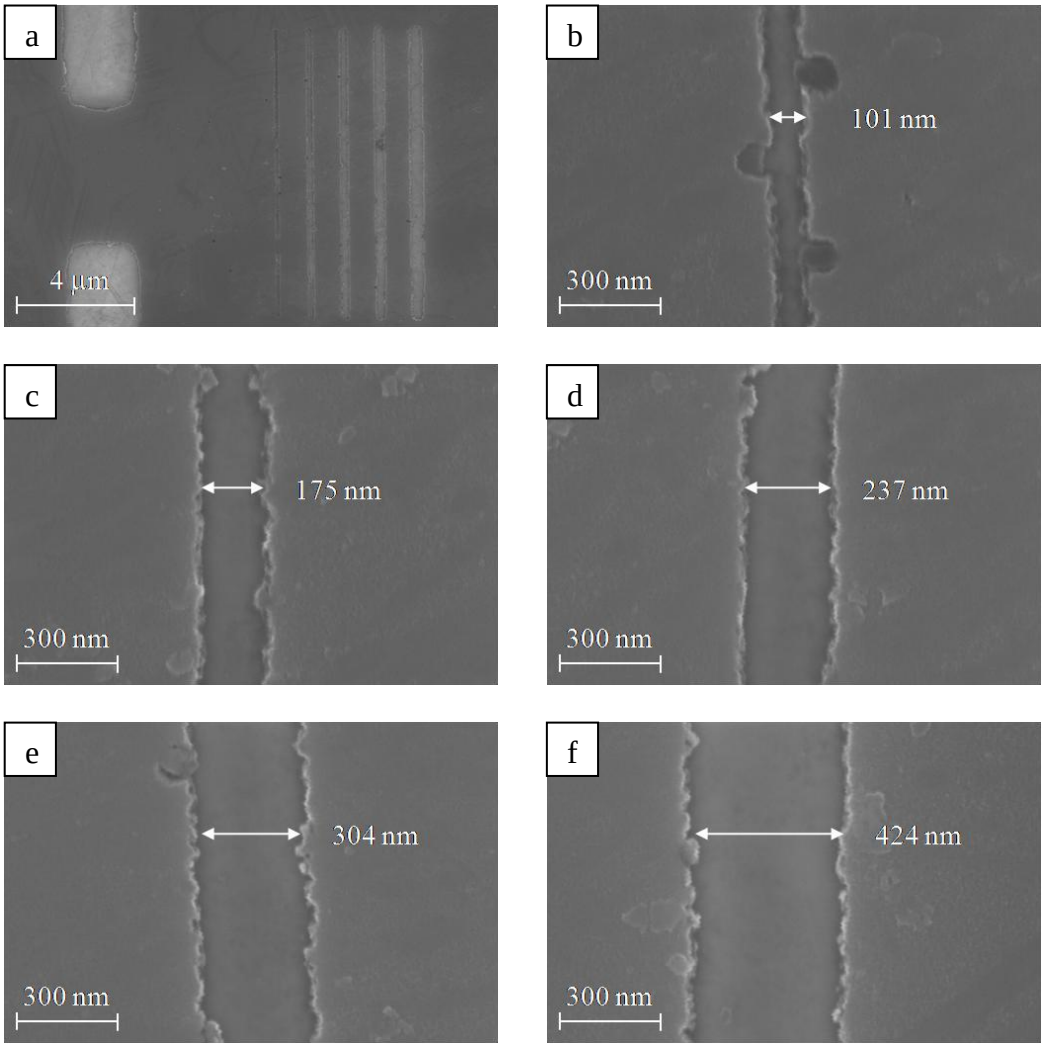

Fig. 5.20. SEM images of mask pattern fabricated using optimum parameters, but with no sidewall deposits. (a) All 5 lines. (b) 100 nm line, (c) 150 nm line, (d) 200 nm line, (e) 250 nm line, (f) 300 nm line.

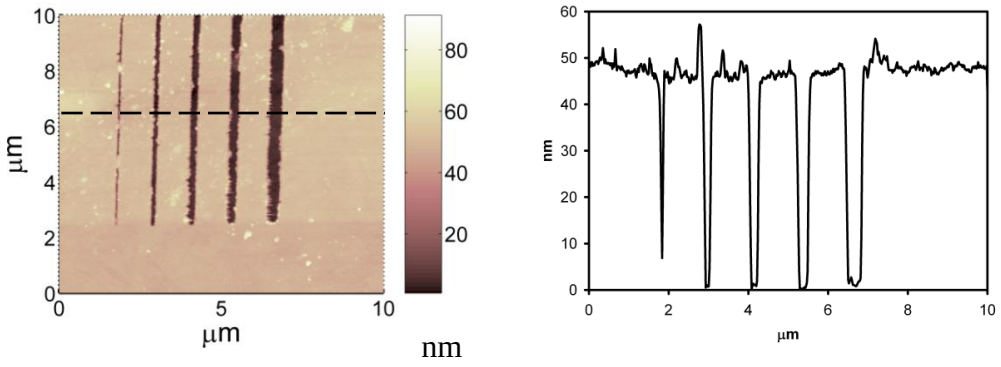

Fig. 5.21. AFM cross section of the structure in Fig. 5.20(a).

To investigate if it is possible to minimise the sidewall deposition through the position of the substrate during e-beam evaporation, several samples were placed at various locations on the substrate holder. Sample A is placed directly above the target, whereas samples B to D are placed at various positions away from that line-of-sight (Fig. 5.22).

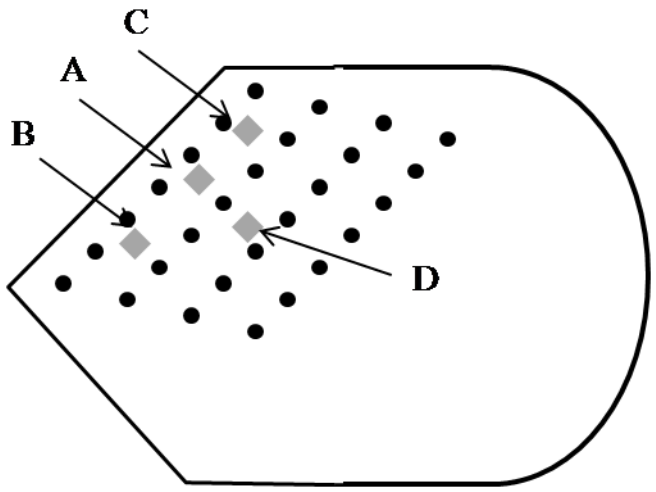

Fig. 5.22. Sample positions on substrate holder for e-beam evaporation. Sample A is directly above the crucible containing the Cr granules.

The sidewall build-up is minimised when the sample is in direct line-of-sight with the target (Fig. 5.23(a)). This is expected since evaporation tends to be anisotropic and hence is less likely to deposit on the sidewalls. There is slightly more sidewall build-up away from the line-of-sight (Fig. 5.23(b) and (c)). The increase in the build-up is likely due to some of the resist sidewall not being parallel to the evaporation path. This means that there is metal deposition on the sidewalls exposed to the evaporation path. For a sample that is significantly far away from the line-of-sight of the evaporation (Fig. 5.23(d)), the build up is more severe on one side. This is consistent with much greater surface area being exposed for deposition on one side when compared to the direction of the evaporation. Since the planarisation of the fabricated mask pattern will be limited by the sidewall build-up, the planarisation layer must be at least 50 nm thick. Furthermore, the sample should be located in direct line-of-sight for Cr deposition to minimise the sidewall build-up. It should be noted that the lack of sidewall build-up shown in Fig. 5.21 cannot be reproduced. It is possible that the sample position was at precisely the right location for that particular negligible sidewall deposition. The

most reproducible result that minimises sidewall deposition appears to be placing the samples in what can be perceived as the direct line-of sight.

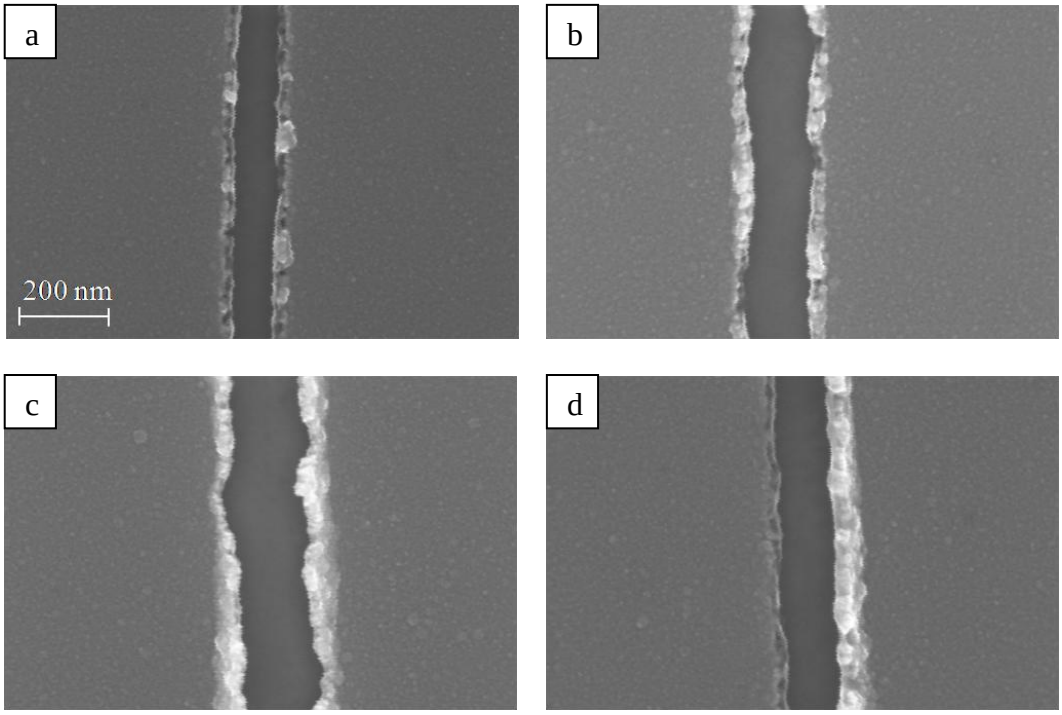

Fig. 5.23. SEM images of samples at position (a) A, (b), B, (c) C, and (d) D. Sample A was located directly line-of-sight of the evaporation. Samples B and C were located slightly away from the line-of-sight of the evaporation. Sample D was located far away from the line-of-sight of the evaporation.

5.4 Planarisation of Mask Patterns

As found previously in Section 5.3, the minimum planarisation layer must be at least 50 nm to ensure that the Cr layer is completely planarised. The planarisation layer used is poly(methyl methacrylate) (PMMA), which has high transparency to the UV wavelengths to be used during imaging experiments. A planarised layer for subsequent Ag and ZnO growth is crucial to ensure that those layers have low roughness.

Fang et al. [88] used an A4 PMMA (495 kg/mol) from Microchem Inc. A 1 μm thick PMMA layer was created via multiple spin-coatings of the PMMA layer. A Tegal plasma asher was then used to O_2 plasma etch the PMMA down to 40 nm, using several etching and measurement steps. The PMMA was finally planarised by reflowing the PMMA above its glass transition temperature; Fang et al. reported achieving an rms surface roughness of 0.5 nm for the final layer.

Melville [92] also used PMMA as a planarisation layer. A solution of 4% PMMA (495 kg/mol) was spun several times at 4000 rpm for a thickness of 150 nm. The PMMA was then baked overnight at 185°C to reflow the PMMA. Using RIE, the PMMA was O_2 plasma etched to 35 nm. The etching was done in several steps to minimise the substrate heating since an insulating substrate poorly dissipates the heat from the etching process. The rms roughness achieved was 0.4 nm.

In this thesis, the process used for the PMMA layer deposition is similar to that used by Melville [92]. A solution of 5% LMW PMMA dissolved in chlorobenzene was spin coated twice at 6000 rpm for 1 minute each, resulting in a thickness of 150 nm to 180 nm per layer. Each layer was baked at 185°C for 30 minutes to reduce the solvent content of the layers. The PMMA was then thinned using RIE, with the parameters in Table 5.1. It should be noted that two etches were performed for 15 s and then paused for 5 minutes, for each etch. The etching sequence used minimises the heating caused by the etching, as heating can change the etch rate. As the etch rate does not vary evenly with this process (0.3 to 8 nm/s with a typical etch rate of 1.47 nm/s), the thickness of the PMMA was measured by generating crude EBL patterns after each etching pair. The PMMA was coated with PEDOT/PSS to reduce the charging and steps were patterned near the features, which were then measured with the profilometer after removing the PEDOT/PSS and developing the exposed region.

Table 5.1. RIE etching parameters.

Pressure	O_2 flow rate	RF Power	Temperature	Electrode	Time
800 mTorr	40 sccm	100 W	295K	SiO_2	15 s

The RIE etch/EBL measurement sequences were repeated until the PMMA was at the desired 50 nm. Typical roughness was around 7.3 nm rms for a 1 μm × 1 μm scan (Fig. 5.24(a)). The sample was then left overnight in the 185°C oven to reflow the PMMA and decrease the roughness to 1.5 nm rms for a 1 μm × 1 μm scan (Fig. 5.24(b)). The inhomegeneity still present after overnight baking may be due to the large variety of PMMA particle sizes in the in-house created PMMA solution. The variation in particle sizes may also contribute towards anistropic etching. Hence for future work, it may be worth exploring a commercial grade

PMMA solution with more uniform particle size to encourage isotropic etching and low roughness PMMA films.

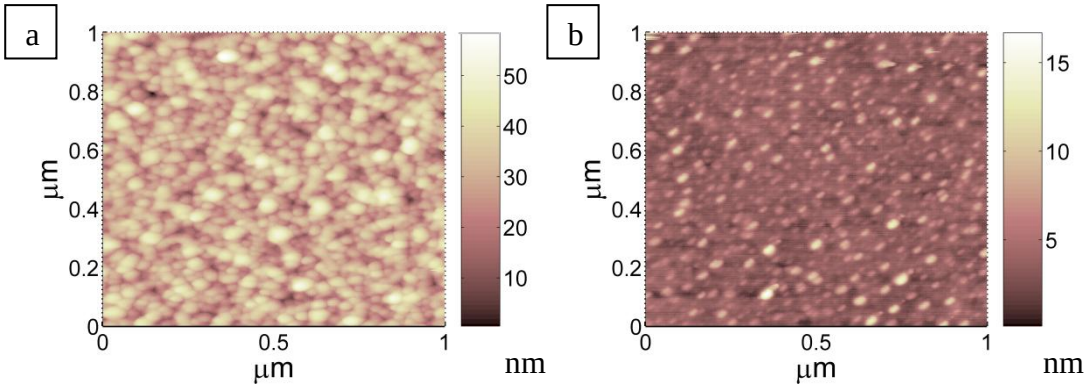

Fig. 5.24. AFM images of the sample after (a) RIE etching, (b) baking overnight.

Initial experimental results involved planarising the PMMA over the Cr apertures via an RIE based process. By increasing the process pressure, the roughness of the PMMA after etching appears to decrease. This is not unexpected since the higher the process pressure, the more readily collisions occur and over shorter length scales. Hence, the etching process becomes more isotropic at higher pressures.

An alternative option for etching the PMMA during the planarisation process is by using a plasma asher. As with an RIE process, an RF generated plasma is used to ionise O_2 into oxygen ions. Plasma ashing is typically used to remove residual resist from a substrate due to its isotropic nature. In contrast, the primary application of RIE is in formation of trenches, which require anisotropic etching. The anisotropic nature of RIE comes from the directional nature of ion bombardment. In contrast, plasma ashers create a high density plasma encompassing the substrate, resulting in isotropic etching. The plasma ashing parameters using the Emitech K1050X are summarised in Table 5.2. As with RIE etching, plasma etching was also done in multiple steps. The etch rate was approximately 1 nm/s and hence about 50 to 60 nm of PMMA was removed for every 1 minute cycle. It should be noted that the etch rate can also sometimes double to 2 nm/s. Therefore, the PMMA thickness was measured using AFM after each etch step. The step height in the PMMA was created by scratching the surface. The sample was also baked at 185°C for 30 minutes, after each etch step, to allow the PMMA to reflow. Another advantage of plasma etching over RIE is that the process is significantly faster with the plasma asher due to the shorter

pump down time. The RIE pumps down the vacuum to between medium and high pressure, whereas the plasma asher pumps down to low pressures only. The difference was a total of several minutes for the plasma asher, compared to up to two hours with the RIE, for each etching step.

Table 5.2. Plasma asher parameters for creating a planarised PMMA layer.

Pressure	O_2 flow rate	RF Power	Temperature	Time
0.9 mbar	5 sccm	100 W	300K	1 min

Some typical AFM images of the sample after planarisation using the plasma asher are shown in Fig. 5.25. After multiple etching and baking steps, the resultant roughness was 1.3 nm, with none of the underlying Cr apertures observed. The PMMA was typically thinned down to 50 nm thick. It should also be noted that the PMMA after plasma ashing was smoother (1.3 nm rms roughness) than after RIE etching (1.5 nm rms roughness). Hence, plasma ashing was the PMMA planarisation method of choice.

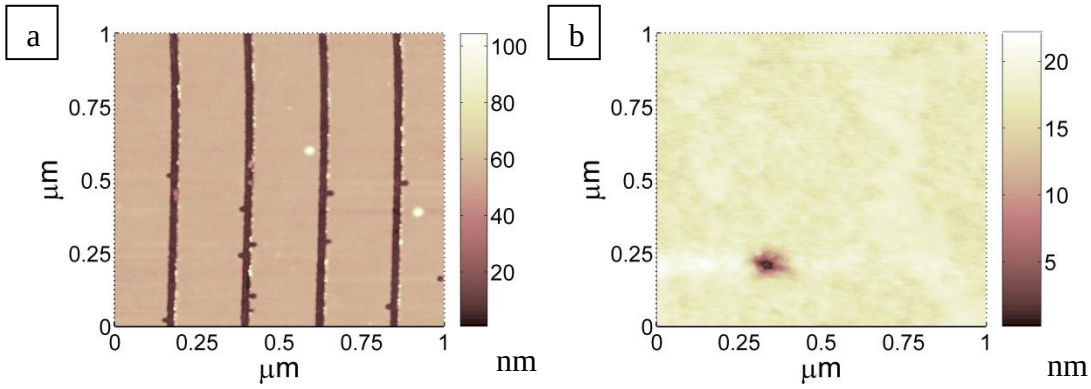

Fig. 5.25. AFM images of the sample after (a) Cr deposition, (b) after planarization.

5.5 Ag/ZnO Stack Fabrication

Before the Ag/ZnO stack can be grown on the planarised mask pattern, several experiments are necessary to determine to growth rate and optimum parameters for growing low roughness Ag and ZnO thin films. One factor that has been often neglected by regular users of the sputtering system at the University of Canterbury is the growth rate. As most applications require thin film sputtering of at least 50 nm, few users have carefully calibrated the parameters for accurate automatic deposition rate acquisition. As the Ag/ZnO stack requires a very thin

film of only 10 nm, the first step is to determine the growth rate of each individual film. After several experiments, it was discovered that the shutters covering the sputtering targets were insufficient to completely cover the target, resulting in unintended and uncontrolled sputtering during plasma stabilisation times. Hence, a bigger shutter was crudely fashioned out of aluminium foil to mitigate that effect.

5.5.1 DC Sputtering of Ag

To determine the optimum conditions for DC sputtering of Ag, several thin Ag films were grown on quartz. These films were then measured using AFM and SEM to determine the film roughness and coverage. Fig. 5.26 shows that as the DC power was increased from 25 W to 150 W, the film became more continuous. The coverage of the film was increased at higher DC power because the growth rate was faster. The substrate was a quartz substrate and hence island growth will be dominant at slower growth rates. With faster growth rates, the island growth mechanism was suppressed, resulting in better coverage across the substrate. At 150 W, the growth time was around 22 seconds (Fig. 5.27). While it was possible to increase the DC power further, and hence increase the Ag deposition rate, reproducibility and controllability were more difficult. The faster the deposition rate, the greater the effect of transient measurements as detected by the deposition rate monitor. For example, it is typical for the monitor to detect negative thickness and negative growth rates for the first few seconds upon opening the shutter.

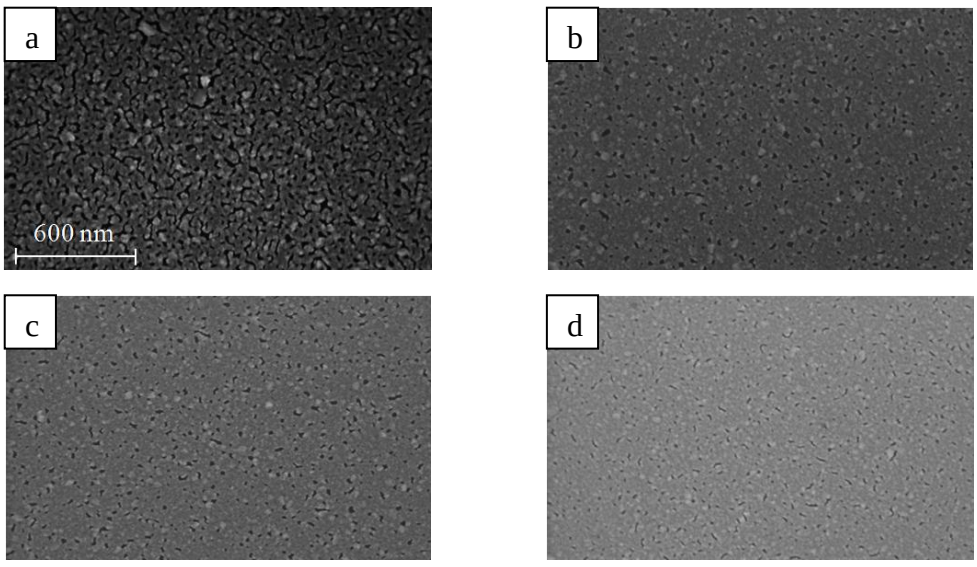

Fig. 5.26. SEM images of 10 nm Ag films grown at (a) 25 W, (b) 100 W, (c) 125 W, (d) 150W.

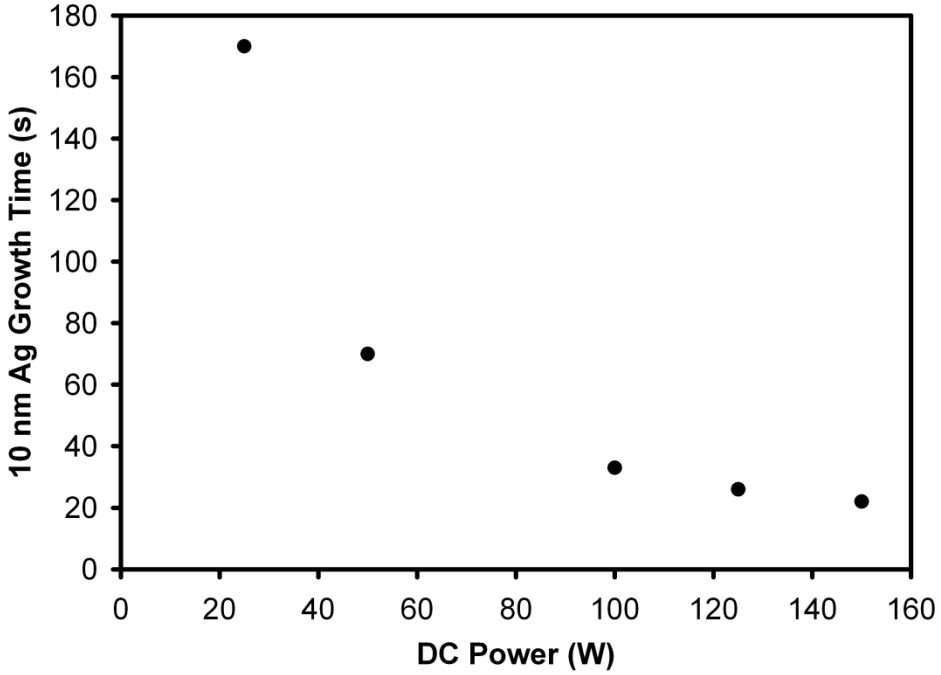

Fig. 5.27. Growth times to deposit 10 nm of Ag at various DC power levels.

The thin Ag films, shown in Fig. 5.28, consist of many grains, consistent with an island growth mode. Nevertheless, as the coverage was greater with the higher DC power, the rms roughness should also decrease, which was the case as shown in Fig. 5.29. The lower rms roughness of 1.31 nm with a DC power of 25 W was due to its discontinuous film coverage (Fig. 5.26(a)). The discontinuous film resulted in a lower average roughness than it actually was. The film coverage increased when the DC power was increased from 25 W to 100 W, with a corresponding increase in the film roughness. The peak roughness of 1.61 nm occurred at 100 W, which then steadily decreased with increases in the DC power, consistent with a more continuous film at higher DC powers. The lowest rms roughness of 0.86 nm occurred at 150 W. As the DC power increased, the film was also more homogenous, as evident by the similar rms roughness values for both 1 μm by 1 μm and 5 μm by 5 μm scans.

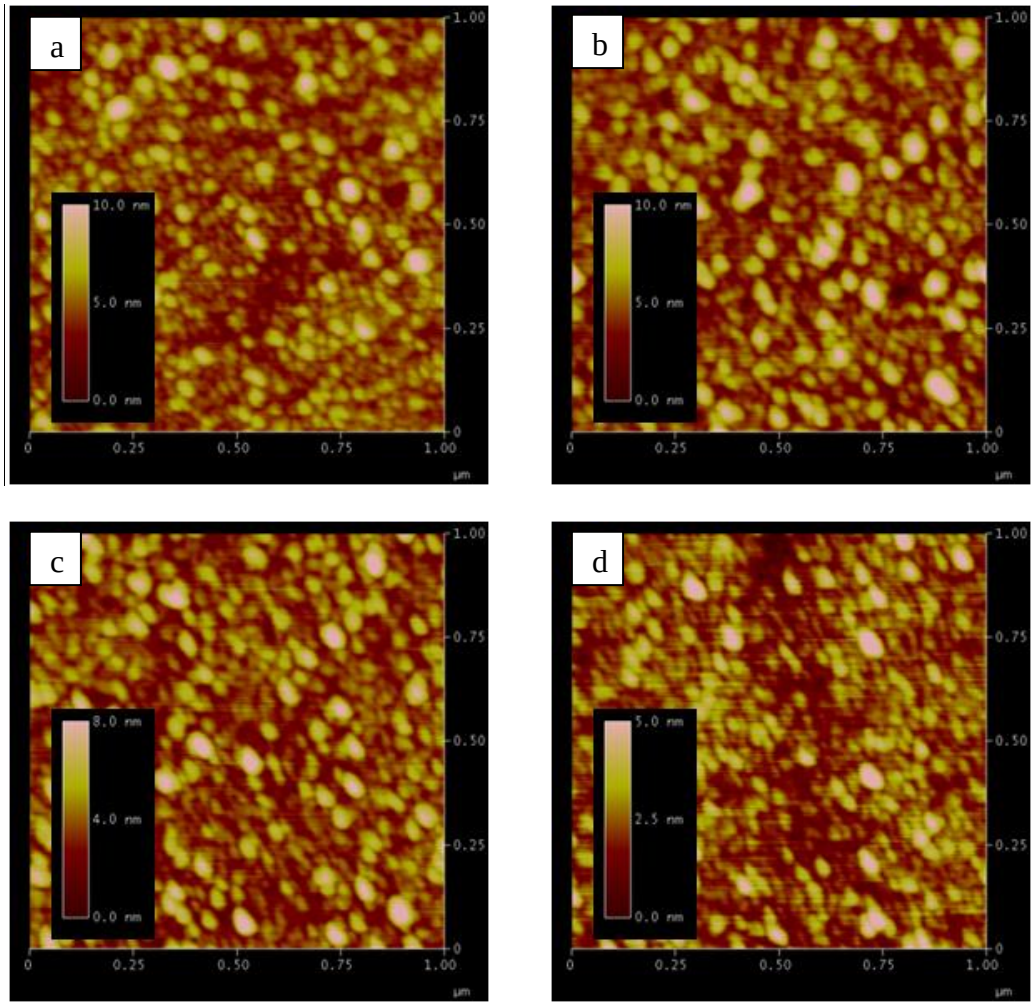

Fig. 5.28. AFM images of 10 nm Ag films grown at a DC power of (a) 25 W, (b) 100 W, (c) 125 W, (d) 150 W. All scans are 1 µm by 1 µm.

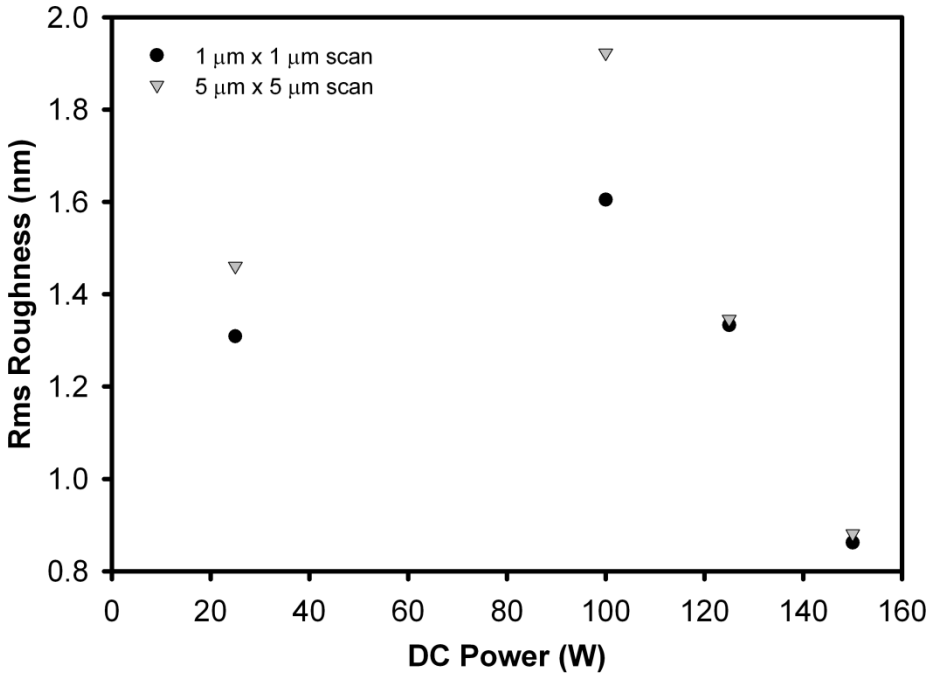

Fig. 5.29. Rms roughness of Ag films at various DC power.

5.5.2 RF Sputtering of ZnO

The ZnO was also sputtered in the same deposition system as the Ag, albeit with a different sputtering source. The ZnO (3N) target from ACI Alloys Inc. was ramped up from 20 W to 100 W over 20 minutes (Fig. 5.30) to prevent the target from suffering from thermal shock and subsequently cracking. Higher RF powers were found to result in the RF power supply freezing and no longer following the ramp set-up. Therefore, the ramp power of 100 W was used as it was found to be the most stable. Once at 100 W, the shutter was opened for about 4.5 minutes to deposit 10 nm of ZnO.

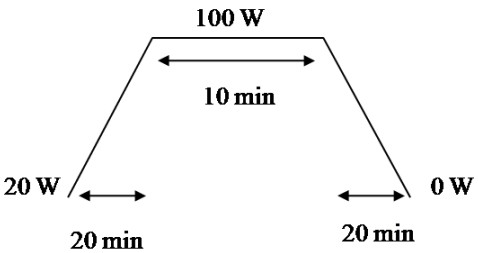

Fig. 5.30. RF power ramp for ZnO target.

As with the DC sputtering of Ag, the shutter also needed to be modified to minimise undesired deposition. Such a problem was greater for RF sputtering of ZnO films due to the significant ramp up and ramp down time. Hence, it should also be kept in mind that the quality of the film might be slightly variable due to the slight deposition at various RF powers during the ramp periods.

However, unlike Ag, the ZnO was clearly continuous even at 10 nm, as shown in Fig. 5.31. The film can also be inferred as insulating from the clear charging observed during SEM, consistent with typical ZnO sputtering growth. The typical rms roughness of such a film was 0.68 nm for a 1 μm by 1 μm area.

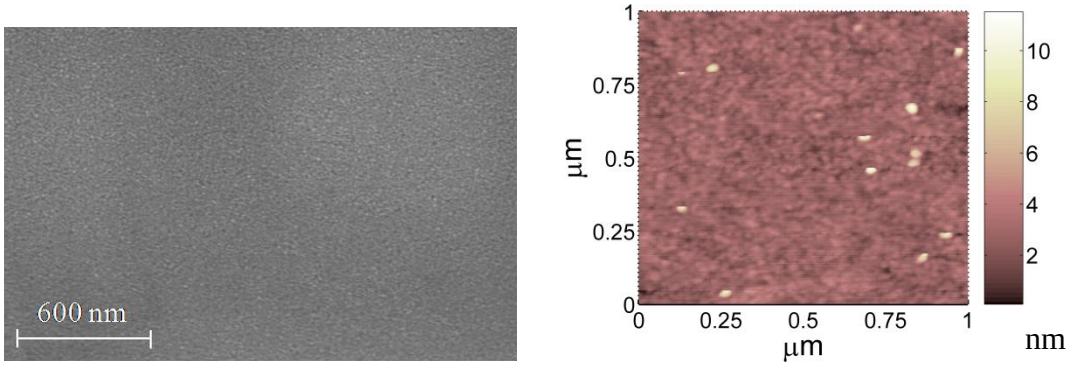

Fig. 5.31. (a) SEM, and (b) AFM image of a 10 nm ZnO film on quartz.

5.6 Initial Multilayer Ag/ZnO Stack Results

After optimising parameters for the Ag and ZnO thin films, the 10 layer stack consisting of alternating Ag/ZnO layers was grown. Initially, three different sets of $(Ag/ZnO)^X$ stacks were grown to compare their relative performance, where ^{x} is the number of Ag/ZnO sets: $(Ag/ZnO)^1$, $(Ag/ZnO)^2$, and $(Ag/ZnO)^5$. The imaging method used was essentially a modified version of contact lithography, as shown in Fig. 5.32. The light source was an unfiltered 350 W Hg lamp and hence filters at wavelengths of 365 nm (i-line), 405 nm (h-line), and 436 nm (g-line), were used to select particular exposure wavelengths. The filter was placed on top of a glass holder as that ensures a vacuum contact was applied to the superlens and the imaging substrate. The superlens was placed with the mask pattern facing towards the light source and the lens structure facing the imaging substrate.

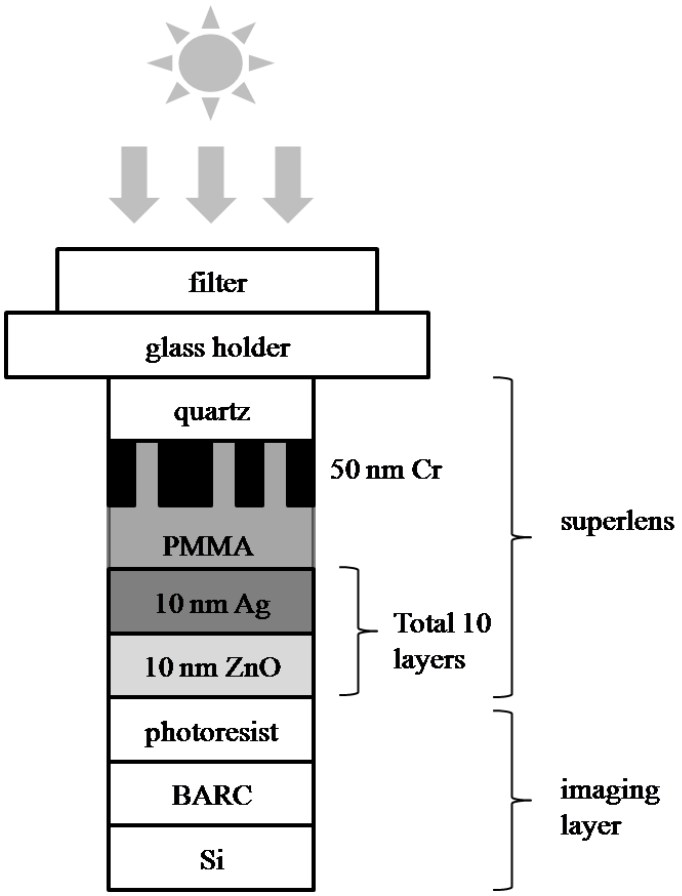

Fig. 5.32. Configuration used for imaging experiments with the superlens.

Initial superlens imaging experiments employed the i-line (365 nm wavelength) of the mercury lamp on the mask aligner using a combination of AZ BARLi-II (anti-reflective coating) and AZ HiR 1075 (ultra-high resolution photoresist). While there were some indications of the beneficial effects of having a 10 layer stack of alternating Ag/ZnO layers, feature sizes larger than expected were observed. This was believed to be attributed to the age of the photoresist, as most resists only have a 6-month shelf life, whereas the resist used was approximately 7 years old. Therefore, an order was placed for a new stock of photoresist, anti-reflective coating, thinner, and developer. While it was possible to order a new stock of AZ BARLi-II, a new stock of AZ HiR 1075 resist cannot be obtained since it has been discontinued. Upon discussion with MMRC and MicroChemicals representatives, it was decided to purchase AZ MiR 701 positive photoresist, as this was the best resolution i-line/g-line/broadband photoresist available from MicroChemicals.

5.6.1 Imaging Substrate Preparation

As received, AZ MiR 701 spin coats to an approximate thickness of 1 μm and is optimised for 300 nm to 400 nm line widths. However, data sheets from AZ Electronic Materials indicate the ability to produce features as small as 260 nm at a 1 μm resist thickness. Typically, it is not necessary to develop i-line/broadband photoresists with a higher resolution limit, at least for conventional lithography. However, an expert from MicroChemicals suggested that AZ MiR 701 might be suitable for imaging sub 100 nm line features, provided the resist is thinned significantly rather than using the resist as received. Beyond this, an anti-reflective coating (ARC), a soft post-exposure bake (PEB), and a low developer concentration (higher selectivity) are all employed to maximize the resolution limits of the AZ MiR 701 resist. The recommended PEB of 110°C on a hot-plate for 60 seconds was utilised. A lower dissolution rate developer, AZ 726 MIF, was also acquired to have a better control over developing the small width of the features.

Before the resist can be spin coated on 10 mm × 10 mm SSP n-Si substrates, it is important to clean the substrates properly for optimal adhesion of the photoresist to the substrate. The substrate is first blown with N_2 gas to remove any dust

particles from the scribing and cleaving process. The Si substrate is then ultrasonically cleaned in acetone for 5 minutes, rinsed in methanol, and blown dry with N_2 gas. This truncated cleaning process is used to minimise Si dust particle formation due to the aggressive nature of ultrasonic cleaning, since particle formation is detrimental to the subsequent spin coating of the photoresist.

Before any imaging experiments can be undertaken, the first step was to determine an appropriate dilution ratio of AZ MiR 701 to the AZ EBR thinner. It should be noted that diluted resists are sensitive to particle formation; therefore, it is important that the dilution ratio not be excessive. The cleaned Si substrate is therefore coated at 6000 rpm for 1 minute with AZ MiR 701 that has been diluted to different ratios. The coated substrate is then baked on the hot-plate at 90°C for 60 seconds. A step is then created by scratching the surface in order to measure the thickness using profilometry. Fig. 5.33 shows that the final thickness of the AZ MiR 701 is highly dependent on the dilution ratio, with a sharp drop in thickness with dilution. The photoresist thickness has a minimum thickness of approximately 25-33 nm at a dilution ratio of 1:5 (resist:thinner), above which we saw no significant change in the thickness. For the imaging experiments, a photoresist thickness of 50 nm was decided based on previous experience within the department [92]. This thickness correlates to a dilution ratio of 1:4.

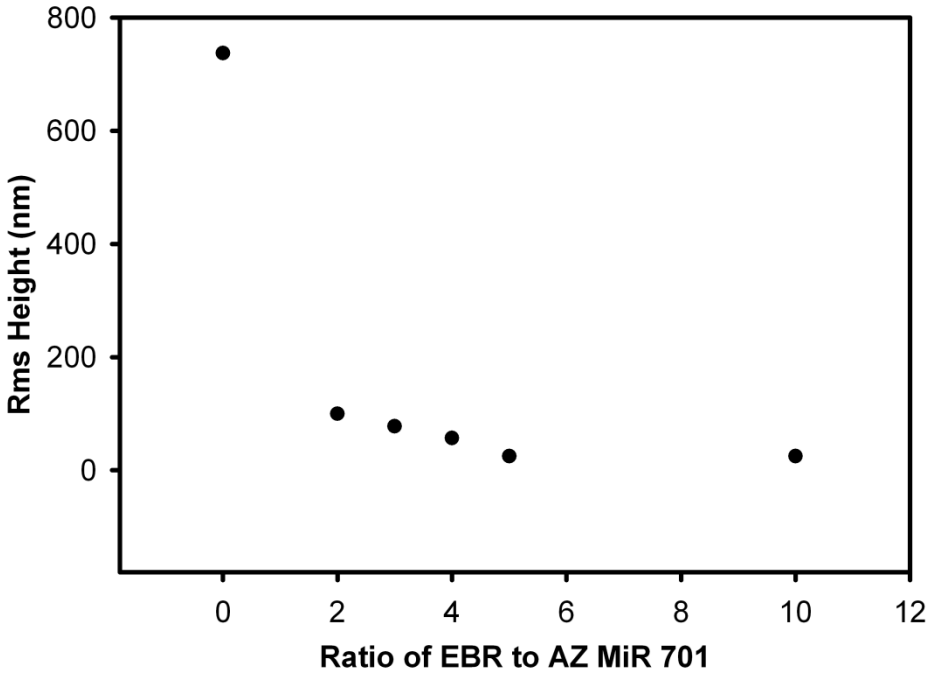

Fig. 5.33. Thicknesses of AZ MiR 701 photoresist after diluting with different ratios.

After determining an appropriate photoresist thickness, it is necessary to check the thickness of the AZ-BARLi-II (BARC) layer and ultimately the thickness of the AZ MiR 701 when spin coated on the BARC layer. Using the same cleaning procedure detailed previously, BARC is spin coated on cleaned Si substrates at 3000 rpm for 60 seconds. Then, the BARC layer is baked on a hot-plate at 200°C for 60 seconds, and the thickness is measured to be approximately 180 nm using the profilometer. Finally, a 1 to 4 ratio of AZ MiR 701 to AZ EBR solution is spun on the BARC at 6000 rpm (ramped up at 3000 rpm/second) for 60 seconds. The resultant resist is then baked at 90°C on a hot-plate for 60 seconds. A step height created via scratching the surface provided a combined height of 247 nm, indicating the AZ MiR 701 resist possessed a thickness of 67 nm and confirming that the AZ MiR 701 does indeed adhere to the BARC layer. A more accurate thickness measurement through overexposing the AZ MiR 701 layer and measuring with AFM found the thickness to be 55 nm, which is as expected. Fig. 5.34 shows that the photoresist is fairly smooth and absent of any observable particulates, with an rms roughness of 0.495 nm.

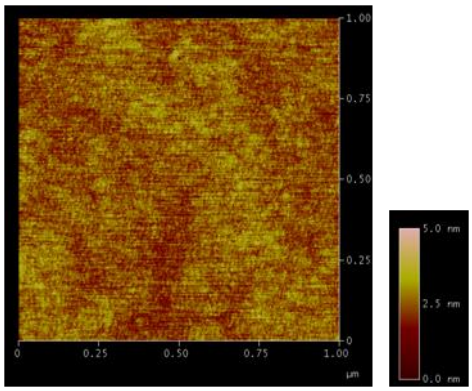

Fig. 5.34. AFM image of AZ MiR 701 (diluted to 1:4 ratio with EBR solvent) on top of a BARC layer.

5.6.2 Initial Experimental Results

Please note that from herein for simplicity, the AZ MiR 701 photoresist will be referred to as PR. In order to determine proper exposure and developing times for the PR, experiments were carried out utilizing a patterned Cr sample that had not been planarised with PMMA or deposited with a stack structure. This sample will be referred to as pattern Cr-59A, and the exposures were performed using a 365 nm filter. The Si substrate coated with PR was placed in “soft-contact” mode with

the mask aligner, and a post-exposure bake (PEB) of 110°C for 60 s was utilised. The summary of experiments conducted for this study is provided in Table 5.3.

Table 5.3. Summary of exposure and developing time experiments with sample Cr-59A.

Sample	Exp. Time (s)	Dev. Time (s)
59A-1	60	60
59A-2	80	60

Fig. 5.35 shows that instead of observing 5 lines spaced at 1 μm consisting of 100 nm, 150 nm, 200 nm, 250 nm and 300 nm lines as would be expected, there are at least 10 lines spaced about 600 nm from trough to trough. The spacing between the deeper lines is 1.2 μm apart, as shown in Fig. 5.35. Furthermore, the smaller features have also become enlarged. These additional features appear to be due to "frequency doubling", which occurs due to diffraction effects from closely spaced and narrow apertures [197, 198]. Hence, wave interferences resulted in weaker lines in between the main lines being exposed. This explanation is supported by the similarity in the line widths for all lines, implying that wave interference from surrounding apertures are present in all the lines. Furthermore, the middle features (150 nm, 200 nm, and 250 nm) appear to have the highest vertical depth (higher exposure) compared to the 100 nm and 300 nm features, confirming wave interference effects are more pronounced for these features.

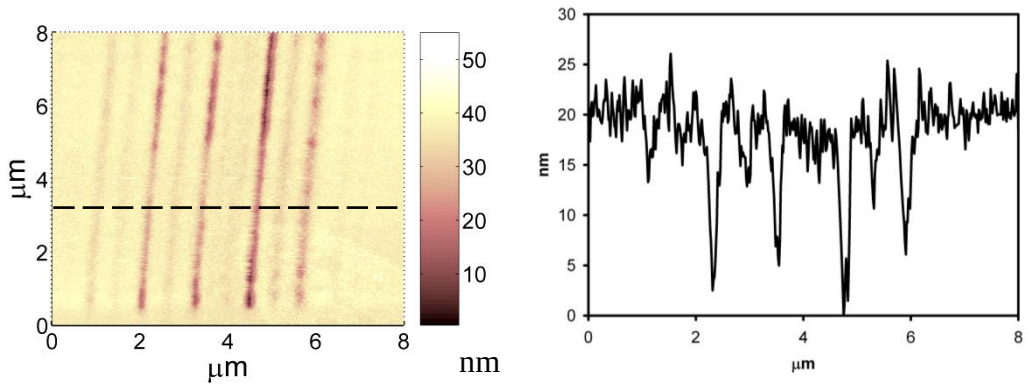

Fig. 5.35. AFM image and line profile for sample 59A-1 (60 s exposure and 60 s developing time).

Figure 5.36 shows the interference effect more clearly due to the longer exposure time, providing deeper, more defined features. Note that as with Fig. 5.35, Fig.

5.36 clearly shows that the deepest features are located in the middle of the set of lines. Interestingly, no additional lines are present between the main lines (Fig. 5.36), unlike the sample exposed for a shorter time (Fig. 5.36). The lines may be too shallow to be detected in between the features; however, weak replicas are found surrounding the set of lines, spaced 1.2 μm apart as shown in Fig. 5.36. The weaker lines in Fig. 5.35 are only about 8 nm deep, compared to the stronger lines which are about 15 nm deep. On the other hand, with an extra 20 seconds of exposure time, the deepest line in Fig. 5.36 is about 45 nm, which is about the thickness of the PR resist. Hence, an exposure time of 80 seconds and a developing time of 60 seconds are the minimum conditions in order to see all the features, with no attenuation from the PMMA planarisation or superlens structure, at a wavelength of 365 nm.

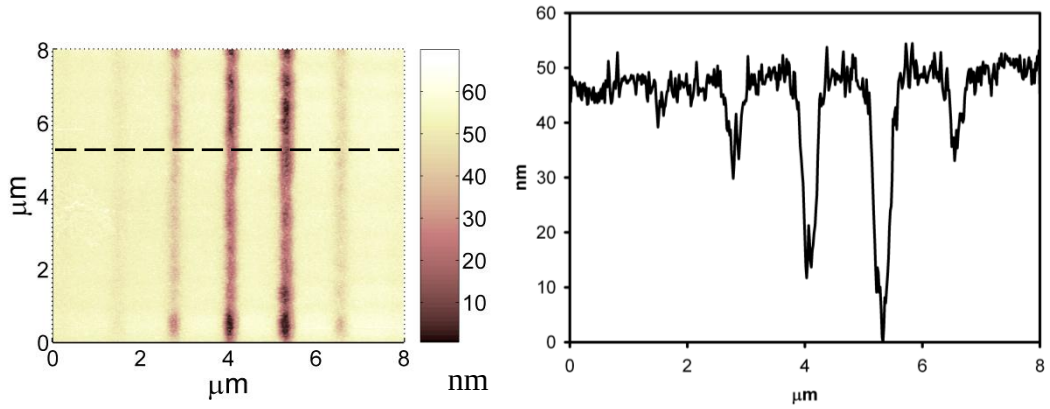

Fig. 5.36. AFM image and line profile for sample 59A-2 (80 s exposure and 60 s developing time).

As the diffraction problem appears to arise from the Cr layer, subsequent planarisation and superlens fabrication are also expected to suffer from the same issue. Fig. 5.37 shows that this is indeed the case, as evident from the extra features observed. There are also weaker lines in between each of the main features, similar to Fig. 5.35, but are not as visible due to the height scale used.

In theory, the stack consisting of PMMA of equivalent thickness to the superlens should have the worst resolution, and the ten-layer stack should have the best resolution. However, due to the clear interference effects observed in Fig. 5.37, multiple lines of the same width are transferred and superimposed, preventing evaluation of the resolution improvement with the ten-layer stack.

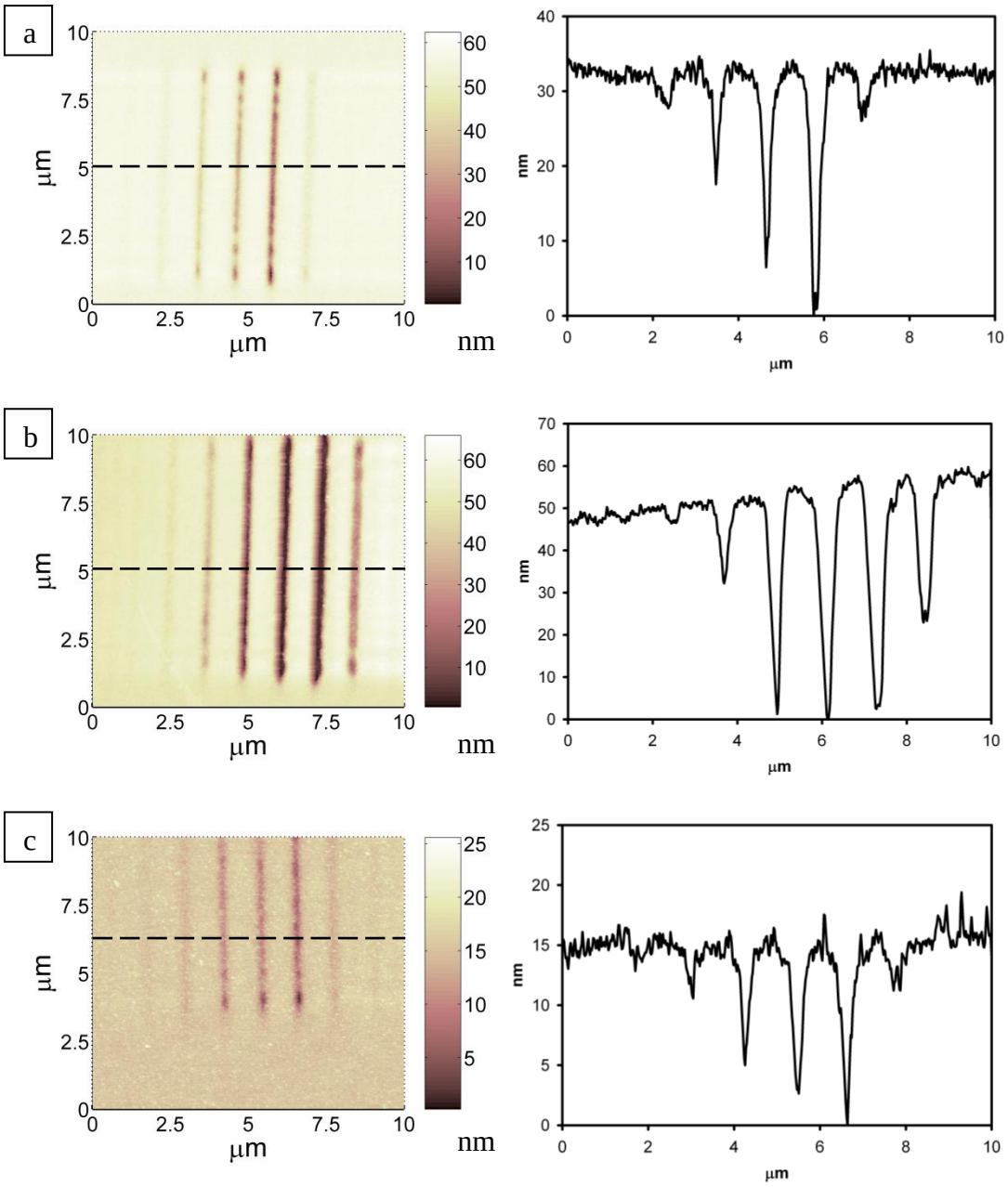

Fig. 5.37. AFM images and line profiles for (a) PMMA only (180s exposure time), (b) two layer stack (360s exposure time), and (c) ten layer stack (999.9s exposure time). All samples were exposed at a wavelength of λ = 405 nm and developed for 60s.

While this set of experiments cannot determine the resolution improvement with the superlens structure, it can still be used to estimate the optimum exposure and developing times for various structures and exposure wavelengths, which will help in later experiments. To quickly determine the ranges of values that are closest to the optimum values, optical microscopy is used to detect the presence or absence of certain features. If a feature appears rounded and enlarged, it is considered overexposed. If features are missing, it is considered unexposed. Table

5.4 summarises the optimum imaging conditions for various structures and exposure wavelengths. As expected, the presence of PMMA attenuates the intensity of the light, and hence it takes longer to expose a sample with a PMMA layer, compared with just a Cr mask. As the number of layers is increased in the superlens structure, the intensity is further attenuated, as evident from the longer exposure times required. Furthermore, the longest exposure times are with the 405 nm wavelength, and the shortest exposures with the 365 nm wavelength, which is consistent with typical Hg lamps having highest intensity at 365 nm and lowest intensity at 405 nm.

Table 5.4. Summary of correct exposure and developing times for various structures and exposure wavelengths.

Structure	λ (nm)	Exposure Time (s)	Developing Time (s)
Cr only	365	80 - 100	30 - 60
Two Layer	405	120 - 180	-
Two Layer	365	60 -120	-
10 Layer	365	120 - 240	-
10 Layer	436	> 760	-
10 Layer	405	880 – 999.9	15 - 60
PMMA	405	150 - 180	-

5.7 Modified Mask Pattern

In order to mitigate the wave interference effects, a new mask pattern was fabricated. The mask pattern consists of multiple rows, with each row consisting solely of one type of aperture width. The aperture widths were varied between 100 nm to 300 nm, at each separate row. Figure 5.38 shows the AFM images of the sample from the Cr aperture fabrication, to the PMMA planarisation using the plasma asher, and finally to the growth of the ten layer Ag/ZnO stack. Note that there are still some sidewall deposits on the aperture edges, but as these features are quite small, the sidewall deposits only occur irregularly and do not exceed 50 nm in height. As the rms roughness is 1.3 nm after planarisation (Fig. 5.38(b)), it is therefore not unexpected that the rms roughness after the stack growth is 2.3 nm (Fig. 5.38(c)). Hence, the growth of the 10 layer stack only added an additional 1 nm to the overall roughness, which is reasonable for the room temperature sputtered growth of these layers.

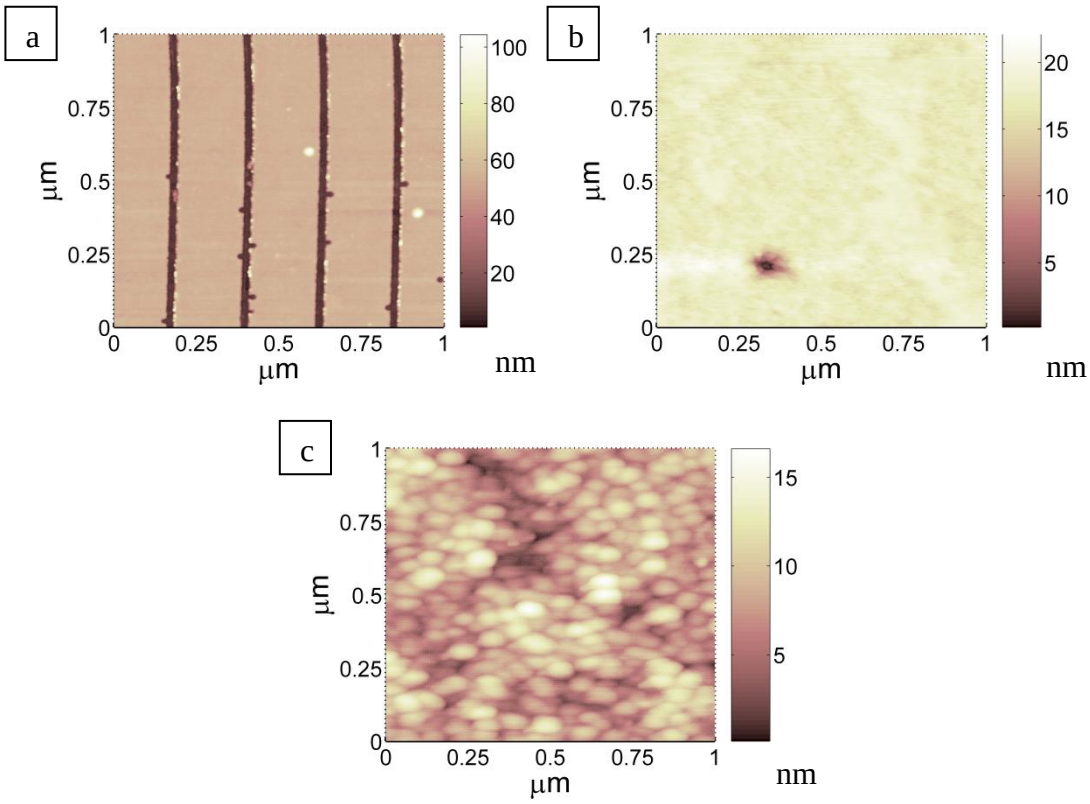

Fig. 5.38. AFM images of (a) Cr apertures 100 nm wide and 1 μm apart, (b) after planarization with the plasma asher, (c) after growth of ten layer Ag/ZnO stack.

Using the 405 nm wavelength, several resist-coated samples were exposed with the 10 layer stack for 40 minutes and then developed for several different times. This set of experiments is to determine the minimal developing time necessary to avoid overdevelopment, as the transferred features can be enlarged by overdevelopment. This was determined by measuring the trench of a larger micron size feature for various developing times. From the datasheet, the recommended developing time is 60 s for the undiluted 1 μm thick resist. Therefore, when diluted down to 55 nm to 60 nm thick, it was found that 2 s to 5 s was sufficient to fully develop the features. As it is difficult to manually control developing times below 2 s, the developer solution was diluted with DIW in a 1:1 ratio. Further experiments showed that 2 s of undiluted developer solution is the minimum developing time.

The exposure time was also increased until the transferred features can be clearly observed. This was found to occur at one hour exposure. Fig. 5.39 shows clear lines transferred onto the imaging resist. The FWHM of the imaged trench is 132 nm, for the 100 nm aperture. The larger width may be due to several reasons such

as resist limitation, since the resist is optimised for 0.3 to 0.4 μm linewidths, or due to the resolution limit of the lens itself. Another reason as to why the lens does not have the resolution theoretically predicted may be due to the effect of roughness. The roughness of each layer may contribute to the weakening of the evanescent field and hence, degrading the performance of the lens. Other factors that may degrade the performance of the lens are variability in the thickness of each layer, roughness of the planarisation layer, or roughness of the total stack structure. Nevertheless, Fig. 5.40 shows that there is improvement in the resolution with a superlens since the FWHM of the 100 nm line feature is 332 nm with an equivalent PMMA thick sample.

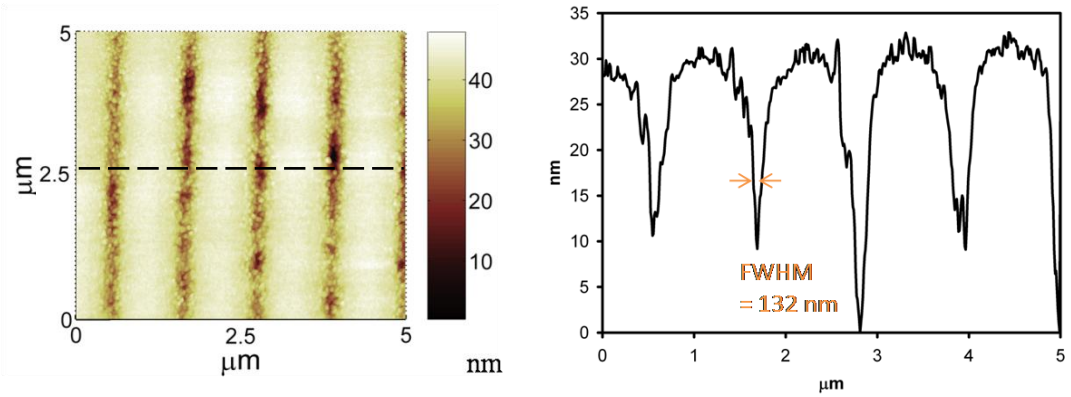

Fig. 5.39. AFM image and line profile of 100 nm lines from a 10 layer Ag/ZnO stack exposed at 405 nm for 1 hour and developed for 2 s.

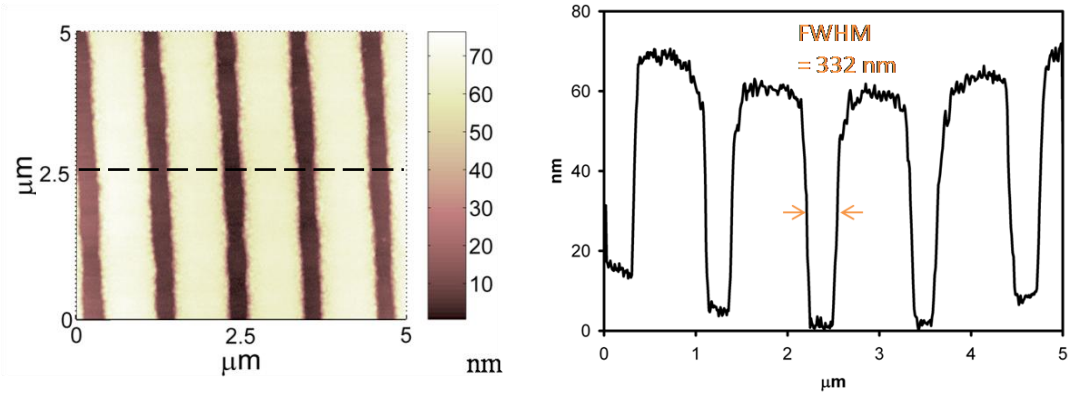

Fig. 5.40. AFM image and line profile of 100 nm lines from a 140 nm PMMA stack exposed at 405 nm for 1 hour and 20 minutes, and developed for 2 s.

If the definition of width is the width after exposing through the entire resist, then the width is larger, as shown in Fig. 5.41. The top of the trench is actually 430 nm. It is likely that this value is much larger than in Fig. 5.39 due to the higher

exposure time used. Determining what constitute the “top” of the trench is also non-trivial, as shown in Fig. 5.41.

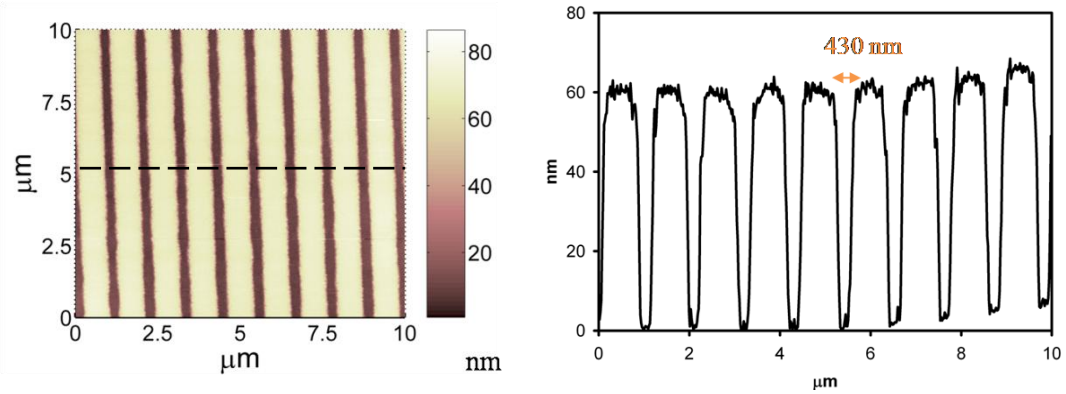

Fig. 5.41. AFM image and line profile of 100 nm lines from a 10 layer Ag/ZnO stack exposed at 405 nm for 1 hour and 20 minutes, and developed for 2 s.

It should be noted that the transferred width can vary depending on the definition of width. Melville [92] created an array of line widths with a duty cycle of 50%. He then employed a fast fourier transform (FFT) to calculate the periodicity of the transferred pattern, from which he inferred the transferred width. With such a technique, low intensity images that can barely be discerned by AFM can be extracted. Furthermore, if the transferred image does not have precisely a duty cycle of 50% due to enlarged features, then there is error in the actual width being measured. Fang et al. [88] also extracted the FWHM of the transferred width from an incompletely exposed resist, similar to that used in Fig. 5.39. This width is then put forward as the resolution of the superlens. No experimental reports thus far actually provided measures from edge to edge of a perfectly rectangular image transfer, exposed all the way through the resist. Such measurement is non-trivial due to the ambiguous edges of the transferred pattern (Fig. 5.41). Underexposure and/or underdevelopment can both lead to smaller features. Hence, one must use caution when interpreting any literature reports currently claiming small resolutions measured indirectly.

It should also be noted that it is possible that the test pattern might transfer its image even without the superlens. The ultimate resolution test is with two apertures, with the distance between the apertures varied until no image is successfully transferred. The center-to-center distance is then considered the resolution limit of the lens. In this work, the center-to-center distance is around 1

μm, well above the diffraction limit. Nevertheless, the 132 nm width measured is likely to be below the diffraction limit, using measures reported in literature, and hence is consistent with superlensing.

Chapter 6

Conclusions and Future Work

ZnO is an important material for optoelectronic applications. However, several fundamental properties of ZnO are still under debate and must be understood before its commercial potential can be realised. In this thesis, the effect of combining ZnO and Ag towards optoelectronic applications were studied. The key findings of this study and possible future research routes are presented in this chapter.

6.1 Undoped ZnO Growth

The molecular beam epitaxy (MBE) growth environment is critical in determining the properties of a film for specific applications. A key issue - the growth rate - requires an accurate knowledge of transient flux measurement effects. The effects of transients can be minimised by discarding the first 20 s of flux measurements and only start taking flux measurements after the effusion cell shutter has been opened for at least five minutes. For ZnO growth, the stoichiometric point occurs at a Zn flux of 4×10^{14} atoms/cm^{2}s, when the RF power is 400 W, O_2 flow rate is 0.5 sccm, and growth temperature is 700°C. These conditions generally lead to the highest quality undoped ZnO.

The substrate temperature is clearly crucial in thin film growth. The most common methods of substrate measurement are pyrometry and thermocouple readings. The approach used in the MBE system in the University of Canterbury has been to assume that the substrate temperature is essentially the same as the thermocouple reading, which is in mechanical contact with the growth block.

However, there is weak thermal coupling between the thermocouple and the poor thermally conductive sapphire substrate. The actual surface temperature, as measured by using an optical bandedge measurement technique, found that the surface temperature is typically 100°C lower than the thermocouple reading. The surface temperature also decreases over time due to reduction in radiative heat provided by the heater. This is caused by the growth block requiring less power supplied to the heater over time once it has reached an equilibrium condition. That is, more energy than necessary is usually applied to the heater to ensure that the desired temperature can initially be reached. Consequently, the reduction in radiative heat results in a decrease in substrate temperature. Furthermore, there can be a 15 minutes time lag between the thermocouple reading the desired temperature and the surface temperature stabilising. This study shows that a feedback system consisting of both BandiT and the Micristar controllers to ensure better control of the surface temperature during growth is worth pursuing.

The substrate most typically used for ZnO growth is sapphire. However, the major drawback of using sapphire is that it represents a large lattice mismatch to ZnO. Several experiments were undertaken to investigate the optimum buffer layer conditions to mitigate the lattice mismatch between c-plane sapphire and ZnO. A combination of MgO and low temperature ZnO was employed. The optimum MgO growth time was found to be 10 s under 2 sccm O_2 flow rate at an RF power of 400 W and a substrate temperature of 750°C. These conditions resulted in an MgO buffer layer approximately 1 nm thick. This is the point where MgO is in the transition between 2D and 3D growth, as confirmed by both examining the RHEED patterns, and the lattice spacing inferred from the streak spacing.

Nevertheless, several additional studies can be taken to further optimise the MgO buffer layer growth. A growth rate study should be performed to determine the growth rate of MgO and to ensure growth under an O-rich regime as literature has recommended growth in that regime. A flux ratio study should also be undertaken to investigate if other growth regimes for MgO growth are advantageous. In this thesis, the MgO growth temperature was selected based on work by others. A MgO growth temperature series should be undertaken to find the optimum growth

temperature. Annealing of the MgO buffer layer can also be explored to investigate its effects.

Through careful RHEED studies, the optimum LT-ZnO growth time was found to be two minutes. The conditions used for LT-ZnO buffer layer growth was an O_2 flow rate of 0.5 sccm at an RF power of 400 W, with a substrate temperature of 450°C. A study was also performed on the effect of LT-ZnO buffer layer annealing on subsequent HT-ZnO quality. A short (3.5 minutes) oxygen plasma annealing, at 800°C with plasma conditions of 400 W and O_2 flow rate of 0.5 sccm, was found to give the best results structurally, optically and electrically. It was also found that it is important that the subsequent HT-ZnO growth occur soon after the end of the O_2 plasma annealing, due to the detrimental effect of vacuum annealing. The lowest rms roughness achieved was 6.3 nm, with carrier concentration of 8.9×10^{17} cm^{-3} and mobility of 50 cm^2/Vs. In all the LT-ZnO annealed samples, the 4 K PL show I_6 peaks, most likely due to Al diffusion from the sapphire substrate at the high annealing temperature of 800°C.

In summary, films grown between 400°C to 800°C were characterised structurally, optically and electrically. While RHEED images did not show any significant differences across this temperature range, SEM and AFM images showed clear rough and hillock-filled surfaces for lower growth temperatures. PL measurements indicated that low temperature growth was structurally poorer as evident from lack of LO phonon replicas and wider PL peaks. All growth temperatures yielded PL features related to In and Al, indicating temperature independent sources. Lower temperatures growth also resulted in increased carrier concentrations and lower mobility. The growth at 800°C was consistently superior to all the other growth temperatures, with the lowest rms roughness of 2.9 nm, smallest FWHM of the main NBE PL peak (2.2 meV), lowest carrier concentration of 3.6×10^{16} cm^{-3}, and highest mobility of 105 cm^2/Vs.

6.2 Silver Doped ZnO

To realise the potential of ZnO in optoelectronic devices, it is necessary to be able to control the electrical conductivity. High electron concentration n-type doping of ZnO has been widely reported. In contrast, high hole concentration and high

hole mobility p-type ZnO has not yet been reproducibly achieved. A possible obstacle in realising p-type ZnO may be due to the existence of the Fermi level stabilisation energy (E_{FS}) of ZnO near the conduction band minimum (CBM). A possible candidate to overcome the self-compensation issue is through using group IB dopants, in particular Ag. Ag acceptors theoretically form more favourably under O-rich conditions, which is beneficial as the formation energy of compensating hole-killer defects are minimised under O-rich conditions.

At low Ag flux levels (below 4×10^{10} atoms/cm^{2}s) or at high substrate temperatures (above 600°C), no clear structural effects were observed, as evident by the streaky RHEED and smooth surfaces observed under SEM. However, clear degradation in surface morphology was observed for higher Ag flux levels and lower substrate temperatures, as evident from the appearance of concentric arcs in the RHEED patterns and rough surfaces seen under SEM. This implies that doping occurs more readily at lower substrate temperatures, consistent with previous doping studies.

However, the disadvantage of growing at low temperatures is that the structural quality is poorer due to both increased incorporation of strain inducing dopants, and shorter diffusion lengths of adatoms. One way to reduce the severe surface morphology degradation with high doping at low substrate temperatures is by growing a thinner doped epilayer. From observing the RHEED pattern evolution, a reasonable morphology can be maintained for a Ag flux of 4×10^{11} atoms/cm^{2}s and substrate temperature of 400°C by growing films less than 133 nm thick.

RBS channelling experiments indicate that most of the Ag incorporated substitutionally (94%) at a Ag flux of 4×10^{10} atoms/cm^{3}s and substrate temperature of 600°C. With an increase by an order of magnitude Ag flux level, the ratio of substitutional and interstitial Ag remains similar, confirming the solubility of Ag in ZnO, as well as the ability to increase the desired acceptor concentration to high levels. The increase in the lattice constant with increasing Ag flux levels further confirms incorporation of Ag in ZnO. Further studies of RBS channelling for additional samples should be undertaken to better understand the effect of substrate temperatures on the type of defect formation favoured.

However, even though there are indications of substitutional Ag in the ZnO:Ag films, Hall effect measurements indicate that all ZnO:Ag films are n-type. Variable magnetic field Hall effect measurements detected the existence of only one distinct electron carrier population in such films, and no significant contribution from surface or interface degenerate layers. Nevertheless, a decrease in electron concentration with doping can be observed for growth at 400°C, with an increase in electron concentration at the highest doping levels due to increased formation of donor-like structural defects.

However, the effect of Ag doping for growth at 800°C is more variable, likely due to Ag incorporation limits at high substrate temperatures. The variety of electron concentration is thought to arise from oxidation-induced Zn flux instability during growth, as supported by the much lower growth rates for the high electron concentration films grown at 800°C. The limitation of Ag incorporation is nevertheless consistent with literature reports of the temperature dependence of dopant incorporation. The mobility values for the ZnO:Ag are variable and no clear trend can be seen. The comparison of measurements for ZnO:Ag and undoped ZnO is also slightly complicated due to the possible structural improvement that should be achieved for ZnO:Ag layers from an additional undoped HT-ZnO layer grown as the third buffer layer for ZnO:Ag growth, which are absent for the undoped ZnO growth.

Low temperature PL for films grown at 600°C and 800°C has very similar emissions, with the spectra dominated by I_9 (In), I_6 (Al), I_4 (H), and I_{3a} lines. The exception is a lack of LO phonon replicas at the highest doping concentration for the growth at 600°C due to poorer structural quality. Nevertheless, there are indications of Ag incorporation from the red-shift of the peaks with Ag doping, consistent with expected lattice dilation. For Ag flux level of 4×10^{10} Ag atoms/cm^{2}s and a substrate temperature of 400°C, there appears to be ionised donor bound excitons (I_0) related to $I_{6/6a}$, indicating the presence of compensating acceptors, consistent with Hall effect measurements.

By switching from the near stoichiometric growth condition to O-rich, the electrical properties appeared relatively unchanged, but several optical effects were observed. The defect band centred at around 2.3 eV appears to be

suppressed with Ag doping. If the defect band is due to V_{Zn}, then the substitution of Ag at some V_{Zn} sites will suppress the emission due to V_{Zn}.

In the absence of acceptor related features in the low temperature PL, DLTS can be used to investigate the defect levels in a material, to gain a better understanding of Hall effect results. Unfortunately, the material quality of the ZnO:Ag was not of sufficient quality to form a good Schottky contact with which to perform DLTS measurements. Nevertheless, due to the highly mobile nature of Ag, it was possible to fabricate a AgO_x contact on an undoped film that could be used to investigate acceptor defects which may be introduced by the Ag diffusion from the contact to the underlying material. DLTS detected an acceptor peak at 319 meV, which was attributed to Ag_{Zn}, and was consistent with theoretical reports of an acceptor level at 400 meV above the VBM. To confirm that this was indeed due to Ag diffusion, it would be beneficial to fabricate a non Ag-based contact on a comparable undoped film and check that that particular acceptor peak is absent. It has also been reported that annealing in an oxygen ambient is require to activate acceptors. However, it was found that O_2 annealing actually increased the donor concentration in the ZnO:Ag films grown in this thesis.

A previous study [21] suggested that ions produced by the plasma source, used on the MBE system at the University of Canterbury, could have detrimental effects on the optical and electrical properties of films. A possibility to reduce the ion content of the plasma is by using a plasma source with ion removal plates. Such a feature is unavailable for the MDP21 plasma source used in this thesis. However, a newer model of that plasma source (HD25) has recently been purchased. After installing the new plasma source in place of the current plasma source, benchmark undoped films at varying degrees of ion removal should be grown for comparison. If the reduction of ions in the plasma does result in superior films, especially at low temperatures and under O-rich conditions, it may be worthwhile to continue with Ag doping experiments.

In addition, a high degree of compensation has been observed in hydrothermal bulk ZnO, thought to be partly due to Li incorporating as a deep acceptor ($N_D \sim N_A \sim 10^{13}$ cm^{-3} yet $N_D - N_A \sim 10^{12}$ cm^{-3} has been measured [199]). Therefore, in-situ Li doping during MBE growth could prove to be useful as well.

6.3 Use of Ag and ZnO as a Superlens Structure

Most of the studies into ZnO have been geared towards using ZnO as an optoelectronic device. A lesser-known application of ZnO is as a dielectric material to form part of a superlens structure. Such a structure is theoretically able to transfer an image with a resolution beyond the diffraction limit, allowing photolithography to image smaller features than currently possible. Previously reported experimental results involving a single Ag layer surrounded by PMMA spacer layers proved that this is indeed possible. Collaborators at Purdue University suggested that Ag/ZnO could be grown in alternating layers with five sets of each layer to further improve the resolution that can be achieved, creating what is more properly termed a metamaterial.

One of the most difficult parts of the fabrication of the superlens structure was the mask pattern fabrication step. Proper utilisation of EBL is quite an art, as parameters need to be optimised whenever a different feature is to be written, especially if there are changes to the overall mask pattern as well. Through several trial and error experiments, the optimum exposure dose for imaging 100 nm linewidth features spaced 1 μm apart was found to be 20 $\mu As/cm^2$, with an optimum developing time of 40 s. If the resist or developer solutions have aged significantly, the optimum dose and developing time increases significantly as well.

The main problem with a lift-off process arises from the limited ability to adequately create a small and cleanly lifted-off feature. Therefore, even with optimised EBL parameters, there can exist some lift-off problems, in particular sidewall deposits. Sidewall deposits mean that some Cr patches are sticking out of the sidewalls of the apertures, requiring a thicker planarisation layer. In order to minimise this effect, a bilayer resist stack was investigated, with a MicroChem PMGI layer as the lift-off layer. However, the dissolution of the PMGI cannot be adequately controlled to form the undercut required.

In hindsight, it is possible that the convection oven baking of the ma-N 2403 resist may have undesirable consequences for the underlying PMGI layer, specifically that the long bake time of 30 minutes affected the profile for the

PMGI layer. It might be worthwhile using a shorter, heat conduction dominated, hot plate bake for the subsequent ma-N 2403 layer to minimise the heating effects on the PMGI layer. Furthermore, the dissolution of the PMGI layer is isotropic as used. It may be possible to turn it more anisotropic by using a cap-on bilayer lift-off process. In this process, after developing the imaging resist (i.e. ma-N 2403 in this case), the PMGI is flood exposed using deep UV (240 nm to 290 nm). This exposure enhances the development rate in the exposed region and hence reduces the undercut. However, it will be necessary to acquire an additional developer solution, such as the PMGI 101 developer, and ensure that the imaging resist is not affected by this developer.

Initial Ag/ZnO growth on the planarised mask pattern reveal another problem imaging with small apertures, namely, diffraction. Diffraction resulted in interference-related replicas of the apertures occurring in between the regions exposed by the actual apertures. Furthermore, wave interference effects were found to also result in contributions from all the line features being transferred to every other line feature in the same row. Several lines of different widths were fabricated in a row to allow for easier comparison of the resolution limits of the mask. However, wave interference effects resulted in the largest line width being transferred to all the other line features, preventing the resolution limits to be determined as all the features ended up being similar sizes.

To mitigate wave interference effects, a new mask pattern was fabricated, where all the same width features were located on the same row. Different linewidths were placed on different rows. Using an exposure time of one hour and a developing time of 2 s, an image with a FWHM of 132 nm was transferred through a 100 nm line, imaged with the 405 nm wavelength of a Hg lamp. An equivalent PMMA sample transferred the 100 nm line feature as a feature with a FWHM of 332 nm. This indicated that the superlens did confer a resolution improvement, and may have possibly achieved subwavelength imaging as well.

However, to properly test the resolution of the stack, future work should employ a dry etch, as opposed to a lift-off process, to enable the fabrication of smaller features that are closer together. Furthermore, better roughness and thickness control would allow for a structure closer to theoretical designs. An alternative

resist with PMMA type resolution but with Hg lamp exposure wavelengths would enable one to rule out the resist limitation as a factor in the limited resolution achieved. However, such a resist has not been investigated by industry and as such, will need to be created from scratch. Therefore, there are many areas of research still of interest in the superlens area.

References

[1] L. Quintana-Murci, H. Quach, C. Harmant, F. Luca, B. Massonnet, E. Patin, L. Sica, P. Mouguiama-Daouda, D. Comas, S. Tzur, O. Balanovsky, K. K. Kidd, J. R. Kidd, L. Van Der Veen, J. M. Hombert, A. Gessain, P. Verdu, A. Froment, S. Bahuchet, E. Heyer, J. Dausset, A. Salas, and D. M. Behar, "Maternal traces of deep common ancestry and asymmetric gene flow between Pygmy hunter-gatherers and Bantu-speaking farmers," *Proceedings of the National Academy of Sciences of the United States of America*, vol. 105, pp. 1596-1601, 2008.

[2] S. M. Sze, *Semiconductor devices: Physics and Technology*. New York: John Wiley & Sons, Inc., 2002.

[3] M. Fukuda, *Optical Semiconductor Devices*. Canada: John Wiley & Sons, Inc., 1999.

[4] R. L. Gunshor and L. A. Kolodziejski, "Recent advances in the molecular beam epitaxy of the wide-bandgap semiconductor ZnSe and its superlattices," *IEEE Journal of Quantum Electronics*, vol. 24, pp. 1744-1757, 1988.

[5] C. E. Kendrick, "PhD Thesis: Revisiting Nitride Semiconductors : Epilayers, p-Type Doping and Nanowires," 2008.

[6] B. Johnstone, *Brilliant! Shuji Nakamura and the Revolution in Lighting Technology*. New York: Prometheus Books, 2007.

[7] K. Takahashi, A. Yoshikawa, and A. Sandhu, *Wide bandgap semiconductors: fundamental properties and modern photonic and electronic devices*: Springer, 2007.

[8] M. Kawasaki and T. Makino, "Oxide semiconductors," *Semiconductor Science and Technology*, vol. 20, pp. i-ii, 2005.

[9] U. Ozgur, Y. I. Alivov, C. Liu, A. Teke, M. A. Reshchikov, S. Dogan, V. Avrutin, S. J. Cho, and H. Morkoc, "A comprehensive review of ZnO materials and devices," *Journal of Applied Physics*, vol. 98, pp. 041301-103, 2005.

[10] D. C. Look, "Recent advances in ZnO materials and devices," *Materials Science and Engineering B*, vol. 80, pp. 383-387, 2001.

[11] A. P. Casas and J. De Andrés Llopis, "A spot test for zinc white," *Studies in Conservation*, vol. 47, pp. 273-276, 2002.

[12] E. R. Gonzaga, "Role of UV light in photodamage, skin aging, and skin cancer: Importance of photoprotection," *American Journal of Clinical Dermatology*, vol. 10, pp. 19-24, 2009.

[13] L. Pysklo, P. Pawlowski, W. Parasiewicz, and L. Slusarski, "Study on reduction of zinc oxide level in rubber compounds part I," *KGK Kautschuk Gummi Kunststoffe*, vol. 60, pp. 548-553, 2007.

[14] E. Bodrumlu, "Biocompatibility of retrograde root filling materials: a review," *Australian endodontic journal : the journal of the Australian Society of Endodontology Inc*, vol. 34, pp. 30-35, 2008.

[15] M. Singanan, "Effective control of corrosion of steel in concrete structures by using chemically modified cement and water quality - A novel method," *Electronic Journal of Environmental, Agricultural and Food Chemistry*, vol. 6, pp. 1703-1710, 2007.

[16] V. D. Borisevich, A. V. Pavlov, and I. A. Okhotina, "Depleted zinc: Properties, application, production," *Applied Radiation and Isotopes*, vol. 67, pp. 1167-1172, 2009.
[17] C. Jagadish and S. J. Pearton, *Zinc Oxide Bulk, Thin Films and Nanostructures: Processing, Properties and Applications*. Hong Kong: Elsevier Ltd., 2006.
[18] L. M. Levinson and H. R. Philipp, "ZnO Varistors For Transient Protection," *IEEE Transactions on Parts, Hybrids, and Packaging*, vol. PHP-13, pp. 338-343, 1977.
[19] C. Klingshirn, "ZnO: From basics towards applications," *Physica Status Solidi (B) Basic Research*, vol. 244, pp. 3027-3073, 2007.
[20] A. R. H. Preston, B. J. Ruck, L. F. J. Piper, A. Demasi, K. E. Smith, A. Schleife, F. Fuchs, F. Bechstedt, J. Chai, and S. M. Durbin, "Band structure of ZnO from resonant x-ray emission spectroscopy," *Physical Review B - Condensed Matter and Materials Physics*, vol. 78, 2008.
[21] W. C. T. Lee, "PhD Thesis: Harvesting Philosopher's Wool: A Study in the Growth, Structure and Optoelectrical Behaviour of Epitaxial ZnO," 2007.
[22] X. Yang and N. C. Giles, "Hall effect analysis of bulk ZnO comparing different crystal growth techniques," *Journal of Applied Physics*, vol. 105, pp. 063709, 2009.
[23] M. W. Cho, C. Harada, H. Suzuki, T. Minegishi, T. Yao, H. Ko, K. Maeda, and I. Nikura, "Issues in ZnO homoepitaxy," *Superlattices and Microstructures*, vol. 38, pp. 349-363, 2005.
[24] H. Wenisch, V. Kirchner, S. K. Hong, Y. F. Chen, H. J. Ko, and T. Yao, "Evaluation of ZnO substrates for homoepitaxy," *Journal of Crystal Growth*, vol. 227-228, pp. 944-949, 2001.
[25] D. P. Norton, Y. W. Heo, M. P. Ivill, K. Ip, S. J. Pearton, M. F. Chisholm, and T. Steiner, "ZnO: growth, doping & processing," *Materials Today*, vol. 7, pp. 34-40, 2004.
[26] Q. Bao, C. Chen, D. Wang, Q. Ji, and T. Lei, "Pulsed laser deposition and its current research status in preparing hydroxyapatite thin films," *Applied Surface Science*, vol. 252, pp. 1538-1544, 2005.
[27] J.-H. Park and T. S. Sudarshan, *Chemical Vapor Deposition*. USA: ASM International, 2000.
[28] C. A. Bishop, *Vacuum Deposition onto Webs, Films, and Foils*. New York: William Andrew Inc., 2007.
[29] D. L. Smith, *Thin-Film Deposition: Principles and Practice*. USA: McGraw-Hill Inc., 1995.
[30] M. A. Herman and H. Sitter, *Molecular Beam Epitaxy: Fundamentals and Current Status*. Germany: Springer-Verlag Berlin Heidelberg, 1996.
[31] A. Ede, *The chemical element: a historical perspective*. Portsmouth: Greenwood Publishing Group, 2006.
[32] http://www.veeco.com/library/resources/element_information.aspx?id=42, accessed 2007.
[33] B. P. Binks, *Modern characterization methods of surfactant systems*. New York: Marcel Dekker, Inc., 1999.
[34] M. Liu, C. Y. Ma, and Q. Y. Zhang, "Effect of O_2 partial pressure and substrate temperature on the plasma emission spectra and ZnO growth

behavior," *Physica Status Solidi (A) Applications and Materials*, vol. 205, pp. 961-964, 2008.
[35] J. A. Venables, G. D. T. Spiller, and M. Hanbucken, "Nucleation and growth of thin films," *Reports on Progress in Physics*, vol. 47, pp. 399-459, 1984.
[36] Y.-S. Kim and C. H. Park, "Rich Variety of Defects in ZnO via an Attractive Interaction between O Vacancies and Zn Interstitials: Origin of n-Type Doping," *Physical Review Letters*, vol. 102, pp. 086403-4, 2009.
[37] A. Janotti and C. G. Van De Walle, "Native point defects in ZnO," *Physical Review B - Condensed Matter and Materials Physics*, vol. 76, pp. 165202, 2007.
[38] S. B. Zhang, S. H. Wei, and A. Zunger, "Intrinsic n-type versus p-type doping asymmetry and the defect physics of ZnO," *Physical Review B*, vol. 63, pp. 075205, 2001.
[39] T. Minami, H. Nanto, and S. Takata, "High conductive and transparent aluminium doped zinc oxide thin films prepared by rf magnetron sputtering," *Japanese Journal of Applied Physics, Part 2: Letters*, vol. 23, pp. 280-282, 1984.
[40] H. J. Ko, Y. F. Chen, S. K. Hong, H. Wenisch, T. Yao, and D. C. Look, "Ga-doped ZnO films grown on GaN templates by plasma-assisted molecular-beam epitaxy," *Applied Physics Letters*, vol. 77, pp. 3761-3763, 2000.
[41] B. M. Ataev, A. M. Bagamadova, A. M. Djabrailov, V. V. Mamedov, and R. A. Rabadanov, "Highly conductive and transparent Ga-doped epitaxial ZnO films on sapphire by CVD," *Thin Solid Films*, vol. 260, pp. 19-20, 1995.
[42] E. C. Lee and K. J. Chang, "Possible p-type doping with group-I elements in ZnO," *Physical Review B - Condensed Matter and Materials Physics*, vol. 70, 2004.
[43] D. C. Look and B. Claflin, "P-type doping and devices based on ZnO," *physica status solidi (b)*, vol. 241, pp. 624-630, 2004.
[44] R. M. Park, M. B. Troffer, C. M. Rouleau, J. M. DePuydt, and M. A. Haase, "p-type ZnSe by nitrogen atom beam doping during molecular beam epitaxial growth," *Applied Physics Letters*, vol. 57, pp. 2127-2129, 1990.
[45] E. Tournié, P. Brunet, and J. P. Faurie, "Evidence of N-related compensating donors in lightly doped ZnSe:N," *Applied Physics Letters*, vol. 74, pp. 2200-2202, 1999.
[46] X. Li, S. E. Asher, S. Limpijumnong, B. M. Keyes, C. L. Perkins, T. M. Barnes, H. R. Moutinho, J. M. Luther, S. B. Zhang, S.-H. Wei, and T. J. Coutts, "Impurity effects in ZnO and nitrogen-doped ZnO thin films fabricated by MOCVD," *Journal of Crystal Growth*, vol. 287, pp. 94-100, 2006.
[47] Y. Marfaing and A. Lusson, "Doping engineering of p-type ZnO," *Superlattices and Microstructures*, vol. 38, pp. 385-396, 2005.
[48] C. H. Park, S. B. Zhang, and S. H. Wei, "Origin of p-type doping difficulty in ZnO: The impurity perspective," *Physical Review B - Condensed Matter and Materials Physics*, vol. 66, pp. 732021-732023, 2002.

[49] E. C. Lee, Y. S. Kim, Y. G. Jin, and K. J. Chang, "Compensation mechanism for N acceptors in ZnO," *Physical Review B - Condensed Matter and Materials Physics*, vol. 64, pp. 851201-851205, 2001.

[50] Y. Yan, M. M. Al-Jassim, and S.-H. Wei, "Doping of ZnO by group-IB elements," *Applied Physics Letters*, vol. 89, pp. 181912-3, 2006.

[51] Y. Yan, J. Li, S. H. Wei, and M. M. Al-Jassim, "Possible approach to overcome the doping asymmetry in wideband gap semiconductors," *Physical Review Letters*, vol. 98, pp. 135506, 2007.

[52] W. Walukiewicz, "Intrinsic limitations to the doping of wide-gap semiconductors," *Physica B: Condensed Matter*, vol. 302-303, pp. 123-134, 2001.

[53] P. D. C. King, T. D. Veal, D. J. Payne, A. Bourlange, R. G. Egdell, and C. F. McConville, "Surface electron accumulation and the charge neutrality level in In2O3," *Physical Review Letters*, vol. 101, pp. 116808, 2008.

[54] A. Schleife, F. Fuchs, C. Rodl, J. Furthmuller, and F. Bechstedt, "Branch-point energies and band discontinuities of III-nitrides and III-/II-oxides from quasiparticle band-structure calculations," *Applied Physics Letters*, vol. 94, pp. 012104, 2009.

[55] T. D. Veal, L. F. J. Piper, W. J. Schaff, and C. F. McConville, "Inversion and accumulation layers at InN surfaces," *Journal of Crystal Growth*, vol. 288, pp. 268-272, 2006.

[56] S. B. Zhang, S.-H. Wei, and A. Zunger, "A phenomenological model for systematization and prediction of doping limits in II--VI and I--III--VI[sub 2] compounds," *Journal of Applied Physics*, vol. 83, pp. 3192-3196, 1998.

[57] S. Lany, J. Osorio-Guille?n, and A. Zunger, "Origins of the doping asymmetry in oxides: Hole doping in NiO versus electron doping in ZnO," *Physical Review B - Condensed Matter and Materials Physics*, vol. 75, pp. 241203, 2007.

[58] A. Icshba, J. Ueno, K. Ogura, S. Katsuta, and M. Kobayashi, "Growth and optical property characterizations of ZnTe:(Al,N) layers using two co-doping techniques," presented at Physica Status Solidi C: Conferences, Warsaw, 2006.

[59] Q. Wan, Z. Xiong, J. Dai, J. Rao, and F. Jiang, "First-principles study of Ag-based p-type doping difficulty in ZnO," *Optical Materials*, vol. 30, pp. 817-821, 2008.

[60] J. Hu and B. C. Pan, "Electronic structures of defects in ZnO: Hybrid density functional studies," *Journal of Chemical Physics*, vol. 129, pp. 154706, 2008.

[61] L. Duan, B. Lin, W. Zhang, S. Zhong, and Z. Fu, "Enhancement of ultraviolet emissions from ZnO films by Ag doping," *Applied Physics Letters*, vol. 88, pp. 232110-3, 2006.

[62] J. Chai, R. Mendelsberg, R. Reeves, J. Kennedy, H. v. Wenckstern, M. Schmidt, M. Grundmann, K. Doyle, T. Myers, and S. Durbin, "Identification of a Deep Acceptor Level in ZnO Due to Silver Doping," *Journal of Electronic Materials*, in press.

[63] Y. Zhang, Z. Zhang, B. Lin, Z. Fu, and J. Xu, "Effects of Ag doping on the photoluminescence of ZnO films grown on Si substrates," *Journal of Physical Chemistry B*, vol. 109, pp. 19200-19203, 2005.

[64] J. Xu, Z. Y. Zhang, Y. Zhang, B. X. Lin, and Z. X. Fu, "Effect of Ag doping on optical and electrical properties of ZnO thin films," *Chinese Physics Letters*, vol. 22, pp. 2031-2034, 2005.
[65] L. J. Sun, S. Zhong, W. Y. Zhang, Z. Wang, B. X. Lin, and Z. X. Fu, "Electrical and optical properties of Ag doped p-type ZnO films and its homojunctions properties," *Chinese Journal of Luminescence*, vol. 29, pp. 304-308, 2008.
[66] E. K. Jeong, I. S. Kim, D. H. Kim, and S. Y. Choi, "Effect of deposition and annealing temperature on structural, electrical and optical properties of Ag doped ZnO thin films," *Korean Journal of Materials Research*, vol. 18, pp. 84-91, 2008.
[67] H. Y. Lee, H. J. Ko, and T. Yao, "Effect of Ag photodoping on deep-level emission spectra of ZnO epitaxial films," *Applied Physics Letters*, vol. 82, pp. 523-525, 2003.
[68] L. Duan, W. Gao, R. Chen, and Z. Fu, "Influence of post-annealing conditions on properties of ZnO:Ag films," *Solid State Communications*, vol. 145, pp. 479-481, 2008.
[69] S. H. Jeong, B. N. Park, S. B. Lee, and J. H. Boo, "Structural and optical properties of silver-doped zinc oxide sputtered films," *Surface and Coatings Technology*, vol. 193, pp. 340-344, 2005.
[70] B. D. Ahn, H. S. Kang, J. H. Kim, G. H. Kim, H. W. Chang, and S. Y. Lee, "Synthesis and analysis of Ag-doped ZnO," *Journal of Applied Physics*, vol. 100, pp. 093701-6, 2006.
[71] U. Wahl, E. Rita, J. G. Correia, T. Agne, E. Alves, and J. C. Soares, "Lattice sites of implanted Cu and Ag in ZnO," *Superlattices and Microstructures*, vol. 39, pp. 229-237, 2006.
[72] Y. Kanai, "Admittance spectroscopy of ZnO crystals containing Ag," *Japanese Journal of Applied Physics, Part 1: Regular Papers and Short Notes and Review Papers*, vol. 30, pp. 2021-2022, 1991.
[73] H. S. Kang, B. D. Ahn, J. H. Kim, G. H. Kim, S. H. Lim, H. W. Chang, and S. Y. Lee, "Structural, electrical, and optical properties of p-type ZnO thin films with Ag dopant," *Applied Physics Letters*, vol. 88, pp. 202108, 2006.
[74] W. Bin, Z. Yue, M. Jiahua, and S. Wenbin, "Ag-N dual-accept doping for the fabrication of p-type ZnO," *Applied Physics A: Materials Science and Processing*, vol. 94, pp. 715-718, 2009.
[75] I. S. Kim, E.-K. Jeong, D. Y. Kim, M. Kumar, and S.-Y. Choi, "Investigation of p-type behavior in Ag-doped ZnO thin films by E-beam evaporation," *Applied Surface Science*, vol. 255, pp. 4011-4014, 2009.
[76] F. J. Lugo, H. S. Kim, S. J. Pearton, C. R. Abernathy, B. P. Gila, D. P. Norton, Y. L. Wang, and F. Ren, "Rectifying ZnO:Ag/ZnO:Ga Thin-Film Junctions," *Electrochemical and Solid State Letters*, vol. 12, pp. H188-H190, 2009.
[77] S. H. Jeong, B. N. Park, S. B. Lee, and J. H. Boo, "Metal-doped ZnO thin films: Synthesis and characterizations," *Surface and Coatings Technology*, vol. 201, pp. 5318-5322, 2007.
[78] A. N. Gruzintsev, V. T. Volkov, and E. E. Yakimov, "Photoelectric properties of ZnO films doped with Cu and Ag acceptor impurities," *Semiconductors*, vol. 37, pp. 259-262, 2003.

[79] N. M. Litchinitser and V. M. Shalaev, "Photonic metamaterials," *Laser Physics Letters*, vol. 5, pp. 411-420, 2008.
[80] P. Chaturvedi, K. Hsu, S. Zhang, and N. Fang, "New frontiers of metamaterials: Design and fabrication," *MRS Bulletin*, vol. 33, pp. 915-920, 2008.
[81] H. J. Levinson, *Principles of Lithography*, 2nd ed. USA: SPIE - The International Society for Optical Engineering, 2005.
[82] V. G. Veselago, "The Electrodynamics of Substances With Simultaneously Negative Values of Epsilon and Mu," *Soviet Physics Uspekhi*, vol. 10, pp. 509-514, 1968.
[83] R. A. Shelby, D. R. Smith, and S. Schultz, "Experimental verification of a negative index of refraction," *Science*, vol. 292, pp. 77-79, 2001.
[84] E. N. Economou, M. Kafesaki, C. M. Soukoulis, and T. Koschny, "The fourth quadrant in the ε, μ plane: A new frontier in optics," *Journal of Computational and Theoretical Nanoscience*, vol. 6, pp. 1827-1836, 2009.
[85] W. Park and J. Kim, "Negative-index materials: Optics by design," *MRS Bulletin*, vol. 33, pp. 907-914, 2008.
[86] J. B. Pendry, "Negative Refraction Makes a Perfect Lens," *Physical Review Letters*, vol. 85, pp. 3966, 2000.
[87] X. Zhang and Z. Liu, "Superlenses to overcome the diffraction limit," *Nature Materials*, vol. 7, pp. 435-441, 2008.
[88] N. Fang, H. Lee, C. Sun, and X. Zhang, "Sub-diffraction-limited optical imaging with a silver superlens," *Science*, vol. 308, pp. 534-537, 2005.
[89] R. J. Blaikie, D. O. S. Melville, and M. M. Alkaisi, "Super-resolution near-field lithography using planar silver lenses: A review of recent developments," *Microelectronic Engineering*, vol. 83, pp. 723-729, 2006.
[90] H. Liu, Shivanand, and K. J. Webb, "Subwavelength imaging opportunities with planar uniaxial anisotropic lenses," *Opt. Lett.*, vol. 33, pp. 2568-2570, 2008.
[91] D. O. S. Melville, R. J. Blaikie, and M. M. Alkaisi, "A comparison of near-field lithography and planar lens lithography," *Current Applied Physics*, vol. 6, pp. 415-418, 2006.
[92] D. Melville, "Planar Lensing Lithography: Enhancing the Optical Near Field," in *Electrical and Electronic Engineering*, vol. Doctor of Philosophy. Christchurch: University of Canterbury, 2006.
[93] S. Johnson, C. H. Kuo, M. Boonzaayer, W. Braun, U. Koelle, Y. H. Zhang, and J. Roth, "In situ temperature control of molecular beam epitaxy growth using band-edge thermometry," *Journal of Vacuum Science and Technology B: Microelectronics and Nanometer Structures*, vol. 16, pp. 1502-1506, 1998.
[94] K. Mohamed, M. M. Alkaisi, and R. J. Blaikie, "Surface charging suppression using PEDOT/PSS in the fabrication of three dimensional structures on a quartz substrate," *Microelectronic Engineering*, vol. 86, pp. 535-538, 2009.
[95] J. A. Bondur, "Dry Process Technology (Reactive Ion Etching)," *J Vac Sci Technol*, vol. 13, pp. 1023-1029, 1976.
[96] D. K. Schroder, *Semiconductor Material and Device Characterization*, 3rd ed. New Jersey: John Wiley & Sons, Inc., 2006.
[97] M. W. Allen, X. Weng, J. M. Redwing, K. Sarpatwari, S. E. Mohney, H. von Wenckstern, M. Grundmann, and S. M. Durbin, "Temperature-

dependent properties of nearly ideal ZnO schottky diodes," *IEEE Transactions on Electron Devices*, vol. 56, pp. 2160-2164, 2009.
[98] M. W. Allen, M. M. Alkaisi, and S. M. Durbin, "Metal Schottky diodes on Zn-polar and O-polar bulk ZnO," *Applied Physics Letters*, vol. 89, pp. 103520, 2006.
[99] L. J. van der Pauw, "A method of measuring specific resistivity and hall effect of discs of arbitrary size," *Philips Research Reports*, vol. 13, pp. 1-9, 1958.
[100] Y. Gui, B. Li, G. Zheng, Y. Chang, S. Wang, L. He, and J. Chu, "Evaluation of densities and mobilities for heavy and light holes in p-type Hg[sub 1 - x]Cd[sub x]Te molecular beam epitaxy films from magnetic-field-dependent Hall data," *Journal of Applied Physics*, vol. 84, pp. 4327-4331, 1998.
[101] B. Yang, "Electrical characteristics of As-doped p-type HgCdTe epilayers grown on CdZnTe(211)B substrates by molecular beam epitaxy," *Journal of Vacuum Science and Technology B: Microelectronics and Nanometer Structures*, vol. 17, pp. 1205-1208, 1999.
[102] C. H. Swartz, R. P. Tompkins, N. C. Giles, T. H. Myers, H. Lu, W. J. Schaff, and L. F. Eastman, "Investigation of multiple carrier effects in InN epilayers using variable magnetic field Hall measurements," *Journal of Crystal Growth*, vol. 269, pp. 29-34, 2004.
[103] J. R. Meyer, C. A. Hoffman, F. J. Bartoli, D. A. Arnold, S. Sivananthan, and J. P. Fauri, "Methods for magnetotransport characterization of IR detector materials," *Semiconductor Science and Technology*, vol. 8, pp. 805-823, 1993.
[104] G. Vincent, D. Bois, and P. Pinard, "Conductance and capacitance studies in GaP Schottky barriers," *Journal of Applied Physics*, vol. 46, pp. 5173-5178, 1975.
[105] H. von Wenckstern, "PhD Thesis: Doping, contacting, defect levels and transport properties of ZnO," 2007.
[106] M. G. Buehler, "Defects in PN Junctions and MOS Capacitors Observed Using Thermally Stimulated Current and Capacitance Measurements Videotape Script," in *Semiconductor measurement technology*, 1976.
[107] M. G. Buehler, "Impurity centres in PN junctions determined from shifts in the thermally stimulated current and capacitance response with heating rate," *Solid-State Electronics*, vol. 15, pp. 69-79, 1972.
[108] N. G. Semaltianos, G. Karczewski, B. Hu, T. Wojtowicz, and J. K. Furdyna, "Deep-level defects responsible for persistent photoconductivity in Ga-doped Cd1-xMnxTe," *Physical Review B*, vol. 51, pp. 17499-17505, 1995.
[109] C. T. Sah, W. W. Chan, H. S. Fu, and J. W. Walker, "Thermally stimulated capacitance (TSCAP) in p-n junctions," *Applied Physics Letters*, vol. 20, pp. 193-195, 1972.
[110] A. M. Armstrong, "Investigation of deep level defects in GaN:C, GaN:Mg and pseudomorphic AlGaN/GaN films," The Ohio State University, 2006.
[111] H. Witte, A. Krtschil, M. Lisker, D. Rudloff, J. Christen, A. Krost, M. Stutzmann, and F. Scholz, "Fermi level pinning at GaN-interfaces: Correlation of electrical admittance and transient spectroscopy," *Materials Research Society Symposium - Proceedings*, vol. 595, pp. W11821-W11826, 2000.

[112] D. V. Lang, "Deep-level transient spectroscopy: A new method to characterize traps in semiconductors," *Journal of Applied Physics*, vol. 45, pp. 3023-3032, 1974.
[113] D. C. Look, *Electrical Characterization of GaAs Materials and Devices*. USA: John Wiley & Sons, 1989.
[114] A. A. Istratov, O. F. Vyvenko, H. Hieslmair, and E. R. Weber, "Critical analysis of weighting functions for the deep level transient spectroscopy of semiconductors," *Measurement Science and Technology*, vol. 9, pp. 477-484, 1998.
[115] P. Nubile, "Characterization of Defects in Solar Cells Using Trigonometric Weight Functions," *Brazilian Journal of Physics*, vol. 27/A, pp. 97, 1997.
[116] C. Marton, *Advances in electronics and electron physics*, vol. 57, 1981.
[117] R. Kossowsky, "Surface Modification Engineering: Fundamental aspects," 1989.
[118] I. M. Govil, "Proton induced X-ray emission - A tool for non-destructive trace element analysis," *Current Science*, vol. 80, pp. 1542-1549, 2001.
[119] T. H. Gfroerer, "Photoluminescence in Analysis of Surfaces and Interfaces," *Encyclopedia of Analytical Chemistry*, pp. 9209-9231, 2000.
[120] J. I. Pankove, *Optical Processes In Semiconductors*. New York: Dover Publications, Inc., 1971.
[121] B. K. Meyer, H. Alves, D. M. Hofmann, W. Kriegseis, D. Forster, F. Bertram, J. Christen, A. Hoffmann, M. Straßburg, M. Dworzak, U. Haboeck, and A. V. Rodina, "Bound exciton and donor-acceptor pair recombinations in ZnO," *Physica Status Solidi (B) Basic Research*, vol. 241, pp. 231-260, 2004.
[122] R. Mendelsberg, "PhD Thesis: Photoluminescence of ZnO Grown by Eclipse Pulsed Laser deposition," 2009.
[123] M. Schirra, R. Schneider, A. Reiser, G. M. Prinz, M. Feneberg, J. Biskupek, U. Kaiser, C. E. Krill, R. Sauer, and K. Thonke, "Acceptor-related luminescence at 3.314 eV in zinc oxide confined to crystallographic line defects," *Physica B: Condensed Matter*, vol. 401-402, pp. 362-365, 2007.
[124] K. Hirano, M. Fujita, M. Sasajima, T. Kosaka, and Y. Horikoshi, "ZnO epitaxial films grown by flux-modulated RF-MBE," *Journal of Crystal Growth*, vol. 301-302, pp. 370-372, 2007.
[125] M. W. Cho, A. Setiawan, H. J. Ko, S. K. Hong, and T. Yao, "ZnO epitaxial layers grown on c-sapphire substrate with MgO buffer by plasma-assisted molecular beam epitaxy (P-MBE)," *Semiconductor Science and Technology*, vol. 20, pp. S13-S21, 2005.
[126] H. J. Ko, T. Yao, Y. Chen, and S. K. Hong, "Investigation of ZnO epilayers grown under various Zn/O ratios by plasma-assisted molecular-beam epitaxy," *Journal of Applied Physics*, vol. 92, pp. 4354, 2002.
[127] kSA, "Band Edge Thermometry vs. Emissivity-Corrected Pyrometry," 2007.
[128] I. Farrer, J. J. Harris, R. Thomson, D. Barlett, C. A. Taylor, and D. A. Ritchie, "Substrate temperature measurement using a commercial band-edge detection system," *Journal of Crystal Growth*, vol. 301-302, pp. 88-92, 2007.

[129] H. Matsui, H. Saeki, T. Kawai, A. Sasaki, M. Yoshimoto, M. Tsubaki, and H. Tabata, "Characteristics of polarity-controlled ZnO films fabricated using the homoepitaxy technique," *Journal of Vacuum Science and Technology B: Microelectronics and Nanometer Structures*, vol. 22, pp. 2454-2461, 2004.
[130] H. Kato, M. Sano, K. Miyamoto, and T. Yao, "Homoepitaxial growth of high-quality Zn-polar ZnO films by plasma-assisted molecular beam epitaxy," *Japanese Journal of Applied Physics Part 2-Letters*, vol. 42, pp. L1002-L1005, 2003.
[131] I. C. Robin, A. Ribeaud, S. Brochen, G. Feuillet, P. Ferret, H. Mariette, D. Ehrentraut, and T. Fukuda, "Low residual doping level in homoepitaxially grown ZnO layers," *Applied Physics Letters*, vol. 92, pp. 141101-3, 2008.
[132] Y. Chen, D. M. Bagnall, H. J. Koh, K. T. Park, K. Hiraga, Z. Zhu, and T. Yao, "Plasma assisted molecular beam epitaxy of ZnO on c-plane sapphire: Growth and characterization," *Journal of Applied Physics*, vol. 84, pp. 3912-3918, 1998.
[133] Y. Chen, D. M. Bagnall, Z. Zhu, T. Sekiuchi, K. T. Park, K. Hiraga, T. Yao, S. Koyama, M. Y. Shen, and T. Goto, "Growth of ZnO single crystal thin films on c-plane (0 0 0 1) sapphire by plasma enhanced molecular beam epitaxy," *Journal of Crystal Growth*, vol. 181, pp. 165-169, 1997.
[134] B. Pecz, A. El-Shaer, A. Bakin, A. C. Mofor, A. Waag, and J. Stoemenos, "Structural characterization of ZnO films grown by molecular beam epitaxy on sapphire with MgO buffer," *Journal of Applied Physics*, vol. 100, pp. 103506-7, 2006.
[135] Y. Chen, H. J. Ko, S. K. Hong, T. Yao, and Y. Segawa, "Two-dimensional growth of ZnO films on sapphire(0001) with buffer layers," *Journal of Crystal Growth*, vol. 214, pp. 87-91, 2000.
[136] A. Setiawan, H. J. Ko, S. K. Hong, Y. Chen, and T. Yao, "Study on MgO buffer in ZnO layers grown by plasma-assisted molecular beam epitaxy on Al2O3(0001)," *Thin Solid Films*, vol. 445, pp. 213-218, 2003.
[137] H. Goto, H. Makino, A. Setiawan, T. Suzuki, C. Harada, T. Minegishi, M. W. Cho, and T. Yao, "Reduction of dislocation density and improvement of optical quality in ZnO layers by MgO-buffer annealing," *Current Applied Physics*, vol. 4, pp. 637-639, 2004.
[138] Y. F. Chen, H. J. Ko, S. K. Hong, K. Inaba, Y. Segawa, and T. Yao, "Plasma-assisted molecular beam epitaxy of ZnO thin films on sapphire substrates with an MgO buffer," *Journal of Crystal Growth*, vol. 227-228, pp. 917-922, 2001.
[139] Y. Chen, H. J. Ko, S. K. Hong, T. Yao, and Y. Segawa, "Morphology evolution of ZnO(000-1) surface during plasma-assisted molecular-beam epitaxy," *Applied Physics Letters*, vol. 80, pp. 1358, 2002.
[140] Y. Chen, H. J. Ko, S. K. Hong, and T. Yao, "Layer-by-layer growth of ZnO epilayer on Al2O3(0001) by using a MgO buffer layer," *Applied Physics Letters*, vol. 76, pp. 559-561, 2000.
[141] K. Miyamoto, M. Sano, H. Kato, and T. Yao, "High-electron-mobility ZnO epilayers grown by plasma-assisted molecular beam epitaxy," *Journal of Crystal Growth*, vol. 265, pp. 34-40, 2004.
[142] A. El-Shaer, A. Bakin, A. Che Mofor, J. Stoimenos, B. PÃ©cz, and A. Waag, "Layer by layer growth of ZnO on (0001) sapphire substrates by

radical-source molecular beam epitaxy," *Superlattices and Microstructures*, vol. 42, pp. 158-164, 2007.
[143] H. Kato, M. Sano, K. Miyamoto, and T. Yao, "Polarity control of ZnO on c-plane sapphire by plasma-assisted MBE," *Journal of Crystal Growth*, vol. 275, pp. e2459-e2465, 2005.
[144] X. H. Wei, W. J. Jie, W. Huang, J. Zhu, and Y. R. Li, "Effect of symmetry of substrate surfaces on the orientation and growth mode of ZnO films," *Journal of Crystal Growth*, vol. 311, pp. 2391-2396, 2009.
[145] Y. Nukaga, M. Ohtake, M. Futamoto, F. Kirino, N. Fujita, and N. Inaba, "Structure and Magnetic Properties of Co Epitaxial Thin Films Grown on MgO Single-Crystal Substrates," *Magnetics, IEEE Transactions on*, vol. 45, pp. 2519-2522, 2009.
[146] T. L. Goodrich, Z. Cai, M. D. Losego, J. P. Maria, L. Fitting Kourkoutis, D. A. Muller, and K. S. Ziemer, "Improved epitaxy of barium titanate by molecular beam epitaxy through a single crystalline magnesium oxide template for integration on hexagonal silicon carbide," *Journal of Vacuum Science and Technology B: Microelectronics and Nanometer Structures*, vol. 26, pp. 1110-1114, 2008.
[147] J. J. Chen, B. P. Gila, M. Hlad, A. Gerger, F. Ren, C. R. Abernathy, and S. J. Pearton, "Determination of MgO/GaN heterojunction band offsets by x-ray photoelectron spectroscopy," *Applied Physics Letters*, vol. 88, pp. 042113-3, 2006.
[148] H. Kato, K. Miyamoto, M. Sano, and T. Yao, "Polarity control of ZnO on sapphire by varying the MgO buffer layer thickness," *Applied Physics Letters*, vol. 84, pp. 4562-4564, 2004.
[149] T. Minegishi, J. Yoo, H. Suzuki, Z. Vashaei, K. Inaba, K. Shim, and T. Yao, "Selective growth of Zn- and O-polar ZnO layers by plasma-assisted molecular beam epitaxy," *Journal of Vacuum Science and Technology B: Microelectronics and Nanometer Structures*, vol. 23, pp. 1286-1290, 2005.
[150] H. Tampo, P. Fons, A. Yamada, K. K. Kim, H. Shibata, K. Matsubara, H. Yoshikawa, H. Kanie, and S. Niki, "Determination of crystallographic polarity of ZnO bulk crystals and epilayers," presented at Physica Status Solidi C: Conferences, Warsaw, 2006.
[151] B. J. Kwon, Y. Sun, J. S. Chung, Y. H. Cho, J. S. Park, and T. Yao, "Optical properties and carrier dynamics of polarity controlled ZnO films grown on (0001) Al2O3 by Cr-compound intermediate layers," *Applied Physics Letters*, vol. 94, pp. 061918, 2009.
[152] A. N. Mariano and R. E. Hanneman, "Crystallographic Polarity of ZnO Crystals," *Journal of Applied Physics*, vol. 34, pp. 384-388, 1963.
[153] H. Tampo, P. Fons, A. Yamada, K. K. Kim, H. Shibata, K. Matsubara, S. Niki, H. Yoshikawa, and H. Kanie, "Determination of crystallographic polarity of ZnO layers," *Applied Physics Letters*, vol. 87, pp. 141904-3, 2005.
[154] F. Vigué, C. Deparis, P. Vennéguès, S. Vézian, M. Laügt, P. Lorenzini, C. Morhain, F. Raymond, J. Guion, and J. P. Faurie, "2D versus 3D Growth Mode in ZnO Layers Grown by Plasma-Enhanced Molecular Beam Epitaxy on (0001) Sapphire," *physica status solidi (b)*, vol. 229, pp. 931-934, 2002.

[155] I. C. Robin, C. Tavares, J. Rothman, G. Feuillet, A. H. El-Shaer, A. Bakin, A. Waag, and L. S. Dang, "Structural and spectroscopic properties of a 2 inch ZnO-on-sapphire epiwafer grown by using molecular beam epitaxy," *Journal of the Korean Physical Society*, vol. 53, pp. 2877-2879, 2008.
[156] Y. S. Jung, Y. S. No, J. S. Kim, and W. K. Choi, "The effect of ZnO homo-buffer layer on ZnO thin films grown on c-Al 2O3(0 0 0 1) by plasma assisted molecular beam epitaxy," *Journal of Crystal Growth*, vol. 267, pp. 85-91, 2004.
[157] H. Tampo, A. Yamada, P. Fons, H. Shibata, K. Matsubara, K. Iwata, K. Nakahara, and S. Niki, "Effects of low temperature buffer layer treatments on the growth of high quality ZnO films," *physica status solidi (c)*, vol. 1, pp. 888-891, 2004.
[158] Y. S. Jung, O. Kononenko, J. S. Kim, and W. K. Choi, "Two-dimensional growth of ZnO epitaxial films on c-Al2O 3 (0 0 0 1) substrates with optimized growth temperature and low-temperature buffer layer by plasma-assisted molecular beam epitaxy," *Journal of Crystal Growth*, vol. 274, pp. 418-424, 2005.
[159] T. E. Murphy, S. Walavalkar, and J. D. Phillips, "Epitaxial growth and surface modeling of ZnO on c -plane Al2 O3," *Applied Physics Letters*, vol. 85, pp. 6338-6340, 2004.
[160] B. K. Meyer, S. Lautenschlager, S. Graubner, C. Neumann, and J. Sann, "Photoluminescence investigations on a native donor in ZnO," presented at Materials Research Society Symposium Proceedings, Boston, MA, 2006.
[161] K. Iwata, H. Tampo, A. Yamada, P. Fons, K. Matsubara, K. Sakurai, S. Ishizuka, and S. Niki, "Growth of ZnO and device applications," *Applied Surface Science*, vol. 244, pp. 504-510, 2005.
[162] U. Fano, "Effects of configuration interaction on intensities and phase shifts," *Physical Review*, vol. 124, pp. 1866-1878, 1961.
[163] S. J. Xu, S.-J. Xiong, and S. L. Shi, "Resonant coupling of bound excitons with LO phonons in ZnO: Excitonic polaron states and Fano interference," *The Journal of Chemical Physics*, vol. 123, pp. 221105-5, 2005.
[164] W. C. T. Lee, M. Henseler, P. Miller, C. H. Swartz, T. H. Myers, R. J. Reeves, and S. M. Durbin, "Effect of annealing on the morphology and optoelectrical characteristics of ZnO thin films grown by plasma-assisted molecular beam epitaxy," *Journal of Electronic Materials*, vol. 35, pp. 1316-1321, 2006.
[165] O. Bierwagen, T. Ive, C. G. Van de Walle, and J. S. Speck, "Causes of incorrect carrier-type identification in van der Pauw--Hall measurements," *Applied Physics Letters*, vol. 93, pp. 242108-3, 2008.
[166] J. G. Lu, Y. Z. Zhang, Z. Z. Ye, L. P. Zhu, L. Wang, B. H. Zhao, and Q. L. Liang, "Low-resistivity, stable p-type ZnO thin films realized using a Li-N dual-acceptor doping method," *Applied Physics Letters*, vol. 88, 2006.
[167] Y. J. Zeng, Z. Z. Ye, W. Z. Xu, L. L. Chen, D. Y. Li, L. P. Zhu, B. H. Zhao, and Y. L. Hu, "Realization of p-type ZnO films via monodoping of Li acceptor," *Journal of Crystal Growth*, vol. 283, pp. 180-184, 2005.
[168] B. Xiao, Z. Ye, Y. Zhang, Y. Zeng, L. Zhu, and B. Zhao, "Fabrication of p-type Li-doped ZnO films by pulsed laser deposition," *Applied Surface Science*, vol. 253, pp. 895-897, 2006.

[169] L. L. Chen, Z. Z. Ye, J. G. Lu, and P. K. Chu, "Control and improvement of p-type conductivity in indium and nitrogen codoped ZnO thin films," *Applied Physics Letters*, vol. 89, pp. 252113-3, 2006.
[170] T. E. Murphy, D. Y. Chen, E. Cagin, and J. D. Phillips, "Electronic properties of ZnO epilayers grown on c-plane sapphire by plasma-assisted molecular beam epitaxy," *Journal of Vacuum Science and Technology B: Microelectronics and Nanometer Structures*, vol. 23, pp. 1277-1280, 2005.
[171] F. X. Xiu, Z. Yang, L. J. Mandalapu, and J. L. Liu, "Donor and acceptor competitions in phosphorus-doped ZnO," *Applied Physics Letters*, vol. 88, pp. 152116-3, 2006.
[172] F. X. Xiu, Z. Yang, L. J. Mandalapu, D. T. Zhao, J. L. Liu, and W. P. Beyermann, "High-mobility Sb-doped p-type ZnO by molecular-beam epitaxy," *Applied Physics Letters*, vol. 87, pp. 1-3, 2005.
[173] M. F. Al-Kuhaili, "Characterization of thin films produced by the thermal evaporation of silver oxide," *Journal of Physics D: Applied Physics*, vol. 40, pp. 2847-2853, 2007.
[174] Y. Abe, T. Hasegawa, M. Kawamura, and K. Sasaki, "Characterization of Ag oxide thin films prepared by reactive RF sputtering," *Vacuum*, vol. 76, pp. 1-6, 2004.
[175] J. F. Pierson, D. Wiederkehr, and A. Billard, "Reactive magnetron sputtering of copper, silver, and gold," *Thin Solid Films*, vol. 478, pp. 196-205, 2005.
[176] S. B. Rivers, G. Bernhardt, M. W. Wright, D. J. Frankel, M. M. Steeves, and R. J. Lad, "Structure, conductivity, and optical absorption of Ag2-xO films," *Thin Solid Films*, vol. 515, pp. 8684-8688, 2007.
[177] U. Kumar Barik, S. Srinivasan, C. L. Nagendra, and A. Subrahmanyam, "Electrical and optical properties of reactive DC magnetron sputtered silver oxide thin films: role of oxygen," *Thin Solid Films*, vol. 429, pp. 129-134, 2003.
[178] M. A. Thomas and J. B. Cui, "Investigations of acceptor related photoluminescence from electrodeposited Ag-doped ZnO," *Journal of Applied Physics*, vol. 105, pp. 093533, 2009.
[179] S. H. Park, T. Minegishi, M. Ito, J. S. Park, I. H. Im, J. H. Chang, D. C. Oh, H. J. Ko, M. W. Cho, and T. Yao, "The effect of growth temperature on nitrogen incorporation into ZnO film grown on Al2O3 substrate," *Journal of Crystal Growth*, vol. 311, pp. 466-469, 2009.
[180] S. H. Park, J. H. Chang, H. J. Ko, T. Minegishi, J. S. Park, I. H. Im, M. Ito, D. C. Oh, M. W. Cho, and T. Yao, "Lattice deformation of ZnO films with high nitrogen concentration," *Applied Surface Science*, vol. 254, pp. 7972-7975, 2008.
[181] G. M. Gavaza, Z. G. Yu, and P. Wu, "A universal theoretical approach for examining the efficiency of doping processes in semiconductors," *Journal of Applied Physics*, vol. 105, pp. 113711, 2009.
[182] B. K. Meyer, J. Sann, S. Lautenschlager, M. R. Wagner, and A. Hoffmann, "Ionized and neutral donor-bound excitons in ZnO," *Physical Review B (Condensed Matter and Materials Physics)*, vol. 76, pp. 184120-4, 2007.
[183] Y. S. Park, C. W. Litton, T. C. Collins, and D. C. Reynolds, "Exciton spectrum of ZnO," *Physical Review*, vol. 143, pp. 512-519, 1966.

[184] J. Jenny, R. Jones, J. E. Van Nostrand, D. C. Reynolds, D. C. Look, and B. Jogai, "Source of the yellow luminescence band in GaN grown by gas-source molecular beam epitaxy and the green luminescence band in single crystal ZnO," *Solid State Communications*, vol. 106, pp. 701-704, 1998.
[185] Y. W. Heo, D. P. Norton, and S. J. Pearton, "Origin of green luminescence in ZnO thin film grown by molecular-beam epitaxy," *Journal of Applied Physics*, vol. 98, pp. 073502-6, 2005.
[186] M. W. Allen, S. M. Durbin, and J. B. Metson, "Silver oxide Schottky contacts on n-type ZnO," *Applied Physics Letters*, vol. 91, pp. 053512, 2007.
[187] H. von Wenckstern, A. Lajn, A. Laufer, B. K. Meyer, H. Hochmuth, M. Lorenz, and M. Grundmann, "Ag related defect state in ZnO thin films," *AIP conference proceedings, in press*, 2009.
[188] H. Von Wenckstern, H. Schmidt, M. Grundmann, M. W. Allen, P. Miller, R. J. Reeves, and S. M. Durbin, "Defects in hydrothermally grown bulk ZnO," *Applied Physics Letters*, vol. 91, pp. 022913, 2007.
[189] M. W. Allen and S. M. Durbin, "Influence of oxygen vacancies on Schottky contacts to ZnO," *Applied Physics Letters*, vol. 92, 2008.
[190] D. C. Oh, T. Suzuki, J. J. Kim, H. Makino, T. Hanada, M. W. Cho, and T. Yao, "Electron-trap centers in ZnO layers grown by molecular-beam epitaxy," *Applied Physics Letters*, vol. 86, pp. 032909-3, 2005.
[191] K. Liu, B. F. Yang, H. Yan, Z. Fu, M. Wen, Y. Chen, and J. Zuo, "Strong room-temperature ultraviolet emission from nanocrystalline ZnO and ZnO:Ag films grown by ultrasonic spray pyrolysis," *Applied Surface Science*, vol. 255, pp. 2052-2056, 2008.
[192] J. Benschop, V. Banine, S. Lok, and E. Loopstra, "Extreme ultraviolet lithography: Status and prospects," *Journal of Vacuum Science and Technology B: Microelectronics and Nanometer Structures*, vol. 26, pp. 2204-2207, 2008.
[193] E. R. Kieft, J. J. A. M. van der Mullen, G. M. W. Kroesen, V. Banine, and K. N. Koshelev, "Characterization of a vacuum-arc discharge in tin vapor using time-resolved plasma imaging and extreme ultraviolet spectrometry," *Physical Review E*, vol. 71, pp. 026409, 2005.
[194] T. Itani, "Recent status and future direction of EUV resist technology," *Microelectronic Engineering*, vol. 86, pp. 207-212, 2009.
[195] MicroChemicals, *Lithography: Theory and Application of Photoresists, Developers, Solvents and Etchants*, 2008.
[196] K. Mohamed, M. M. Alkaisi, and R. J. Blaikie, "Fabrication of three dimensional structures for an UV curable nanoimprint lithography mold using variable dose control with critical-energy electron beam exposure," *Journal of Vacuum Science and Technology B: Microelectronics and Nanometer Structures*, vol. 25, pp. 2357-2360, 2007.
[197] C. P. Moore, R. J. Blaikie, and M. D. Arnold, "An improved transfer-matrix model for optical superlenses," *Optics Express*, vol. 17, pp. 14260-14269, 2009.
[198] G. O. Reynolds, J. B. Develis, G. B. Parrent, and B. J. Thompson, *The New Physical Optics Notebook: Tutorials in Fourier Optics*. Washington: SPIE (Society of Photo-Optical Instrumentation Engineers), 1990.
[199] M. Allen, private communication.

[200] S. Anantha Ramakrishna, "Physics of negative refractive index materials," *Reports on Progress in Physics*, vol. 68, pp. 449-521, 2005.
[201] R. A. Shelby, D. R. Smith, S. C. Nemat-Nasser, and S. Schultz, "Microwave transmission through a two-dimensional, isotropic, left-handed metamaterial," *Applied Physics Letters*, vol. 78, pp. 489-491, 2001.
[202] D. R. Smith and N. Kroll, "Negative Refractive Index in Left-Handed Materials," *Physical Review Letters*, vol. 85, pp. 2933, 2000.
[203] W. J. Padilla, D. N. Basov, and D. R. Smith, "Negative refractive index metamaterials," *Materials Today*, vol. 9, pp. 28-35, 2006.
[204] V. Veselago, L. Braginsky, V. Shklover, and C. Hafner, "Negative refractive index materials," *Journal of Computational and Theoretical Nanoscience*, vol. 3, pp. 189-218, 2006.

Appendix A : Film Identification

All MBE films grown at the University are catalogued using a standard code, namely A-B/C/D-E, where A is the number of MBE films grown so far, B is the epitaxial layer grown, C is the buffer layer material, D is the substrate used and E is the film number in the growth series. For example, 345-ZnO/MgO/Sa-1 represents the 345th film grown by the MBE group, and is the first ZnO epilayer film with a MgO buffer layer, grown on a sapphire substrate.

Figure/Table	Identifier	Catalogue Code
Fig. 3.4		589-ZnO/MgO/Sa
Fig. 3.6		589-ZnO/MgO/Sa
Fig. 3.15		586-ZnO/MgO/Sa
Fig. 3.16		597-ZnO/MgO/Sa
Fig. 3.19		597-ZnO/MgO/Sa
Fig. 3.17		607-MgO/Sa
Fig. 3.18		607-MgO/Sa
Fig. 3.20		597-ZnO/MgO/Sa
Fig. 3.24	A1	602-ZnO/MgO/Sa
Fig. 3.22	A1	602-ZnO/MgO/Sa
Fig. 3.22	A2	603-ZnO/MgO/Sa
Fig. 3.22	A3	600-ZnO/MgO/Sa
Fig. 3.22	A4	593-ZnO/MgO/Sa
Table 3.12	A5	597-ZnO/MgO/Sa
Fig. 3.29	(a), 400°C	626-ZnO/MgO/Sa
Fig. 3.29	(b), 600°C	599-ZnO/MgO/Sa
Fig. 3.29	(c), 700°C	593-ZnO/MgO/Sa
Fig. 3.29	(d), 800°C	597-ZnO/MgO/Sa
Fig. 4.2	(a), 400°C, undoped	626-ZnO/MgO/Sa
Fig. 4.2	(b), 600°C, undoped	599-ZnO/MgO/Sa
Fig. 4.2	(c), 800°C, undoped	597-ZnO/MgO/Sa
Fig. 4.2	(d), 400°C, 1.5×10^{18} Ag/cm^3	646-ZnO:Ag/ZnO/MgO/Sa
Fig. 4.2	(e) , 600°C, 1.5×10^{18} Ag/cm^3	631-ZnO:Ag/ZnO/MgO/Sa
Fig. 4.2	(f) , 800°C, 1.5×10^{18} Ag/cm^3	643-ZnO:Ag/ZnO/MgO/Sa
Fig. 4.2	(g) , 400°C, 1.5×10^{19} Ag/cm^3	623-ZnO:Ag/ZnO/MgO/Sa
Fig. 4.2	(h) , 600°C, 1.5×10^{19} Ag/cm^3	622-ZnO:Ag/ZnO/MgO/Sa
Fig. 4.2	(i) , 800°C, 1.5×10^{19} Ag/cm^3	625-ZnO:Ag/ZnO/MgO/Sa
Fig. 4.2	(j) , 400°C, 1.5×10^{20} Ag/cm^3	618-ZnO:Ag/ZnO/MgO/Sa
Fig. 4.2	(k) , 600°C, 1.5×10^{20} Ag/cm^3	616-ZnO:Ag/ZnO/MgO/Sa
Fig. 4.2	(l) , 800°C, 1.5×10^{20} Ag/cm^3	614-ZnO:Ag/ZnO/MgO/Sa
Fig. 4.4	AZ1	622-ZnO:Ag/ZnO/MgO/Sa
Fig. 4.4	AZ2	616-ZnO:Ag/ZnO/MgO/Sa
Fig. 4.9	800°C, 1.5×10^{20} Ag/cm^3	614-ZnO:Ag/ZnO/MgO/Sa
Fig. 4.9	800°C, 1.5×10^{19} Ag/cm^3	625-ZnO:Ag/ZnO/MgO/Sa

Figure/Table	Identifier	Catalogue Code
Fig. 4.9	800°C, 1.5×10^{18} Ag/cm^3	643-ZnO:Ag/ZnO/MgO/Sa
Fig. 4.9	800°C, undoped	597-ZnO/MgO/Sa
Fig. 4.10	600°C, 1.5×10^{20} Ag/cm^3	616-ZnO:Ag/ZnO/MgO/Sa
Fig. 4.10	600°C, 1.5×10^{19} Ag/cm^3	622-ZnO:Ag/ZnO/MgO/Sa
Fig. 4.10	600°C, 1.5×10^{18} Ag/cm^3	631-ZnO:Ag/ZnO/MgO/Sa
Fig. 4.10	600°C, undoped	599-ZnO/MgO/Sa
Fig. 4.11	400°C, 1.5×10^{20} Ag/cm^3	618-ZnO:Ag/ZnO/MgO/Sa
Fig. 4.11	400°C, 1.5×10^{19} Ag/cm^3	623-ZnO:Ag/ZnO/MgO/Sa
Fig. 4.11	400°C, 1.5×10^{18} Ag/cm^3	646-ZnO:Ag/ZnO/MgO/Sa
Fig. 4.11	400°C, undoped	626-ZnO/MgO/Sa
Fig. 4.15	7.5×10^{19} Ag/cm^3, O-rich	659-ZnO:Ag/ZnO/MgO/Sa
Fig. 4.15	1.5×10^{18} Ag/cm^3, O-rich	638-ZnO:Ag/ZnO/MgO/Sa
Fig. 4.15	Undoped, O-rich	641-ZnO/MgO/Sa
Fig. 4.16	600°C, 1.5×10^{19} Ag/cm^3	622-ZnO:Ag/ZnO/MgO/Sa
Fig. 4.17	800°C, undoped	597-ZnO/MgO/Sa
Fig. 4.18	800°C, undoped	597-ZnO/MgO/Sa
Fig. 4.19	800°C, undoped	597-ZnO/MgO/Sa
Fig. 4.20	800°C, undoped	597-ZnO/MgO/Sa
Fig. 4.21	600°C, 1.5×10^{19} Ag/cm^3	622-ZnO:Ag/ZnO/MgO/Sa
Fig. 4.22	600°C, 1.5×10^{19} Ag/cm^3	622-ZnO:Ag/ZnO/MgO/Sa
Fig. 4.23	600°C, 1.5×10^{19} Ag/cm^3	622-ZnO:Ag/ZnO/MgO/Sa

Appendix B : Example Growth Procedure

1. Heat the growth manipulator/substrate heater (GM) to 750°C over 30 minutes. Wait for at least 30 minutes for the temperature to stabilise. At the same time, set the RF power to 50 W and the RHEED gun to 1.0 A.
2. Heat the Zn cell to 390°C over 30 minutes. Then heat the Zn cell from 390°C to desired flux level over 30 minutes. Wait at least 2 hours for the Zn flux to stabilise.
3. Heat the Mg cell to desired flux level over 30 minutes. Wait at least 1 hour for the Mg flux to stabilise.
4. Heat the Ag cell to desired flux level over 1.5 hours. Wait at least 1 hour for the Ag flux to stabilise.
5. Once all the fluxes are close to being stable, ramp up the RF power to 400 W, at a rate of 50 W per increase, and pausing for 3 minutes after each 50 W increase. Make sure the ion pump valve is closed and the turbo pump valve is opened before increasing the RF power above 50 W.
6. Slowly leak in the O_2. The plasma should strike at around 1×10^{-6} Torr. Slowly increase the O_2 flow rate to 2 sccm, keeping in mind the lag between the MFC reading and chamber pressure gauge. The pressure should be around 1×10^{-5} Torr once the O_2 flow rate is stable at 2 sccm. Wait at least 15 minutes for the plasma to stabilise once the O_2 flow rate is at 2 sccm.
7. When the Mg flux is stable, close all of the shutters and raise the GM. Then start a 10 s MgO growth by opening the O_2 shutter, and then the Mg shutter.
8. After the MgO growth, close the Mg shutter, and then the O_2 shutter. Now lower the GM.
9. Re-open all shutters.
10. Set the Mg cell to 0°C. Set the GM from 750°C to 450°C over 15 minutes. Wait at least 30 minutes for the substrate temperature to stabilise.

11. Slowly reduce the O_2 flow rate to 0.5 sccm, at around 0.01 sccm every few minutes. Once the O_2 flow rate is at 0.5 sccm, let the plasma stabilise for at least 15 minutes. The chamber pressure should be at around 2.4×10^{-6} Torr.
12. Once the plasma is stabilised, check the Zn flux. If small Zn flux changes are needed (eg. 1°C or so), then just set the Zn cell setpoint to that. Wait at least 5 minutes for the Zn flux to re-stabilise before re-measuring the Zn flux. If the Zn flux is still not yet at the desired flux, repeat the process until it is at the desired flux. Note that whenever a shutter is closed and then opened again, a wait of at least 5 minutes is required before the flux is stable and is suitable for measurement.
13. Once the desired Zn flux is reached, close all of the shutters and raise the GM.
14. Start a 2 minute LT-ZnO growth by opening the O_2 shutter, and then the Zn shutter.
15. End the LT-ZnO growth by closing the Zn shutter, and then the O_2 shutter.
16. Lower the GM.
17. Re-open all shutters.
18. Set the GM from 450°C to the desired growth temperature over 15 minutes. Wait at least 30 minutes for the substrate temperature to stabilise.
19. Close all of the shutters and raise the GM.
20. Start the HT-ZnO growth by opening the O_2 shutter, and then the Zn shutter.
21. End the HT-ZnO growth by closing the Zn shutter, and then the O_2 shutter.
22. Start the ZnO:Ag growth by opening the O_2 shutter, and then simultaneously open both the Zn and Ag shutters.
23. End the growth by simultaneously closing the Zn and Ag shutters first, and then the O_2 shutter.
24. Lower the GM and re-open all of shutters.
25. Set the GM to 0°C. Kill plasma by slowly reducing the RF power by 50W every 3 minutes. Once plasma flames out, completely close all the O_2 valves. Then re-open the ion pump valve.

26. Wait at least 5 minutes for the fluxes to re-stabilise and re-measure the Zn (and if possible Ag) flux.
27. If the Ag cell is below 950°C, set the Ag cell to 0°C. Otherwise, ramp it down at around 1°C per minute to 950°C. Then set the Ag cell to 0°C.
28. Set the Zn cell to 350°C over 30 minutes. After 30 minutes has elapsed, set the Zn cell to 0°C.
29. Once all of the effusion cell temperatures and the GM temperature are below 200°C, close the turbo pump valve and spin down the turbo. Then turn off the diaphragm pump.

Appendix C : Multipeak Fitting Results for LT PL

Below are a summary of results from using the multipeak fitting program in IGOR Pro, to deconvolute the various peaks in photoluminescence data. The equations used are either Gaussian (Gaus) (equation (2.33)) or Lorentzian (Lor) (equation (2.34)). The following notations are employed:

- NBEx is the peaks fitted to the near bandedge, typically between 3.34 eV and 3.38 eV. x denotes the peak number, in order of increasing energy.
- 3.3eVx is the peaks fitted to around the 3.3eV region, typically between 3.28 eV and 3.34 eV, and are usually two-electron satellites (TES) or the first LO phonon replicas of neutral donor bound excitons (1LO) peaks. x denotes the peak number, in order of increasing energy.
- 3.21eVx is the peaks fitted to around the 3.21eV region, and is usually the second LO phonon replicas of neutral donor bound excitons (2LO) peaks. x denotes the peak number, in order of increasing energy.
- Otherx are individual peaks fitted at various regions, typically the 1LO or 2LO peaks. x denotes the peak number, in order of increasing energy.

Film Number	Fit Used	Peak	k0	k1	k2	k3
597	Gaus	NBE1	4742	1.0683×10^5	3.3561	0.0038941
		NBE2	4742	1.4619×10^5	3.3569	0.001348
		NBE3	4742	94062	3.3606	-0.001421
		NBE4	4742	84513	3.3636	0.0043971
	Gaus	Other1	609.73	384.71	3.217	0.006226
		Other2	831.53	514.64	3.2879	0.0068838
599	Lor	NBE1	-2407.3	0.45396	3.3564	5.1979×10^{-6}
		NBE2	-2407.3	0.38211	3.3599	2.1567×10^{-6}
		NBE3	-2407.3	0.36162	3.3648	6.1711×10^{-6}
	Gaus	Other1	422.52	321.06	3.2176	0.004916
		Other2	647.24	379.99	3.2879	0.0062198
600	Gaus	NBE1	10628	3.6668×10^5	3.3611	0.0038502
		NBE2	10628	2.3055×10^5	3.3621	0.0011534

Film Number	Fit Used	Peak	k0	k1	k2	k3
		NBE3	10628	57834	3.3684	0.0029754
	Gaus	3.3eV1	5890.1	29362	3.3058	0.013335
		3.3eV2	5890.1	28628	3.3175	0.0055667
		3.3eV3	5890.1	14197	3.3257	0.0051298
602	Gaus	NBE1	3633.3	2.4837×10^{5}	3.3606	0.0039252
		NBE2	3633.3	2.1743×10^{5}	3.362	0.0014238
		NBE3	3633.3	35340	3.3677	-0.0030117
	Gaus	3.3eV1	4445.3	26388	3.3025	0.0093422
		3.3eV2	4445.3	23460	3.3174	0.0078635
603	Gaus	NBE1	5406.6	1.3613×10^{5}	3.3555	0.0040412
		NBE2	5406.6	1.7439×10^{5}	3.3562	0.0013912
		NBE3	5406.6	61390	3.3602	0.001879
		NBE4	5406.6	75520	3.3651	0.0034255
	Gaus	3.3eV1	749.1	575.45	3.2862	0.0064905
		3.3eV2	749.1	243.13	3.294	0.0020929
	Gaus	3.21eV1	509.44	399.65	3.2135	0.0036501
		3.21eV2	509.44	217.14	3.2197	0.0051963
614	Lor	NBE1	-7470.7	1.6658	3.3538	4.058×10^{-6}
		NBE2	-7470.7	0.31913	3.355	8.8969×10^{-7}
		NBE3	-7470.7	0.19838	3.3586	1.72×10^{-6}
		NBE4	-7470.7	0.76822	3.3626	1.3292×10^{-5}
	Lor	Other1	790.81	0.057309	3.2841	3.0138×10^{-5}
616	Lor	NBE1	-1182.1	1.1171	3.355	8.0364×10^{-6}
		NBE2	-1182.1	0.18289	3.3562	9.1632×10^{-7}
		NBE3	-1182.1	0.054021	3.3605	2.2224×10^{-6}
	Lor	3.31eV1	-526.11	1.0644	3.2957	7.7173×10^{-5}
		3.31eV2	-526.11	0.62716	3.3061	9.3294×10^{-5}
		3.31eV3	-526.11	0.54579	3.318	8.3927×10^{-5}
622	Lor	NBE1	-2440.1	1.1972	3.3553	2.0261×10^{-6}
		NBE2	-2440.1	0.97393	3.359	1.2739×10^{-6}
		NBE3	-2440.1	0.18377	3.364	2.7599×10^{-6}
	Gaus	3.31eV1	797.23	923.94	3.3084	0.0056034
		3.31eV2	797.23	3814	3.3225	0.0086221
623	Lor	NBE1	-10.522	0.038143	3.3545	2.7374×10^{-6}
		NBE2	-10.522	0.022602	3.3559	7.4496×10^{-7}
		NBE3	-10.522	0.1343	3.3596	2.1191×10^{-6}
		NBE4	-10.522	0.0046589	3.3618	4.0203×10^{-7}
		NBE5	-10.522	0.026385	3.3643	5.034×10^{-6}
	Lor	3.31eV1	129.47	0.001206	3.3087	1.3904×10^{-5}
		3.31eV2	129.47	0.048624	3.3247	9.588×10^{-5}
	Gaus	Other1	203.35	121.85	3.2876	0.0050939

Film Number	Fit Used	Peak	k0	k1	k2	k3
625	Gaus	NBE1	4521.3	1.4945×10^{5}	3.355	0.0036088
		NBE2	4521.3	1.6765×10^{5}	3.3561	0.0010027
		NBE3	4521.3	15242	3.3615	0.0015917
	Gaus	Other1	588.09	662.37	3.2864	0.0048365
	Gaus	3.31eV1	458.35	309.73	3.3064	0.0064151
		3.31eV2	458.35	2181.9	3.3298	0.018217
626	Lor	NBE1	-1151.8	0.55423	3.3611	6.4466×10^{-6}
		NBE2	-1151.8	0.11059	3.3567	5.7864×10^{-6}
	Gaus	3.3eV1	1448.6	2230.9	3.3025	0.010679
		3.3eV2	1448.6	1345	3.3178	0.0077127
		3.3eV3	1448.6	1035.3	3.325	0.0039397
631	Lor	NBE1	-5988.2	1.3105	3.3575	5.2533×10^{-6}
		NBE2	-5988.2	0.92799	3.3599	1.1402×10^{-6}
		NBE3	-5988.2	0.15179	3.366	2.7482×10^{-6}
	Lor	Other1	1186.7	0.16618	3.3227	3.949×10^{-5}
638	Lor	NBE1	-3198.9	1.2271	3.3581	6.1652×10^{-6}
		NBE2	-3198.9	0.56667	3.3602	1.029×10^{-6}
		NBE3	-3198.9	0.24878	3.366	3.9106×10^{-6}
	Lor	3.31eV1	1260.4	0.01742	3.2891	1.3982×10^{-5}
		3.31eV2	1260.4	0.0029532	3.3092	9.0653×10^{-6}
		3.31eV3	1260.4	0.28313	3.3217	5.933×10^{-5}
641	Gaus	NBE1	10643	3.6842×10^{5}	3.3593	-0.0035682
		NBE2	10643	5.1655×10^{5}	3.3604	0.0011696
		NBE3	10643	32586	3.3662	0.0021058
	Gaus	Other1	1947.6	1320	3.2894	0.0043801
		Other2	2029	4302.1	3.3235	0.0097352
643	Lor	NBE1	847.77	0.31591	3.3565	1.2321×10^{-5}
646	Lor	NBE1	-241.58	0.059042	3.3573	2.7263×10^{-6}
		NBE2	-241.58	0.28327	3.3611	2.3721×10^{-5}
		NBE3	-241.58	0.032136	3.3679	4.2561×10^{-6}
	Gaus	3.31eV1	807.3	815.77	3.294	0.0060445
		3.31eV2	807.3	1232.1	3.3034	0.0080681
		3.31eV3	807.3	768.38	3.3215	0.0077503
659	Lor	NBE1	-11133	4.475	3.3531	1.3722×10^{-5}
		NBE2	-11133	3.9608	3.3555	5.4745×10^{-6}
		NBE3	-11133	0.22454	3.3653	3.7073×10^{-6}
	Gaus	3.31eV1	2116	1731.5	3.2846	0.0040351
		3.31eV2	2116	7025.4	3.2947	0.0070135
		3.31eV3	2116	717.86	3.3066	0.0027871
		3.31eV4	2116	14638	3.3139	0.032919

Appendix D: Lithography Sample Identification

In order to keep track of various samples used in the fabrication of the superlens structure, each of the samples is given a numerical identity, corresponding to each EBL session (eg. Cr-29). Multiple samples patterned during the same EBL session are given the same number but a different suffix (eg. Cr-29A). For superlens imaging experiments, the identifier used is resist-x, where x is a numerical number for each exposure/developing time/wavelength experiment.

Figure/Table	Description	Identifier
Fig. 5.3	Old solutions, Si, dose 100	Cr-29
Fig. 5.4	Old solutions, Si, dose 100	Cr-29
Fig. 5.5	Old solutions, Si, 80s dev	Cr-30
Fig. 5.6	Old solutions, Si, 80s dev	Cr-30
Fig. 5.7	Old solutions, quartz, 80s dev, dose 100	Cr-33
Fig. 5.8	New solutions	Cr-39, 41, 42
Fig. 5.12	Si, Dose 20, with PMGI	Cr-45
Fig. 5.13	Si, Dose 20, with PMGI	Cr-45
Fig. 5.15	Si, line exposures	Cr-50A, B
Fig. 5.16	Quartz, line exposures	Cr-51B
Fig. 5.17		Cr-58A
Fig. 5.18		Cr-62A
Fig. 5.20		Cr-58A
Fig. 5.22	A, B, C, D	Cr-70A, B, C, D
Fig. 5.33		Resist-30 to 35
Fig. 5.34	PR and BARC on Si	Resist-37
Table 5.3	Cr-59A, Cr only	Resist-38 to 41
Fig. 5.35	59A-1	Resist-38
Fig. 5.36	59A-2	Resist-39
Fig. 5.37(a)	PMMA only	Resist-64
Fig. 5.37(b)	2 layer stack	Resist-56
Fig. 5.37(c)	10 layer stack	Resist-74
Fig. 5.25		Cr-86a
Fig. 5.38		Cr-86a
Fig. 5.39	70 min exp., 2s dev.	Resist-87
Fig. 5.40	140 nm PMMA, 700s exp., 2s dev.	Resist-118
Fig. 5.41	80 min exp., 2s dev.	Resist-88

Appendix E: Superlens Fabrication Procedure

1. Ultrasonically clean the quartz substrate in TCE, acetone and methanol for 15 minutes each. Blow dry with N_2 gas after the final solvent clean.
2. Apply one monolayer of HMDS by spin coating at 4000 rpm for 1 minute.
3. Apply 400 nm of ma-N 2403 by spin coating at 4000 rpm for 1 minute.
4. Bake in a convection oven at 95°C for 30 minutes.
5. Apply PEDOT/PSS by spin coating at 5000 rpm for 1 minute at a ramp of 2500 rpm/s.
6. Bake on a hot plate at 80°C for 2 minutes.
7. Write the relevant pattern with EBL using an exposure dose of 20 $\mu As/cm^2$.
8. Remove the PEDOT/PSS layer by soaking in DIW for a few minutes. Blow dry with N_2 gas after all the PEDOT/PSS has been dissolved.
9. Develop with ma-D 525 for 40s at room temperature.
10. E-beam evaporate 50 nm of Cr using gun parameters of 5 kV and 24 mA.
11. Spin coat 150 nm to 180 nm of 5% LMW PMMA, dissolved in chlorobenzene, onto the patterned substrate at 6000 rpm for 1 minute.
12. Bake the sample at 185°C for 30 minutes in a convection oven.
13. Repeat steps 10 and 11.
14. RIE etch the PMMA for 15 s using the parameters in Table 5.1.
15. Wait for 5 minutes and then repeat step 13.
16. Wait for 5 minutes, then measure the resultant PMMA thickness by forming a step height using EBL. Coat with PEDOT/PSS to reduce the charging effects prior to the EBL. Using profilometry or AFM, measure the step height.
17. Repeat steps 13 to 15 until the PMMA is at 50 nm.
18. Leave the sample in the 185°C oven overnight to reflow the PMMA.
19. DC sputter 10 nm of Ag at 150 W.
20. RF sputter 10 nm of ZnO at 100 W.
21. Repeat steps 18 and 19 until 10 layers have been grown.

Appendix F: Vapour Pressure Data

The vapour pressure data reproduced here were taken from ref. [32] to calculate theoretical flux curves for Ag, Mg, and Zn.

Pressure (Torr)	Ag Temperature (°C)	Mg Temperature (°C)	Zn Temperature (°C)
1	1,322	605	487
1×10^{-1}	1,162	509	408
1×10^{-2}	1,027	439	344
1×10^{-3}	922	377	292
1×10^{-4}	832	327	247
1×10^{-5}	752	282	209
1×10^{-6}	685	246	177
1×10^{-7}	626	214	147
1×10^{-8}	574	185	123

Appendix G: Negative Refractive Index

Maxwell's equations are given by [84, 200]

$$\boldsymbol{k} \times \boldsymbol{E} = \omega\mu\mu_0\boldsymbol{H} \tag{1}$$

and

$$\boldsymbol{k} \times \boldsymbol{H} = \omega\varepsilon\varepsilon_0\boldsymbol{E} \tag{2}$$

where **k** is the wave vector, **E** is the electric field, and **H** is the magnetic field. By time averaging and cross multiplying (1) and (2), we obtain [84]

$$\boldsymbol{k} = \frac{\omega\mu\mu_0}{{E_0}^2}\boldsymbol{E_0} \times \boldsymbol{H_0} = \frac{\omega\varepsilon\varepsilon_0}{{H_0}^2}\boldsymbol{E_0} \times \boldsymbol{H_0} \tag{3}$$

The time-averaged energy flux density **S** is given by

$$\boldsymbol{S} = u\boldsymbol{v_g} = \boldsymbol{E_0} \times \boldsymbol{H_0} \tag{4}$$

where u is the time-averaged energy density, $\mathbf{v_p}$ is the group velocity, and $\mathbf{E_0} \times \mathbf{H_0}$ is the time-averaged Poynting vector. By combining (3) and (4), we obtain

$$\boldsymbol{k} = \frac{\omega\mu\mu_0}{{E_0}^2}\boldsymbol{S} = \frac{\omega\varepsilon\varepsilon_0}{{H_0}^2}\boldsymbol{S} \tag{5}$$

and

$$\boldsymbol{k} = \frac{\omega\mu\mu_0}{{E_0}^2}u\boldsymbol{v_g} = \frac{\omega\varepsilon\varepsilon_0}{{H_0}^2}u\boldsymbol{v_g} \tag{6}$$

Therefore for negative ε and μ, the propagation of the phase **k** is anti-parallel to the propagation of the energy **S**. In addition, the phase velocity $\mathbf{v_p}$ and group velocity $\mathbf{v_g}$ are anti-parallel [82, 84, 200-204].

Now assume a material with positive ε and μ located next to a material with negative ε and μ (Fig. G.1). As the parallel component of **k** at the planar interface is conserved [82, 84, 204], to satisfy Snell's law

$$\frac{\sin\varphi}{\sin\phi} = \frac{n_2}{n_1} \tag{7}$$

n_2 must be negative, since the phase and group velocities are anti-parallel. That is, the path taken for negative ε and μ is path 1-3. Hence a negative ε and μ requires that the negative root is taken.

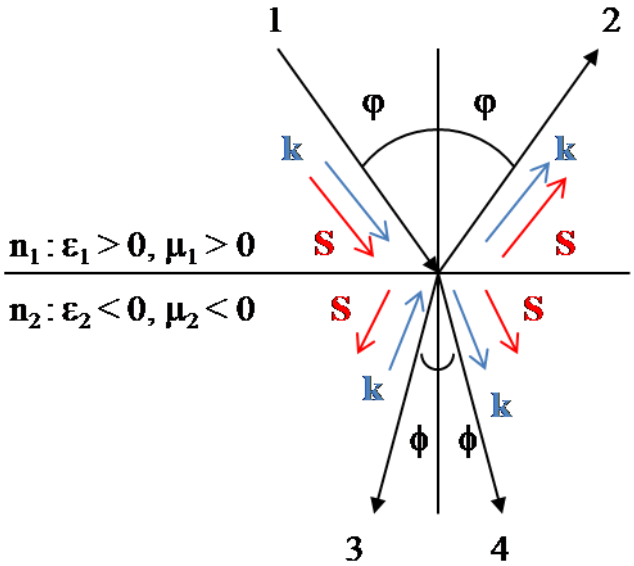

Fig. G.1. Reflection and refraction at the interface between materials with opposite handedness [82, 84, 204].